MODELING CATHODIC PROTECTION FOR PIPELINE NETWORKS

By

DOUGLAS P. RIEMER

A DISSERTATION PRESENTED TO THE GRADUATE SCHOOL
OF THE UNIVERSITY OF FLORIDA IN PARTIAL FULFILLMENT
OF THE REQUIREMENTS FOR THE DEGREE OF
DOCTOR OF PHILOSOPHY

UNIVERSITY OF FLORIDA

2000

ACKNOWLEDGEMENTS

This work was jointly supported by the Pipeline Research Council International and the Gas Research Institute through Contract Number PR-101-9512.

TABLE OF CONTENTS

LIST OF TABLES

Table page

LIST OF FIGURES

Figure page

KEY TO SYMBOLS

Φ = Potential and potential distribution

V = Voltage distribution in the pipe steel and anode material

$\boldsymbol{i}$ = Current density

E_i = Equilibrium potential for species i

β_i = Tafel slope

F = Faraday's constant

R = Gas constant

T = Temperature

k = Kinetic parameter

κ = Conductivity

c_i = Concentration of species i

t = Time

$\boldsymbol{J}_i$ = Flux vector of species due to fields

$\mathbf{N}_i$ = Net flux vector of species i

R_i = Rate of generation of species i

D_i = Diffusion coefficient for species i

z_i = Charge on species i

u_i = Mobility of species i

I = Ionic strength

q_i = Kirchhoff transformation variable for species i

Q = Quasi-potential

Ω = Domain for which a differential equation applies

Γ = Boundary of a domain

$\vec{n}$ = Outward normal vector of boundary

w = Arbitrary weighting function

G = Green's function

ξ = Source point in Green's function

x = Field point in Green's function

δ = Dirac delta function

r = Euclidian distance between two points

$\boldsymbol{G}$ = Matrix of coefficients from the right hand integral of 3-9

$\boldsymbol{H}$ = Matrix of coefficients from the left hand integral of 3-9

$\boldsymbol{A}$ = Matrix of columns from the $\boldsymbol{H}$ and $\boldsymbol{G}$ matrices

Ψ = defined as $V - \Phi$

$\vec{n}$ = Outward normal vector of boundary

$\boldsymbol{K}$ = Matrix resulting from Finite Element Method

n = total number of nodes in a problem

ne = total number of elements in a problem

nen = number of nodes in an element

nce = number of elements having a given node in common

Abstract of Thesis Presented to the Graduate School
of the University of Florida in Partial Fulfillment of the
Requirements for the Degree of Doctor of Philosophy

MODELING CATHODIC PROTECTION FOR PIPELINE NETWORKS

By

Douglas P. Riemer

December 2000

Chair: Dr. Mark E. Orazem
Major Department: Chemical Engineering

An extensive network of buried steel pipelines is used throughout the world to transport natural gas and liquid petroleum products. In the United States alone, there are over 1.3 million miles of pipe used to transport natural gas. Failure to prevent external corrosion of pipelines can have disastrous consequences. A butane line explosion, which cost the lives of two persons, was caused by external corrosion attributed to inadequate cathodic protection. Proper cathodic protection is particularly important today because the pipelines constructed during the construction boom of the 1960s and 1970s are aging, and the encroachment of suburban housing construction increases the potential for property damage and loss of life.

Standard cathodic protection design equations, based on the assumptions that pipes are isolated and have a uniform bare metal surface, are not valid for modern complex pipeline networks. The object of this work was to develop a

mathematical model that can describe correctly the complex interactions seen in cathodic protection of complex pipeline networks. The governing differential equation is solved in 3-dimensions for the conductance of current through the soil, steel, and connections between pipes and anodes. The model accounts for the kinetics of the corrosion, mass-transfer-limited oxygen reduction, and hydrogen evolution reactions. It also accounts for the nonuniform current and potential distributions due to pipe-pipe interactions, coating flaws, and anode locations. Current and potential distributions are calculated around the circumference and along the length of the pipes.

This dissertation describes the solution techniques needed to solve the system of equations that couple nonlinear reaction kinetics, passage of current through soil, and passage of current through pipeline steel. Sample calculations will be presented to show the complicated nature of the interactions between adjacent pipelines.

CHAPTER 1
PIPELINES AND CATHODIC PROTECTION

1.1 Introduction

Since the beginning of the 20th century, petroleum products and natural gas have been transported over long distances by buried steel pipelines. There are over 1.28 million miles of buried steel main-line pipe for the transport of natural gas alone. [1] There are, in addition, 170,000 miles of pipeline for transport of crude oil and refined products.[2]

These pipes are generally in soil environments which contain oxygen in an electrolyte and therefore are subject to corrosion. By the late 1920s, the number of leaks had begun to increase alarmingly, and, by the early 1930s, all major pipeline owners were providing some measure of corrosion mitigation to their pipelines, including application of coatings and cathodic protection.[3] The application of corrosion mitigation strategies has in general been successful. Most pipeline failures are now attributed to mechanical damage. Nevertheless, over a six-year period, (1994-1999), 408 separate incidents were attributed to corrosion, resulting in a net loss of $75 million and 4 lives.* Additional failures, later deemed to have been caused by corrosion, are listed under "other." It is therefore difficult to assess,

* Data compiled from the U.S. Office of Pipeline Safety statistics for 1994-1999 for transmission and distribution of liquid petroleum products and natural gas.

Figure 1-1: Post explosion flare-off of leaking gas from a burst pipeline. The burst was later attributed to corrosion weakened walls of the pipe.[2]

from government statistics, the net loss of property and life that can be attributed to failure to provide proper corrosion protection.

For example, a pipeline that ran through a residential neighborhood in a small Texas valley burst releasing butane in 1996.[2] Two persons tried to escape by driving away, but the ignition system of their vehicle ignited the vapor cloud, killing them. The post explosion results of the effects of unmitigated corrosion are shown in Figure 1-1.

Investigation of the section of pipe showed that the burst was caused by weakening of the steel through corrosion from the outside of the pipe Figures 1.2(a) and 1.2(b). It was determined in the investigation that the cathodic protection systems were not properly maintained to U.S. DOT standards. The pipeline operating company was fined (January 2000) 30 million dollars for this and other non-fatal leaks.[4]

There are other examples of catastrophic failure due to corrosion, but the larger problem is often small leaks due to coating failure and insufficient cathodic protection. There are currently 7 bills before congress (October 2000) that address

(a)

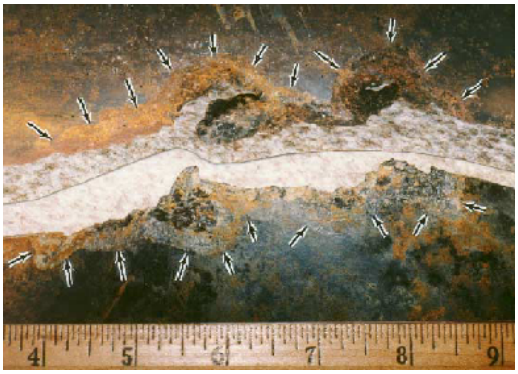

(b)

Figure 1-2: Failed section of the butane pipe. a) an overview showing the size of the ruptured seam; b) a closeup of the failed section of pipe. The burst seam in the pipe followed a line of severe corrosion.[2]

pipeline safety. The joint bill[5] and amendments[6] propose new research that includes a call for better understanding of corrosion and cathodic protection of pipelines.

Typically such catastrophic failures are prevented by aggressive monitoring of the cathodic protection systems coupled with inspection of suspect regions of the pipeline. Yet, wall loss due to corrosion is sometimes evident even on pipes that, according to standard CP monitoring techniques, are nominally well protected. There is clearly a need to improve our understanding of cathodic protection. The issue of cathodic protection is particularly relevant today because the pipelines constructed during the construction boom of the 1960s and 1970s are aging, and the encroachment of suburban housing construction increases the potential of property damage and loss of life. The design of cathodic protection systems is complicated by the current practice of placing an increasing number of pipes in a right-of-way, and by the increasing number of crossings due to more pipes being laid. The combination of these factors greatly increases the potential for stray current effects.

Cathodic protection is a means in which an undesirable reaction is replaced by a more desirable one on another surface. In the case of buried metallic structures, the undesirable reaction is the dissolution of the metal.

$$\mathrm{M} \rightarrow \mathrm{M}^{n+} + ne^{-} \tag{1-1}$$

Cathodic protection works by having a second surface within the conductive soil or electrolyte at a more negative potential than the pipe steel would have. This surface is then connected to the pipe with a wire as shown in Figure 1-3.

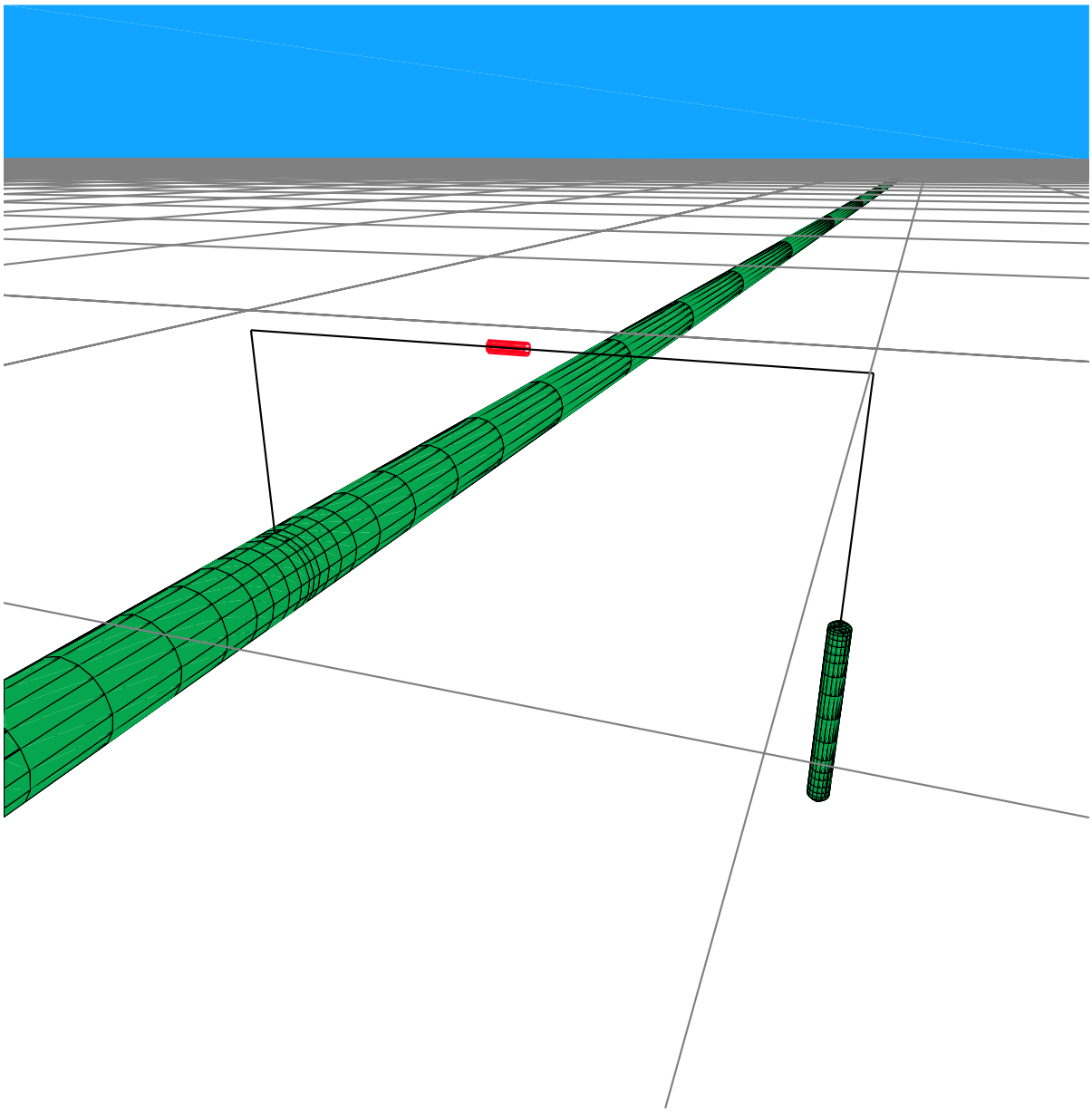

Figure 1-3: Pipe and anode system used for cathodic protection of buried pipelines. The anode is the smaller vertical cylinder on the right. The red cylinder in-line with the connecting wire is a resistor that is usually inserted in the circuit to control the amount of current driven to the pipe in order to limit hydrogen evolution.

Since the anode and pipe are electrically linked, the more active (negative) surface will tend to favor a reduction reaction, while an oxidation reaction will be favored on the more positive surface. With careful selection of anode metals, the rate of oxidation of the pipe steel can be reduced to a level which will result in a much longer service life.

High resistance coatings are used on most pipelines to reduce the amount of current necessary to protect the pipeline. However, the introduction of nicks and scrapes which expose bare steel cannot be avoided during installation. Its is therefore absolutely necessary to use cathodic protection (CP) on coated pipes since experience has shown that not using CP results in accelerated failure.[7] Even though CP is necessary for coated pipes, the cost savings when coatings are used makes the practice desirable.

A better understanding of the behavior of a coated pipeline under cathodic protection can be obtained by solving a mathematical model of the governing differential equations. A model is usually set up in a rectangular domain where the boundary conditions are constant on any given side. However, the boundary conditions for pipelines under cathodic protection are not uniform or constant on any plane (i.e., $\Phi = 0\text{V}$ at $z = 1\text{ft}$ or $\vec{n} \cdot \nabla\Phi = 1\mu\text{A/cm}^2$ at $r = R$). There are three reasons for this. The first is that the pipes are cylindrical. Laplace's equation for right circular parallel cylinders can be solved analytically if the boundary condition is constant on the surface of the pipe.[8] However, this method of solution cannot be used for the problem treated here because the anodes do not run parallel to the pipe (see Figure 1-3). Second, coating failures can be discrete. One cannot use the uniform boundary condition ($\Phi = c$ at $z = 0$ or $\vec{n} \cdot \nabla\Phi = c$ at $r = R$) since

the potential and current density will be different for a discrete holiday than for coated steel. The boundary conditions are nonlinear mathematical expressions that relate the net current density of the chemical reactions on the pipe surface to the potential driving force.

1.2 Electrode Kinetics (Butler-Volmer)

Some assumptions about the knowledge of the reader are made in the following sections. It is assumed he has a basic knowledge of electrochemistry. Good sources of the necessary concepts can be found in Bockris and Reddy[9, 10] and in Bard and Faulkner.[11] The best treatment of the mathematics describing the physics is in Newman.[12]

The first step taken in developing a mathematical model for cathodic protection of steel is to understand the role of the electrochemical reactions that take place on the steel and anode surfaces.

Bockris *et al.* [13] have developed a pH-dependent mechanism for an iron electrode. They proposed that the electrochemical reactions that take place on the surface of an electrode may be developed in the following way:

Iron corrodes according to two mechanisms depending on the pH. Buried structures under cathodic protection in soil form alkaline environments.[3] The corrosion step for high pH values is

$$\mathrm{Fe} + 2\mathrm{OH}^- \xrightarrow{\text{R.D.S.}} \mathrm{Fe(OH)_2} + 2\mathrm{e}^- \tag{1-2}$$

and

$$\mathrm{Fe(OH)_2} \rightleftharpoons \mathrm{Fe}^{2+} + 2\mathrm{OH}^- \tag{1-3}$$

where R. D. S. stands for Rate-Determining Step. The sum of reactions (1-2) and (1-3) results in the net reaction

$$\mathrm{Fe} \rightleftharpoons \mathrm{Fe}^{2+} + 2\mathrm{e}^{-} \tag{1-4}$$

which is an anodic reaction when the reaction proceeds from left to right.

For iron deposition the reactions are written as

$$\mathrm{Fe(OH)_2} \rightleftharpoons \mathrm{Fe}^{2+} + 2\mathrm{OH}^{-} \tag{1-5}$$

and

$$\mathrm{Fe(OH)_2} + 2\mathrm{e}^{-} \xrightarrow{\text{R.D.S.}} \mathrm{Fe} + 2\mathrm{OH}^{-} \tag{1-6}$$

which are cathodic reactions when proceeding from left to right.

Newman provides a development for reactions with multiple single electron steps in Chapter 8 of his text.[12] The anodic current density as a function of pH and potential was given by Bockris *et al.* to be[13]

$$i_a = k_{a,\mathrm{Fe}} a_{\mathrm{OH}^-} e^{\left[\frac{VF}{RT}\right]} \tag{1-7}$$

where $k_{a,\mathrm{FE}}$ is the kinetic rate constant, a_{OH^-} is the activity of OH^- ions, V is defined as $\Phi_{\text{metal}} - \Phi_{\text{solution}}$, F is Faraday's constant (96487 coulombs /equiv), R is the Gas Constant and T is temperature. The activity of the OH^- ions is linear with respect to pH.

The cathodic current was given by

$$i_c = k_{c,\mathrm{Fe}} a_{\mathrm{Fe}^{2+}} a_{\mathrm{OH}^-} e^{\left[\frac{-VF}{RT}\right]} \tag{1-8}$$

where $a_{\mathrm{Fe}^{2+}}$ is the activity of Fe^{2+} ions, and the net current density i is given by

$$i = i_a + i_c \tag{1-9}$$

At equilibrium, where only equations (1-7) and (1-8) are taking place, the equilibrium potential V_o can be found by equating equations (1-7) and (1-8) and solving for V

$$V_o = \frac{RT}{F} \ln \left[\frac{\kappa_{c,\mathrm{Fe}} a_{\mathrm{Fe}^{2+}}}{\kappa_{a,\mathrm{Fe}}} \right] \tag{1-10}$$

where V_o is defined as the equilibrium potential. Then the exchange current density can be defined to be

$$i_o = \kappa_{a,\mathrm{Fe}} a_{\mathrm{OH}^-} e^{\left[\frac{V_o F}{RT}\right]} \tag{1-11}$$

using the anodic term. The cathodic term would have the same current density at V_o. Substituting in the expression for V_o into equation (1-11) obtains the proper expression

$$i_o = \kappa_{a,Fe}^{1/4} \kappa_{c,Fe}^{3/4} a_{Fe^{2+}}^{3/4} a_{OH^-} \tag{1-12}$$

Equation (1-9 can be rewritten in terms of the exchange current density as

$$i = i_o \left(e^{\left[\frac{VF}{RT}\right]} - e^{\left[\frac{-VF}{RT}\right]} \right) \tag{1-13}$$

or

$$i = i_o 2 \sinh \left(\frac{VF}{RT} \right) \tag{1-14}$$

The number of unknowns in equation (1-13) can be reduced by changing the base from e to 10 and defining Tafel slopes as

$$\beta_a = \frac{2.303F}{RT} \tag{1-15}$$

$$\beta_c = \frac{2.303F}{RT} \tag{1-16}$$

and then moving all pre-exponential terms into the exponent to get

$$i = 10^{\left[\frac{V-E_a}{\beta_a}\right]} - 10^{\left[\frac{V-E_c}{\beta_c}\right]} \tag{1-17}$$

where E_a is fit to experimental data. Using large-scale experiments, ARCO personnel found values of E_a to be around -0.56 V referenced to $Cu/CuSO_4$.[14]

1.3 Mixed Potential Kinetics

For freely corroding systems, conservation of charge requires that the anodic corrosion reaction, *e.g.*

$$Fe \rightarrow Fe^{2+} + 2e^- \tag{1-18}$$

be balanced by a cathodic reaction such as

$$O_2 + 2H_2O + 4e^- \rightarrow 4OH^- \tag{1-19}$$

which is called the oxygen-reduction reaction. The expression for the rate of the oxygen reaction can also be assumed to be Tafelian in nature. Thus, a two-parameter expression can be obtained in the same way as was done for the iron reactions. When an active metal anode (Zn or Mg) is connected to a pipe, the potential shifts sufficiently negative and a second cathodic reduction reaction takes place

$$2H_2O + 2e^- \rightarrow H_2 + 2OH^- \tag{1-20}$$

Reaction (1-20) is commonly called the hydrogen evolution reaction. The mechanism of the hydrogen evolution reaction is currently a topic of research.[15, 16, 17, 18, 19] The hydrogen evolution reaction follows Tafel kinetics so an equation of the same type as the cathodic reaction for iron is used. It also can have the number of unknowns reduced to two following equation (1-17)

$$i = 10^{\left[\frac{V-E_{a,H_2}}{\beta_{a,H_2}}\right]} - 10^{\left[\frac{V-E_{c,H_2}}{\beta_{c,H_2}}\right]} \tag{1-21}$$

The corrosion potential V_{corr} is the potential difference between a reference electrode and a freely corroding surface. The corrosion potential differs from equilibrium potential described by equation (1-10) because more than one reaction takes place. The corrosion potential is also a function of the oxygen content and transport characteristics for oxygen within the electrolyte of the system. When the level of oxygen is low, a more negative corrosion potential is seen which can be associated with a lower corrosion rate.

The total current is given by the sum of equations of the form of (1-17). There is one for each reaction, and the sum can be written as

$$\begin{aligned} i \quad = & 10^{\left[\frac{V-E_{a,Fe}}{\beta_{a,Fe}}\right]} - 10^{\left[\frac{V-E_{c,Fe}}{\beta_{c,Fe}}\right]} + \\ & 10^{\left[\frac{V-E_{a,O_2}}{\beta_{a,O_2}}\right]} - 10^{\left[\frac{V-E_{c,O_2}}{\beta_{c,O_2}}\right]} + \\ & 10^{\left[\frac{V-E_{a,H_2}}{\beta_{a,H_2}}\right]} - 10^{\left[\frac{V-E_{c,H_2}}{\beta_{c,H_2}}\right]} \end{aligned} \tag{1-22}$$

Equation (1-22) can often be simplified by observing that some terms can be ignored in the potential range of interest. A corrosion potential may be calculated from this equation by setting it equal to zero and solving for $V = V_{\text{corr}}$. This is the same potential that is measured under a zero current experimental condition. A potential is taken with a reference electrode just outside the surface of the metal.

1.4 Application to Corrosion in an Electrolyte

If there are two different interconnected metals contained in a continuous electrolyte, one metal will corrode at a higher rate than it would alone while the other metal will corrode at a lower rate. If the kinetics are known, they can be used as boundary conditions in a numerical method. Equations of the form of (1-22) are

used to describe the kinetics at the boundary. Often, one of the reactions will have a mass-transfer limitation. This is because the reactant must come from the electrolyte. One common form is one that was published by Nisoncioglu[20, 21, 22] and adapted for steady state soil systems by Yan *et al.* [23] and Kennelly *et al.* [24] For bare steel it takes the form

$$i = 10^{\frac{V-\Phi-E_{Fe}}{\beta_{Fe}}} - \left(\frac{1}{i_{\text{lim},O_2}} - 10^{\frac{V-\Phi-E_{O_2}}{\beta_{O_2}}} \right)^{-1} - 10^{\frac{-(V-\Phi-E_{H_2})}{\beta_{H_2}}} \tag{1-23}$$

where i_{lim,O_2} is the mass transfer limited current density for oxygen reduction. This means that the portion of the current due to oxygen reduction cannot exceed the value i_{lim,O_2}. There is no such limitation for the hydrogen-evolution-reaction, since it is assumed that there is always sufficient water next to the pipe for that reaction to proceed under kinetic limitation.

1.5 Passivation and Film Formation

The production of OH^- by oxygen reduction and hydrogen evolution reactions (1-19) and (1-20), respectively, increases the value of pH at the pipe surface. The pH on bare steel has been reported to be on the order of 10-12.[3] This is because the by product of corrosion is the formation of hydroxide ions. At this pH level, $Fe(OH)_2$ becomes insoluble and forms a film on the surface of the metal. Such films can block the transport of oxygen and cause the corrosion potential to change.[25] One may use a Pourbaix diagram to determine what films are stable (if any) at a given pH (see Figure 1-4).

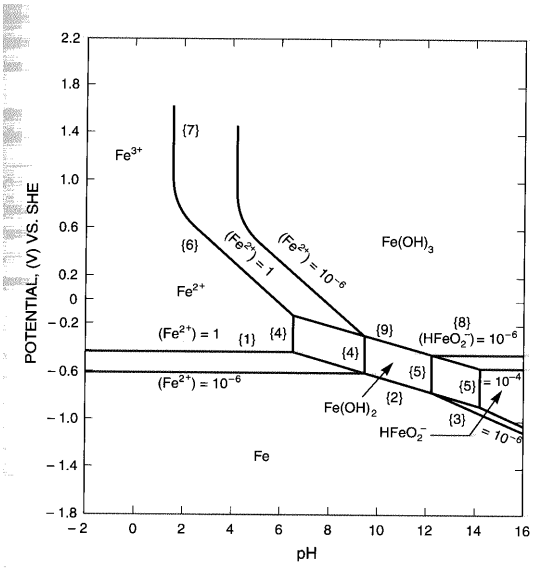

Figure 1-4: Pouraix diagram for iron.[25]

1.6 Coatings

To reduce the amount of current required to provide cathodic protection, coatings are applied to the steel surface before burial. These coatings are usually polymers but can sometimes be cement-based products.

When a coating is applied to a buried pipeline, cathodic protection must be used, or the pipeline will experience perforation due to corrosion in a far shorter time than would be experienced if the pipe were left bare. Isolated faults in the coating (holidays) can form a galvanic couple with the coated parts, accelerating the corrosion rate of the holiday.

It is then necessary to model the behaviour of coatings and the steel under the coating when under cathodic protection. It is known that some current will pass through some coatings after they have absorbed water.[26, 27, 28, 29, 30] Corfias *et al.* have shown that the pore structure expands as the coating absorbs water.[27] They also shown that the conductivity greatly increases with immersion time.

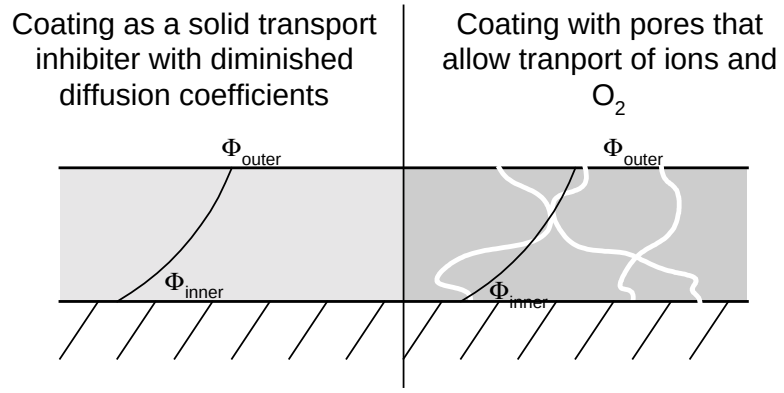

Figure 1-5: Diagram of coating model.

Riemer and Orazem have modified equation (1-23) to take into account the existence of an electrically resistive diffusion barrier.[31, 32] This barrier may be an insoluble oxide film or a polymeric coating applied before the pipe was buried. Figure 1-5 shows two possible behaviours of a conducting coating model. The left side of the figure shows a uniform diffusion/electrical barrier. The right side shows a barrier with small micropores through which an electrolyte can flow and form an electrical connection.

The Potential drop through the film or coating can be expressed as [33]

$$i = \frac{\Phi - \Phi_{in}}{\rho\delta} \tag{1-24}$$

where Φ is the potential in the electrolyte next to the coating, Φ_{in} is the potential at the underside of the coating just above the steel, ρ is the resistivity of the coating and δ is the thickness of the coating. The current density can also be written in terms of the electrochemical reactions that take place under the coating if the

coating is viewed as either a porous structure or as a uniform diffusion barrier

$$i = \frac{A_{\text{pore}}}{A}\left[10^{\frac{V-\Phi_{in}-E_{Fe}}{\beta_{Fe}}} - \left(\frac{1}{(1-\alpha_{block})\, i_{lim,O_2}} - 10^{\frac{V-\Phi_{in}-E_{O_2}}{\beta_{O_2}}}\right)^{-1} - 10^{\frac{-\left(V-\Phi_{in}-E_{H_2}\right)}{\beta_{H_2}}}\right] \tag{1-25}$$

where $\frac{A_{\text{pore}}}{A}$ is the effective surface area available for reactions, and α_{block} is the reduction to the transport of oxygen through the barrier. It is also assumed that the coating has absorbed enough water that the hydrogen evolution reaction is not mass-transfer limited. Equations (1-24) and (1-25) are solved simultaneously to get a value of the current density. The current density is eliminated to give

$$\frac{A\left(\Phi-\Phi_{\text{in}}\right)}{A_{\text{pore}}\rho_{\text{film}}\delta_{\text{film}}} = 10^{\frac{V-\Phi_{\text{in}}-E_{\text{Fe}}}{\beta_{\text{Fe}}}} - \left(\frac{1}{(1-\alpha_{\text{block}})\, i_{\text{lim},O_2}} - 10^{\frac{V-\Phi_{\text{in}}-E_{O_2}}{\beta_{O_2}}}\right)^{-1} - 10^{\frac{-\left(V-\Phi_{\text{in}}-E_{H_2}\right)}{\beta_{H_2}}} \tag{1-26}$$

which is solved by a Newton-Ralphson method to get Φ_{in}. The current density can subsequently be readily calculated from equation (1-24).

Recent work by NOVA Gas[34] and CC Technologies,[29, 35, 36] showed that the coatings on steel pipe form a diffusion barrier when placed in aqueous environments and that the coating absorbs water. They have shown that it is possible to polarize slightly the steel under a disbonded coating.

Examples of polarization curves associated with equations (1-23) and (1-25) are given in Figure 1-6. The corrosion potential can be calculated from equation (1-25) since there is no current through the coating. If $(1-\alpha_{\text{block}})$ is smaller than the pore ratio, then the metal will be more active than bare steel. If they are the same, then the coated pipe and bare steel will have the same corrosion potential. If $(1-\alpha_{\text{block}})$ is larger than the pore ratio, the metal under the coating will be more noble than bare steel and form a galvanic couple that enhances the corrosion rate of the holiday with no CP.

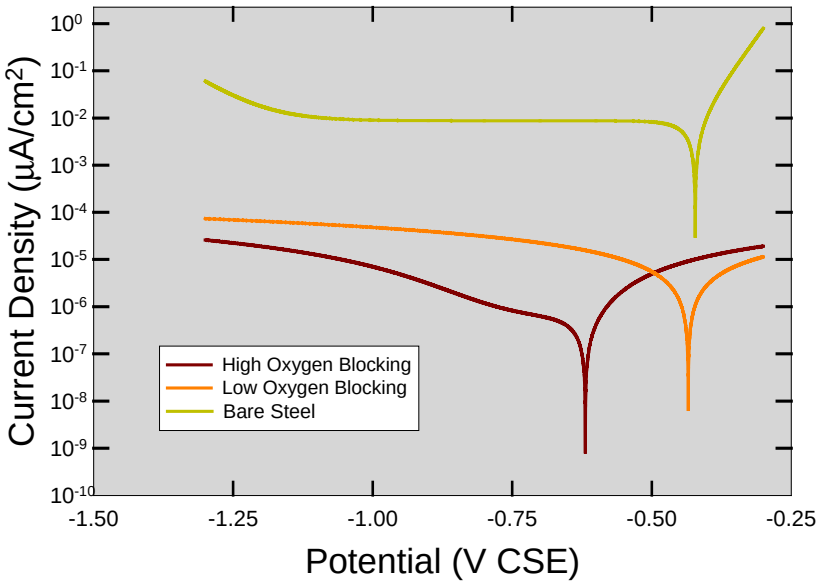

Figure 1-6: Typical polarization curves associated with bare and coated steel.

1.7 Anode Polarization

Anodes undergo similar electrochemical processes as the pipes. The corrosion term can again be expressed as one half of an oxidation-reduction reaction where the half of interest is the corrosion (oxidation) of the anode material. Both galvanic and impressed current anodes are used.

1.7.1 Galvanic Anodes

A galvanic anode is a metal that is more active than the metal that needs to be protected. For carbon steel, zinc and magnesium are used in soil environments and aluminum is used in sea water. Aluminum does not have a large enough driving force to be effective in soil where the resistivity is much higher.

A simple model for a galvanic anode would be:

$$i = i_{O_2}\left(10^{(V-\Phi-E_{corr})/\beta_{anode}} - 1\right) \tag{1-27}$$

Table 1.1: Parameters for common galvanic anodes.[7]

Anode Type	E_{eql} (mV CSE)	β (mV/decade)	i_{O_2} (μA/cm^2)
Al	-1.0	60	1.0
Zn	-1.1	60	1.0
Mg (Standard)	-1.5	60	1.0
Mg (High Potential)	-1.75	60	1.0

where i_{O_2} is the mass-transfer-limited current density for oxygen reduction, E_{corr} is the free corrosion (equilibrium) potential of the anode and β is the Tafel slope for the anode corrosion reaction. Hydrogen evolution was ignored for galvanic anodes because it only makes a small contribution to the net current at operating potentials.

The reduction reaction term (the negative contribution to equation (1-27)) was assumed to be constant because the operating conditions are such that the reduction is always mass-transfer-limited. The reaction is mass-transfer-limited because the driving force for the reduction reaction is higher than that for steel which when freely corroding, is at the mass-transfer-limitation.

The three parameters of the model are generally known for all types of galvanic anodes. Some typical values are given in Table 1.1.

1.7.2 Impressed Current Anodes

Impressed current anodes do not obtain their driving force from the activity of one metal relative to another. Instead, an outside current source such as a rectifier provides the activity. This means that the current densities obtainable on impressed current systems are usually an order of magnitude higher than can be obtained with galvanic anodes.

Impressed current systems consist of a dimensionally stable anode connected to the positive terminal of a direct-current (DC) rectifier. The negative terminal of the rectifier is connected to the pipe. The rectifier can then be used to push the potential of the anode to any desired potential that is more negative than the pipe. Impressed current system can protect a much longer section of pipe because they can provide a larger potential driving force for current flow in the soil. They also can be used to greater effect in highly resistive soils.

Since the anodes do not react, the usual reaction of metal dissolution, equation (1-4), is not appropriate. The most likely reactions are water oxidation and chloride oxidation. They proceed respectively as follows

$$2H_2O \rightarrow O_2 + 4H^+ + 4e^- \tag{1-28}$$

and

$$2Cl^- \rightarrow Cl_2 + 2e^- \tag{1-29}$$

The model for an impressed current anode is similar to that for galvanic anodes. An additional term is added to the exponent to account for the potential setting of the rectifier, *i.e.*,

$$i = i_{O_2}\left(10^{(V-\Phi-\triangle V_{\text{rectifier}}-E_{O_2})/\beta_{O_2}} - 1\right) \tag{1-30}$$

where $\triangle V_{\text{rectifier}}$ is the voltage added by the rectifier, V is the voltage of the anode, Φ is the voltage just outside the surface of the anode, E_{O_2} is the equilibrium potential for the oxygen evolution reaction, and β_{O_2} is the tafel slope for the oxygen evolution reaction.

Table 1.2: Parameters for the oxygen and chlorine evolution reactions.[25]

reaction	Equil Potential (E)	Tafel Slope (β)
O_2 evolution	-172 mV (CSE)	100 mV/decade
Cl_2 evolution	50 mV (CSE)	100 mV/decade

If chloride ions are present, reaction (1-29) can occur which is the chlorine evolution reaction. the reaction occurs in environments such as salt mashes and estuaries where there is salt in the soil.

Parameters for reactions (1-28) and (1-29) are given in Table 1.2 except for i_{O_2} which must be determined experimentally.

1.8 Conclusions

This chapter has presented the problems facing engineers combating corrosion of buried pipelines. Cathodic protection is used to slow the rate of corrosion but is not well understood for complicated pipeline networks. To further the understanding of the operation of cathodic protection systems, a mathematical model has been developed under the constraints of the kinetics are transport associated with corrosion in a soil system.

The model is developed in the next three chapters under the assumption that the reader is familiar with the principles of the calculus of variations, vectors and tensors, and transport in electrolytes. Chapter 11 of Newman's text provides a good introduction to transport in electrolytes.[12] Aris provides an excellent treatise on vectors and tensors.[37]

Furthermore, the appendices assume the reader is well instructed in the C and C++ programing languages and Microsoft® Windows program development. There are several good sources for C and especially C++ programing informa-

tion. One standard textbook is by Deitel and Deitel.[38] One of the best books to convey the concepts and power of C++ is by Bruce Eckel.[39] There are a myriad of books that concern themselves with how to write Microsoft Windows based applications. Almost any bookstore will have an entire aisle devoted to them.

The mathematical model for cathodic protection of pipeline networks is reported in the next chapters. Chapter 2 shows the derivations for the equations that describe the flow of current through the soil and through the pipe steel. Chapter 3 describes the numerical techniques that were used to solve the differential equations. Finally, Chapter 4 goes into the details of applying the nonlinear mathematical expressions for the kinetics of pipes under cathodic protection as boundary conditions for the differential equations. Chapter 4 also describes how addition equations and unknowns are added to the numerical method to describe several more aspects of the physics that are not accounted for in the differential equations derived in Chapter 2, such as multiple independent cathodic protection systems within the same environment.

Results of the model and their implications for design of cathodic protection systems are reported in Chapters 10 to 12. Specifically, Chapter 10 shows how holidays affect neighboring pipes and other holidays in the vicinity.

The intervening chapters discuss how the model was verified, and how performance and accuracy were obtained.

CHAPTER 2
MATHEMATICAL DEVELOPMENT

The model for cathodic protection must account for the flow of current in the soil, in the pipes, and in the circuitry. Until recently, most models of cathodic protection of pipelines assumed that the pipe steel was an equipotential surface. While it may be true for small electrodes with high conductivities and low current densities, long pipes exhibit a non-negligible potential difference along the steel.[3, 7, 40]

Therefore, there are two separate domains for the flow of current. The first is the soil domain up to the surfaces of the pipes and anodes. The boundary conditions for the soil domain are the kinetics of the corrosion reactions as described in section 1.2. The second domain is the internal pipe metal, anode metal and connecting wires for the return path of the cathodic protection current.

2.1 Soil Domain

The corrosion problem discussed in Chapter 1 serves as the boundary conditions for the soil domain which is governed by Laplace's equation. The equation can be derived by imposing conservation of charge on Ohm's Law. Ohm's Law is given by

$$\boldsymbol{i} = -\kappa \nabla \Phi \tag{2-1}$$

where $\boldsymbol{i}$ is the current density vector, κ is the conductivity of the domain and Φ is the potential distribution through the domain. Conservation of charge in the

bulk yields

$$\nabla \cdot \boldsymbol{i} = 0 \tag{2-2}$$

The result in terms of potential and constant conductivity is

$$\nabla^2 \Phi = 0 \tag{2-3}$$

which is known as Laplace's equation.

The solution can also be obtained by performing a material balance over a small volume element

$$\frac{\partial c_i}{\partial t} = -(\nabla \cdot \boldsymbol{N}_i) + R_i \tag{2-4}$$

where c_i is the concentration of species i, $\boldsymbol{N}_i$ is the net flux vector for species i and R_i is the rate of generation of species i due to homogeneous reactions. In a dilute electrolyte, the flux for any species can be written as the sum of three contributions: convection, diffusion and migration:

$$\boldsymbol{N}_i = \boldsymbol{v}c - D_i \nabla c_i - z_i u_i F c_i \nabla \Phi \tag{2-5}$$

where $\boldsymbol{v}$ is the fluid velocity, D_i is the diffusion coefficient for species i, z_i is the charge on species i, u_i is the mobility, F is Faraday's constant, and Φ is the potential. The mobility is related to the diffusion coefficient by the Nerst-Einstein equation

$$D_i = RTu_i \tag{2-6}$$

The current density $\boldsymbol{i}$, that results from equations (2-4) and (2-5) can be expressed as

$$\boldsymbol{i} = F \sum_i z_i N_i \tag{2-7}$$

which is the charge flux within the continuum.

A derivation of the governing differential equation can be obtained by making two assumptions concerning the electrolyte. Under the assumption of electroneutrality

$$\sum_i z_i c_i = 0 \tag{2-8}$$

and that heterogeneous reactions only take place at the boundaries, then one can multiply equation (2-4) by Fz_i and sum over all species.[12] The final assumption is that each of the species in the domain has a uniform concentration distribution. This causes the diffusion term to vanish and the convection term to sum to zero by equation (2-8)

$$\nabla \cdot \left(\boldsymbol{v} \left(F \sum_i z_i c_i \right) \right) = 0 \tag{2-9}$$

The reaction terms also sum to zero because of charge conservation in a homogeneous reaction

$$F \sum_i z_i R_i = 0 \tag{2-10}$$

The term involving the time derivative also sums to zero

$$\frac{\partial}{\partial t} \left(F \sum_i z_i c_i \right) = 0 \tag{2-11}$$

This leaves a time independent equation

$$\nabla \cdot \left(F \left(\sum_i z_i^2 u_i c_i \right) \nabla \Phi \right) = 0 \tag{2-12}$$

where the conductivity κ

$$\kappa = F^2 \sum_i z_i^2 u_i c_i \tag{2-13}$$

is a constant due to uniform concentration. Equation (2-12) then reduces to Laplace's equation

$$\nabla^2 \Phi = 0 \tag{2-14}$$

2.2 Justification of Dilute Approximation

The electrolyte must be dilute for equations (2-5) and (2-6) to hold. For soil environments, the assumption that the soil is dilute can be justified by calculating the ionic strength. A soil with a low resistivity will be in the range of $\rho = 1000\Omega$cm. The ionic strength is defined to be

$$I = \frac{1}{2}\sum_i z_i^2 c_i \tag{2-15}$$

The conductivity of an electrolyte is given in terms of mobility by

$$\kappa = F^2 \sum_i z_i^2 u_i c_i \tag{2-16}$$

and in terms of diffusivities by

$$\kappa = \frac{F^2}{RT}\sum_i z_i^2 D_i c_i \tag{2-17}$$

The diffusivity of a typical species is10^{-5}(cm^2/s). The conductivity is then written as

$$\kappa = \frac{1}{\rho} = \frac{F^2 D}{RT}\sum_i z_i^2 c_i \tag{2-18}$$

Substituting for the sum in equation (2-18), with equation (2-15), and accounting for the porosity of the soil an expression for the ionic strength is obtained:

$$I = \frac{RT}{2F^2 D\rho\epsilon^{1.5}} \tag{2-19}$$

Using typical values of $T = 290$K, and D, and ρ taking values as above, a value for the ionic strength is:

$$I = 0.013\frac{\text{mol}}{\text{l}} \tag{2-20}$$

Since this value is closer to a maximum value in soil environments, the dilute solution approximations used in equation (2-5) holds.

2.3 Internal Domain

The resistivity of pipe steel is 9.6 x $10^{-6}\Omega$cm. For an 18 inch diameter pipe, the resistance per linear foot of pipe is about 2.3 x $10^{-6}\frac{\Omega}{\text{ft}}$. If 10 Amps must travel 5 miles on this pipe, the potential drop in the steel must be 600 mV which is a significant potential drop. Therefore the assumption that there is no potential drop in the pipe steel made by Esteban *et al.* cannot be made for long pipes.[33] The amount of pipe modeled by Esteban was approximately 40 ft.

The flow of current through the pipe steel, anodes and connecting wires is also governed by the 3D Laplace equation

$$\nabla \cdot (\kappa \nabla V) = 0 \tag{2-21}$$

where V is the departure of the potential of the metal from an uniform value and κ is the material conductivity. κ does not necessarily have to be uniform. For instance, the wire connecting the pipe the anode will be made of a different material *i.e.*, copper.

Equation (2-21) can be derived following the approach presented in section 2.1 if one treats electrons as a species.[12] On a pipe surface, the analysis must account for injection of current through bonds and through the pipe wall itself. If the wires can be assumed to be well insulated, the potential drop though a wire can be obtained by Ohm's law

$$\Delta V = IR = I\rho\frac{L}{A} \tag{2-22}$$

where R is the resistance of the wire, ρ is the electrical resistivity, L is the length of wire, and A is the cross-sectional area.

2.4 Quasipotential Transformation

As described in section 2.1, use of Laplace's equation is predicated on the assumption that concentrations of ionic species are uniform. This assumption, which is generally valid, does not apply within a diffusion layer (about 50 μm in thickness[41]) near the pipe and anode where electrochemical reactions generate large surface concentrations of ionic species. The relaxation of the assumption of a uniform concentration is possible within the context of the boundary element formulation by use of the quasipotential formulation.[42, 43, 44, 45]

The basic assumptions of the quasipotential transformation are that convection can be neglected, the system is at steady-state, and that concentration and potential can be written as single valued functions of a common variable, q_i. Equation (2-5) therefore appears as the Nernst-Planck equation

$$\boldsymbol{J}_i = -D_i \nabla c_i - z_i u_i F c_i \nabla \Phi \tag{2-23}$$

Since c_i is a function of Φ,

$$\nabla c_i = \frac{dc_i}{d\Phi} \nabla \Phi \tag{2-24}$$

thus

$$\boldsymbol{J}_i = \left(-D_i \frac{dc_i}{d\Phi} - z_i u_i F c_i \right) \nabla \Phi \tag{2-25}$$

Under the assumption that the diffusion coefficient is constant,

$$\boldsymbol{J}_i = f_i(\Phi) \nabla \Phi \tag{2-26}$$

where

$$f_i(\Phi) = -D_i \left(-D_i \frac{dc_i}{d\Phi} - \frac{z_i F}{RT} c_i \right) \tag{2-27}$$

A new variable, obtained through the Kirchhoff transformation,[43] has the properties

$$-\nabla q_i = f_i(\Phi)\nabla\Phi \tag{2-28}$$

and

$$q_i = -\int_0^{\Phi} f_i(\Phi)d\Phi \tag{2-29}$$

which allows the flux for species i to be written as

$$\boldsymbol{J}_i = -\nabla q_i \tag{2-30}$$

The current density is given by the sum of contributions from the flux of each of the charged species, *i.e.*,

$$\boldsymbol{i} = F\sum_i z_i \boldsymbol{J}_i \tag{2-31}$$

Equation (2-31) can be written in terms of the transformation variable as

$$\boldsymbol{i} = -F\sum_i z_i \nabla q_i \tag{2-32}$$

The quasipotential is defined to be

$$Q = F\sum_i z_i q_i \tag{2-33}$$

such that

$$\boldsymbol{i} = -\nabla Q = F\sum_i z_i \boldsymbol{J}_i \tag{2-34}$$

Under the assumption that charge is conserved, $\nabla \cdot \boldsymbol{i} = 0$, and Q is seen to satisfy Laplace's equation

$$\nabla^2 Q = 0 \tag{2-35}$$

The quasipotential could be used to correct for local concentration gradients by patching an inner solution of Laplace's equation for Q to an outer solution of

Laplace's equation for Φ. The correction can be expected to be on the order of the diffusion potential for the estimated concentration gradients, and this correction is typically less than 40 mV. The importance of the transformation is not so much in the correction it gives to the calculated potential but the insight it leads to changes in the local electrolyte chemistry caused by electrochemical reactions.[46] The pH at the surface of the pipe was calculated by Allahar and Orazem to reach values as high as 12 when the solution far from the pipe had a pH value of 7.[46] Such dramatic changes in pH have significant influence on deposition of corrosion products or calcareous films.

2.5 Conclusions

Through the developments in sections 2.1 and 2.4, a complete model for current transport through the soil for pipes under cathodic protection is obtained. The quasipotential transformation accounts for the necessary effects of concentration gradients near the surface of the pipes and anodes. However, it is desired to not have to break the domain into two parts, one where convection is important and one where it is not. Through experiments by Jeffers, the thickness of the region that is governed by the quasipotential transformation is only a few microns. Therefore, because the parameters of the expressions for the kinetics are fit to experimental data and because they contains expressions to account for transport effects, the region governed by the quasipotential transformation is lumped into the boundary condition.

CHAPTER 3
SOLUTION OF GOVERNING PDE

Laplace's equation has been solved for many boundary conditions and domains.[47] In the case of this research it is desired to be able to solve this equation for arbitrary arrangements of pipes and anodes within the domain. It is also desired to introduce the nonlinear boundary conditions that arise from the chemistry at the boundaries as discussed in Chapter 1.

The first task is to find a method to solve the differential equation given arbitrary boundary geometry. One way is to use complex transformations to map the boundaries to a form for which a solution exists. Moulton first described the technique for conduction of current through a solid.[48] Bowman supplies details for analytic solutions using the Schwaz-Christoffel transformation.[49] Orazem and Newman provide a semi-analytical implementation of the Schwarz-Christoffel transformation for the more complicated structure of a slotted electrode.[50] Orazem used the technique for a compact tension fracture specimen[51] which was later further refined.[52] Diem *et al.* take the semi-analytical technique a step further by allowing for insulating surfaces to form an arbitrary angle with the electrode.[53]

Unfortunately, there are not enough of these transformations to cover all the possible configurations of pipes within a domain. Also, the soil domain is not bounded. The other way to solve the equation is to use a completely numerical technique. Of the available techniques, the boundary element method is very attractive. It can provide the same level of quality as the Schwarz-Christoffel

transformations while not being restricted to any geometry. The method only solves the governing equation on the boundaries. This is ideal for corrosion problems since all the activity takes place at the boundaries. Brebbia first applied the boundary element method for potential problems governed by Laplace's equation.[54] Aoki and also Telles provided the first practical demonstrations of utilizing the boundary element method with simple nonlinear boundary conditions.[55, 56] Zamani and Chuang demonstrated optimization of cathodic current through adjustment of anode location.[57]

The pipe steel domain is solved using the finite element method. Brichau first demonstrated the technique of coupling a finite element solution for pipe steel to a boundary element solution for the soil.[58] He also demonstrated stray current effects from electric railroad interference utilizing the same solution formulation.[59] However, Brichau's method was limited in that it assumed that the potential and current distributions on the pipes and anodes were axisymmetric allowing only axial variations. Since it is desired to have a solution for the current and potential distributions both around the circumference and along the length of the pipe, Brichau's method must be modified. Aoki presented a technique similar to Brichau's that included optimization of anode locations and several soil conductivity changes for the case of a single pipe with no angular variations in potential and current distributions.[60, 61]

3.1 Boundary Element Method Development

The boundary element method can be derived from the same technique used to obtain the classical finite element method. One starts by writing a variational

or weighted residual of the governing differential equation. If the PDE takes the form

$$\nabla^2 u - f = 0 \tag{3-1}$$

where f is a forcing term that is a function of position only, then one would write the weighted residual as

$$\int_\Omega w\left(\nabla^2 u - f\right) d\Omega = 0, \forall w \tag{3-2}$$

where Ω is the domain and w is any weighting function. In the case of Laplace's equation, $f = 0$ and $u = \Phi$; thus

$$\int_\Omega w \nabla^2 \Phi d\Omega = 0, \forall w \tag{3-3}$$

This equation holds for all weighting functions w. Equation (3-3) is integrated analytically by using the divergence theorem

$$\int_\Omega \nabla w \nabla \Phi d\Omega - \int_\Gamma w\left(\vec{n} \cdot \nabla \Phi\right) d\Gamma = 0, \forall w \tag{3-4}$$

with Γ being the boundary of the domain. Equation (3-4) is classical weak form of the finite element method for Laplace's equation. At this stage, the boundary element method development departs from the finite element method by using a second application of the divergence theorem. The highest order derivative is thereby moved to the weighting function, *i.e.,*

$$\int_\Omega \Phi \nabla^2 w d\Omega - \int_\Gamma w\left(\vec{n} \cdot \nabla \Phi\right) d\Gamma + \int_\Gamma \Phi\left(\vec{n} \cdot \nabla w\right) d\Gamma = 0, \forall w \tag{3-5}$$

At this point the weighting function function needs to be specified to show why the second application of the divergence theorem was done. If one observes that the solution to the equation

$$\nabla^2 G_{i,j} + \delta_i = 0 \tag{3-6}$$

is the Greens function for Laplace's equation, one can simplify equation (3-5) by picking the weighting function to be the Green's function.[62] The first integral in equation (3-5) becomes

$$\int_{\Omega} \Phi\,(-\delta_i)\,d\Omega = -\Phi_i \tag{3-7}$$

Substitution of equation(3-7) into equation (3-5) yields a simpler equation valid within the domain

$$\Phi_i + \int_{\Gamma} \Phi\left(\vec{n}\cdot\nabla G_{i,j}\right) d\Gamma = \int_{\Gamma} G_{i,j}\,(\vec{n}\cdot\nabla\Phi)\,d\Gamma \tag{3-8}$$

where the highest order derivative has been removed and all the integrals are along the boundaries only. Equation (3-8) is still exact in so far as the Green's function is known and is valid for determining the values of the potential at any interior point in the domain given that the potential and current density distributions on the boundary are known. This implies that, for Laplace's equation, values of interior points are fully specified by integrals along the boundary only.

The last step in deriving the Boundary Element method is to take Φ_i to the boundary. A Cauchy principle value is introduced in the integral on the left side of equation (3-8). It is usually represented by a constant appearing in front of the first term in equation (3-8)

$$c_i\Phi_i + \int_{\Gamma} \Phi\left(\vec{n}\cdot\nabla G_{i,j}\right) d\Gamma = \int_{\Gamma} G_{i,j}\,(\vec{n}\cdot\nabla\Phi)\,d\Gamma \tag{3-9}$$

For a smooth surface at the point i, the constant, c_i, is equal to π.[63]

3.2 Symmetric Galerkin Boundary Element Method

The direct Boundary Element Method as described above results in dense, non-symmetric matrices. Even though the diagonals of the matrices have the

largest magnitude, they are not diagonally dominant. This means that the fast iterative techniques of solving $\boldsymbol{A}x = \boldsymbol{b}$ cannot be used. A form of the boundary element method that is symmetric has been developed.[64] Symmetric formulations are possible because both the Greens function for Laplace's equation and its normal derivatives are symmetric. The method can be derived as follows:[65] start with the standard boundary element formulation (equation (3-8)) and take the normal derivative of it with respect to the source point (point i)

$$\vec{n}_i \cdot \nabla \Phi_i + \int_\Gamma \Phi \left(\vec{n}_i \cdot \nabla \left(\vec{n}_j \cdot \nabla G_{i,j} \right) \right) d\Gamma = \int_\Gamma \left(\vec{n}_i \cdot \nabla G_{i,j} \right) \left(\vec{n}_j \cdot \nabla \Phi \right) d\Gamma \tag{3-10}$$

which is known as the hyper-singular boundary integral formulation. It is called hyper-singular because the highest order singularity is greater than two. The next step is to multiply through equations (3-8) and (3-10) by the shape function, ϕ, of the source element, i, and integrate the resulting equations over the entire boundary

$$\int_\Gamma \phi_i \Phi_i d\Gamma_i + \int_\Gamma \phi_i \int_\Gamma \Phi \left(\vec{n} \cdot \nabla G_{i,j} \right) d\Gamma_j d\Gamma_i = \int_\Gamma \phi_i \int_\Gamma G_{i,j} \left(\vec{n} \cdot \nabla \Phi \right) d\Gamma_j d\Gamma_i \tag{3-11}$$

and

$$\int_\Gamma \phi_i \kappa \left(\vec{n}_i \cdot \nabla \Phi_i \right) d\Gamma_i + \int_\Gamma \phi_i \int_\Gamma \Phi \kappa \left(\vec{n}_i \cdot \nabla \left(\vec{n}_j \cdot \nabla G_{i,j} \right) \right) d\Gamma_j d\Gamma_i = \int_\Gamma \phi_i \int_\Gamma \left(\vec{n}_i \cdot \nabla G_{i,j} \right) \kappa \left(\vec{n}_j \cdot \nabla \Phi \right) d\Gamma_j d\Gamma_i \tag{3-12}$$

The additional outer integration now results in a symmetric matrix on the left side. Equation (3-11) is written on Dirichlet surfaces and equation (3-12) is written for Neumann surfaces. The symmetry of the left-hand-side matrix is only seen when all the unknown variables have been moved to the left hand side. The integration can be more easily seen in Figure 3-1 on page 34.

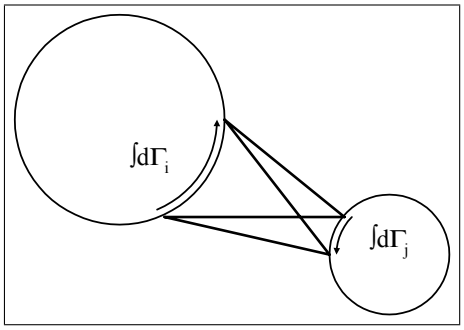

Figure 3-1: Symmetric integration. Lines between the two circles represent the Green's function relation between the two integration points on the surfaces $d\Gamma_i$ and $d\Gamma_j$.

The symmetric positive definite system of equations resulting from this method can now utilize Cholesky decomposition for their solution. This method is significantly faster than LU decomposition which is needed for the standard boundary element method. However, the symmetric Galerkin boundary element method can only be used when the boundary conditions are constant. The symmetry falls apart for nonlinear boundary conditions as demonstrated in Chapter 4.

3.3 Boundary Conditions

The form of the boundary conditions for steel pipe under cathodic protection have been developed in Chapter 1. They take three possible forms one for bare steel, one for coated steel and one for anodes.

3.3.1 Bare Steel

For the static problem, the boundary condition relates the potential difference between the steel and the soil just outside the outer Helmholtz plane, $V - \Phi$, to the current density, $i = \kappa \vec{n} \cdot \nabla \Phi$ at the soil - pipe interface. The expression for the

corrosion kinetics developed in Chapter 1, equation (1-23), is used for sections of the buried structure where bare steel is exposed to the soil (coating holiday or uncoated pipe).

3.3.2 Coated Steel

Coated steel has a transport barrier in the form of the coating. The coating is also bonded to the steel and therefore many of the reaction sites are blocked. The equation developed in Chapter 1 also relates the net current density at the pipe - soil interface to the voltage difference between the pipe steel at the interface and the potential in the soil just above the interface (past the outer Helmholtz plane). The expression, equation (1-26), also introduces an inner potential which is defined to be the potential at the coating - steel interface. This is the potential that is used to drive the kinetics.

3.3.3 Anodes

The boundary conditions for the anodes must be an essential type boundary condition in order to have a well-posed problem. An essential type boundary condition is one imposed on the potential at the boundary. A condition imposed on the normal flux at the boundary would be referred to as a natural boundary condition. However, the equations describe the reactions on the anode are also nonlinear functions of the potential. Equation (1-27) can be quickly solved for the potential

$$V - \Phi = E_{\text{eql}} + \beta_{\text{anode}} \log\left(i/i_{O_2} + 1\right) \tag{3-13}$$

which can then serve as an essential boundary condition. Many cathodic protection systems may not have a galvanic anode but an impressed current anode. The equation for the current density for impressed current anodes, equation (1-30) can also be rewritten in where i is the independent variable

$$V - \Phi = E_{O_2} + \triangle V_{\text{rectifier}} + \beta_{O_2} \log\left(i/i_{\text{eql}} + 1\right) \tag{3-14}$$

Equations (3-13) and (3-14) are then used to form a well-posed problem definition for the solution the governing differential equations.

3.4 Infinite Domains

Everything done to this point has been done under the assumption that the boundary encloses the domain. In many situations, the domain lies outside the boundary. In order to get a solution for this situation, it is necessary to introduce a second boundary, $\bar{\Gamma}$, placed around the surface of interest and centered on the source point on that surface. Adding the enclosing boundary to equation (3-9), one obtains

$$\begin{aligned} c_i\Phi_i + \int_\Gamma \Phi\left(\vec{n}\cdot\nabla G_{i,j}\right)d\Gamma + \int_{\bar{\Gamma}} \Phi\left(\vec{n}\cdot\nabla G_{i,j}\right)d\bar{\Gamma} = \\ \int_\Gamma G_{i,j}\left(\vec{n}\cdot\nabla\Phi\right)d\Gamma + \int_{\bar{\Gamma}} G_{i,j}\left(\vec{n}\cdot\nabla\Phi\right)d\bar{\Gamma} \end{aligned} \tag{3-15}$$

If the radius of the new boundary is taken to infinity the limit of the integrals over the external boundary are taken to infinity

$$\lim_{R\to\infty}\left(\int_{\bar{\Gamma}} \Phi\left(\vec{n}\cdot\nabla G_{i,j}\right)d\bar{\Gamma} - \int_{\bar{\Gamma}} G_{i,j}\left(\vec{n}\cdot\nabla\Phi\right)d\bar{\Gamma}\right) \tag{3-16}$$

When integrating across this boundary the integral will be

$$-\int_{\Gamma_\infty} \Phi\left(\vec{n}\cdot\nabla G_{i,j}\right)d\Gamma_\infty = H_{i,\infty} = 4\pi\Phi \tag{3-17}$$

where the minus sign indicates the direction of the normal vector. The other integral vanishes as the limit is taken. The value of integral in (3-17) can be more easily seen if it is transformed to spherical coordinates

$$\lim_{r\to\infty}\left(-\int_0^{\pi}\int_0^{2\pi}\frac{\Phi}{r^2}\left(r^2\sin\phi\right)d\theta d\phi\right)=4\pi\Phi \tag{3-18}$$

where r is also the normal vector since the surface is a sphere centered at a source point. Φ at infinity is often assumed to be zero; thus satisfying the zero radiation condition at infinity exactly.

3.5 Half Spaces

A half space is simply an infinite domain split by a plane. The half space is the space lying on one side of the plane. If either the Dirichlet or Neumann condition vanishes at the plane, the Green's function presents an interesting opportunity to satisfy that condition exactly with a very small additional computation when evaluating the kernels of the integrals. This is done by making use of the Green's functions reflection properties.[63, 64, 65, 66] In the case of buried pipelines, the Neumann condition vanishes at the plane boundary, that is there is no current flowing out of the soil into the air, and none is flowing from the air into the soil.

If one starts with the boundary condition on the plane being zero normal current and places a source at x and its reflection about the plane at x', one may write[66]

$$\sigma\left(x\right)\left(\vec{n}\cdot\nabla G\left(x,\xi\right)\right)+\sigma\left(x'\right)\left(\vec{n}\cdot\nabla G\left(x',\xi\right)\right)=0 \tag{3-19}$$

which implies that the two source intensities $\sigma(x)$, and $\sigma(x')$ are equal and have the same sign. The sign is the same because the outward normal vectors have

opposite signs. The final form of the Green's function is

$$G_{i,j} = \frac{1}{4\pi r(x_i, x_j)} + \frac{1}{4\pi r(x_i, x'_j)} \tag{3-20}$$

where x'_j is the reflected source point.

3.6 Layers

Layers are created using the same types of Green's function reflections as described above. The only restriction being that one of the two boundary conditions at the interface between the two layers must be zero (either $\Phi = 0$ V or $\vec{n} \cdot \nabla\Phi = 0 \mu\text{A/cm}^2$).[66] In the context of cathodic protection of buried pipelines, the only boundary condition that has physical meaning is a zero normal current condition since there is no easy way to have an arbitrary plane within the electrolyte that has a potential equal to zero. Including a plane with a zero Neuman (natural) condition implies that there is one region in which current may flow that is bounded by regions of zero conductivity whose boundaries are defined by the Green's function reflections. An example would be an underlying rock layer which has zero conductivity.

The resulting functions can be obtained by using equations of the form of (3-19). The Green's function in three dimensions would then be of the form

$$G_{i,j} = \sum_{k}^{Reflections+1} \frac{1}{4\pi r(x_i, x_{j,k})} \tag{3-21}$$

where the index $k > 1$ refers to the reflection about some plane k. For $k = 1$, $x_{j,k}$ is the field point on the real object. If the soil surface is the only reflection used, the result is the same as equation (3-20).

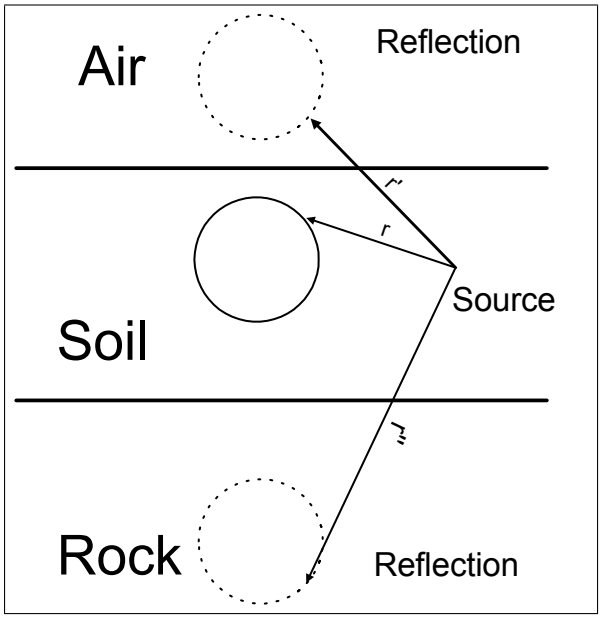

Figure 3-2: Reflections of Green's function to account for boundaries with zero normal current.

An example of a pipeline in a halfspace with an underlying rock layer is shown in Figure 3-2 on page 39. There are two reflections used. The first is to account for the zero normal current at the air soil interface. This is represented by the dashed pipe in the air. The second reflection is to account for the zero normal current at the rock soil interface and is represented by the lower dashed pipe.

A model was run where the non-conducting layer was placed at a couple of inches below the pipe and slowly moved away from the pipe. The total cathodic current that the pipe received from the anode was calculated with no other parameters changed except for the depth of the non-conducting layer. A plot of the total current is given in Figure 3-4.

The influence of the nonconducting layer on the current delivered to a pipe is seen in Figure 3-4. For these calculations, the anode was placed far from the

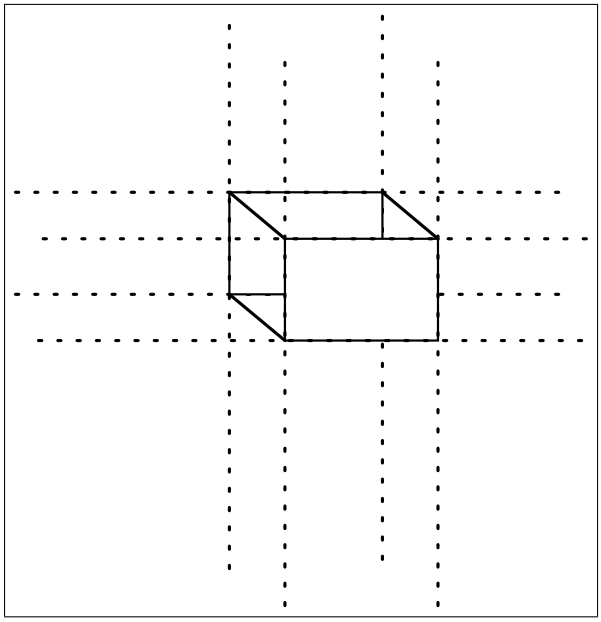

Figure 3-3: Rectangular enclosure created with a primary Green's function and 6 reflections.

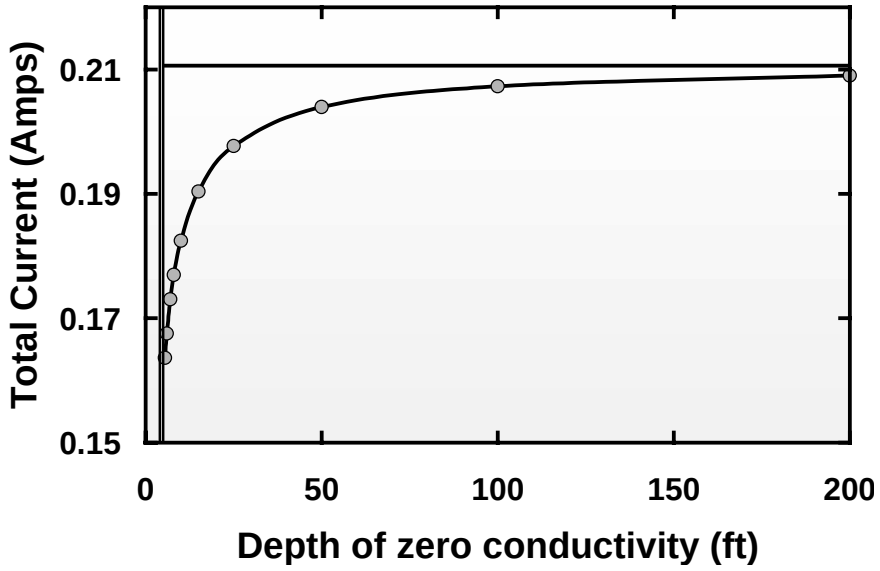

Figure 3-4: Total cathodic current driven to a pipe with an underlying non-conducting region.

pipe such that the current distribution around the circumference of the pipe was affected only by the screening of the insulating ledge. The total current tended toward that predicted by Dwight's formula as the distance between the ledge and the pipe increased. As seen in Figure 3-5, the current increased with the distance according to

$$I = I_{r\to\infty} - \frac{a}{\sqrt{r}} \tag{3-22}$$

where a is a fitted parameter that depends on the geometry and soil resistance and $I_{r\to\infty}$ is the value obtained from Dwight's formula which does not account for the presence of a nonconducting layer.

The data used in Figure 3-4 was then then fit to the equation

$$i = \frac{a}{\sqrt{r}} + i_{r=\infty} \tag{3-23}$$

where a is a fit parameter that contains the area of the pipe, the soil resistivity, the applied voltage of the anode, etc. After calculating a linear fit, the data can be plotted again along with the line representing the linear fit.

3.7 Development of Finite Element Method for Internal Domain

The finite element method has been selected for the domain of the pipe steel, copper connection wires, and internal anode material. It is ideal for completely bounded domains where the material properties change from one location to another, *i.e.*, current flow from the pipe to the copper wire connecting the pipe to the anode.

The development of the finite element method for the pipe steel domain starts by writing a weighted residual for the strong form of Laplace's equation given in

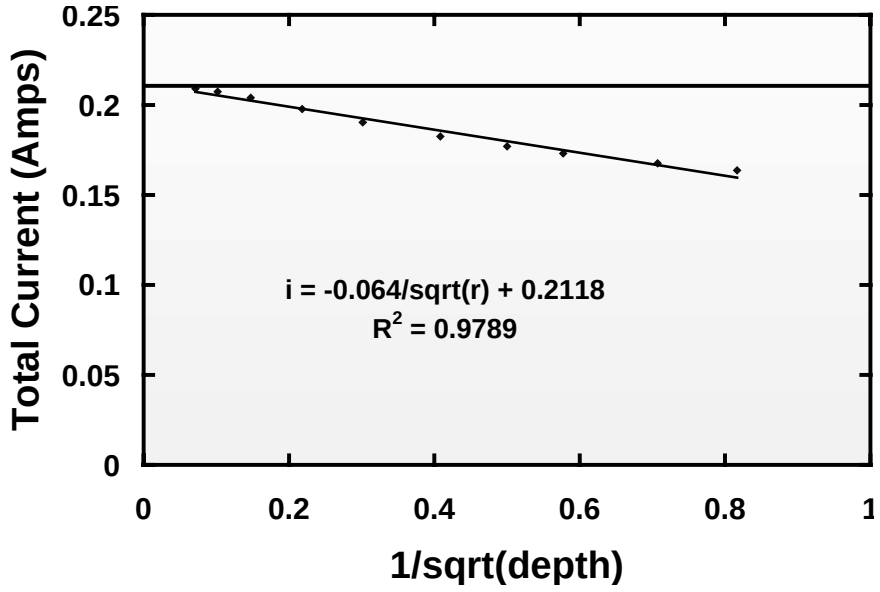

Figure 3-5: Fit of the data from Figure 3-4 to $i = \frac{-0.064}{\sqrt{r}} + 0.2118$.

equation (2-21)

$$\int_{\Omega} w \nabla \cdot \vec{\vec{\kappa}} \cdot \nabla V d\Omega = 0 \tag{3-24}$$

where w is any weighting function. For pipe steel, κ is just a constant times an identity matrix

$$\vec{\vec{\kappa}} = \kappa \begin{bmatrix} 1 & 0 & 0 \\ 0 & 1 & 0 \\ 0 & 0 & 1 \end{bmatrix} \tag{3-25}$$

with step changes in κ when the type of metal changes. After substituting the material properties into equation (3-24) and integrating by parts using the divergence theorem, the following Weak Form is obtained

$$\iiint_{\Omega} \kappa \nabla w \cdot \nabla V dx\, dy\, dz = -\oiint w \kappa \left(\vec{n} \cdot \nabla V\right) ds \tag{3-26}$$

where $\vec{n}$ is the outward normal vector from the boundary of the domain. The domain is divided into elements using piecewise continuous polynomial isopara-

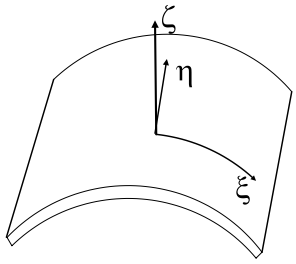

Figure 3-6: Diagram of the shell element used to calculate the potential drop within the pipe steel. The element is assumed to have no variation in the ζ direction. The curvilinear coordinate system is displayed on top of the element.

metric shape functions. The shape functions approximate the geometry and solution, V, over the elements. The discritized form of equation (3-26) is

$$\sum_{j=1}^{n}\left[\int\int\int_{(e)}\kappa\nabla\phi_i^{(e)}\cdot\nabla\phi_j^{(e)}dx\,dy\,dz\right]V_j=-\oint\!\!\int\kappa\phi_i^{(e)}\left(\vec{n}\cdot\nabla V\right)_i^{(e)}ds \tag{3-27}$$

where κ is the scalar component of the property tensor, ϕ_i is a shape function and the sum goes from 1 to the total of all the shape functions of all the elements.

3.7.1 Pipe Shell Elements

A special type of thin shell elements is introduced here and shown in Figure 3-6. They are specifically designed for potential problems on shells where the absolute value of the material property (κ in equation (3-27)) is large.

The elements are defined in orthonormal curvilinear coordinates, ξ, η, and ζ where ξ and η define the outside surface of the pipe and ζ is the outward normal. ζ is obtained through the cross product $\xi\times\eta$.

Variations of the potential in the ζ direction are assumed to be negligible because the scale of the problem is many orders of magnitude greater in the ξ and η directions. Variations of the potential parallel to the surface are allowed to vary in a piece-wise continuous way using bi-quadratic shape functions for the elements.

These functions are obtained through the product of two Lagrange interpolating polynomials of the same order, one in ξ and one in η. The result is a family of elements with square parent elements. They include the four-node linear element, the nine-node quadratic element, the 16 node cubic element, etc.

3.7.2 Applying Elements to the FEM

The integral (3-27) must be transformed to the curvilinear coordinate system of the parent elements. A differential volume, $dx\,dy\,dz$ can be transformed to the curvilinear system by the determinate of the Jacobian of the coordinate transformation

$$dx\,dy\,dz = |\mathbf{J}|\,d\xi\,d\eta\,d\zeta \tag{3-28}$$

where $\mathbf{J}$ is the Jacobian.

The Jacobian is composed of the partial derivatives of the coordinates x, y and z with respect to each of the curvilinear coordinates

$$\mathbf{J} = \begin{bmatrix} \frac{\partial x}{\partial \xi} & \frac{\partial y}{\partial \xi} & \frac{\partial z}{\partial \xi} \\ \frac{\partial x}{\partial \eta} & \frac{\partial y}{\partial \eta} & \frac{\partial z}{\partial \eta} \\ \frac{\partial x}{\partial \zeta} & \frac{\partial y}{\partial \zeta} & \frac{\partial z}{\partial \zeta} \end{bmatrix} \tag{3-29}$$

Integral (3-27) transformed to the curvilinear coordinate system is

$$\sum_i \left[\int\int\int_{\Omega^{(e)}} \sum_k \frac{\partial \phi_i}{\partial x_k} \kappa \cdot \frac{\partial \phi_j}{\partial x_k} |\mathbf{J}| d\xi\,d\eta\,d\zeta \right] = -\oint\!\!\!\!\!\!\int_{\Gamma_{(e)}} w\kappa\,(\vec{n} \cdot \nabla V)\,ds \tag{3-30}$$

where x_k is one of the cartesian coordinates, $|\mathbf{J}|$ is the determinate of the Jacobian, s is the surface of the element $\vec{n}$ is the outward normal vector from the surface, and $\Omega^{(e)}$ is the domain of the parent element. The limits of integration in the parent element are from -1 to +1 for all three of the coordinates. For the special

shell elements used for pipes, the integral is only performed numerically over the surface $d\xi\, d\eta$ which is then scaled by the physical thickness of the shell h, the result of the integral over ζ. This requires the Jacobian to be modified to a surface Jacobian. In this case it is simply the square root of the magnitude of the Jacobian. Rewriting equation (3-30), the two dimensional integral over the surfaces of the pipes is obtained

$$\sum_i \left[h \int\int_{\Omega^{(e)}} \sum_k \frac{\partial \phi_i}{\partial x_k} \kappa \cdot \frac{\partial \phi_j}{\partial x_k} \sqrt{|\mathbf{J}|}\, d\xi\, d\eta \right] = - \oint\!\!\!\!\!\!\int_{\Gamma_{(e)}} w\kappa\, (\vec{n} \cdot \nabla V)\, ds \tag{3-31}$$

with the thickness of the steel, h, a parameter. The normal vector has the same direction as the one from the boundary element method.

Partial derivatives in equation (3-31) with respect to cartesian coordinates need to be expressed in terms of the curvilinear coordinates. Using the chain rule, but starting from the derivatives in cartesian coordinates, one writes

$$\begin{Bmatrix} \frac{\partial \phi}{\partial x}\frac{\partial x}{\partial \xi} + \frac{\partial \phi}{\partial y}\frac{\partial y}{\partial \xi} + \frac{\partial \phi}{\partial z}\frac{\partial z}{\partial \xi} \\ \frac{\partial \phi}{\partial x}\frac{\partial x}{\partial \eta} + \frac{\partial \phi}{\partial y}\frac{\partial y}{\partial \eta} + \frac{\partial \phi}{\partial z}\frac{\partial z}{\partial \eta} \\ \frac{\partial \phi}{\partial x}\frac{\partial x}{\partial \zeta} + \frac{\partial \phi}{\partial y}\frac{\partial y}{\partial \zeta} + \frac{\partial \phi}{\partial z}\frac{\partial z}{\partial \zeta} \end{Bmatrix} = \begin{Bmatrix} \frac{\partial \phi}{\partial \xi} \\ \frac{\partial \phi}{\partial \eta} \\ \frac{\partial \phi}{\partial \zeta} \end{Bmatrix} \tag{3-32}$$

or, in terms of the Jacobian

$$\mathbf{J} \begin{Bmatrix} \frac{\partial \phi}{\partial x} \\ \frac{\partial \phi}{\partial y} \\ \frac{\partial \phi}{\partial z} \end{Bmatrix} = \begin{Bmatrix} \frac{\partial \phi}{\partial \xi} \\ \frac{\partial \phi}{\partial \eta} \\ \frac{\partial \phi}{\partial \zeta} \end{Bmatrix} \tag{3-33}$$

Since ϕ is a function of ξ, η, and ζ, the partial derivatives of ϕ with respect to the cartesian coordinates can be found by inverting the Jacobian.

$$\begin{Bmatrix} \frac{\partial \phi}{\partial x} \\ \frac{\partial \phi}{\partial y} \\ \frac{\partial \phi}{\partial z} \end{Bmatrix} = \mathbf{J}^{-1} \begin{Bmatrix} \frac{\partial \phi}{\partial \xi} \\ \frac{\partial \phi}{\partial \eta} \\ \frac{\partial \phi}{\partial \zeta} \end{Bmatrix} \tag{3-34}$$

If $\mathbf{J}^{-1}_{i,j}$ is the element from the ith row and the jth column of the inverse of the Jacobian, then the needed partial derivatives can be expanded to

$$\begin{aligned}
\frac{\partial \phi_i}{\partial x} &= (J^{-1})_{11}\frac{\partial \phi_i}{\partial \xi} + (J^{-1})_{12}\frac{\partial \phi_i}{\partial \eta} + (J^{-1})_{13}\frac{\partial \phi_i}{\partial \zeta} \\
\frac{\partial \phi_i}{\partial y} &= (J^{-1})_{21}\frac{\partial \phi_i}{\partial \xi} + (J^{-1})_{22}\frac{\partial \phi_i}{\partial \eta} + (J^{-1})_{23}\frac{\partial \phi_i}{\partial \zeta} \\
\frac{\partial \phi_i}{\partial z} &= (J^{-1})_{31}\frac{\partial \phi_i}{\partial \xi} + (J^{-1})_{32}\frac{\partial \phi_i}{\partial \eta} + (J^{-1})_{33}\frac{\partial \phi_i}{\partial \zeta}
\end{aligned} \tag{3-35}$$

The assumption that the thickness of the shell is small with respect to the radius and length of the shell means that there is negligible variation in the potential in the ζ direction. Therefore, all terms in equation (3-35) that involve partial derivatives with respect to ζ can be assumed to be equal to zero. All of the terms in equation (3-31) can be evaluated numerically. Since the shape functions for the geometry and solution vary quadratically in the ξ and η directions, a nine-point Gauss rule (3x3) applied in both directions will give an exact (to machine precision) result.

3.8 Bonds and Resistors

Bonds and resistors are used to electrically tie two pipes or a pipe and an anode together. They are implemented as a linear 1-D element that goes between the connection node on one pipe to the connection node on the second pipe. Therefore, no extra nodes are introduced. The material property is set by accounting for the real length and gauge of the wire that ties the pipes together. If a resistor is specified within the wire, it is added to the total resistance of the bond. An illustration of a bond is given in Figure 3-7. The red cylinders represent a resistor

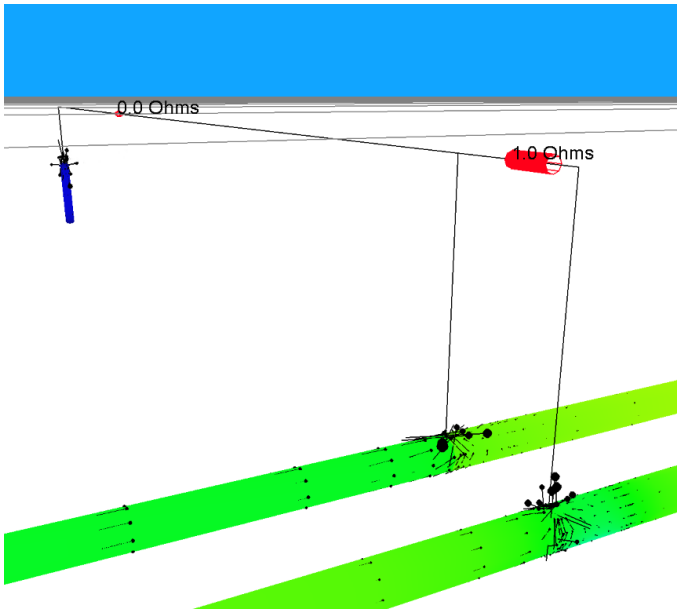

Figure 3-7: Black lines connecting pipes and anode are bonds. The red cylinders represent resistors. They are modeled as 1-D finite elements that connect to the bond connection points.

that is sometimes added in series with the bond. If one is not used, its value of resistance is set to zero.

For a 1-D element, a one-dimensional version of Laplace's is used. The development for the linear 1-D element is done in the same way as in section 3.7. The result of the integration over the bond is the total conductance of the bond or

$$K_e = \begin{bmatrix} \frac{1}{R} & \frac{-1}{R} \\ \frac{-1}{R} & \frac{1}{R} \end{bmatrix} \tag{3-36}$$

where R is the total resistance of the bond.

3.9 Coupling BEM to FEM

The finite element domain is coupled to the boundary element domain at the interface between the two domains. Ohm's Law holds within each domain as

stated in section 2.1. Therefore, at any arbitrary surface that forms a boundary between two domains it can be shown that the flux on either side of the boundary is related by the material property.

$$\kappa_1 \vec{n} \cdot \nabla \Phi_1 = \kappa_2 \vec{n} \cdot \nabla \Phi_2 \tag{3-37}$$

which is simply a balance on charge at the pipe/soil interface, where κ is the material property. For potential problems, κ is the conductivity of the material in Mho/m. Using the variables for potential in the pipe, V, and potential in the soil, Φ, the interface condition is written as

$$(\vec{n} \cdot \nabla V) = \frac{\kappa_{\text{soil}}}{\kappa_{\text{steel}}} (\vec{n} \cdot \nabla \Phi) \tag{3-38}$$

where the quantity $\vec{n} \cdot \nabla V$ is used in the finite element load integral.

Equation (3-38) can be inserted into equation (3-31) to obtain

$$\sum_i \left[h \int\int_{\Omega^{(e)}} \sum_k \frac{\partial \phi_i}{\partial x_k} \kappa \cdot \frac{\partial \phi_j}{\partial x_k} \sqrt{|\mathbf{J}|} d\xi \, d\eta \right] = - \oint\int_{\Gamma_{(e)}} w \kappa_{\text{soil}} (\vec{n} \cdot \nabla \Phi) \, ds \tag{3-39}$$

The right side of equation (3-39) links the soil domain to the steel domain through the current density generated by the kinetics of the corrosion reaction at the steel surface given by equations (1-23) and (1-26).

3.10 Current Flow in the Pipe

In addition to using false-color surfaces to indicate potential or current density normal to the surface, Figure 3-7 includes vectors laid on the surface of the pipe which represent the direction and relative magnitude of the current flowing in the pipe steel. Calculation of the current density within the pipeline steel can be used to isolate regions of inadequate protection, to identify the electrical midpoint, and

to determine the direction of current flowing through a bond. The method for calculating the current within the pipes is presented in this section.

The value of the two components of the current in the parent element at each of the four optimal Gauss points is found by differentiating the shape functions which describe the potential in the steel, *i.e.*,

$$i_\xi(\xi,\eta) = -\kappa \sum_{k=1}^{9} V_k \frac{\partial \phi_k}{\partial \xi} \tag{3-40}$$

and

$$i_\eta(\xi,\eta) = -\kappa \sum_{k=1}^{9} V_k \frac{\partial \phi_k}{\partial \eta} \tag{3-41}$$

Since the current vector is needed in cartesian coordinates, but the currents are only known in the curvilinear system as above, the Jacobian of the coordinate transformation must be used to get the three partial derivatives in cartesian coordinates (see equations (3-32) and (3-34)). The values of the current are found at each of the optimal sampling points through

$$i_{x,I} = -\kappa \frac{\partial V_I}{\partial x} = (J^{-1})_{11} i_\xi(\xi_I,\eta_I) + (J^{-1})_{12} i_\eta(\xi_I,\eta_I) \tag{3-42}$$

for the x component,

$$i_{y,I} = -\kappa \frac{\partial V_I}{\partial x} = (J^{-1})_{21} i_\xi(\xi_I,\eta_I) + (J^{-1})_{22} i_\eta(\xi_I,\eta_I) \tag{3-43}$$

for the y component, and

$$i_{z,I} = -\kappa \frac{\partial V_I}{\partial x} = (J^{-1})_{31} i_\xi(\xi_I,\eta_I) + (J^{-1})_{32} i_\eta(\xi_I,\eta_I) \tag{3-44}$$

for the z component, where (ξ_I,η_I) are the optimal current sampling points and i_ξ and i_η are defined in equations (3-40) and (3-41), respectively.

The values of the flux at the nodes are found by fitting three planes to the three components of the four optimal values of the current by the equation

$$i_x(\xi, \eta) = c_1 + c_2\xi + c_3\eta \tag{3-45}$$

where the constants are found through a least squares regression. Therefore, a transformation matrix is needed to perform the regression

$$\vec{i}_{\text{nodes}} = [TR]\vec{i}_{\text{optimal}} \tag{3-46}$$

where $\vec{i}_{\text{optimal}}$ is a 4-by-3 matrix and $\vec{i}_{\text{nodes}}$ is a 9-by-3 matrix, hence $[TR]$ is a 9-by-4 regression matrix. To find $[TR]$, the error of fitting a plane to the current at each node is minimized through the sum of squares

$$e_x = \sum_{k=I}^{IV}[c_1 + c_2\xi_k + c_3\eta_k - i_k]^2 \tag{3-47}$$

where e_x is the error in the x component of $\vec{i}$. Two more equations of the form of equation (3-47) are written for the y and z components of $\vec{i}$. The error is minimized for each component by setting

$$\frac{\partial e_x}{\partial c_j} = 0 \tag{3-48}$$

which yields

$$\sum_{k=I}^{IV}[c_1 + c_2\xi_k + c_3\eta_k - i_k] = 0 \tag{3-49}$$

for $j = 1$

$$\sum_{k=I}^{IV}[c_1 + c_2\xi_k + c_3\eta_k - i_k]\xi = 0 \tag{3-50}$$

for $j = 2$, and

$$\sum_{k=I}^{IV}[c_1 + c_2\xi_k + c_3\eta_k - i_k]\eta = 0 \tag{3-51}$$

for $j = 3$. Equations (3-49) through (3-51) can be written in matrix form as

$$\begin{bmatrix} \sum_{k=I}^{k=IV} 1 & \sum_{k=I}^{k=IV} \xi_k & \sum_{k=I}^{k=IV} \eta_k \\ \sum_{k=I}^{k=IV} \xi_k & \sum_{k=I}^{k=IV} \xi_k \xi_k & \sum_{k=I}^{k=IV} \xi_k \eta_k \\ \sum_{k=I}^{k=IV} \eta_k & \sum_{k=I}^{k=IV} \xi_k \eta_k & \sum_{k=I}^{k=IV} \eta_k \eta_k \end{bmatrix} \begin{pmatrix} c_1 \\ c_2 \\ c_3 \end{pmatrix} = \begin{bmatrix} 1 & 1 & 1 & 1 \\ \xi_I & \xi_{II} & \xi_{III} & \xi_{IV} \\ \eta_I & \eta_{II} & \eta_{III} & \eta_{IV} \end{bmatrix} \begin{pmatrix} i_I \\ i_{II} \\ i_{III} \\ i_{IV} \end{pmatrix} \tag{3-52}$$

or in matrix notation as

$$[P]\{c\} = [Q]\{i\}_{\text{optimal}} \tag{3-53}$$

Then c for each component of $\vec{i}$ can be written as

$$\{c\} = [P]^{-1}[Q]\{i\}_{\text{optimal}} \tag{3-54}$$

For the optimal Gauss points, $\{\pm\frac{1}{\sqrt{3}}, \pm\frac{1}{\sqrt{3}}\}$, $[P]$ is

$$[P] = \begin{bmatrix} 4 & 0 & 0 \\ 0 & \frac{4}{3} & 0 \\ 0 & 0 & \frac{4}{3} \end{bmatrix} \tag{3-55}$$

and $[Q]$ is

$$[Q] = \begin{bmatrix} 1 & 1 & 1 & 1 \\ \frac{1}{-\sqrt{3}} & \frac{1}{-\sqrt{3}} & \frac{1}{\sqrt{3}} & \frac{1}{\sqrt{3}} \\ \frac{1}{-\sqrt{3}} & \frac{1}{\sqrt{3}} & \frac{1}{-\sqrt{3}} & \frac{1}{\sqrt{3}} \end{bmatrix} \tag{3-56}$$

so that $[P]^{-1}[Q]$ is

$$[P]^{-1}[Q] = \frac{1}{4}\begin{bmatrix} 1 & 1 & 1 & 1 \\ -\sqrt{3} & -\sqrt{3} & \sqrt{3} & \sqrt{3} \\ -\sqrt{3} & \sqrt{3} & -\sqrt{3} & \sqrt{3} \end{bmatrix} \tag{3-57}$$

The 9 nodal values of the flux are then found from equation (3-45) and written in matrix form as

$$\begin{pmatrix} i_1 \\ i_2 \\ i_3 \\ i_4 \\ i_5 \\ i_6 \\ i_7 \\ i_8 \\ i_9 \end{pmatrix} = \begin{bmatrix} 1 & -1 & -1 \\ 1 & 0 & -1 \\ 1 & 1 & -1 \\ 1 & -1 & 0 \\ 1 & 0 & 0 \\ 1 & 1 & 0 \\ 1 & -1 & 1 \\ 1 & 0 & 1 \\ 1 & 1 & 1 \end{bmatrix} \begin{pmatrix} c_1 \\ c_2 \\ c_3 \end{pmatrix} \tag{3-58}$$

Upon substituting the values of c_j from equation (3-54), the transformation matrix becomes

$$[TR] = \frac{1}{4} \begin{bmatrix} 1+2\sqrt{3} & 1 & 1 & 1-2\sqrt{3} \\ 1+\sqrt{3} & 1-\sqrt{3} & 1+\sqrt{3} & 1-\sqrt{3} \\ 1 & 1-2\sqrt{3} & 1+2\sqrt{3} & 1 \\ 1+\sqrt{3} & 1+\sqrt{3} & 1-\sqrt{3} & 1-\sqrt{3} \\ 1 & 1 & 1 & 1 \\ 1-\sqrt{3} & 1-\sqrt{3} & 1+\sqrt{3} & 1+\sqrt{3} \\ 1 & 1+2\sqrt{3} & 1-2\sqrt{3} & 1 \\ 1-\sqrt{3} & 1+\sqrt{3} & 1-\sqrt{3} & 1+\sqrt{3} \\ 1-2\sqrt{3} & 1 & 1 & 1+2\sqrt{3} \end{bmatrix} \tag{3-59}$$

Thus, the three components of the flux are found through

$$\{i_x\}_{\text{nodes}} = [TR]\{i_x\}_{\text{optimal}} \tag{3-60}$$

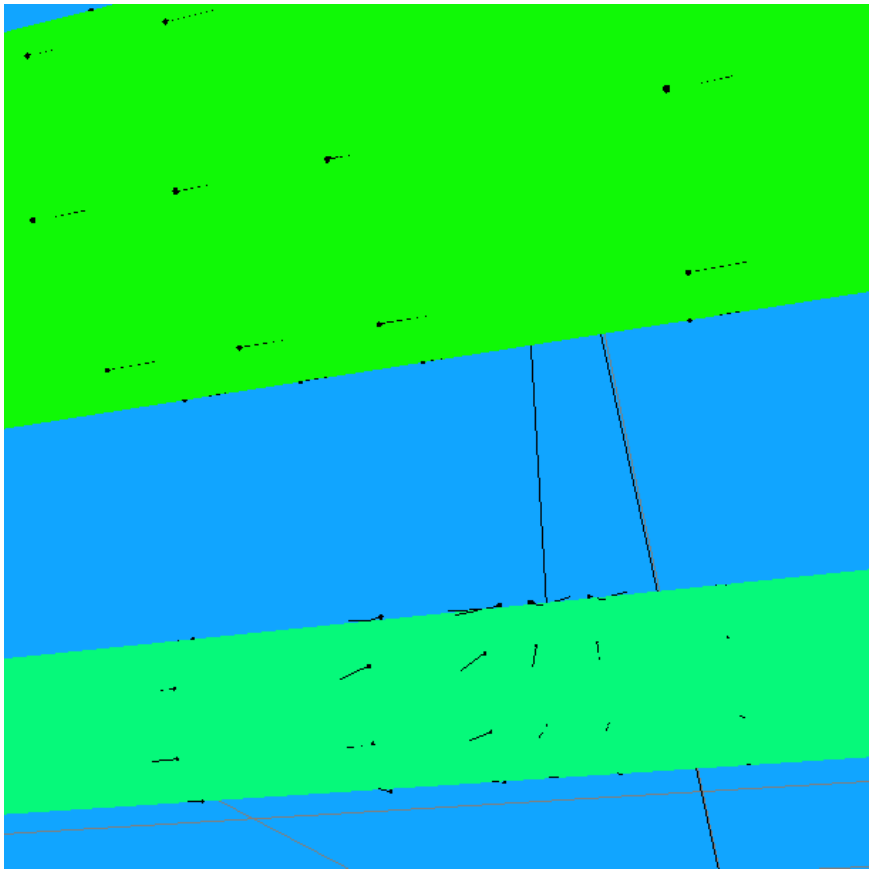

Figure 3-8: Normalized current vectors drawn on top of the pipe. Three components of the vectors are calculated in cartesian coordinates even though the flow of current is only in two directions. The fact that the vectors are always tangent to the pipe indicates that the coordinate transformation was done correctly.

$$\{i_y\}_{\text{nodes}} = [TR]\{i_y\}_{\text{optimal}} \tag{3-61}$$

and

$$\{i_z\}_{\text{nodes}} = [TR]\{i_z\}_{\text{optimal}} \tag{3-62}$$

The production code normalizes the current vectors by the largest current vector when they are drawn to the screen. An example of the vectors that are calculated with the above method is shown in Figure 3-8. The concepts presented in this section represent an extension of the methods described by Burnett.[67]

3.11 Conclusions

This chapter has presented the numerical method for solution of the governing differential equations within the soil domain and within the steel domain. Special elements have been introduced to simplify the solution for the potential distribution within the pipe steel. Techniques have also been introduced to deal with the soil surface and underlying rock ledge without the need to discretize those boundaries. The reason is that both boundaries have a normal current density equal to zero, which can be explicitly handled by the Green's function for Laplace's equation.

The boundary conditions for the differential equations and the coupling between the steel and soil domains have been briefly mentioned for completeness. Details of the application of the boundary conditions to the numerical methods and coupling of the two domains are contained in the next chapter.

CHAPTER 4
APPLYING KINETICS TO THE BEM AND FEM

A numerical method has been developed in Chapter 3 for solution of the governing differential equations for pipelines under cathodic protection. Now, the soil domain boundaries must be divide into elements and the pipe steel domain must be divided into finite volumes. The volumes will use the elements described in section 3.7.1, so that the loads (current density) at the boundary with the soil domain will match what is calculated in the soil domain.

While the boundary conditions have been mentioned in section 3.3, it is not been explained how they are applied to the numerical method. This chapter covers the application of the boundary condition to the numerical methods in detail.

4.1 Pipe Discretization

New pipelines are often placed very close to old pipes because there are a limited number of right-of-way corridors. The need to place pipelines in close proximity means there is a strong possibility of pipes interfering with the protective current being supplied to other pipes. To account adequately for any variations in the current and potential distributions, the pipes need to be discritized in both the angular and axial directions. This allows any type of distributions to be approximated by the basis functions. It also makes the matrices generated by the BEM very large.

4.1.1 Discretization of the Boundary Element Method

Equation (3-9) may now be applied to a surface that has its boundaries broken up into individual finite elements (see Chapter 5 for details of the mesh generation). The solution to the differential equation can be represented by approximate functions on each individual element. Example functions may be 0th order or constant value, 1st order or linear, etc. The simplest case is the constant element. The value of Φ is assumed to be constant across each element. Then one can write an equation of the form of (3-9) for each degree of freedom that makes up the surface and where the subscript i refers to the element number. The integrals are broken up into N sub-intervals corresponding to N elements that when summed together form the complete integral over the entire boundary

$$c_i\phi_i + \sum_j \int_{\Gamma_j} \Phi \left(\vec{n} \cdot \nabla G_{i,j}\right) d\Gamma_j = \sum_j \int_{\Gamma_j} G_{i,j} \left(\vec{n} \cdot \nabla \Phi\right) d\Gamma_j \tag{4-1}$$

When constant element are used, the unknown element potentials and normal current densities can be brought outside the integrals. Since a well posed problem has one half of the boundary conditions specified, the result is N equations with N unknowns.

Since it is desired to be able to change the boundary condition type as well as value, the notation used here will denote the matrix resulting from the left hand integral as $\boldsymbol{H}$ and the right side as $\boldsymbol{G}$

$$\boldsymbol{H}\Phi = \boldsymbol{G}\left(\vec{n} \cdot \nabla \Phi\right) \tag{4-2}$$

where $\vec{n} \cdot \nabla \Phi$ is the normal current density divided by the conductivity at the boundary.

The diagonal elements of the matrix $\boldsymbol{H}$ are often unknown at this point because linear or higher order elements have been used and the constant c_i in equation (4-1) is know only as a Cauchy principle value. A theorem by Gibbs can be used to easily find the values of the diagonal.[68] The theorem states that for any domain governed by Laplace's equation, if the potential is the same everywhere throughout the domain and that the gradient of the potential at any boundary of the domain including infinity if it exists is equal to zero, then the gradient of the potential is equal to zero everywhere within the domain. The theorem is implemented by setting a uniform potential equal to one throughout the domain. Then the gradients of potential are known to be zero everywhere which leads to the matrix equation

$$\begin{bmatrix} H_{1,1} H_{1,2} \\ H_{2,1} H_{2,2} \end{bmatrix} \begin{bmatrix} 1 \\ 1 \end{bmatrix} = \begin{bmatrix} 0 \\ 0 \end{bmatrix} \tag{4-3}$$

where the diagonal terms are unknown. The diagonal terms are now specified by the negative sum of the off-diagonal terms of each row

$$H_{i,i} = -\sum_{j \neq i} H_{i,j} \tag{4-4}$$

where j goes from one to the number of terms in a row.

When the known boundary conditions are applied, columns are swapped between the two matrices such that all the known variables are on the right side. If the resulting matrix is multiplied against the known boundary conditions, a standard linear system is obtained

$$\boldsymbol{A}x = \boldsymbol{b} \tag{4-5}$$

The solution to this system of equations yields the necessary unknown boundary conditions. Following the solution on the boundary, the value of the potential

may be obtained at any point within the domain by use of equation (3-8). In this case Φ_i is the unknown potential inside the domain, and Φ, and $(\vec{n} \cdot \nabla\Phi)$ are the solutions and known boundary conditions found previously.

If one wishes to obtain current densities within the domain, a little more work is needed. The gradient of equation (3-8) is taken to get the components of the current density vector within the domain

$$\nabla\Phi_i + \int_\Gamma \Phi\nabla\left(\vec{n} \cdot \nabla G_{i,j}\right) d\Gamma = \int_\Gamma \nabla G_{i,j} \left(\vec{n} \cdot \nabla\Phi\right) d\Gamma \tag{4-6}$$

One immediately notices that the nabla operator has been taken inside the integrals. This can be done because the limits of the integral are not affected. The first integral in equation (4-6) does not vanish. The reason for this is that the normal derivative of the Green's function has been taken at the boundary and so one does not obtain the Laplacian of the Green's function.

Equation (4-6) can be split into 3 separate equations, one for each component of the current density vector. This equation is commonly referred to as the hypersingular boundary element method because it contains a $1/r^3$ singularity. This singularity never appears if the interior point chosen is sufficiently far from the boundary.

4.1.2 Discretization of the Finite Element Domain

The finite element domain is discretized using the same surface mesh that is used in the boundary element method. This means there is a one-to-one correspondence between the degrees of freedom for the boundary element method in the soil domain and the finite element method in the pipe/anode interior domain. It also assumes that the diffusion length at the pipe surface is negligibly

small compared to the size of a pipe or holiday. Therefore, it can be assumed that the point at which Φ is evaluated in the Boundary Element Method, is approximately the spot where V is evaluated and the same nodal locations can be used in both methods.

The match-up is necessary to simplify the evaluations of the boundary conditions, equations (1-23) and (1-26). The boundary conditions use both the solution from the finite element method in the steel and the solution from the boundary element method in the soil. The difference between the two solutions, $V - \Phi$, provides the driving force for the reactions.

4.2 Self-Equilibration

Cathodic protection systems by nature, do not loose or gain electrons from their surroundings. In other words, charge is conserved. The boundary element formulation as developed in Chapter 3 will not show this feature without some modification. Instead of having a specified potential at infinity (most often set to zero) which serves as an infinite source or sink for charge, an unknown value of potential at infinity is used such that no current enters or leaves through that boundary. To implement this condition, an extra equation is added to the system[56, 69]

$$\sum_i \int_{\Gamma_i} \kappa \hat{\vec{n}} \cdot \nabla \Phi d\Gamma_i = 0 \tag{4-7}$$

Equation (4-7) simply states that there is no current lost to or gained from infinity. The left hand side is added as a new row at the bottom of the $\boldsymbol{G}$ matrix of equation (4-2), while the matrix $\boldsymbol{H}$ in (4-2) receives a row of zeros. A column is added to the $\boldsymbol{H}$ matrix which corresponds to the unknown potential at infinity. The

values that are placed in this column come from equation (3-17) and are all 4π or 1 depending on where the 4π from the Green's function is placed. This would make the $\boldsymbol{H}$ matrix singular because there is still a row of zeros in it. However, that would only be the case if Neumann type boundary conditions are specified everywhere. The Neumann problem results in an infinite number of solutions that differ by a constant. Therefore, at least one element in the system must have a Dirichlet boundary condition to make the $\boldsymbol{H}$ matrix nonsingular and result in a unique solution.

4.3 Multiple CP Systems

Riemer and Orazem describe in detail the development needed to model interactions among CP systems.[32] To allow stray current to occur between separate CP systems, additional rows of the type in equation (4-7) can be added.[70] For each separate CP system, one extra column in the $\boldsymbol{H}$ matrix is also added. The appearance of the matrices for 2 CP systems in the same domain will be

$$\boldsymbol{G} = \begin{bmatrix} G_{1,1} & G_{1,2} & G_{1,3} & G_{1,4} \\ G_{2,1} & G_{2,2} & G_{2,3} & G_{2,4} \\ 0 & 0 & A_3 & A_4 \\ A_1 & A_2 & 0 & 0 \end{bmatrix} \tag{4-8}$$

$$\boldsymbol{H} = \begin{bmatrix} H_{1,1} & H_{1,2} & 0 & 1 \\ H_{2,1} & H_{2,2} & 1 & 0 \\ 0 & 0 & 0 & 0 \\ 0 & 0 & 0 & 0 \end{bmatrix} \tag{4-9}$$

with the column matrix $\boldsymbol{u}$ given by

$$\boldsymbol{u} = \begin{bmatrix} u_1 \\ u_2 \\ u_{\infty,\text{System2}} \\ u_{\infty,\text{System1}} \end{bmatrix} \tag{4-10}$$

and the column matrix $\boldsymbol{q}$ defined in the usual way. When there are two or more CP systems within a domain, a Dirichlet condition on at least one element in each CP system must be specified to prevent the $\boldsymbol{H}$ matrix from being singular. The added equations and unknown potentials at infinity are sufficient to allow several CP system to interact with each other while enforcing that the total current on each CP system sum to zero.

4.4 Coating Holidays

A coating holiday is a small region of pipe where the coating has somehow been removed. This can happen during handling, back fill, or digging in the region of the pipe. In this way, bare steel is exposed to the corrosive soil environment. Without cathodic protection, such exposed areas corrode very rapidly. The design equations of Morgan are incapable of handling nonuniform potential and current distribution in the angular direction. Therefore another solution method is needed. Early attempts at solving this problem used finite elements.[24] While the method used had a 15% error in the sum of all current being zero, it did show that the majority of current entered the pipe through the holiday. Boundary element techniques fared much better at correctly calculating the current.[33] Kennelly *et al.* used constant triangular elements to represent the potential and

current distributions.[24] This meant a great many triangles were needed where the discontinuities in the boundary conditions occurred in order to represent the sharp profile of the solution in these regions. Therefore, only small sections of pipe (about 20 feet) could be modeled successfully when holidays were to be included.

To include holidays in the boundary element model, one must have a group of elements whose outside boundary form the edge of the holiday. Since it has been stated that the discontinuity of the solution at the holiday/coating boundary results in a very sharp curve in the solution, there must be sufficient elements in the neighborhood of the boundary condition change such that the solution can be adequately represented by their basis functions.

4.5 Nonlinear Boundary Conditions without Attenuation in the Pipe Steel

The boundary conditions described in Chapter 1 are nonlinear and require special methods to enforce them in the boundary element method. Aoki *et al.* describe a method to address nonlinear boundary conditions.[71]

First, it is assumed that V is zero everywhere, in all of the pipes and anodes. This assumption is justified if the conductivity of the steel of the pipes is several orders of magnitude greater than that of the soil environment and the pipes are short. The pipe length is constrained by the requirement that there be no appreciable potential drop from one end of the pipe to the other as compared to the smallest potential drop through the soil between any two points between an anode and pipe.

Then, the procedure is to do a Taylor series expansion of equation (4-2) around the known boundary conditions. A Newton-Raphson iterative procedure is obtained. One starts by writing a residual after the columns corresponding to the unknown boundary conditions have been moved into the matrix $\boldsymbol{H}$

$$\boldsymbol{R}_{\text{Residual}} = \boldsymbol{H}\begin{bmatrix} \vec{n}\cdot\nabla\Phi \\ \cdots\cdots\cdots \\ \Phi \end{bmatrix} - \boldsymbol{G}\begin{bmatrix} \Phi \\ \cdots\cdots\cdots \\ \vec{n}\cdot\nabla\Phi = f(\Phi) \end{bmatrix} \tag{4-11}$$

The residual results because only a nonlinear relationship is know between Φ and $\vec{n}\cdot\nabla\Phi$ so Φ must be guessed in order to obtain the known boundary condition $\vec{n}\cdot\nabla\Phi$. Therefore equation (4-2) does not hold. For exposed steel in a soil environment under cathodic protection, that relationship may be of the form of equation (1-23). The Taylor series expansion truncated at the linear term gives

$$\begin{aligned} 0 = \boldsymbol{H}&\left[\begin{pmatrix} \Phi_i^{(k)} \\ \cdots \\ (\vec{n}\cdot\nabla\Phi)_i^{(k)} \end{pmatrix} + \begin{pmatrix} \Delta\Phi_i^{(k)} \\ \cdots\cdots \\ \Delta(\vec{n}\cdot\nabla\Phi)_i^{(k)} \end{pmatrix}\right] \\ -\boldsymbol{G}&\left[\begin{pmatrix} \Phi_i^{(k)} \\ \cdots\cdots\cdots \\ -f_i\left(\Phi_i^{(k)}\right) \end{pmatrix} + \begin{pmatrix} 0 \\ \cdots\cdots\cdots\cdots\cdots \\ -\frac{\partial f_i\left(\Phi_i^{(k)}\right)}{\partial\Phi}\Delta(\vec{n}\cdot\nabla\Phi)_i^{(k)} \end{pmatrix}\right] \end{aligned} \tag{4-12}$$

The residual error, R_{Residual}, is obtained by subtracting equation (4-11) from equation (4-12)

$$\boldsymbol{R}_{\text{Residual}} = \left[-\boldsymbol{H} + \boldsymbol{G}\begin{pmatrix} 0 & \vdots & 0 \\ \cdots\cdots\cdots\cdots\cdots & & \\ 0 & \vdots & \left[-\frac{\partial f_i\left(\Phi_i^{(k)}\right)}{\partial\Phi}\right] \end{pmatrix}\right]\begin{bmatrix} \Delta\Phi_i^{(k)} \\ \cdots\cdots\cdots \\ \Delta\left(\vec{n}\cdot\nabla\Phi\right)_i^{(k)} \end{bmatrix} \tag{4-13}$$

The matrix containing $\left[-\partial f_i\left(\Phi_i^{(k)}\right)/\partial\Phi\right]$ is an $m \times n$ diagonal matrix which is obtained from the polarization curves (see Appendix A). Since $\mathbf{G}$ is an $n \times m$ matrix, the resultant that is added to the $\mathbf{H}$ matrix is square. The new values of Φ and $\vec{n}\cdot\nabla\Phi$ are obtained from:

$$\begin{aligned} \Phi_i^{(k+1)} &= \Phi_i^{(k)} + \Delta\Phi_i^{(k)} \\ (\vec{n}\cdot\nabla\Phi)_i^{(k+1)} &= (\vec{n}\cdot\nabla\Phi)_i^{(k)} + \Delta(\vec{n}\cdot\nabla\Phi)_i^{(k)} \end{aligned} \tag{4-14}$$

The new values can be substituted back into equation (4-11) to obtain a new residual. The process is repeated until the residual is sufficiently small.

It should be noted that the above method will often fail if the initial guess is not close enough to the solution. Therefore a line search method is needed to insure convergence.[72] The method works by defining an objective function that must be reduced at each iteration of the technique

$$g := \sqrt{\boldsymbol{R}_1^2 + \cdots + \boldsymbol{R}_n^2} \tag{4-15}$$

A subroutine takes the column matrix containing the Newton-Raphson step and updates the unknown variables according the the function

$$\boldsymbol{x} = \boldsymbol{x}_{\text{old}} + \lambda\Delta\boldsymbol{x} \tag{4-16}$$

where $\boldsymbol{x}$ is the column matrix of unknown variables (Φ and $\vec{n}\cdot\nabla\Phi$) and λ is a number with a value $0 < \lambda \leq 1$. The method is illustrated schematically in Figure 4-1. The initial calculation is done with the full Newton step ($\lambda = 1$). If the sum of squares or the residual error, g, obtained from equation (4-15) is reduced, the updated values of $\boldsymbol{x}$ are accepted. If g is not reduced, a smaller value of λ is selected using the same Newton step and a new residual and objective function

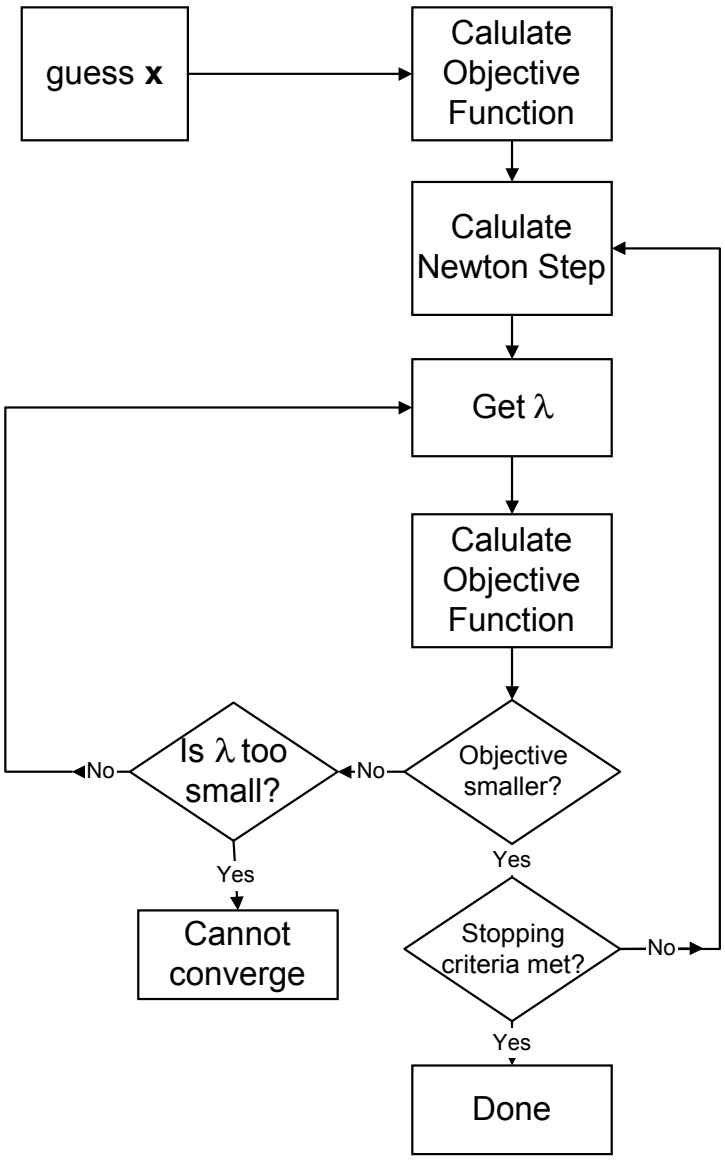

Figure 4-1: Newton-Raphson line search flow diagram.

calculated. This is repeated until the objective function is reduced from that of the previous iteration. Then the boundary conditions are recalculated and a new Jacobian is calculated and the method is repeated until the residual, g is close enough to zero to stop. At any point in the method,if a value of λ cannot be found such that g is reduced, the method fails.

4.6 Nonlinear Boundary Conditions with Attenuation in the Pipe Steel

The external load integral from the finite element method can be written for each node as a sum of contributions from each element that has that node in common

$$f_i = \sum_{\ell=1}^{nce} -\oiint_{\Gamma_{(e)}} w_{\ell,i}\kappa_{\text{soil}}\left(\vec{n}\cdot\nabla\Phi\right)ds \tag{4-17}$$

where f_i is the load for node i and nce is the number of contributing elements to the load at node i. This integral must be evaluated across all nodes on all surfaces of all structures in the model. Since the value of $\vec{n}\cdot\nabla\Phi$ is either a known or unknown boundary condition from the boundary element method, and the kinetics of the electrochemistry, it must be factored out of the integral. Using the shape functions that describe the values of $\vec{n}\cdot\nabla\Phi$ across each element in terms of the nodal values $\vec{n}\cdot\nabla\Phi$ and the weights, one can rewrite equation (4-17) as

$$f_i = \sum_{\ell=1}^{nce} -\oiint_{\Gamma_{(e)}} w_{\ell,i}\kappa_{\text{soil}} \sum_{k=1}^{nen} \phi_{\ell,k}(s)\left(\vec{n}\cdot\nabla\Phi\right)_{\ell,k} ds \tag{4-18}$$

where nen is the number of nodes in the element, $\left(\vec{n}\cdot\nabla\Phi\right)_k$ is the nodal value of the normal electric field within the element n, and $\phi(s)_k$ is the shape function whose value is one at node k. Using the property of integrals that an integral of a

sum is the sum of integrals, equation (4-18) can be rewritten as

$$f_i = \sum_{\ell=1}^{nce} \sum_{k=1}^{nen} - \oint\!\!\!\!\!\!\iint_{\Gamma_{(e)}} w_{\ell,i} \kappa_{\text{soil}} \phi_{\ell,k}(s) \, (\vec{n} \cdot \nabla \Phi)_{\ell,k} \, ds \tag{4-19}$$

Equation (4-19) can then be written in matrix form as

$$f_i = \left[\; \ldots - \oint\!\!\!\!\!\!\iint_{\Gamma_{(e)}} w_{\ell,i} \kappa_{\text{soil}} \phi_{\ell,k}(s) ds \; \ldots \right] \begin{bmatrix} (\vec{n} \cdot \nabla \Phi)_{1,1} \\ \vdots \\ (\vec{n} \cdot \nabla \Phi)_{ne,nen} \end{bmatrix} \tag{4-20}$$

or

$$f_i = \hat{\boldsymbol{F}}_i \, [\vec{n} \cdot \nabla \Phi] \tag{4-21}$$

These sub-matrices are then assembled with the right hand column matrix from equation (4-2) to form the global finite element system

$$\boldsymbol{K} \, [V] = \hat{\boldsymbol{F}} \, [\vec{n} \cdot \nabla \Phi] \tag{4-22}$$

where $\hat{\boldsymbol{F}}$ is a matrix formed from the assembly of equation (4-21) such that the column matrix corresponding to the Boundary Element Method is formed on the right hand side. $\hat{\boldsymbol{F}}$ is not symmetric.

4.7 Solution by Successive Substitutions

The first attempt to couple the FEM to the BEM, was to use a successive substitutions approach. The idea was to assume an initial value of the voltage in the pipe steel to be zero everywhere. Then the current density distribution was calculated using the BEM. The result was the values of the load vector, $[\vec{n} \cdot \nabla \Phi]$ needed in equation (4-22). Then, updated values of $\boldsymbol{V}$ were determined using the FEM as shown in equation (4-22). The advantage of the technique is that

the sparse symmetry of the matrix $\boldsymbol{K}$ is preserved so that a Cholesky decomposition can be used. The drawback, is that the iterative application of the nonlinear polarization curves must be repeated for every update of $\boldsymbol{V}$. Unfortunately, the simplistic approach of successive substitution failed to converge for all but the simplest case of a single short well-coated pipe. Also, the approach took a great deal of time to converge because of the multiple applications of the nonlinear boundary conditions within the BEM.

4.8 Solution of Combined System by Newton-Raphson Technique

The set of variables that appear in the combined soil domain metal domain problem are potentials outside the surface of all pipes or tanks (Φ), unknown normal electric field on anodes ($\vec{n} \cdot \nabla\Phi$), and unknown potential difference ($V - \Phi$) for coated and bare protected structures. Introduction of the attenuation code from equation (4-22) to the problem introduces n more equations and n more unknowns where n is the number of nodes used to describe the boundary mesh for the problem. The total number of algebraic equations to be solved is now $2n + k$, where k is the number of separate CP systems.

The coupled methods are placed into a global matrix system and one instance of equation (4-7) is added for self-equilibriation of each CP system

$$\begin{bmatrix} \boldsymbol{H}_{p,p} & \boldsymbol{H}_{a,p} & 0 & 0 & -4\pi \\ \boldsymbol{H}_{p,a} & \boldsymbol{H}_{a,a} & 0 & 0 & -4\pi \\ 0 & 0 & \boldsymbol{K}_p & 0 & 0 \\ 0 & 0 & 0 & \boldsymbol{K}_a & 0 \\ 0 & 0 & 0 & 0 & 0 \end{bmatrix} \begin{bmatrix} \boldsymbol{\Phi}_p \\ \boldsymbol{\Phi}_a \\ V_p \\ V_a \\ \boldsymbol{\Phi}_\infty \end{bmatrix} = \begin{bmatrix} \boldsymbol{G}_{p,p} & \boldsymbol{G}_{a,p} \\ \boldsymbol{G}_{p,a} & \boldsymbol{G}_{a,a} \\ \hat{\boldsymbol{F}}_p & 0 \\ 0 & \hat{\boldsymbol{F}}_a \\ A_p & A_a \end{bmatrix} \begin{bmatrix} \vec{n} \cdot \nabla\boldsymbol{\Phi}_p \\ \vec{n} \cdot \nabla\boldsymbol{\Phi}_a \end{bmatrix} \tag{4-23}$$

where the subscripts a and p refer to anodes and pipe respectively, double subscripts are from the boundary element method and refer to where the collocation point and field point lie respectively, and A is the area of each section.

The columns of equation (4-23) are sorted such that all of the unknown variables are on the left hand side. For anodes, the unknown variable is the current density ($\vec{n} \cdot \nabla\Phi$), and for all other structures it is the potential (Φ). The reordered system then looks like

$$\begin{bmatrix} \boldsymbol{H}_{p,p} & -\boldsymbol{G}_{a,p} & 0 & 0 & -4\pi \\ \boldsymbol{H}_{p,a} & -\boldsymbol{G}_{a,a} & 0 & 0 & -4\pi \\ 0 & 0 & \boldsymbol{K}_p & 0 & 0 \\ 0 & -\hat{\boldsymbol{F}}_a & 0 & \boldsymbol{K}_a & 0 \\ 0 & -A_a & 0 & 0 & 0 \end{bmatrix} \begin{bmatrix} \Phi_p \\ \vec{n} \cdot \nabla\Phi_a \\ V_p \\ V_a \\ \Phi_\infty \end{bmatrix} = \begin{bmatrix} \boldsymbol{G}_{p,p} & -\boldsymbol{H}_{a,p} \\ \boldsymbol{G}_{p,a} & -\boldsymbol{H}_{a,a} \\ \hat{\boldsymbol{F}}_p & 0 \\ 0 & 0 \\ A_p & 0 \end{bmatrix} \begin{bmatrix} \vec{n} \cdot \nabla\Phi_p \\ \Phi_a \end{bmatrix} \tag{4-24}$$

where the column matrix on the left hand side is the set of unknown variables and the column matrix on the right side is the set of known boundary conditions. Equation (4-24) can be rewritten as

$$[\boldsymbol{A}] \begin{bmatrix} \Phi_p \\ \vec{n} \cdot \nabla\Phi_a \\ V_p \\ V_a \\ \Phi_\infty \end{bmatrix} = [\boldsymbol{B}] \begin{bmatrix} \vec{n} \cdot \nabla\Phi_p \\ \Phi_a \end{bmatrix} \tag{4-25}$$

where $\boldsymbol{A}$ and $\boldsymbol{B}$ correspond to the matrices in equation (4-24).

If the boundary conditions are constant, the unknown variables can be obtained by a simple matrix inversion. For problems in electrochemistry, the set of

known boundary conditions are given as a set of nonlinear functions of the unknown variables. Therefore, the solution must be obtained using a technique for coupled sets of nonlinear algebraic equations. This is done by rewriting equation (4-25) as a function that is equal to zero

$$[\boldsymbol{A}]\begin{bmatrix}\Phi_p\\ \vec{n}\cdot\nabla\Phi_a\\ V_p\\ V_a\\ \Phi_\infty\end{bmatrix}-[\boldsymbol{B}]\begin{bmatrix}\vec{n}\cdot\nabla\Phi_p=f(V,\Phi_p)\\ \Phi_a=f(V,\vec{n}\cdot\nabla\Phi_a)\end{bmatrix}=\begin{bmatrix}0\\0\\0\\0\\0\end{bmatrix} \tag{4-26}$$

Since one of the column matrices contains unknown variables, a guess for the values must be made. Since the guess will not be the correct solution to equation (4-26), the right hand column vector will not be equal to zero, but a residual

$$[\boldsymbol{A}]\begin{bmatrix}\Phi_p\\ \vec{n}\cdot\nabla\Phi_a\\ V_p\\ V_a\\ \Phi_\infty\end{bmatrix}-[\boldsymbol{B}]\begin{bmatrix}f(V,\Phi_p)\\ f(V,\vec{n}\cdot\nabla\Phi_a)\end{bmatrix}=\begin{bmatrix}R\end{bmatrix} \tag{4-27}$$

Rewriting equation (4-26) as a general set of equations of an unknown vector $\boldsymbol{x}$

$$\boldsymbol{F}(\boldsymbol{x})=\boldsymbol{0} \tag{4-28}$$

a Jacobian $\boldsymbol{J}$, of the set of equations can be written where an element in the Jacobian is given by

$$\boldsymbol{J}_{i,j}=\left.\frac{\partial \boldsymbol{F}_i}{\partial \boldsymbol{x}_j}\right|_{\boldsymbol{x}_{\ell\neq j}} \tag{4-29}$$

Then the Newton-Raphson iteration can be performed as in section 4.5 on page 62 to obtain the solution vector $\boldsymbol{x}$ such that equation (4-28) holds. Again the line search is necessary for the the method to work. However, in most non-trivial cases, even the line searches fail.

In order to get the method to converge to a solution, many techniques were tried including the minimal residual techniques such as the modified Powell method,[73] Levenberg-Marquort techniques and other methods such as the conjugate gradient method. These techniques would converge sometimes if the guess was nearly the correct value.

4.9 Variable Transformation to Stabilize Convergence

The system of equation that result from Φ, V, i as the set of variables for the solution has very poor convergence characteristics. Great effort was required to bring the system to convergence. Standard line searches and even minimal residual techniques failed to converge.

A simple variable transformation has been developed that enables good convergence properties using the simple line search method. The variable transformation needed can be seen easily from the equations used to describe the kinetics

$$i = 10^{\frac{V-\Phi-E_{\mathrm{Fe}}}{\beta_{\mathrm{Fe}}}} - \left(\frac{1}{i_{\mathrm{lim},\mathrm{O}_2}} + 10^{\frac{V-\Phi-E_{\mathrm{O}_2}}{\beta_{\mathrm{O}_2}}} \right)^{-1} 10^{-\frac{V-\Phi-E_{\mathrm{H}_2}}{\beta_{\mathrm{H}_2}}} \tag{4-30}$$

In equation (4-30), the difference $V - \Phi$ appears many times. A simple transformation can be written

$$\Psi = V - \Phi \tag{4-31}$$

where Ψ represents the driving force for the electrochemical kinetics. The variable V is then chosen as the dependent variable and rewritten as

$$V = \Psi + \Phi \tag{4-32}$$

All of the equations used for the kinetics, bare metal (1-23), coated metal (1-26), galvanic anodes (1-27), and impressed current anodes (1-30) can be rewritten in terms of the new variable. For bare metal, one obtains

$$i = 10^{\frac{\Psi - E_{\mathrm{Fe}}}{\beta_{\mathrm{Fe}}}} - \left(\frac{1}{i_{\mathrm{lim},\mathrm{O}_2}} + 10^{\frac{\Psi - E_{\mathrm{O}_2}}{\beta_{\mathrm{O}_2}}} \right)^{-1} 10^{-\frac{\Psi - E_{\mathrm{H}_2}}{\beta_{\mathrm{H}_2}}} \tag{4-33}$$

for coated metal there are two simultaneous equations in two unknowns that describe the current density

$$i = \frac{-(\Phi - \Phi_{\mathrm{in}})}{\rho_{\mathrm{film}} \delta_{\mathrm{film}}} \tag{4-34}$$

and

$$i = \frac{A_{\mathrm{pore}}}{A} \left[10^{\frac{\Psi + \Phi - \Phi_{\mathrm{in}} - E_{\mathrm{Fe}}}{\beta_{Fe}}} - \left(\frac{1}{(1 - \alpha_{\mathrm{block}})\, i_{\mathrm{lim},\mathrm{O}_2}} - 10^{\frac{\Psi + \Phi - \Phi_{in} - E_{\mathrm{O}_2}}{\beta_{\mathrm{O}_2}}} \right)^{-1} - 10^{\frac{-\left(\Psi + \Phi - \Phi_{\mathrm{in}} - E_{\mathrm{H}_2}\right)}{\beta_{\mathrm{H}_2}}} \right] \tag{4-35}$$

for galvanic anodes

$$\Psi = E_{\mathrm{anode}} + \beta_{\mathrm{anode}} \log(i / i_{\mathrm{corr}} + 1) \tag{4-36}$$

and finally for impressed current anodes

$$\Psi = \triangle V_{\mathrm{rectifier}} + E_{\mathrm{O}_2} + \beta_{\mathrm{O}_2} \log(i / i_{\mathrm{corr}} + 1) \tag{4-37}$$

where $\triangle V_{\mathrm{rectifier}}$ is the known setting for the rectifier.

The set of equations for the finite element method must also be rewritten as

$$\boldsymbol{K}[\Psi + \Phi] = [f] \tag{4-38}$$

where f and $\boldsymbol{K}$ do not change. The boundary element method is not changed. The set of equations that is solved becomes:

$$\begin{bmatrix} 0 & 0 & \boldsymbol{H}_{p,p} & \boldsymbol{H}_{a,p} & -4\pi \\ 0 & 0 & \boldsymbol{H}_{p,a} & \boldsymbol{H}_{a,a} & -4\pi \\ \boldsymbol{K}_p & 0 & \boldsymbol{K}_p & 0 & 0 \\ 0 & \boldsymbol{K}_a & 0 & \boldsymbol{K}_a & 0 \\ 0 & 0 & 0 & 0 & 0 \end{bmatrix} \begin{bmatrix} \Psi_p \\ \Psi_a \\ \Phi_p \\ \Phi_a \\ \Phi_\infty \end{bmatrix} = \begin{bmatrix} \boldsymbol{G}_{p,p} & \boldsymbol{G}_{a,p} \\ \boldsymbol{G}_{p,a} & \boldsymbol{G}_{a,a} \\ \hat{\boldsymbol{F}}_p & 0 \\ 0 & \hat{\boldsymbol{F}}_a \\ A_p & A_a \end{bmatrix} \begin{bmatrix} \vec{n} \cdot \nabla \Phi_p \\ \vec{n} \cdot \nabla \Phi_a \end{bmatrix} \tag{4-39}$$

At this point the essential boundary condition for V $(\Psi + \Phi)$ is applied. There is one degree of freedom in the problem for this potential so one node on one pipe is selected to have a 0 potential. This is done be replacing the FEM equation for the single selected node in the system given by equation (4-39) with the equation

$$\Psi + \Phi = 0 \tag{4-40}$$

The FEM equation (lower half of the system) is replaced because that is where the degree of freedom in the reference potential is. If there are multiple CP systems, then there must be an equal number of essential boundary conditions on $\Psi + \Phi$. Once the equations are set up, all unknown variables are placed on the left-hand-side, which are Φ and Ψ for cathodes (pipes, tank bottoms, ship hulls, etc.) and $\vec{n} \cdot \nabla \Phi$ and Φ for anodes. The reordered system of equations is

$$\begin{bmatrix} 0 & -\boldsymbol{G}_{a,p} & \boldsymbol{H}_{p,p} & \boldsymbol{H}_{a,p} & -4\pi \\ 0 & -\boldsymbol{G}_{a,a} & \boldsymbol{H}_{p,a} & \boldsymbol{H}_{a,a} & -4\pi \\ \boldsymbol{K}_p & 0 & \boldsymbol{K}_p & 0 & 0 \\ 0 & -\hat{\boldsymbol{F}}_a & 0 & \boldsymbol{K}_a & 0 \\ 0 & -A_a & 0 & 0 & 0 \end{bmatrix} \begin{bmatrix} \Psi_p \\ \vec{n} \cdot \nabla \Phi_a \\ \Phi_p \\ \Phi_a \\ \Phi_\infty \end{bmatrix} = \begin{bmatrix} \boldsymbol{G}_{p,p} & 0 \\ \boldsymbol{G}_{p,a} & 0 \\ \hat{\boldsymbol{F}}_p & 0 \\ 0 & -\boldsymbol{K}_a \\ A_p & 0 \end{bmatrix} \begin{bmatrix} \vec{n} \cdot \nabla \Phi_p \\ \Psi_a \end{bmatrix} \tag{4-41}$$

The above system of equations is then solved using the same technique as described in section 4.5. This system has excellent convergence characteristics and uses about the same number of iterations as the method without attenuation.

4.10 Conclusions

A method has been developed to model cathodic protection of complicated pipeline networks. It utilizes the boundary element method to solve Laplac's equation within the soil and it accounts for the non-zero voltage drop in long pipes using a finite element solution.

A new variable transformation has been described to stabilize the convergence of the application of the nonlinear boundary conditions.

There are still some issues to be dealt with in the development of a working model. The creation of an optimized mesh is treated in the next chapter. Verification of the solution techniques is done in Chapter 7.

CHAPTER 5
MESH GENERATION

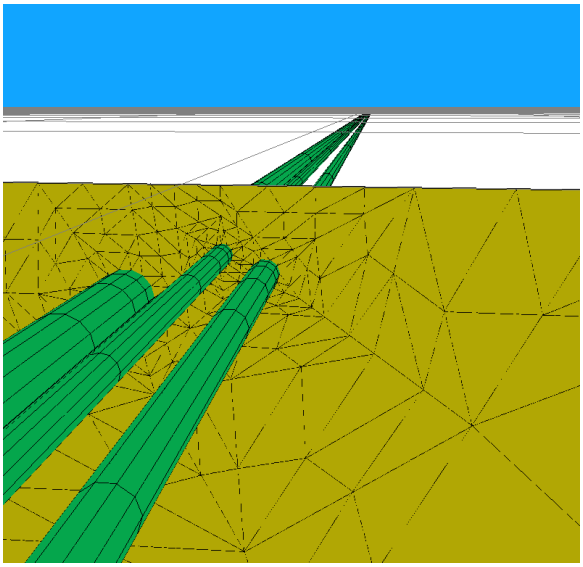

Figure 5-1: Type of mesh needed for model. Three pipes are shown passing through a point where the soil conductivity changes.

The Boundary Element Method (BEM) and the Finite Element Method (FEM) rely on a mesh in order to solve the differential equations. A mesh is a set of lines, triangles, rectangles or other shapes that when pieced together, form the boundaries of the geometry of interest. The finite element method also must have the domain enclosed by the boundaries divided up into these shapes. The BEM needs a mesh on the boundaries only. These shapes are called elements hence the name of the numerical methods.

Elements use a shape function to approximate the solution along the geometry described by the element. The number of elements should be sufficient to

allow the shape functions to approximate the solution to the governing differential equation.

One of the most difficult problems to address in computer code is how to discretize an object such that the solution obtained from the BEM and FEM contains a desired minimum level of information. For a discretization method to succeed, it must not only be able to describe the solution accurately, but must also describe the geometry sufficiently well so that the solution can be obtained.

5.1 Basic Mesh

The basic mesh must account for the current and potential distribution both axially and around the circumference of the pipe. It is accomplished be dividing the pipe surface (boundary to the soil domain) into 2-dimensional elements that are piece-wise continuous. The elements are not planar. They are wrapped onto the pipe geometry like wrapping paper to a gift. Therefore the elements are 2-dimensional only in a curvi-linear coordinate system. A coordinate transformation must be derived to map the 2-dimensional curvi-linear system to the 3-dimensional cartesian system where the differential equation is solved. In the curvi-linear system, the element is called the parent element since all the elements have the same size and shape in that system.

5.1.1 Discretization and Shape Functions

The family of elements that use the same basis (shape) functions to describe the geometry over the surface of the element as well as the solution to the differential equation over the element are called iso-parametric elements.[67, 74] These

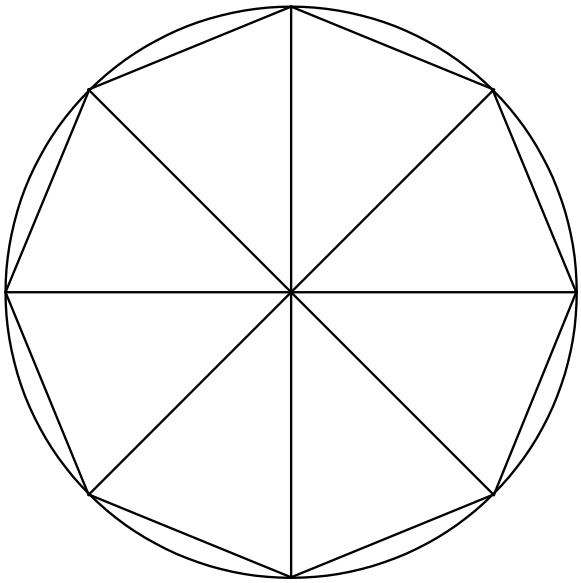

Figure 5-2: Circle discretized with 8 linear triangular elements. The area is $2\sqrt{2}r^2$ for the 8 triangles which is a 10.% error.

elements have been used in the code that has been developed. The choice of element shape has been dictated by the geometry being represented. The element that best fits the sides of a cylinder is a quadrilateral element while triangles are best used on the ends. The only remaining issue then is to choose how many nodes and therefore the order of the basis polynomials used to describe the variation of the geometry and solution over the individual elements.

Basis functions considered for the elements were: 1) constant, 2) linear, 3) quadratic, and 4) cubic. Of these, the curved functions, quadratic and higher, make the most sense because of the curvature of the geometry. They also make sense for representing the solution since they can more easily describe the curve heading into the singularity in the current density that occurs at junctions between different boundary conditions where the angle of the geometry at the junction is not 90 degrees. Table 5.1 shows the capability of 3 types of elements to rep-

Table 5.1: Error of Constant, Linear, and Quadratic elements in representing a circle whose circumference is π and has unit diameter.

Nodes	Constant	%err	Linear	%err	Quadratic	%err
6	3.464	10.3%	3.0	4.51%	3.094	1.51%
8	3.314	5.48%	3.062	2.55%	3.125	0.53%
10	3.249	3.43%	3.090	1.64%	3.134	0.23%
12	3.215	2.35%	3.106	1.14%	3.138	0.12%
16	3.183	1.31%	3.121	0.64%	3.140	0.038%
24	3.160	0.58%	3.133	0.29%	3.1414	0.0077%

resent a circle as a boundary to an area.[32] At 12 degrees of freedom, the quadratic element is better by an order of magnitude in the error. In fact, 32-36 degrees of freedom are needed with linear or constant elements to achieve the same accuracy representing a circle as do 12 degrees of freedom using quadratic elements. Figure 5-3 shows eight linear triangles used to represent a circle. The error in the surface area is 10.%. That error may not be the most important however. In the end, it is how well the mesh can approximate the solution to the differential equation that is most important.

5.1.2 Continuity of the Shape Functions

It is known from examination of Laplace's equation that the potential distribution along any boundary is at least piece-wise continuous. Therefore, the basis functions must also exhibit this type of continuity. These elements are commonly referred to as C^0 continuous elements. Since it is not required for the elements to be square integrable $(H^0)^\dagger$ for the boundary element method or that their derivatives be continuous (C^1) or square integrable (H^1), just about any piece-wise con-

†These terms (C^0, H^0, etc.) refer to Sobolev spaces.[74]

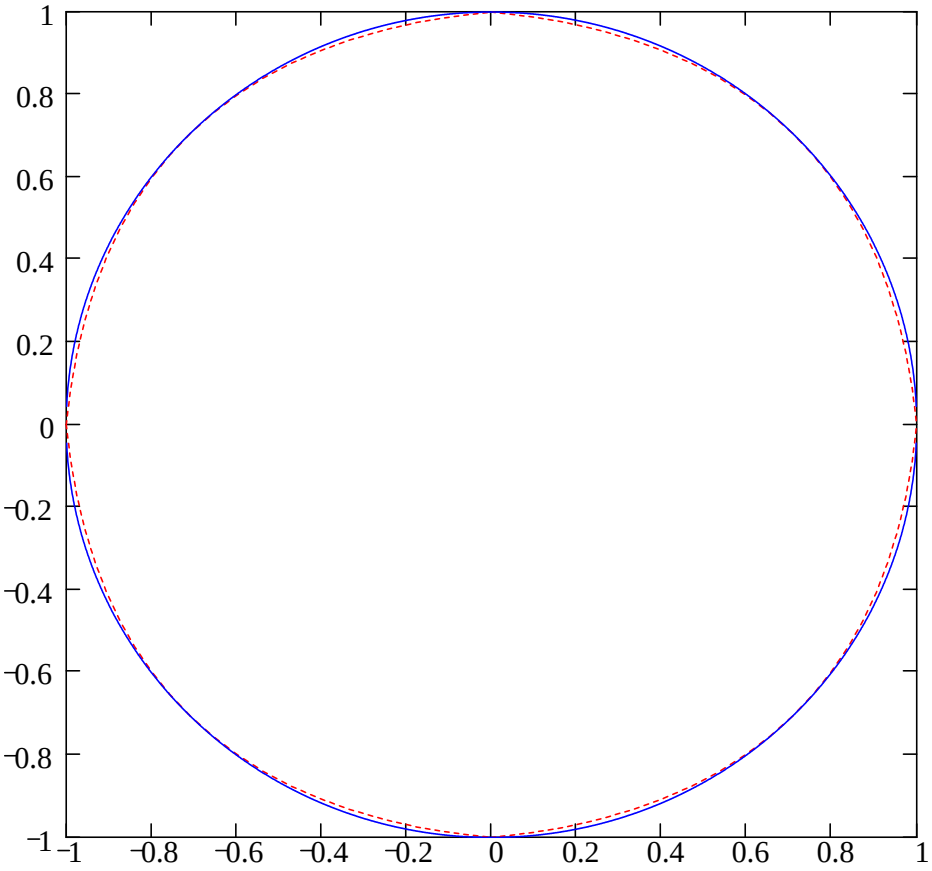

Figure 5-3: Four quadratic elements with eight degrees of freedom representing a circle.

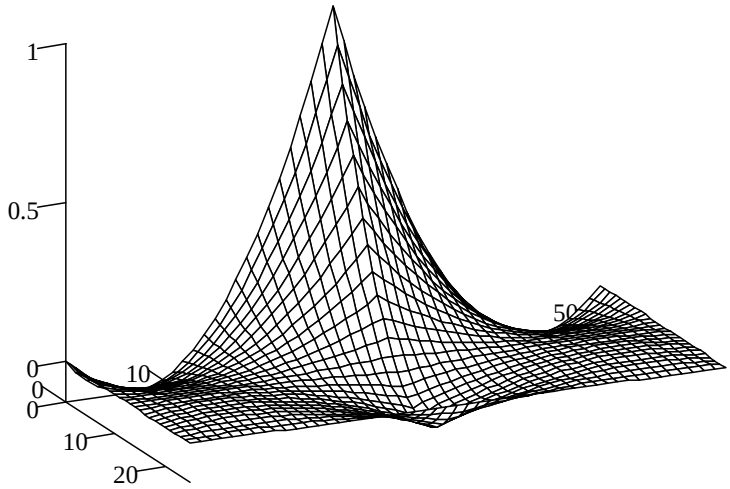

Figure 5-4: Continuity of the basis functions. Two elements are shown. Basis functions that share a node with a value of one must be continuous.

tinuous function could be used as the basis functions. However, the finite element method used within the steel of the pipe must use square integrable (H^0) shape functions.[74] It is also necessary to have the solutions between the soil and steel match up. Therefore the same element needs to be used in both numerical methods. Lagrange polynomial basis functions are very well developed in the literature,[67, 74] and are often needed for boundary element methods.[63] They work well for FEM, so they are used when rectangular shapes are needed such as the walls of the pipe. In the case of this code, quadratic Lagrangian iso-parametric elements are used which exhibit the necessary quality of H^0 continuity.

It is often required to include triangular elements to properly describe the geometry. The triangles must be piece-wise continuous and be continuous with any rectangular elements they may be in contact with. Quadratic iso-parametric triangles are used for this purpose. They exhibit C^0 continuity with the Lagragian type elements. The triangles can then be used to increase or decrease the local

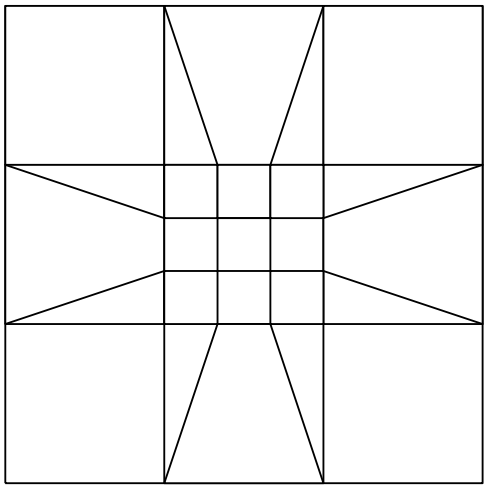

Figure 5-5: Use of triangles to increase the degrees of freedom in the center region while maintaining C^0 continuity.[67]

density of nodes while maintaining continuity throughout the boundary. They can also be used to describe difficult shapes such as coating holidays, ends of pipes, and tank bottoms. Figure 5-5 shows how triangular elements can be used to increase the density of elements in a small region. Small regions occur any time a holiday is placed on the pipe.

5.1.3 Quadratic Iso-Parametric Rectangles

Quadratic Lagrangian iso-parametric rectangular elements are used for most of the mesh that constitutes the pipes and anodes. The parent element contains 9 nodes and nine shapes functions. The geometry and solution is written in terms of the shape functions, i.e.

$$u(\eta, \xi) = \sum_{i=1}^{9} \phi_i(\eta, \xi) u_i \tag{5-1}$$

where ϕ_i is the shape function and η and ξ are homogeneous coordinates in the parent element that take values from -1 to 1, u is the quantity of interest such as

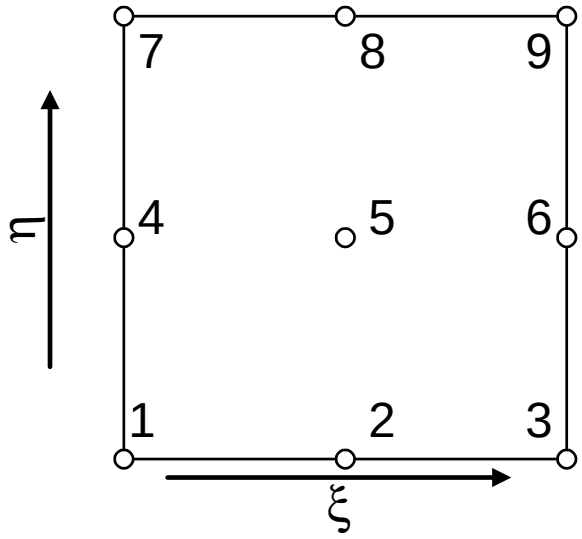

Figure 5-6: Quadratic iso-parametric rectangular parent element. Numbering of nodes and shape functions given in figure.

the x coordinate or the solution to the differential equation, and u_i is the value of the quantity of interest at node i. The nodes are numbered as in Figure 5-6. The shape functions corresponding to each node are given respectively

$$\phi_1 = \frac{1}{4}\eta(\eta-1)\xi(\xi-1) \tag{5-2}$$

$$\phi_2 = \frac{1}{2}(1-\eta^2)\xi(\xi-1) \tag{5-3}$$

$$\phi_3 = \frac{1}{4}\eta(1+\eta)\xi(\xi-1) \tag{5-4}$$

$$\phi_4 = \frac{1}{2}\eta(\eta-1)(1-\xi^2) \tag{5-5}$$

$$\phi_5 = (1-\eta^2)(1-\xi^2) \tag{5-6}$$

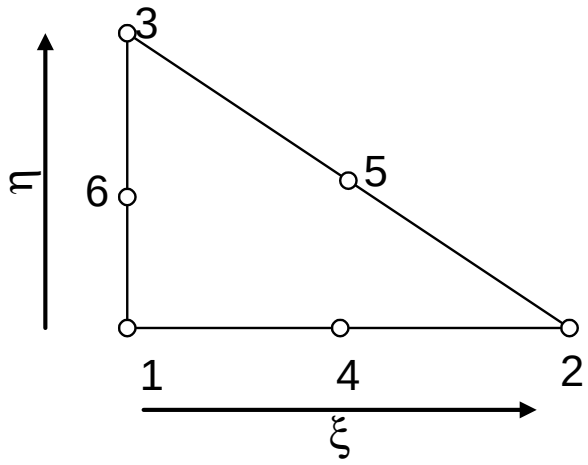

Figure 5-7: Quadratic iso-parametric triangular parent element. Numbering of nodes and shape functions given in figure.

$$\phi_6 = \frac{1}{2}\eta(1+\eta)(1-\xi^2) \tag{5-7}$$

$$\phi_7 = \frac{1}{4}\eta(\eta-1)\xi(1+\xi) \tag{5-8}$$

$$\phi_8 = \frac{1}{2}(1-\eta^2)\xi(1+\xi) \tag{5-9}$$

and

$$\phi_9 = \frac{1}{4}\eta(1+\eta)\xi(1+\xi) \tag{5-10}$$

5.1.4 Quadratic Triangles

Quadratic triangles used in this code have 6 nodes per triangle and are C^0 continuous with the rectangular elements also used. Figure 5-7 shows the numbering of the nodes in the parent element. The shape functions for each node are:

$$\phi_1 = [1-(\xi+\eta)]\,[1-2(\xi+\eta)] \tag{5-11}$$

$$\phi_2 = \xi(2\xi - 1) \tag{5-12}$$

$$\phi_3 = \eta(2\eta - 1) \tag{5-13}$$

$$\phi_4 = 4\xi\,[1 - (\xi + \eta)] \tag{5-14}$$

$$\phi_5 = 4\xi\eta \tag{5-15}$$

and

$$\phi_6 = 4\eta\,[1 - (\xi + \eta)] \tag{5-16}$$

5.2 Long Pipes

Long pipes must be meshed with a minimum number of nodes, yet account for the nature of the solution. If elements of an aspect ratio of one are used to create the mesh for the entire pipe, only very short sections of pipe could be modeled before memory limitations of the computer would be exceeded. Therefore, the aspect ratio of any element cannot be restricted to something near one. In fact, the aspect ratios need to be as large as 5000 to 1 (length to width) to model the complete potential and current distributions for long pipes with the limited resources available on a PC (October, 2000 - 1GB RAM). However, there are severe numerical difficulties encountered with elements of these aspect ratios. The solution to these problems is addressed in section 6.2.

High aspect-ratio elements cannot be used at the ends of the pipe or where there is a change in the nature of the boundary condition *i.e.,* a change in the

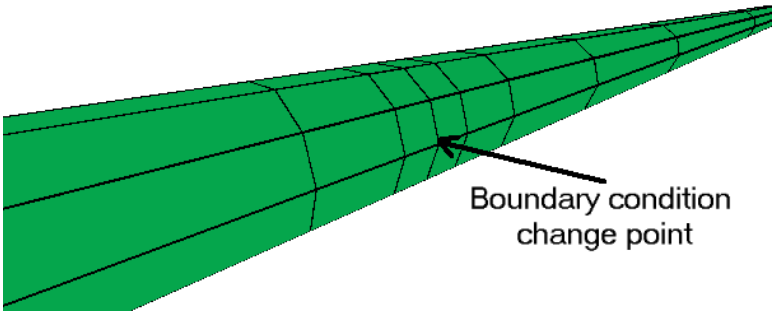

Figure 5-8: Decrease of element aspect ratio at a boundary condition change.

parameters for the boundary condition. It is also not wise to have extremely high aspect-ratio elements next to low aspect-ratio elements.[67, 74] The solution is to gradually increase the aspect ratio until a maximum value is reached. At that point, elements of the same size are used until a point that a change in boundary conditions or the end of the pipe is approached. Then, the aspect ratio must be gradually decreased until a low aspect ratio element is placed at the point of change. The trick is have the meshing algorithm place the low aspect ratio element at precisely the point of the change. The algorithm creates the mesh from both end simultaneously, meeting in the middle with a high aspect-ratio element. The effect is to make the mesh between any two boundary condition changes symmetric about the center of the segment of pipe being meshed. Figure 5-8 illustrates a mesh utilizing the above strategy.

5.3 Holidays

As stated in chapter 1, coating flaws that expose steel to the soil environment (holidays) are a serious problem. Therefore, the model must be able to account for the higher rates of reaction that take place on the exposed section of steel. This

is done through the kinetic expressions used as the boundary conditions. Since any individual element must have the same boundary condition expression, the mesh must provide entire elements that define the size and location of a holiday. Also, when using second order polynomials to describe the solution over any individual element, more than one element is needed on the holiday to account properly for the nonuniform current distribution. The sample calculations presented in Figure 5-9 illustrate the need for refined meshing of coating holidays. For even small values of $J = -\alpha_c Fr_o i_{\text{avg}}/RT\kappa$, a single second order polynomial cannot adequately represent the solution. Therefore, the diameter of the holiday needs at least two quadratic elements for small values of J and four or more for larger values.

Holidays are meshed is two possible ways. If the holiday is round, it is easiest to use a constrained Dalauny mesh generator.[75, 76] If the holiday is not round such as a gouge in the coating due to mechanical damage, a different approach uses rectangular elements is used.

5.3.1 Round Holidays

For the this model, the method that was used to generate a Dalauny mesh comes from Jonathan Richard Shewchuck.[77] The code is publically available with documentation (October, 2000).[78] The generator takes an input of a planar straight line graph (PSLG). It then creates a mesh of linear or quadratic triangles that conform to the mesh.

The generator is included as a black-box library function in the program. The author of the code provided a simple interface to the generator that utilized the

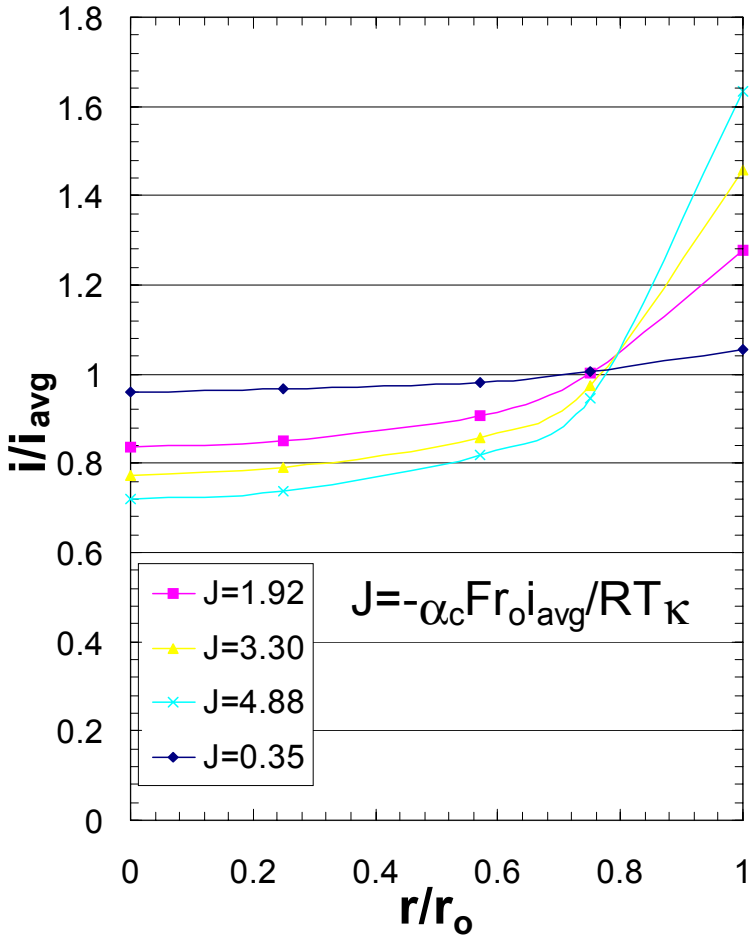

Figure 5-9: Current density distribution on a circular holiday. Parameter J is a function of the average current density i_{avg}, the inverse Tafel slope $\frac{\alpha_c F}{RT}$, the holiday radius r_o, and the soil resistivity κ.

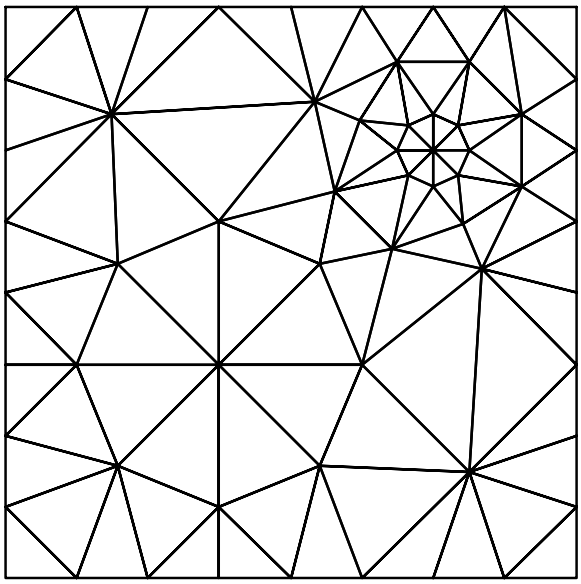

Figure 5-10: A mesh that includes two round holidays. This is the output from a standard mesh generator.[77] Further processing is needed to map the mesh to a pipe and adjust the holidays so they are round.

same command line options as the stand-alone code. The PSLG input is created as the boundary to the region being divided into elements. This is usually a rectangle, a circle, or a half circle which are trivial to create and a list of holes (holidays) that must be included. The output is then the mesh created by the library.

The output of the generator is not ideally suited for for a pipe. The code generates a mesh that is on a 2-dimensional plane as in Figure 5-10. The mesh must then be post-processed in order to have all the desired properties. The holidays are dealt with first. The output along the edge of the holiday is a piece-wise set of straight lines. Since the elements are quadratic in nature, a better job can be done by moving the center node of each line segment onto the circle used to define the holiday. As seen in Figure 5-3, the quadratic nature of each side of the element can be utilized to more closely follow the correct geometry.

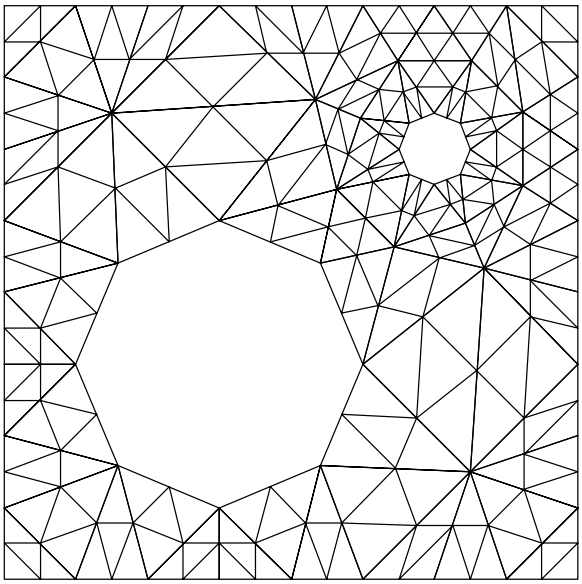

Figure 5-11: The same mesh as shown in Figure 5-10. Here the elements for the holiday have been removed. The elements have been divided into four triangles to illustrate the locations of the center nodes on each side of the triangles.

Figure 5-11 shows the locations of the center nodes on each side of an element by subdividing each element up into four smaller elements using the center nodes. Segments of the holiday boundary are seen to bee straight lines consisting of two segments. After the nodes at the center of the lines are moved to their proper positions, the circle is defined as best that can be done with a fixed number of quadratic line segments see Figure 5-12. The movement can be done so long as the angle at any corner of the triangle is greater than 0 degrees. In fact, it is desirable to have the angles of all the corners of the elements be greater than about 15 degrees.[67] This avoids numerical difficulties with large aspect ratio triangles when blind Gaussian integration is used. The problem is greatly alleviated using integration techniques described in section 6.2.

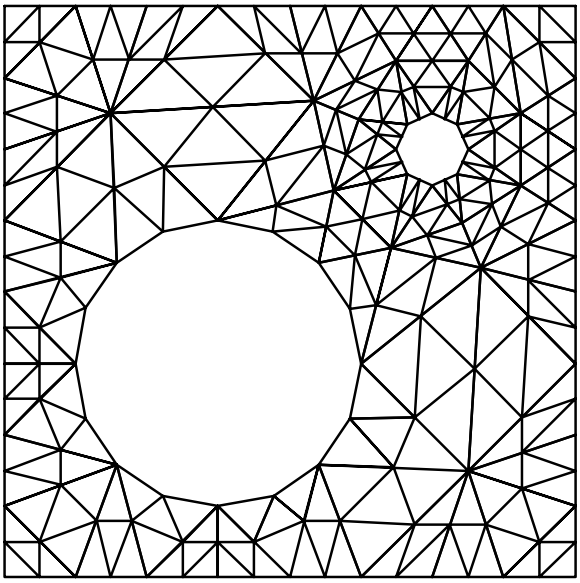

Figure 5-12: The same mesh as shown in Figures 5-10 and 5-11. The nodes on a holiday boundary that did not lie on the circle defining the holiday have been moved for the large holiday. The task has not yet been done for the small holiday.

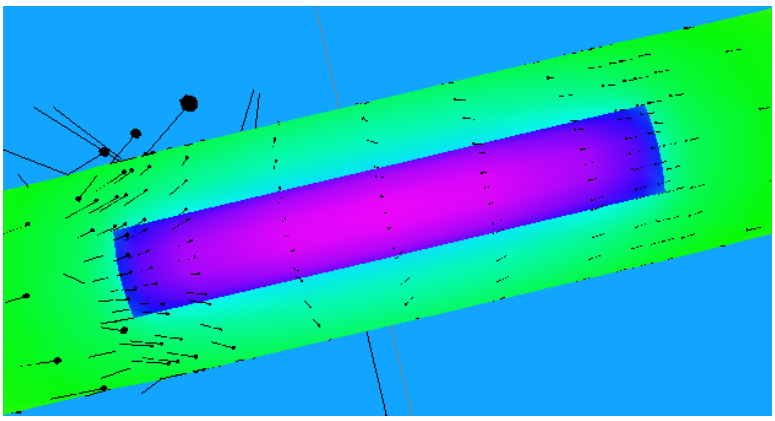

Figure 5-13: A gouge at the bottom of a pipe that was meshed using rectangular elements.

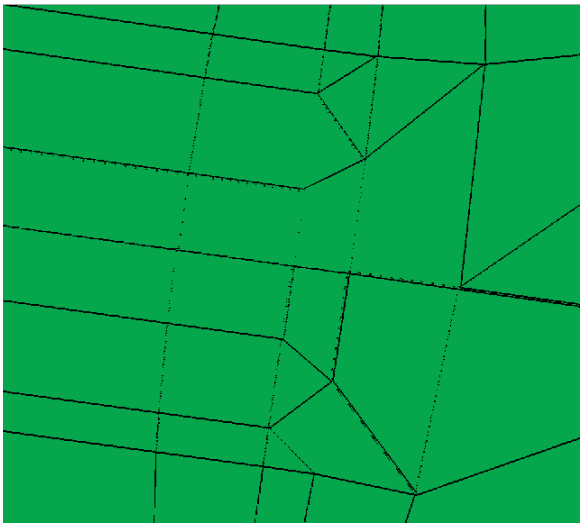

Figure 5-14: Closeup of one edge of a rectangular holiday where two triangles have been used to increase the element density of the holiday.

5.3.2 Rectangular Holidays

Rectangular holidays such as a gouge, use a different mesh technique. In order to adequately approximate the current and potential distribution across the gouge, three elements are needed. Along the length of the gouge, a minimum of three elements would be needed. Because the shape of a gouge is roughly rectangular, it is best to use the rectangular elements to create the mesh. In this case triangular elements are used to increase the element density at the holiday as described in section 5.1.2. Two triangles are placed at either end of the holiday to increase the number of elements across the holiday from one to three. See Figure 5-14 for details of the arrangement.

There are a number of problems placing holidays on the pipe. For both meshing practices described, there can be some distortion of the pipe surface due to wrapping the planar elements to the pipe. It is most often seen as a ripple in the surface near the edge of the holiday. Great effort has been made to minimize the

unwanted effect, but if too few nodes are specified to mesh the circumference of the pipe, the problem is exacerbated.

5.4 Pipe Crossings and Shadowing

When two pipes cross, attention must be paid to the nature of the mesh generated. Both pipes must account for, in their solution, the effect of the close approach of the other pipe. Pipeline operating companies can attest to the fact that the pipes will greatly interfere with each other and that special precautions are needed.

In order to account for the close approach of another pipe in the solution, the mesh must be adjusted. There must be sufficient nodes located at the point of closest approach, but too many nodes is a waste of computer time. For simplicity, the same technique used for a change in coating properties is used. At the point of crossing, a coating property change in placed to force the mesh generator to increase the element density at that point, see Figure 5-15. With the addition of the extra elements, the model has the flexibility in the solution to closely approximate the solution at the crossing.

5.5 Soil Type Divisions

The boundary element method must have the boundary of changes in bulk properties meshed. For applications to pipelines contained in semi-infinite domains, the boundary that is to be divided into elements extends to infinity. Mesh generators cannot create a mesh that extends to infinity with standard elements. Therefore, a mesh is created that extends sufficiently far into the domain such

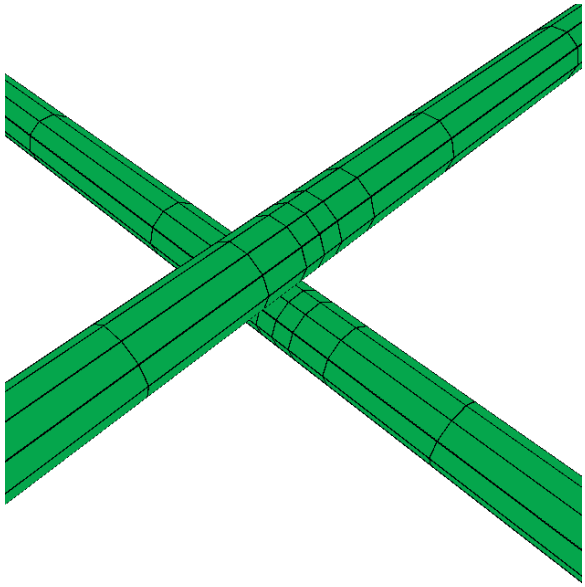

Figure 5-15: Mesh at a crossing of two pipes. Both pipes have the highest density of elements at the crossing point.

that most of the variations in potential and current density have died out. At the end of this mesh, a special element known as an infinite element is placed. The classic definitions for infinite elements are given by Beer.[79]

Soil divisions may need to have holes in the mesh to allow pipes the pass through. Since the location and number of pipes is arbitrary, the same mesh generator used to create holidays is used.[77] Sample output of the mesh generator is shown in Figure 5-16.

Pipes are added to the mesh such that the nodes of the pipe at the point of crossing the soil type division, match exactly the nodes at the edges of the holes in the division. A completed mesh with pipes is shown in Figure 5-17.

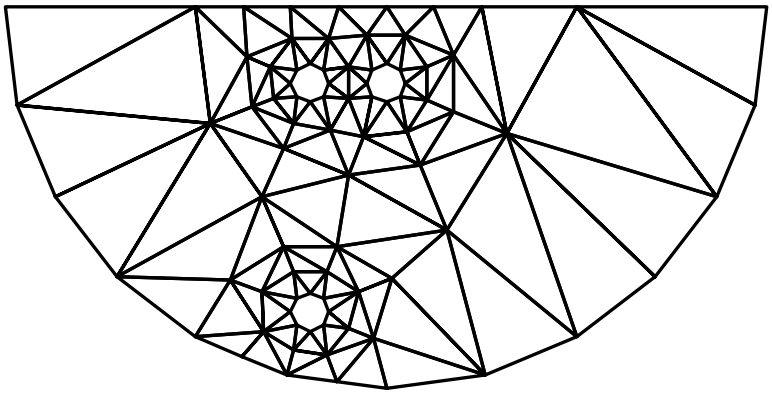

Figure 5-16: Output of the Delauny mesh generator when creating a division between two soil domains. The holes for the pipes need post-processing before the mesh can be used.

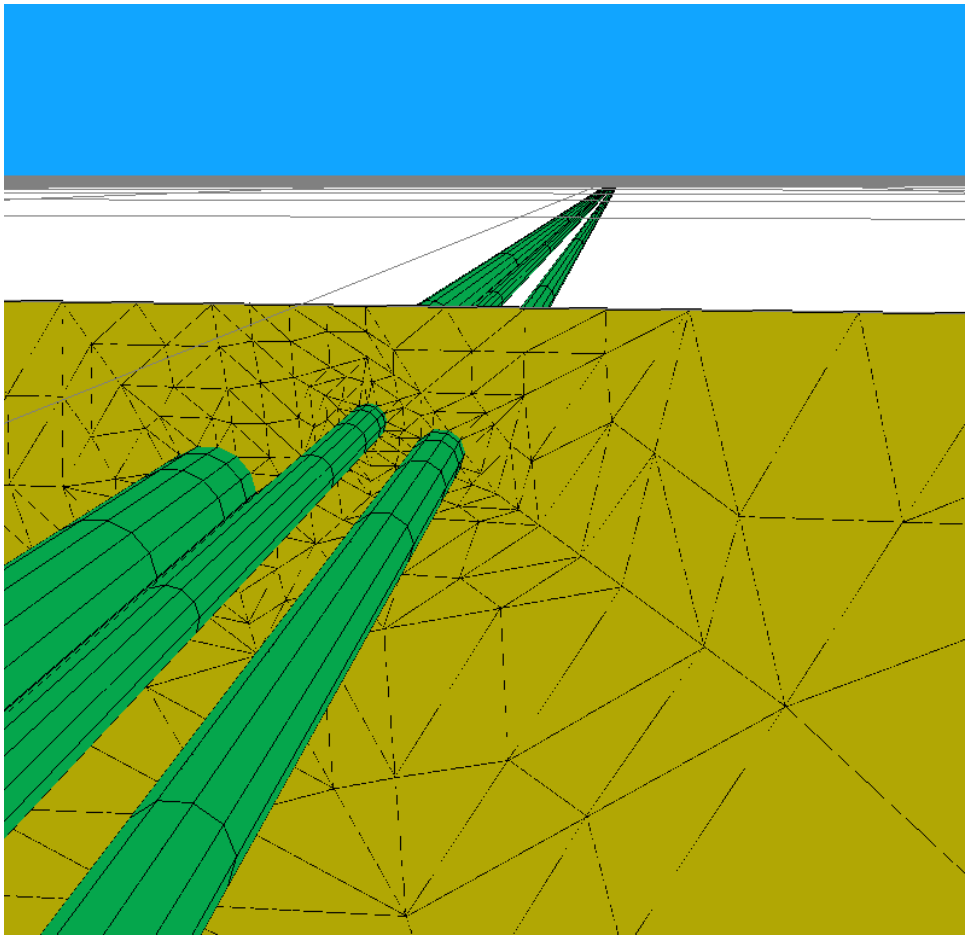

Figure 5-17: Completed mesh with pipes passing through soil type division.

5.6 Conclusions

The generation of the boundary element and finite element mesh is a critical component for the solution of the differential equations describing cathodic protection of pipelines. The solution obtained form the BEM and FEM can only be trusted if the underlying mesh is of sufficient quality such that the shape functions can closely approximate the true solution. The next two chapter discuss how errors using the type of mesh described in this chapter can be reduced and how the solution has been verified.

CHAPTER 6
SOLUTION ACCURACY

There are a great many factors that affect the accuracy of a solution obtained by the Boundary Element Method. These include the basis (shape) functions used to approximate the solution on the finite element, the size and location of an element, and the numerical method used to evaluate the integrals seen in the method - equation (3-9) in the Chapter 2 on page 32.

6.1 Sources of Error

Errors in the boundary element method come from several sources. They can be discretization, integration,[80, 81, 82, 83, 84, 85, 86] shape function choice, and matrix inversions. Of these, discretization and integration can be the largest source of error if not handled carefully.

Discretization presents a tricky balance between minimizing the size of the matrices and having elements whose shape function adequately approximates the solution to the PDE on the element for which it is applied. Choosing a shape function - element size pair that cannot represent the solution to a given error level can greatly affect the solution throughout the domain. This is because the boundary element method applied to any given point in the domain or on the boundary is a function of all the points on the boundary, including the point itself if it is on the boundary.

Another source of error is representing the discontinuity in the derivative at junctions between different boundary conditions. This error can be conveniently eliminated if one is willing to expand the size of one the matrices.[62]

Integration presents one of the most difficult and time consuming aspects of the Boundary Element Method. There have been many papers devoted to easing the difficulty and improving the accuracy of the results.[80, 81, 82, 83, 84, 85, 86, 87, 88, 89] The reason for this is that the integration kernel (in 3D) contains a weak singularity ($1/r$) and a strong singularity ($1/r^2$) which must be evaluated in a Cauchy principle value sense.

6.2 Integration Accuracy

Since the kernel is not a polynomial, a Gaussian integration scheme cannot be found to evaluate it exactly. However, early implementations of BEM simply used a basic Gaussian quadrature to evaluate the singular integrals.[82] After recognizing that the results of the integrals were the major source of error, several techniques have been utilized to remove the singularity. For simple shape functions and elements, a transformation to polar coordinates on the boundaries may be used to evaluate the weakly singular integrals.[81, 82] However, the strongly singular integrals cannot be evaluated easily. All of the strongly singular integrals are located on the diagonal of the $\boldsymbol{H}$ matrix (see section 4.1.1 for details of this matrix). For these integrals there are two choices if the physics of the problem warrant. The first and easiest is to make use of a unit displacement or a constant potential distribution solution which is due to Gibbs.[68] If the body is not elasto-plastic in nature (mechanics) or does not store charge in the domain

(steady-state), then the solution to the normal flux at the boundary is known to be zero. This gives the equation

$$\boldsymbol{H}I = 0 \tag{6-1}$$

where $\boldsymbol{I}$ is a column matrix all of whose elements are 1's. Then the unknown strongly singular integral, of which there is only 1 per row, can be solved explicitly by the equation

$$H_{i,i} = \sum_{j \neq i} H_{i,j} \tag{6-2}$$

The second technique is to solve the Cauchy principle value explicitly. There are techniques for doing this for the direct boundary element method described by Guiggianni [83, 84] and for the Symmetric Galerkin Boundary Element Method by the same author. [90]

6.3 Integration Techniques

There are several ways to improve the accuracy of a given integral over an arbitrary element. The easiest is to increase the order of the Gaussian quadrature. This technique though, can never integrate a weakly singular integral since it cannot be represented as a finite order polynomial.

Two dimensional Gaussian quadrature can be used to speed up the calculations significantly. Cools et al.[91] have made available general integration source code for a variety of two-dimensional shapes. They term two-dimensional Gauss rules as "Cubature."

Singular integrals can benefit from a change of the coordinate system to polar coordinates. Polar coordinates reduce the order of the singularity by one. For

the $1/r$ dependence of the G integral, the singularity is removed as well as all dependence on $1/r$ as one approaches the singularity. For the $1/r^2$ dependence of the H integral, it is now possible to get a rapidly converging result.

6.3.1 Adaptive Integration

The final choice made for this project was to use a specially modified form of a two dimensional cubature rewritten for an adaptive scheme. The possibility of having extremely large aspect ratios in the elements to be integrated required modifications of published integration subroutines. This also meant that standard routines like IMSL could not be used.[92] The routines that are used are based on a 1-dimensional algorithm[93] distributed by NIST at.[94] The routine was modified to solve 2-D integrals by using Gauss-Kronrod cubature formula[95] and to take into account the high aspect ratios. The modified subroutine takes any arbitrary triangle and seeks to subdivide it such that the subdivisions are performed in the area with the largest error contribution to the total error for that element. It also tries to extrapolate the subdivisions with a nonlinear algorithm to reduce the amount of computational time. The Gauss-Kronrod 2-D integration rules provide a value for the integral over a certain specified geometric shape and an estimate of the error in the integration. This is accomplished by actually having two integration rules of different order, where the higher order formula is a super-set of the other. This means that for a 13-15 rule, 13 points form the lower order rule and the addition of only two more points to the rule gives the 15 point formula. It is computationally cheap because the first 13 points of the 15 point rule are identical to the 13 point rule. Adapting the integration routine for high aspect

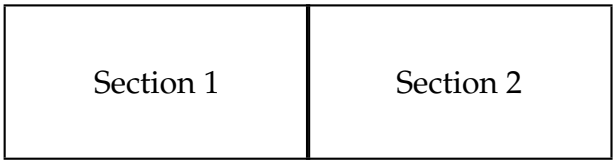

Figure 6-1: Sub-element with a high aspect ratio subdivided by the adaptive integration routine to reduce the aspect ratio of the subsections.

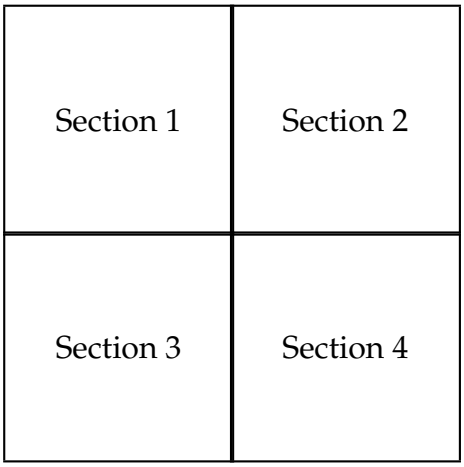

Figure 6-2: Sub-element with a desired aspect ratio subdivided by the adaptive integration routine.

ratio elements is very straight forward. After finding the subsection that has the largest error contribution, the aspect ratio of the real sub-element is calculated. If the ratio is greater than 2 or less than 0.5, the element is divided into two sub-sections such that the aspect ratio of the sub-sections is reduced (or enlarged) to bring it closer to the desired range. If the aspect ratio is already within the desired range, the section is sub-divided into 4 sub-sections.

By implementing the modifications to the adaptive integration routine based on the aspect ratio of the sub-sections, a order-of -magnitude performance improvement was achieved while maintaining the same accuracy.

A new technique has been introduced by Karafiat that could reduce the time to complete the integration by another order of magnitude.[89] This method moves

the vertices of a small number of sub-triangles to optimize the effect of the quadrature. However, there is some ambiguity in the cost function that places these nodes, in that a local minimum can be found without obtaining the global minimum. Also, the technique was only described for a case where the singularity lies in the same transformed plane as the element itself. For 3D models of pipelines, the singularity may be located anywhere (i.e. above the center of the element) in which case the algorithm fails.

6.3.2 Singular Integrals

Singular integrals are handled by first insuring that the point of singularity is at a vertex. This is done by breaking the domain of integration manually into several subsections such that the singularity is on a desirable vertex. Second, it is important for accuracy that the subsections that actually contain the singularity have an aspect ratio of 1.0. For instance, suppose a quadratic Lagrangian element is to be integrated, and the singularity is at the lower left corner. The element is then broken into 3 separate integration domains. One that contains the singularity and two the are "nearly singular" because of the proximity of the singularity. The subsection with the singularity is integrated in polar coordinates to reduce the order of the singularity, while the other two subsections are integrated using the standard adaptive integration.

6.4 Matrix Inversions

The solution of $\boldsymbol{A}x = \boldsymbol{b}$ is another source of error. For large systems of equations, Gaussian elimination is a very poor choice on computers. The reason for

this is the enormous propagation of round-off errors in the solution column $\boldsymbol{b}$. Every division used in Gaussian elimination increases the error of a particular element. That error is added to every other element in the column through the row operation used to eliminate elements in the matrix $\boldsymbol{A}$. This is repeated during back-substitution which carries the error back up through the column to elements which might have a lower contribution from round-off error.

LU decomposition can reduce the error to a reasonable level. This is because of the significant reduction of round-off error of the b vector. The implementation used in the code is a standard subroutine from LAPACK named dgesv and its dependencies.[96] This subroutine makes extensive use of BLAS (Basic Linear Algebra Subroutines).[97] The source code for these libraries can be found on the world-wide-web at the locations given in the references. These subroutines can be linked together to perform almost any type of linear algebra function. There is an added benefit in that the BLAS routines have been highly optimized for almost all computing platforms and are freely available. The optimized versions can have a performance impact of 2 to 16 over just compiling the basic source code. The libraries for Intel® processors running a Win32® operating system can also be obtained on the world-wide-web.[98] At the time of this writing (October, 2000), Intel had not posted the libraries for the Linux/FreeBSD environments yet although beta versions were available for testers.

CHAPTER 7
MODEL VERIFICATION

After the code has been written to solve a differential equation, it is important to benchmark it against known solutions. The code used herein solves Laplace's equation in a half space. There are two analytic solutions to Laplaces equation for a half space that have been used to verify different portion of the code. The first is due to Newman where a disk electrode is placed on the plane defining a half-space and the primary current distribution is found. This solution provides a test on the quality of the solution to Laplace's equation.[99] It contains a singularity in the solution that causes the current density at the edge of the disk to approach infinity. Most numerical solutions have a great deal of difficulty obtaining this solution.

The second analytic solution is due to Kasper.[8] This solution is directly relevant to pipes because it solves Laplace's equation for two parallel infinitely long cylinders. This solution shows the importance of the solution around the circumference of the pipe and can give an indication of the "fineness" of the mesh needed around the circumference of the pipe.

A third related solution is from Dwight.[3] His equation is used to find the resistance between a metal electrode and a point at infinity. It assumes constant potential along the entire surface of the electrode.

7.1 Primary Current Distribution to a Disk

Newman's solution to Laplace's equation for the primary current distribution of a disk electrode in a half-space containing and a counter-electrode at a great distance away is given by[99]

$$\frac{i}{i_{\text{avg}}} = \frac{0.5}{\sqrt{1+(r/r_o)^2}} \tag{7-1}$$

where r_o is the radius of the disk, i is the current density at a distance r from the center of the disk and i_{avg} is the average current density for the entire disk. The disk is placed on the plane that defines the half-space. The counter-electrode must be at a great distance so that it does not interfere with the current distribution. It also should have a greater surface area than the electrode so that the ohmic control is at the electrode.

7.1.1 Disk in a Half Space

The first comparison to the analytic solution given in equation (7-1) is for a model setup that is nearly identical to that used in obtaining equation (7-1). The model setup is shown in Figure 7-1. The model used a disk of 15.24 meters diameter. The anode was placed 500 meters from the disk. Hydrogen evolution Tafel kinetics were used for the boundary condition. At a sufficient current level, the distribution should approach the primary distribution given by equation (7-1).[12] For hydrogen evolution, the numerical calculation approached the primary distribution when the average current density was about $0.75\mu\text{A/cm}^2$. The results of the calculation and the analytic solution are plotted together in Figure 7-2, where the solid line represents the analytic solution. The results show excellent agree-

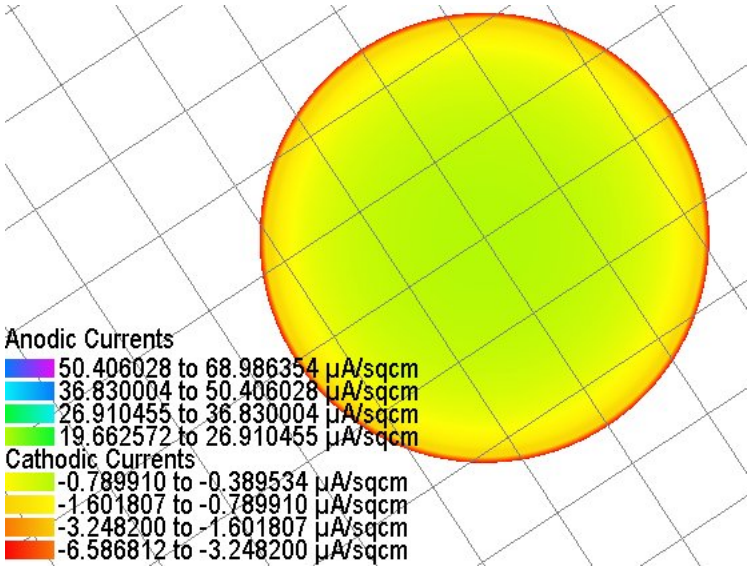

Figure 7-1: Primary current distribution on a disk electrode in a half-plane. Model solution at center of disk is within 2.0% of the analytic solution of $i/i_{\text{avg}} = 0.5$. This view is looking along the z axis toward the disk.

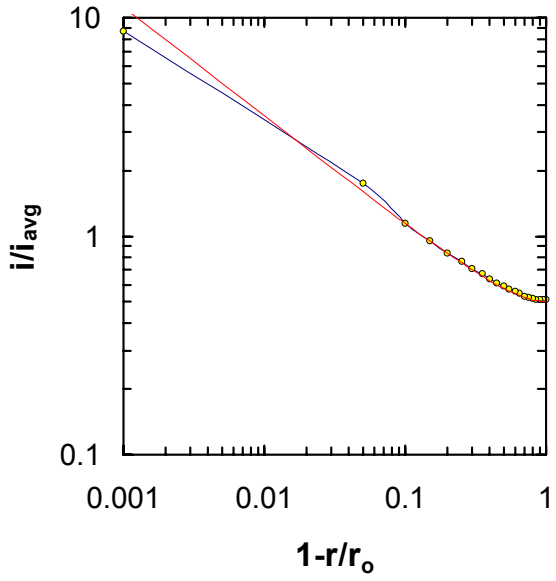

Figure 7-2: Comparison of primary current distribution on a disk electrode in a half-plane. Red line without circles is the analytic solution, blue line is the numerical solution from the disk shown in Figure 7-1.

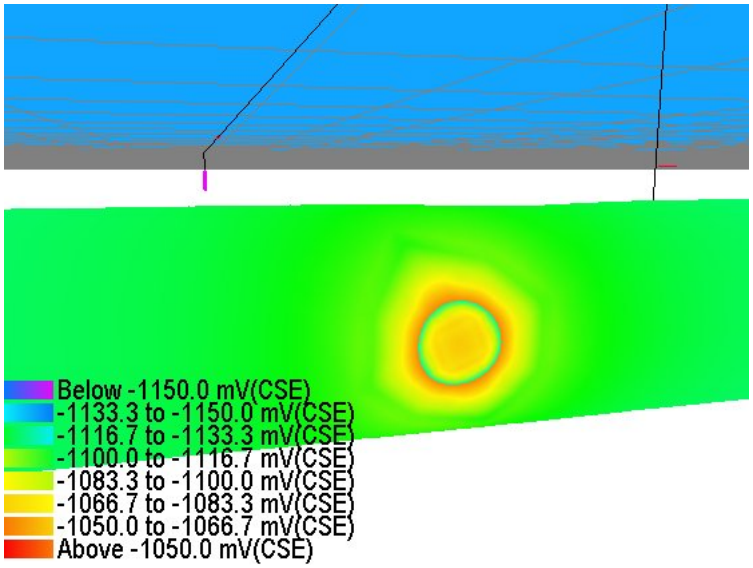

Figure 7-3: Disk holiday on a pipe. Shading corresponds to the off-potential. Note the draw-down of potential in the coated region around the holiday.

ment with the analytic solution over all but the edge of the disk. The difficulty at the edge is that a numerical method cannot approximate infinity very well. When the solution is placed on a log-log plot, a straight line should be seen as $1 - r/r_o$ approaches zero. A good approximation to the straight line is made when the the mesh is sufficiently fine at the edge. This fact must be taken into account when creating the mesh for the calculation (see Chapter 5).

7.1.2 Disk-Shaped Coating Holiday

Since holidays are an important part of the model, it is important to see if a disk shaped holiday on a pipe also responds as theory predicts. A holiday was placed on a 10 mile long pipe of 18 inches diameter. A portion of the pipe with the holiday is shown in Figure 7-3. A single anode was placed 150 meters from the pipe. The anode output was adjusted to obtain certain values of the parameter J

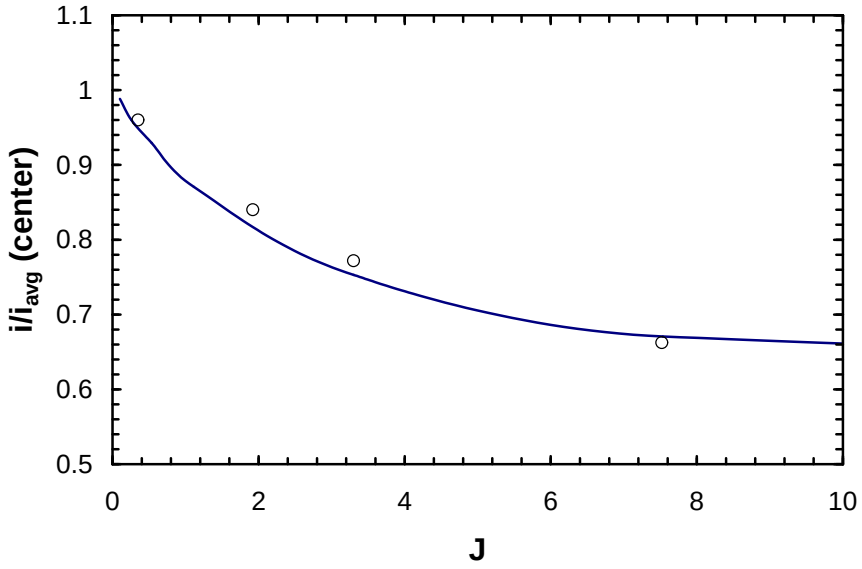

Figure 7-4: Comparison of current density at the center of a disk electrode in a half-plane (solid line) to that of a disk shaped holiday on a pipe (circles).

which is defined for Tafel kinetics as

$$J = \frac{2.303}{\beta_c} \frac{r_o i_{\text{avg}}}{\kappa} \tag{7-2}$$

where β_c is the cathodic tafel slope for the hydrogen evolution reaction, r_o is the radius of the holiday, i_{avg} is the average current density on the holiday, and κ is the soil conductivity.

A comparison is also made between a disk-shaped holiday and a disk in a half-plane. The results of the calculation are shown in Figure 7-4. The mesh for the holiday used two elements in the radial direction from the center of the holiday and eight elements in the angular direction with a total of 15 quadratic triangles (see Figure 10.12(b) for an example of the mesh). The results demonstrate that at least the center of the disk is modeled correctly.

7.2 Comparison to the Solution of Kasper

Kasper[8] has provided a solution to Laplace's equation for 2 parallel right-cylinders that are not concentric. The solution assumes a constant potential distributions around each cylinder and is given in terms of the ratio of the maximum to the minimum current density Figure 7-5.

Kasper also assumed that the cylinders were infinitely long and therefore solved the 2 dimensional problem. To approximate this assumption in a three dimensional model, an aspect ratio for the cylinders of 1000 to 1 was used. The ability of the 3 dimensional model to handle such an aspect ratio and provide an accurate solution is discussed in Chapter 6.

A plot of the current distribution for the case of the cylinders being placed with a separation of 3 time the diameter is given in Figure 7-6. The ratio of the minimum to the maximum current density calculated was 0.72 as compared to Kasper's analytic value of 0.78.

7.3 Dwight's Equation

A final verification is made with Dwight's equation. Dwight's equation was developed as an anode resistance formula. This means that one calculates a resistance with this formula by using the resistivity of the surrounding soil and the surface area of the anode/pipe. After the resistances of a pipe - anode pair is calculated, the amount of current required to achieve a certain potential shift is obtained through the use of the basic form of Ohm's Law, $V = IR$, where V is the potential shift of the pipe from the anode and R the the series resistance of the anode and pipe.

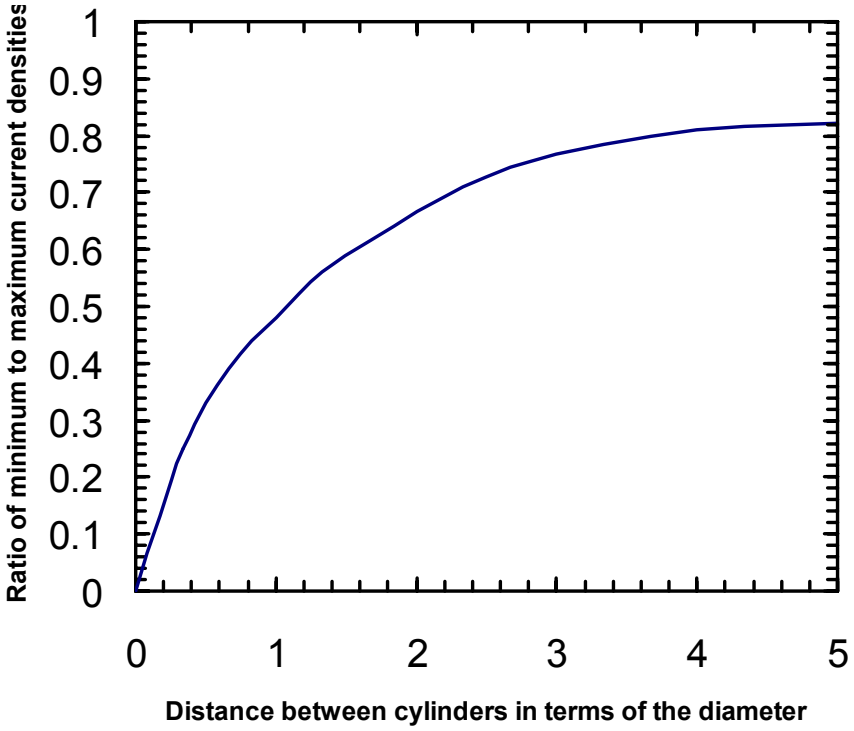

Figure 7-5: Solution to the current distribution on a cylinder given by Kasper. Plot represents the ratio of the maximum to minimum current density.[8] At infinite separation, the ratio becomes 1.

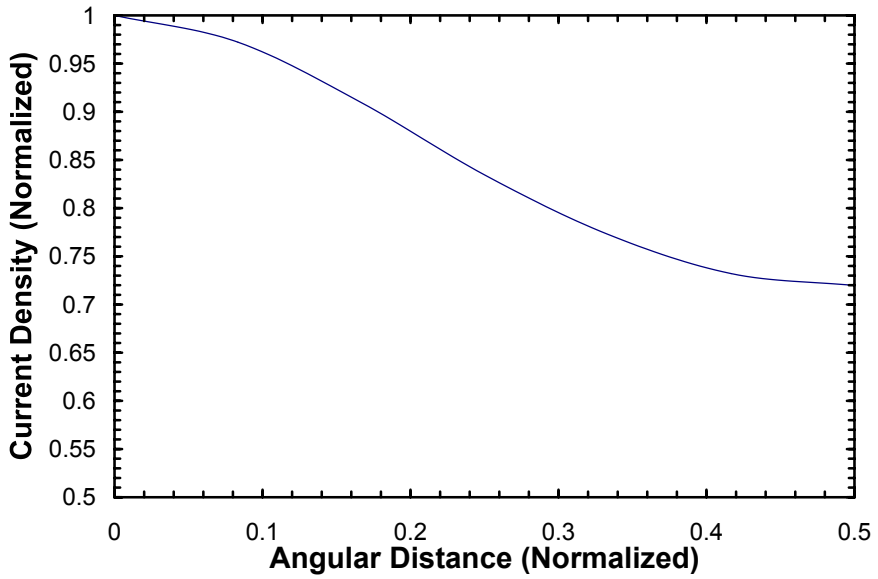

Figure 7-6: Distribution of current around half the circumference when the cylinders are placed at 3.0 diameters separation. The ratio of the max current to the min is 0.72. Kasper's solution is 0.78

Since Dwight's equation is a resistance formula, it is only applicable if the pipe and anode are remote from each other. When the pipe and anode are close to each other (5+ diameters[8]), the distributions have a significant effect on the actual current flowing between the anode - pipe pair. When the anode is outside this limit, the current driven to the pipe is higher than that predicted by Dwight's equation, Figure (7-7).

The solution seen in Figure 7-7 was obtained by setting the potential distribution to be constant on both the anode and pipe and then calculating the current density distribution and integrate to get the total current. The constant potential distribution was used to remove the resistance associated with the kinetics from the solution. These are some of the same assumptions made in deriving Dwight's equation[3]. The others are that the pipe and anode are effectively at an infinite distance from each other. This ensures the current is strictly ohmic controlled. As

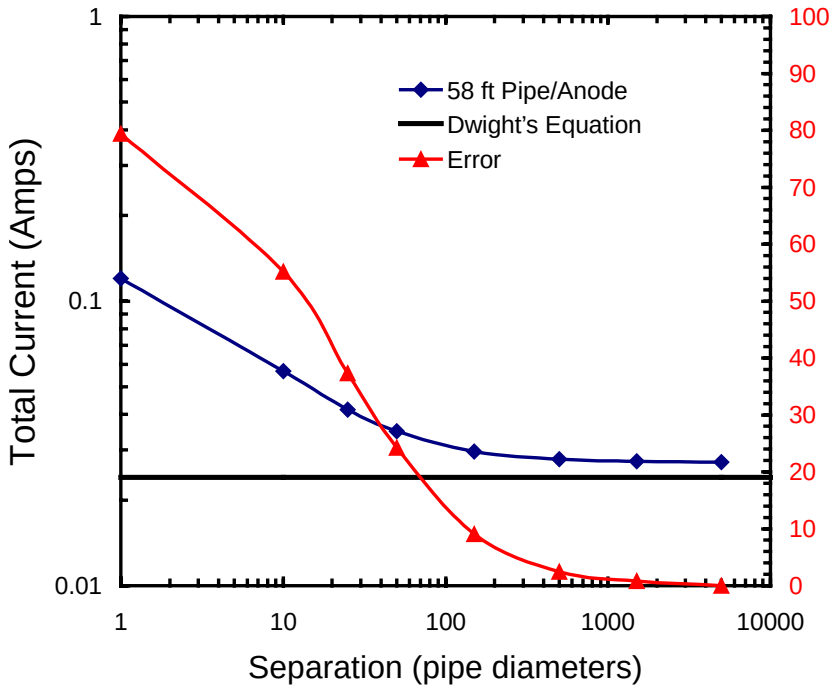

Figure 7-7: Error in Dwight's equation as a function of the separation of two cylinders. Solution given by the 3 dimensional model approaches Dwight's solution at large separation. The difference between Dwight's solution and the model is due to end effects.

can be seen in Figure 7-7, the model approaches Dwight's solution as the pipes are moved far from each other.

CHAPTER 8
SOLUTION VISUALIZATION AND INTERFACE DESIGN

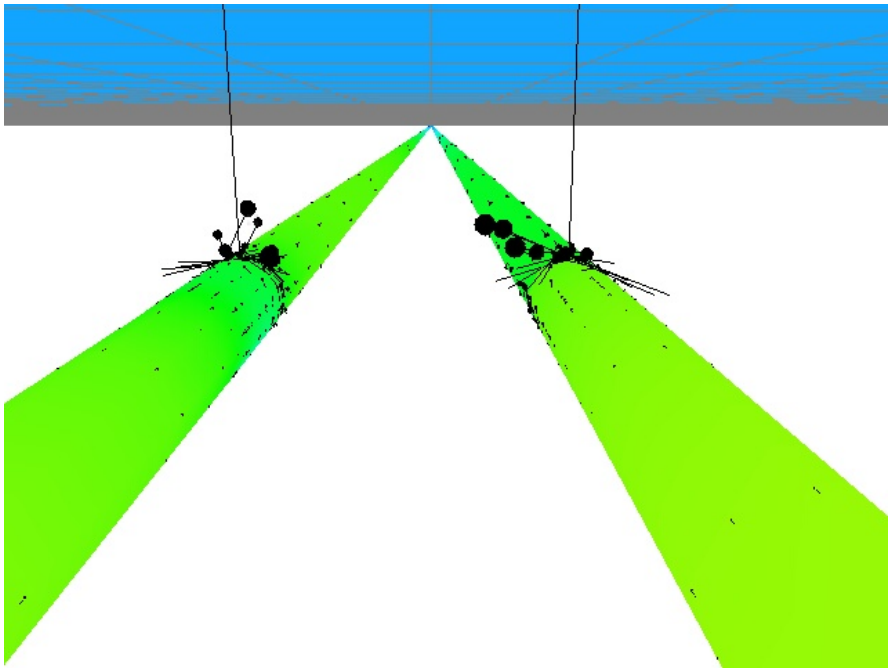

Figure 8-1: A screen shot and movie (click on image above) that shows some of the interactive graphics techniques needed for three dimensional geometry.

8.1 Interface Design

The interface to the model has been designed as a Microsoft Windows® application following guidelines given in "Programming the Windows 95 User Interface "[100] and "The Windows Interface Guidelines for Software Design". [101] The guidelines describe how the user should interact with the data using the mouse and keyboard. However, these two books do not provide information in

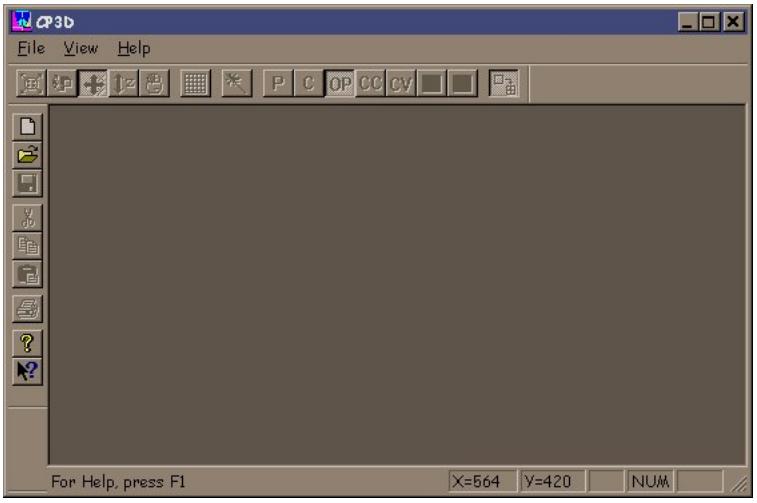

Figure 8-2: A screen shot of the basic window used for the interface to the model. The window contains elements familiar to anyone who uses Microsoft® Windows.

interaction with 3-dimensional data. For this, other sources are needed and are described in section 8.4.

The interface starts with some common elements that most programs use and with which most users would be familiar. First there is the main window as shown in Figure 8-2. The window contains both a standard and application specific tool bar, a menu, and at the bottom, a status bar. The standard toolbar supports common functions such as opening and saving models. The top title bar has the standard button to control the size of the window. The main part of the window is where the models and their interface elements will be displayed.

A model is displayed in the main window when either a new one is created, or one is opened. The model windows is divided into two parts (see Figure 8-3). The left part has dual purpose. The first is calculation control and feedback, the other is for controls related the the right section. The right-hand section is for 3-dimensional display of the model data and solutions.

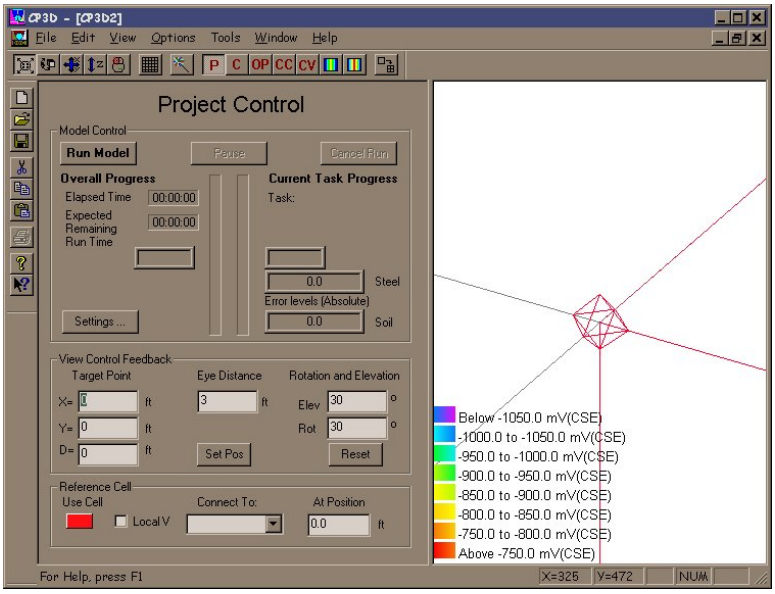

Figure 8-3: A screen shot of the basic window with an empty model. The window has two parts: the first is for control and feedback, the other is for data display in 3 dimensions.

8.2 Data Visualization

A solution of a PDE is only useful if one can examine it and derive useful conclusion from it. One of the simplest ways to examine a solution is to plot it versus position in the domain. This works well for a 1-D problem, but what should be done in a 2D or 3D problem? It is possible to use a 3D graph to plot the solution of a 2D problem on the z axis for a rectangular domain, but these types of plots are difficult to use and precise information cannot be obtained from them. There are no 4D graphs.

A solution to the problem is to use a 3D drawing of the domain and boundaries. The boundaries are then colored using a color scale that corresponds to the solution. Vectors can be overlaid on the surface to indicate flux directions (see

Figure 8-1). This technique requires the ability to interact with the data since not all of the data can be seen simultaneously.

8.3 2D Solution Visualization

Two dimensional problems are straight forward when solutions are obtained by the boundary element method. Since the techniques solves for the unknown essential or natural boundary conditions, a plot of the solutions along the boundary can be made.

The most meaningful plots of the solutions are either one along the length (axial) of the pipe at a particular angle, or a plot along the circumference at some point along the length. Extracting the necessary data involves interpolating between the nodes where the solution is known.

The first case, which is shown in Figure 8-4, is relatively simple. Here, one simply determines the desired angular position to display and then interpolate between the nodes where the solution is known using the shape functions of the elements which define the variation between the nodes.

The second case is significantly more complicated. Again, one should extract the data for the plot such that the angle from the the top of the pipe does not change as one moves along the length extracting the data. However, as seen in Figure 8-5, the mesh may not be regular along the surface of the pipe. Also, the density of nodes changes in the region of the holidays, meaning simple bookkeeping that can be used to make a plot from the data in Figure 8-4 cannot be done.

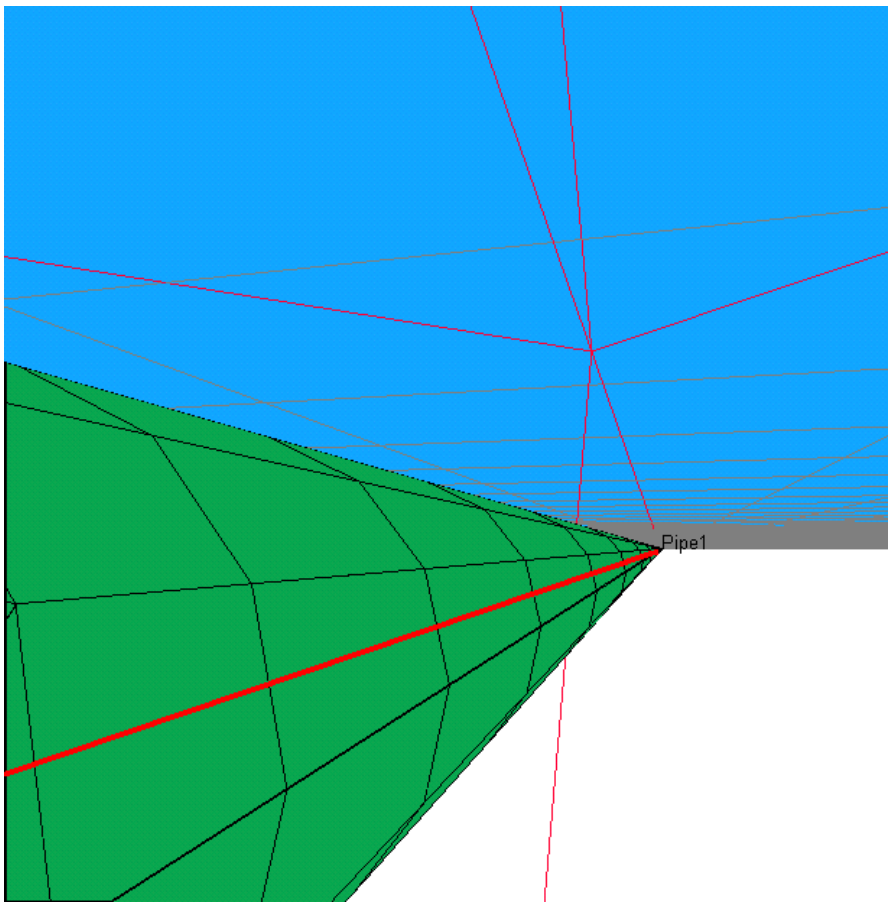

Figure 8-4: Red line represents the points of the pipe surface that are extracted to create a X-Y plot. X values are the how far from the starting end of the pipe the value of the potential, current, off-potential, or corrosion current is taken.

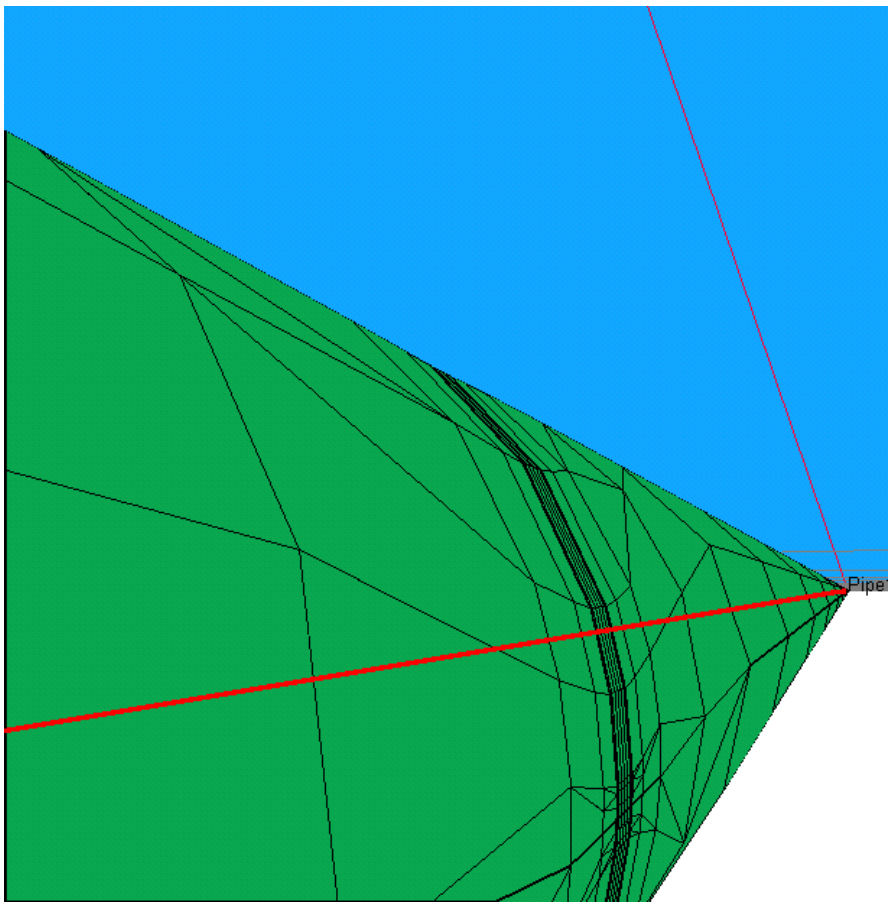

Figure 8-5: The red line represents the points of the pipe surface that are extracted to create a X-Y plot. X values are the how far from the starting end of the pipe the value of the potential, current, off-potential, or corrosion current is taken.

If rectangular holidays are used, a techniques can be devised to extract the plot data with several extra bookkeeping structures that must be created at the time the mesh is generated. When rectangular holidays are used, the mesh is generated using successive circles of nodes. If the center point, and angle of each circle of nodes is saved along with the number of nodes that make up each circle, then once the angular position on the pipe where the plot data is to extracted is calculated, the plot data can be extracted one node circle at a time. At each node circle, a calculation must be done to find the element the plot line passes through and then the homogeneous coordinates for that point. The homogeneous coordinates can then be used with the same element to get the desired solution value - potential or current density.

8.4 3D Visualization

For a 3D model it is necessary to be able to visually examine the mesh for correctness. The best available method to accomplish this is OpenGL. OpenGL is a set of libraries distributed by Silicon Graphics in the form of an Application Programming Interface(API) that allow an object to be drawn with correct depth and perspective.[102] If the video card is fast enough, it also can be made to be interactive. This means that a user of the model can use a mouse to change the viewing angle and distance from the object of interest in a true interactive fashion.

8.4.1 Using OpenGL

The code has been written using interactive techniques described by Hall and Forsyth in their book “Interactive 3D Graphics in Windows”.[103] The techniques

describe how to take the viewer into account when designing the interface. For instance, using the mouse to control how objects move within the display is critical. The mouse is only capable of a 2-dimensional motion, but the objects must move in three-space in a natural intuitive way. The solution is to have several modes of movement: zoom in/out, rotate, translate, and as a new technique in this software, depth control. By selecting the mode of motion, movement of the object is then restricted to that mode.

Hall and Forsyth also supplied a toolkit to learn the techniques.[104] The code in the toolkit was not used for the development of this software. Only the OpenGL API (application programing interface) was used.[105, 106] This meant that the code would be portable across platforms that support the OpenGL API. However, code for other parts of the graphical user interface are not portable. Therefore the code was separated into two distinct sections: portable code which contains the geometry engine and most of the OpenGL drawing primitives, and non-portable code which contains the interface elements such as windows, menus, dialog boxes etc.

OpenGL can draw only primitive objects made up of planar triangles, polygons (subdivided into planar triangles), lines and points. The boundary element method and finite element method also uses polygons to represent the geometry so OpenGL is ideally suited to the task. Additionally, OpenGL can shade the polygons, lines, and points using garuad shading based on colors specified at the vertices of the primitive. Garaud shading is a determining the color at any point in a triangle by linear interpolation of the colors at the vertices using the luminescence, or RGB color model.

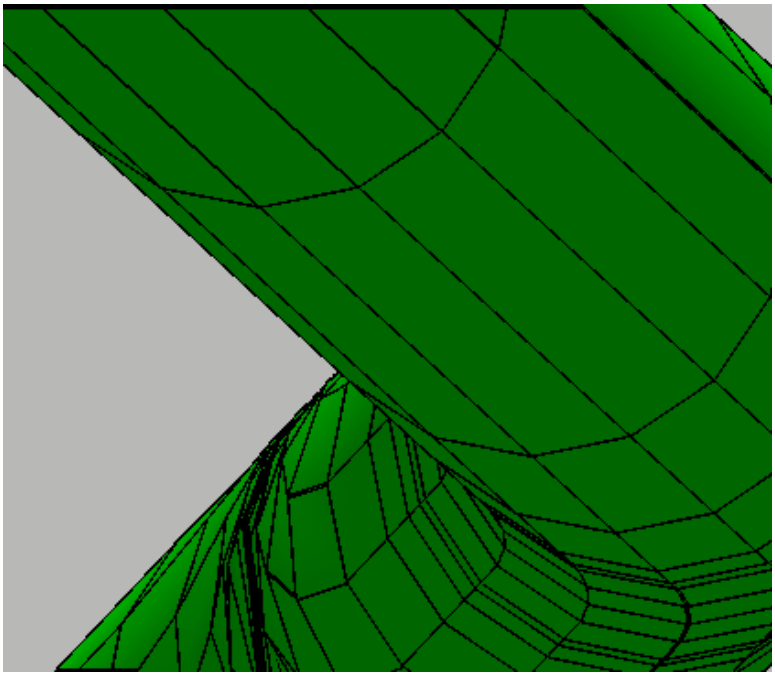

Figure 8-6: Shaded mesh of boundary element calculation grid. OpenGL allows instant visual inspection of the mesh for correctness.

Drawing the objects as they are created (meshed) provides the user with an excellent method for feedback on its correctness. Then, if an object has been misplaced, the user knows immediately and can fix the problem before time is wasted with a calculation.

OpenGL uses linear interpolation schemes and is only fast when linear polygons are used. This means that the polygon lies in a single plane in cartesian coordinates. To alleviate this problem somewhat, the grid used for the calculation can be divided up into smaller sub-units over which the linear interpolation can be applied. For instance, a nine-node Lagrangian element can be divided into four four-node polygons each of which has a linear interpolation done, and are then assembled piece-wise back into the surface.

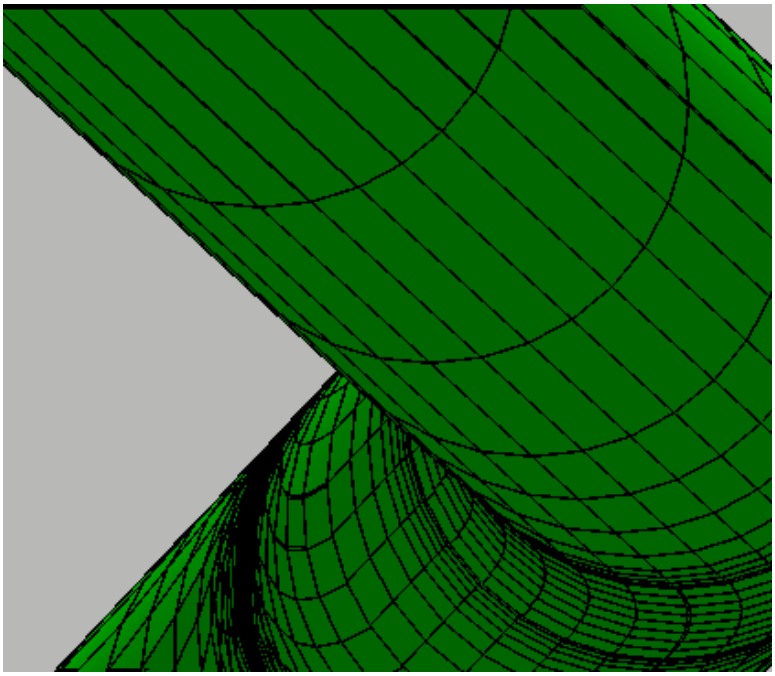

Figure 8-7: Same view as figure 8-6 on page 121, with four times the number of elements. This has been done to better approximate the quadratic nature of the real elements using linear interpolation for the graphics elements.

Figure 8-6 shows a view of a pipe with each quadratic Lagrange element divided up into four linear four-sided polygons. This method does not provide a true estimate of the paraboloid that describes the curvature of each element.

A better way to visualize the true variation of each element in both geometry and values of potential and current when restricted to piece-wise linear 2D surfaces is to break each real element into 16 linear surfaces. Such a subdivision is shown in Figure 8-7. Here, one can see how well a small number of quadratic elements can approximate curved surfaces.

8.4.2 Coding OpenGL for BEM and FEM Meshes

Most of the code for the program was written as a set of C++ classes. Following the philosophy of C++, objects should be self contained black boxes when complete. One of the necessary functions of all geometry objects is that they can draw themselves into the OpenGL rendering engine. Therefore the base class of all geometry classes contains a method `Render(PARAMS *pParams)` which handles drawing tasks for all derived geometry objects. The single argument contains some necessary information such as whether to use shaded polygons or a wireframe and if shaded, which color set to use (potential, current, corrosion current, etc.) This bases class maintains the list of nodes and elements used to describe the geometry.

An example `Render` routine that draws a wire frame is given in Appendix B.

Before `Render` is called, the OpenGL engine is told how all polygons sent to it should be rendered. For wire frame it would be:

```
glPolygonMode(GL_FRONT_AND_BACK,GL_LINE);
```

Other commands can tell the engine to fill the polygons with a color, or to interpolate the color at every point within the polygon by the colors at the vertices.

Setting up the OpenGL engine is platform dependent and one should refer to the appropriate literature for their platform. Because of this, the setup for this software is contained in the interface code. Appendix B has the setup necessary for the Microsoft® platform.

8.5 Visual Feedback

Feedback of the results of a calculation to the user can be done in a number of ways. The first is to use an object that the field engineer will be familiar with, a $Cu/CuSO_4$ reference electrode. The electrode can then be moved over the surface of a pipe to get a reading of the desired quantity. Unlike a real reference electrode, a software version can output more than just a potential. The reference electrode used in model provides on-potential, off-potential, net current, and corrosion current.

CHAPTER 9
COMPUTATIONAL PERFORMANCE

Computer performance for the boundary element method is a very active area of research.[107] Since most of the computational time is spent evaluating the integrals in equation (3-9) on page 32, it is the best place to look for performance improvements. One of the best ways to improve the speed after algorithms have been optimized is to use a parallel computer architecture. Since it is much cheaper to hook several single cpu machines together with a network than to buy a multi-CPU machine and that such arrangements are readily available in most university and industrial settings, this approach will be used.

9.1 Parrallel Computing Methods

There are several ways to break down the Boundary Element Method into tasks that can be executed in parallel.

The smallest tasks that can be executed in parallel are the calculation of the individual Gauss-Kronrod points. In this method, each CPU available evaluates one point until all the points have been calculated. For this method to be efficient, an extremely high speed bus, cache and memory must be present or all of the CPUs may have to wait for one CPU to put its result into memory to allow calculation of the final value of the integral can be calculated. This method is very efficient on vector type computers(Cray C-90, Y-MP) and on shared memory processor arrays (SGI Origin 2000, Intel Paragon). Each processor caches its gauss

point data and instructions and simply receives the physical element where the point will be evaluated. This allows for efficient use of CPU power but requires very precise timing. It fairs very poorly in distributed environments.

The next level up in the size of a parallel task is for each CPU to perform an entire single integration. In this scenario, each cpu receives a set of data necessary to complete a single integral. This integral forms a single entry in one of the matrices in equation (4-2). This method also works well in small processor arrays and for small distributed memory computers. The downside of this method is that the ratio of time spent communicating between processors to the time spent in calculation higher.

A further enhancement to the previous method is to calculate all the integrals associated with a point-element pair. In the case of a 3D problem using linear triangles, there would be 6 integrals to be done using a single set of data. If quadratic Lagrangian elements are used the number jumps to 18 integrals. At this level, the ratio of communication to calculation has been minimized. It is now a matter of determining when the communication takes place. One can assign a CPU a block of point-element pairs and send all the necessary data at the beginning of the calculation. Another choice would be to send the point-element pairs immediately after each set of integrals have been completed and results returned.

9.2 Processor Arrays

These types of computers are made up of a single large block of physical memory with a large number of processors having access to the memory. The SGI

Origin 2000 and Intel Paragon are examples of these types of computers. They have the potential of being the fastest of all types of supercomputers. Generally, the use the first of the parallel techniques as described above.

9.3 Distributed Computation Methods

This class of computer is actually many separate computers linked by a standard networking system. Instead of being able to directly address another processor in the computer, a software layer is required to perform the communication. Another problem, is that the memory is also distributed, so any data needed by the a processor must also be sent along with the calculation commands. This means that the level at which the parallelism is made must be at a coarser level than what is typically done with a processor array type computer.

The point at which the parallelism is applied depends greatly on the overhead of communicating the necessary data and calculation commands to the computers making up the parallel machine. It is important that the overhead of communicating is less than the time required to perform the calculation or the gain of having multiple CPUs is lost.[108] Many people have solved this problem by simply assigning each machine a large block of the matrices that appear in equation (4-2). The method assumes that all the CPUs have the same performance capabilities and that no other processes are running. It also does not allow for any error. If for some reason one of the computers crashes, shuts down or loses contact with the rest of the computers, the entire calculation must be restarted.

There are several codes available to handle the data and command communication between networks of computers linked into a single distributed computer.

These include Parallel Virtual Machine (PVM), and Message Passing Interface (MPI). For the work done here a new approach has been taken. The new method makes use of a faster and lower level interface for inter-computer communication called Remote Procedure Call (RPC). RPC allows a computer program to call a subroutine that actually runs on a separate computer. Section C.3 of Appendix C contains details for writing RPC code to separate functions onto several computers.

9.4 Communication Between Computers

Computers forming the parallel machine must have a method to communicate data to each other. The communication can be greatly simplified if takes a master/slave approach to the problem. This approach can also be referred to as a star configuration with the master computer at the center of the star.

In a star configuration, the master computer takes the input from the user and constructs the mesh for the problem. Boundary conditions are supplied by the user. The master computer then splits up the calculation according to the parallel method being used and sends tasks out to each computer in the star. When the outer point computers complete the assigned task, they return the results to the central computer. The central computer compiles the various result to form the complete solution. Code for the communication on both the client and server side of the RPC is contained in section C.3 of Appendix C.

A plot of the performance of a distributed network of computers using RPC as the low-level communications layer is shown if Figure 9-1.

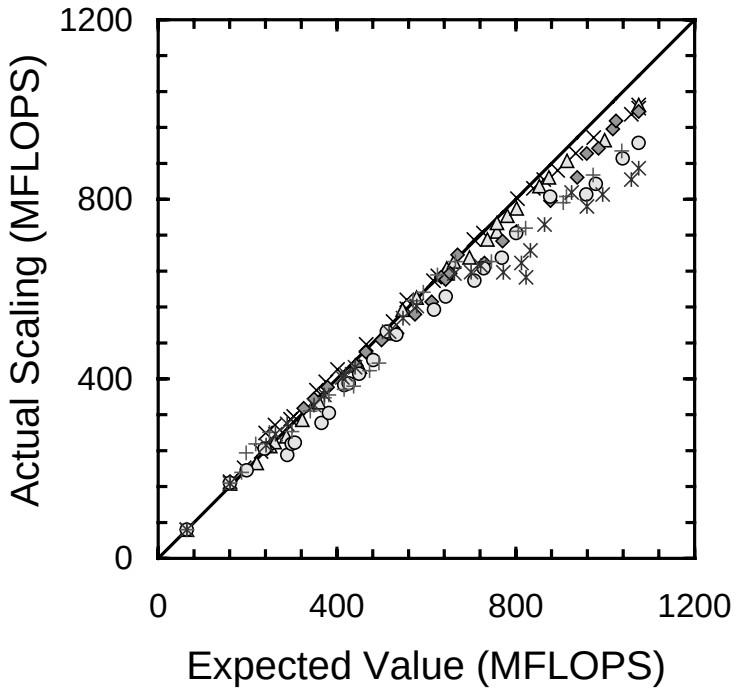

Figure 9-1: Plot of performance vs expected performance for a distributed computer.

Table 9.1: Comparison of location of integration source code.

Calculation module used	Time to complete Calculation
Compiled into main program	00:02:47
Small separate program	00:01:21

9.5 Improving Performance by Separating Calculation Code

A very interesting by product of separating the calculation of the integrals into a separately compiled program that can run on many computers simultaneously, is that on a stand alone setup, the performance can be substantially improved. This is done by installing the remote module on the stand-alone machine and telling the main program to use its own remote module. A simple test gave the results in Table 9.1. The reason for the difference is fairly simple. The amount of data needed by the small integration module is very small and can usually

fit within the CPU cache. This is referred to as good locality of data. The main program also has to keep track of where in the main matrices the data returned by the integration is to be placed, and update information to the user.

9.6 Benchmarks and Scaling

In a heterogeneous computing environment a method is needed to gauge the efficiency of adding more machines to the effort. A consistent method must be used to determine the efficiency of process and the computational power applied to solve the problem.

To evaluate the system of computers used to perform the boundary element calculations, a benchmark is performed using one computer to determine the number of FLOPS needed to complete an example calculation. Then each computer was timed using a random selection of integrals to establish what its maximum stand-alone performance would be. The results have been normalized and are shown in Table 9.2. These results have been checked by using them to predict the time required to solve a real problem and have been found to be accurate to within 5%. By normalizing the result with respect to the master computer, any differences that may have occurred because of the selection of integrals is removed. Since the total FLOPS used to complete the calculation are known, the real throughput of the parallel computer can be estimated.

Evaluation of the heterogeneous distributed computer was done using an actual model of a coated pipeline with coating holidays and a 5 anode ground bed. The total number of floating point operations needed to evaluate all of the integrals in equation 3-9 amounted to 143,500 mega-FLOPS. A machine with a sus-

Table 9.2: Normalized benchmark result data for many types of computers.

Machine	Processor	OS and RAM	Result
1	Pentium II 300Mhz	NT 4.0, 384MB	1.0
2	Alpha 21164, 300Mhz	NT Server 4.0, 128MB	0.976
3	Pentium II 300Mhz	NT 4.0, 128MB	0.923
4	Pentium, 133Mhz	NT 4.0, 32MB	0.298
5	Pentium 84Mhz	NT 4.0, 32MB	0.088
6	Pentium 200Mhz	NT 4.0, 32MB	0.439
7	Pentium 225Mhz	NT 4.0, 32MB	0.494
8	Pentium 200Mhz	Windows 98, 32MB	0.411
9	Pentium 133Mhz	NT 4.0, 32MB	0.296
10	Pentium 100Mhz	NT 4.0, 32MB	0.225
11	Pentium 100Mhz	NT 4.0, 32MB	0.297
12	Dual Pentium 200	NT 4.0, 128MB	0.806
13	Pentium 133Mhz	Window 95, 48MB	0.292
14	AMD K6 300Mhz	NT 4.0, 64MB	0.419
15	Pentium 83Mhz	NT 4.0, 40MB	0.100
16	i486 66hz	NT 4.0, 32MB	0.030
17	Pentium 120Mhz	NT 4.0, 48MB	0.296
18	Pentium 133Mhz	NT 4.0, 64MB	0.296
19	Pentium Pro 200	NT 4.0, 128MB	0.553
20	Pentium 200Mhz	NT 4.0 Server, 64MB	0.450
21	Pentium II 233Mhz	NT 4.0, 64MB	0.747
22	Pentium II 233Mhz	NT 4.0, 128MB	0.773
23	Pentium 200Mhz	NT 4.0, 32MB	0.407
24	Pentium 200Mhz	NT 4.0, 64MB	0.442
25	Pentium II 233Mhz	NT 4.0, 64MB	0.762

tained through-put of 100 mega-FLOPS/sec would need ~25 minutes to complete the calculation.

A timing mechanism was built into the software to check the wall-clock time before and after the calculation was done. Using the time and the number of floating point operations needed, an average through-put for the distributed computer could be found.

The procedure used to build a performance scaling line was to run the model first on the master only to get the first point in the line. Then machines were added to the distributed computer, 1 at a time, with the model being run once as each computer was added. To eliminate any effect that the order of adding computers may have on the shape of the line, several runs were made of adding all of the available computers using a different random order of machine addition for each run. An example run is shown in Table 9.3.

Often, with distributed machines, the actual node in the machine may be used for some job by another user. This effect can be seen in the center section of rows in Table 9.3. Those machines that are under heavy use by other users contribute very little to the distributed computer. On the other hand, if there is very little external activity, the performance scales very well. An abbreviated table of data is shown in Table 9.4. Figure 9-1 shows the pooling of several runs of the type shown in table 9.3. In this case, linear scaling through all of the machines is seen up to about 800 mega-FLOPS which corresponds to 12.5 times the speed of the master computer. Scaling is still good through the tested range of 1100 mega-FLOPS or 17.2 times the master computer speed.

Table 9.3: An example run of the scaling of a heterogeneous distributed computer. Computers are added one by one and the model is timed with each additional computer. This particular run was done when many of the workstations were also being utilized by other users.

Order	Expected Pwr	Time	Actual Pwr	Expected MFLPS	Actual MFLPS
1	1.00		1.00	63.99	63.99
22	2.51	859.2	2.61	160.5	167.0
7	3.77	569.0	3.94	241.2	252.2
11	4.10	518.2	4.33	262.4	276.9
10	4.51	479.0	4.68	288.7	299.6
24	5.45	420.0	5.34	348.4	341.7
20	5.81	394.0	5.69	371.6	364.2
26	6.43	356.0	6.30	411.8	403.1
18	6.55	350.0	6.41	419.1	410.0
21	6.88	337.0	6.65	440.3	425.8
14	8.07	284.0	7.90	516.4	505.3
8	8.56	268.0	8.37	547.7	535.4
17	9.04	255.1	8.79	578.3	562.4
3	10.4	226.2	9.92	662.4	634.5
19	10.9	225.0	9.97	700.1	637.6
13	11.3	220.0	10.2	721.4	652.2
4	12.1	225.2	9.96	772.0	637.2
27	12.7	218.0	10.3	812.5	658.3
28	12.9	229.2	9.79	822.8	626.2
16	13.0	209.2	10.7	832.5	685.9
15	13.5	193.0	11.6	864.3	743.5
23	14.5	176.0	12.7	924.6	815.3
25	15.0	183.0	12.3	959.1	784.1
9	15.5	177.0	12.7	994.5	810.7
2	16.5	170.0	13.2	1058	844.0
12	16.8	165.1	13.6	1075	869.0

Table 9.4: An second example run of the scaling of a heterogeneous distributed computer. This run shows better scaling because the load from other users was less.

Order	Expected Pwr	Time	Actual Pwr	Expected MFLPS	Actual MFLPS
1	1.00		1.00	63.99	63.99
22	2.51	839.3	2.67	160.5	171.0
3	3.82	586.0	3.83	244.6	244.9
⋮	⋮	⋮	⋮	⋮	⋮
19	9.56	251.0	8.93	612.0	571.7
⋮	⋮	⋮	⋮	⋮	⋮
4	16.8	140.1	16.0	1075	1025

It is apparent that this method will scale up to the greatest amount of free CPU time available on all of the machines within a distributed computer. This will happen irregardless of the load placed by other users.

9.7 Hard Drive Performance

Loading and saving data from persistent storage can be a source of slow performance. If data is not written or read as a continuous stream, performance can degrade by over a factor of 100. It is also advantageous to have only one of the matrices (***H*** *or* ***G***) in RAM at any time and to have both matrices only in persistent storage when forming the ***A*** matrix. This can increase the size of the solvable problem by a factor of $\sqrt{2}$.

Since it will be necessary to swap columns between the ***H*** and ***G*** matrices, it is best to store these matrices in the FORTRAN style column major order. This is opposed to C/C++, where the natural form is row major. Some experiments were done using a small set of matrices and a large set. The first experiment involved

Table 9.5: Conditions used for all hard drive performance tests

Computer	Pentium Pro 200
RAM	128 MB
Hard Drive	2GB 5400RPM Ultra SCSI
Small $\boldsymbol{H}$ matrix size	1.2 MB
Small $\boldsymbol{G}$ matrix size	2.8 MB
Large $\boldsymbol{H}$ matrix size	13.7 MB
Large $\boldsymbol{G}$ matrix size	30.7 MB

Table 9.6: Implementing Vector operations in the Residual Vector Calculation

Matrix size	Before Optimization	After Optimization	% time cut
Small Matrices	17 seconds	12 seconds	29%
Large Matrices	97 seconds	57 seconds	41%

calculating a residual error using the formula:

$$R_{Residual} = \boldsymbol{H}\Phi + \boldsymbol{G}\left(\boldsymbol{n} \cdot \nabla\Phi\right) \tag{9-1}$$

where the matrices $\boldsymbol{H}$ and $\boldsymbol{G}$ are stored in persistent storage. Table 9.6 shows the results of the time required to calculate the residual. The conditions for all hard drive tests are given in Table 9.5.

The next test was to build the matrix $\boldsymbol{A}$ as described in section 4.5 on page 62. The results are shown in Table 9.7. Here it is apparent that a substantial performance improvement is seen utilizing block operations and storage methods. The performance improvement get better as the matrices increase in size until the optimum block size for data transfer from the hard drive is reached. The value

Table 9.7: Implementing Vector operations in building the $\boldsymbol{A}$ matrix

Matrix size	Before Optimization	After Optimization	% time cut
Small Matrices	3 seconds	2 seconds	33%
Large Matrices	20 seconds	6 seconds	70%

varies from drive to drive but is usually between 16K and 64K. 64K corresponds to 8192 double precision floating point numbers.

9.8 High Performance Libraries

CPU manufacturers often make special high performance libraries available for their processors. Intel® has built a set of well tuned libraries as made them freely usable in compiled form.[98] These libraries have the added benefit in that they can utilize more than one processor on the machine where the code is run. Intel's data shows linear scaling of CPU efficiency on up to four processors. The code has been tested for this work on single and dual processor machines and linear scaling is seen.

Intel also supplies optimized math functions such as ln, exp, sin and cos. A factor of 2 improvement over the `stdlibc` routines that accompany all compilers can be seen.

CHAPTER 10
HOLIDAY EFFECTS ON SINGLE PIPES AND PIPELINE NETWORKS

The goal of this research was to be able to predict the effects seen in current and potential distributions in pipeline networks. One contributing item was coating holidays. Coating holidays are a small sections of the pipe where the coating has somehow been removed from the pipe and bare steel is exposed to the soil environment (see Figure 10-1).

Figure 10-1: Pipe that exhibits many coating holidays. Pipe was coated in the late 60's and dug up in 1996.[2]

The early work by Kennelly *et al.* [109] and Orazem *et al.* [110] on modeling the influence of coating holidays employed the Finite Element Method. While their results showed that the majority of current from the CP system went to the holiday, there was a significant error in the closure of current (3% to $>$ 12%) when modeling holidays.[109] Thus, their work demonstrated the weakness of using the classical finite element method where the flux is calculated from potential gradi-

ents. In subsequent work, a boundary-element approach was used to model the role of coating holidays.[33, 111, 112] The geometry considered was a single pipeline protected by sacrificial ribbon anodes such as those used for the Trans-Alaska pipeline. As constant triangular elements were used to discretize the surfaces, a large number of triangles were required to model properly the discontinuity of the current near the coating-holiday edge. Their work supported the conclusion that it is much more difficult to drive current to a holiday than to a uniformly poor coating. The results of the model for a pipe protected by ribbon anodes showed that the variation of potential around the pipe at a holiday can be as large as 550-650mV. This value is the difference between the most cathodic potential on the coated pipe and the most anodic potential at the holiday. Numerical difficulties limited the application of the model to short sections of pipe (<40 ft.).

10.1 Single Pipes

The first effect of holidays to investigate is to see how the current and potential distributions are effected by the presence of a holiday on a single pipe. Orazem *et al.* [110] first demonstrated the effects. Figure 10-2 shows a large holiday in an 18in-diameter pipe. The pipe is protected by a remote impressed-current CP system operating at -10 volts from the connection to the pipe. At the edge of the coating next to the holiday, the off-potential reading dips by 30 mV to -850 mV $Cu/CuSO_4$ which is marginally protected. The holiday has the greatest potential at the center, -863 mV $Cu/CuSO_4$. It might be expected that the coated region close to the edge of the holiday is in the worst shape. However, the corrosion rate is what is most important. Examining the corrosion rate at the center of the holi-

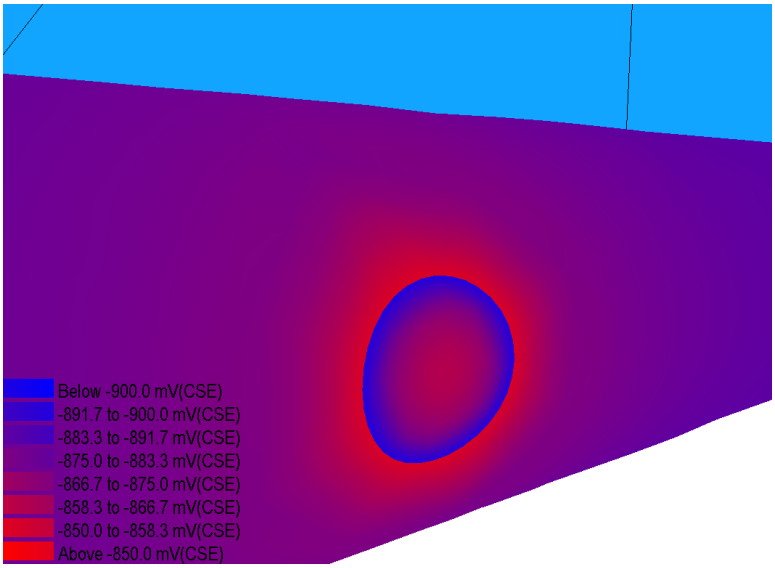

Figure 10-2: Off-potential distribution for a large holiday in a good quality coating. The edge of the coating next to the holiday does not meet the -850 mV criterion while the holiday does. Even so, the corrosion rate at the holiday is much higher than at any of the coated sections.

day reveals that it is corroding at a rate that is 3 orders of magnitude higher than that under the coating. The reason for the low rate under the coating is that the coating causes the rate of oxygen transport to be decreased and it adheres to the steel substrate. Recent experiments by Corfias *et al.* have begun to characterize the transport of electrolytes through coating, and how water uptake affects pore size, adherence properties and transport.[27] They have shown that electrochemical reactions (corrosion, oxygen reduction, etc.) are taking place at the steel surface and the rates are reduced by the coating.

If the CP system output is increased, the phenomenon seen in Figure 10-2 is still observed with larger variations in the off-potential of the coating. A plot of the angular potential and current distributions around the pipe at the holiday is given in Figure 10-3. In this case the off-potential of the coating exhibits a 50

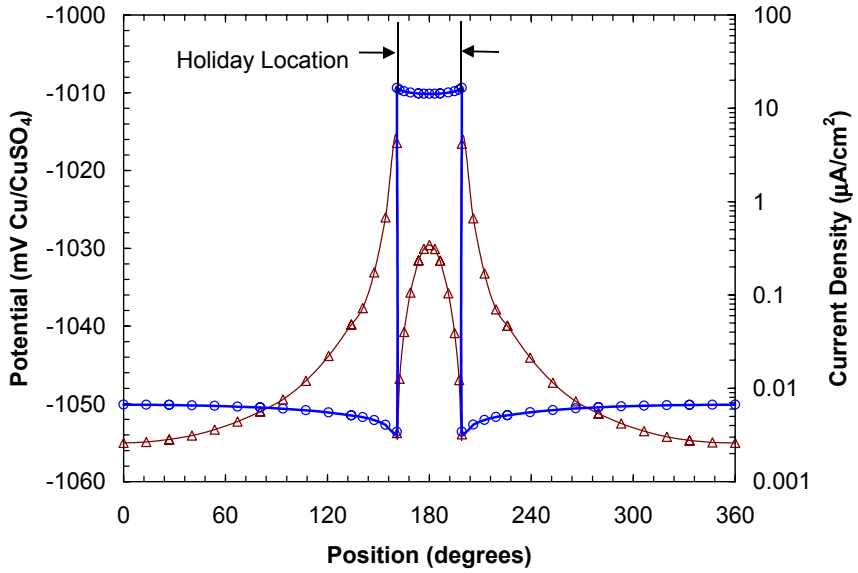

Figure 10-3: Current density and potential distribution around the circumference of a pipe through a holiday. Zero degrees is the top of the pipe. The blue line is the current density.

mV variation. The current distribution shows a factor of 2 decrease in the net current at the edge of the holiday. The reason for the draw down in current is that a galvanic couple forms between the coated steel next to the holiday and the exposed steel of the holiday. The coated pipe is at a more negative potential than the bare steel because, among other things, the coating blocks oxygen transport to the underlying steel thereby causing a shift in the corrosion potential. The effect is magnified by higher levels of CP because it takes significantly more current to shift the potential of bare steel a given amount than coated steel.

10.2 Two Pipes with a Coating Flaw

To investigate situations involving two pipes, a model was set up with two 10-mile-long pipes running parallel to each other in the same right-of-way. Both pipes were protected by a single remote groundbed placed at the 2.5 mile point.

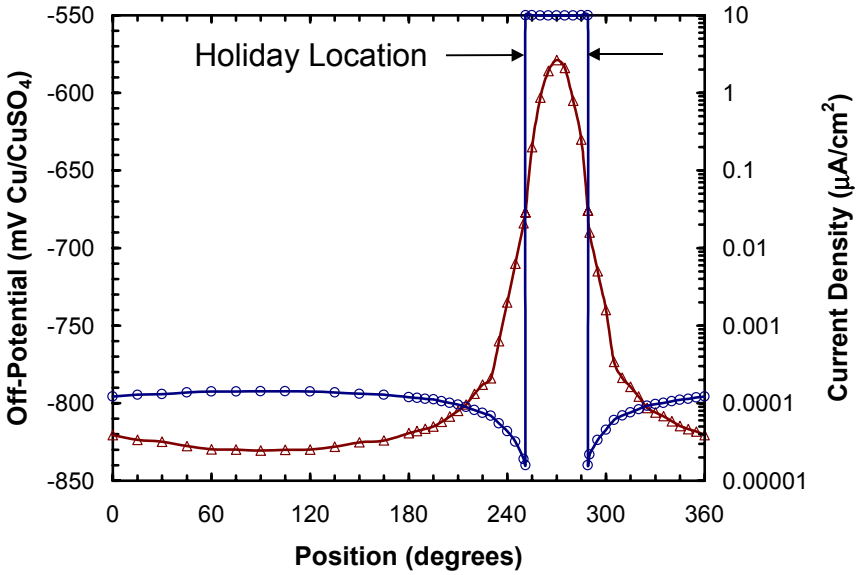

Figure 10-4: Current density and potential distribution around the circumference of a pipe through an under-protected holiday. Zero degrees is the top of the pipe. The blue line is the current density.

The coating of the flawed pipe was assumed to be aged. The adjacent pipe was assumed to have a high-quality coating.

Figure 10-4 shows the potential and current density distribution around the circumference of the pipe at the point of the holiday. The holiday is under-protected at the center and is corroding at a rate of about 0.5 mils per year. The current density near the holiday is an order of magnitude smaller than that seen far from the holiday.

The adjacent pipe shows some effects of the neighboring coating holiday. Figure 10-5 shows the off-potential and current density distributions for the well-coated pipe. The effect of the holiday is apparent but it is not to the extent of that seen for the pipe with the holiday. The effect is called shadowing. The cusp seen at the distributions is a numerical effect due to the joint between elements occurring exactly at the point of closest approach. The effect can be removed by

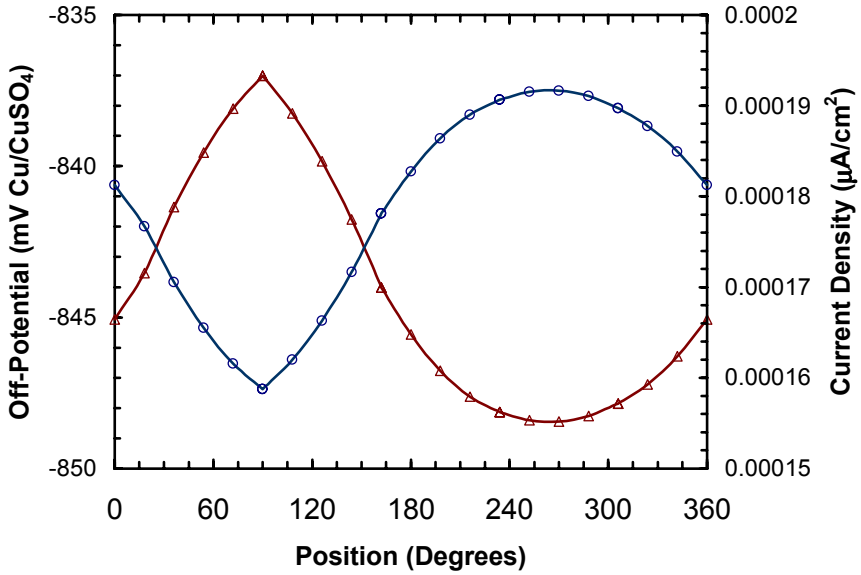

Figure 10-5: Current density and potential distribution around the circumference of a pipe at the spot closest to the under-protected holiday on the neighboring pipe. Zero degrees is the top of the pipe. The blue line is the current density.

changing the number of elements used to create the mesh around the circumference of the pipe such that the center point of an element is at the point of closest approach.

20 feet away from the holiday, the potential distribution on the well-coated pipe is much closer to uniform and all points around the circumference are protected. Even though the section of pipe closest to the holiday has fallen below the -850 mV criteria, the rate of corrosion under the coating is negligible.

10.3 Pipes Exhibiting Stray Current

A technique to allow the possibility of stray current between different CP systems was developed Section 4.3. A pipeline network was setup as shown in Figure 10-6. For this system, two pipes were placed adjacent to each other with one

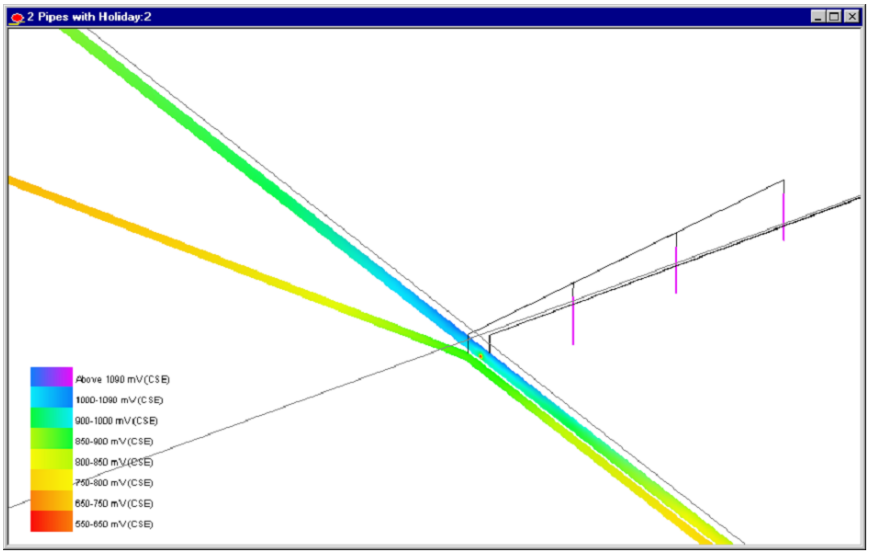

Figure 10-6: Distant view of a under-protected holiday. Lower right portion of pipe with holiday is also exhibiting stray current.

pipe leaving the right-of-way at a 45 degree angle 1 mile from the starting point of the model. The diverging pipe was given two different coatings of the form of equations (1-24) and (1-25). One was for the section that ran parallel to the second pipe with parameters to emulate an "aged" coating. The other section consisting of the part diverging away from the second pipe was given a new coating similar to the original. The second pipe was considered to have a new coating except for a holiday at the bend in the pipe. The two pipes have separate CP systems consisting of distributed groundbeds that are relatively close to each other. This scenario can be thought of as an old oil pipeline and a new gas pipeline sharing a portion of a single right-of-way. The model was used to examine the point where the two pipelines merged into a single right-of-way.

A small portion of the pipes being modeled is shown in Figure 10-7. The shading represents the calculated potential distribution around the pipe. The stray current associated with the two CP systems caused a portion of well-coated pipe

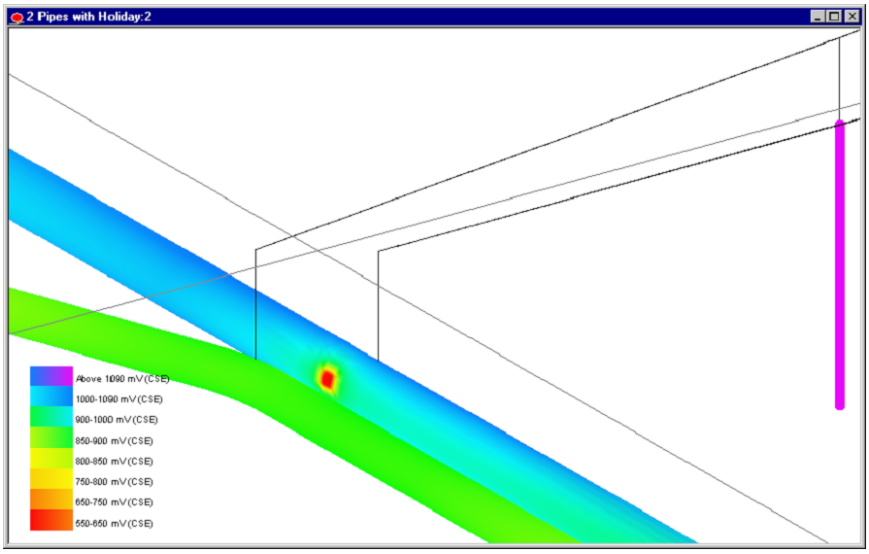

Figure 10-7: Closeup of an under-protected holiday.

to serve as an anode, delivering current to the poorly-coated pipe. This effect is seen more clearly in Figure 10-8 where the current distribution around the well-coated pipe is presented as a function of angular position. The corresponding potential distribution is given in Figure 10-9 for a section of the pipe exhibiting stray current effects and for a section of the pipe farthest from the section of the pipe that exhibits stray current effects. In the region where stray current effects are evident, the entire pipe falls below the -850 mV $Cu/CuSO_4$ protection criterion. The point closest to the neighboring poorly-coated pipe is anodic, and the section opposite the neighboring pipe is at only slightly cathodic potentials. These results can be compared to the current distribution given in Figure 10-8 where the positive current is anodic.

Even in the section of the pipe that was not driven to anodic currents by the interference between CP systems, the pipe is not adequately protected in the region that is closest to the neighboring pipe. For this system, rectifier settings

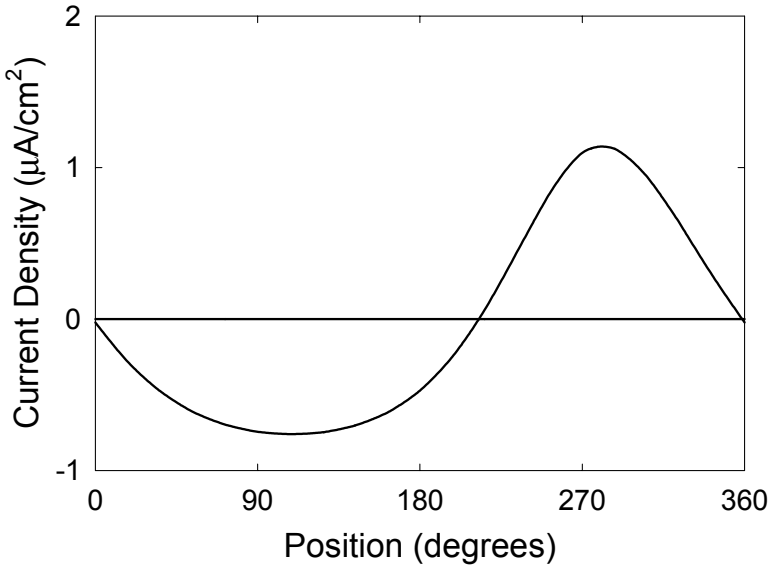

Figure 10-8: Current Density around pipe in area exhibiting stray current in Figure 10-7. Positive current densities are anodic.

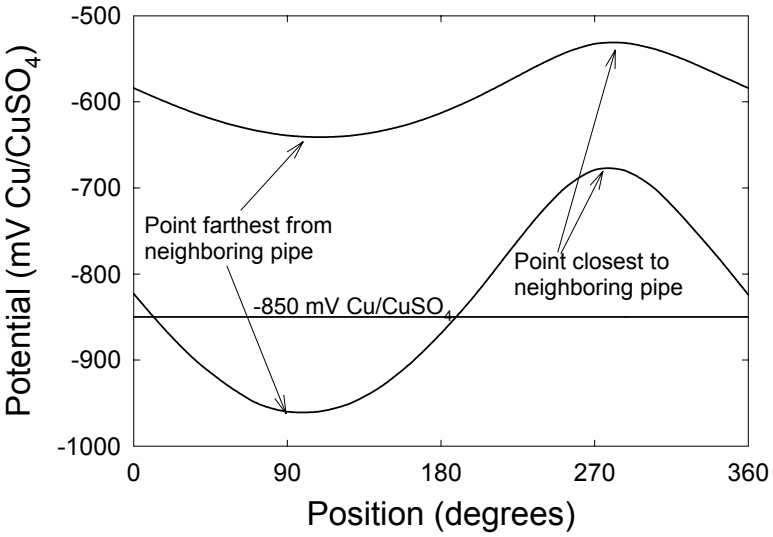

Figure 10-9: Potential distribution around pipe at center of section exhibiting stray current and at end of section where all parts of the circumference of the pipe are cathodic.

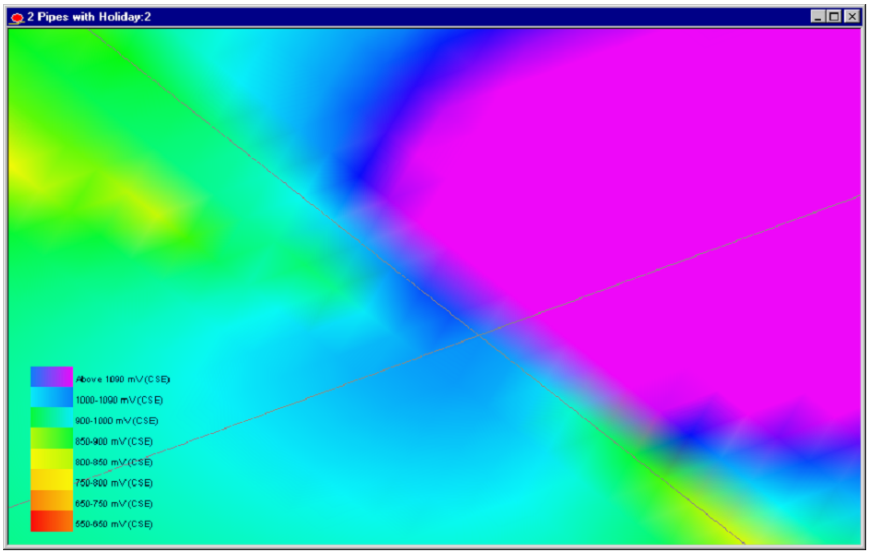

Figure 10-10: Distant view of soil surface on-potentials over an under-protected holiday.

could be found that would cause the entire system to meet or exceed the -850 mV $Cu/CuSO_4$ criterion, but, in doing so, a significant portion of the pipeline was over-protected. Satisfactory protection for this case was achieved only when the pipes were bonded such that stray current effects were eliminated. Again, the smooth distributions presented in Figure 10-8 and Figure 10-9 reflect the accuracy of the meshing and the adaptive integration schemes used in these calculations.

10.4 Soil Surface On-Potentials

Soil surface on-potential distributions were calculated for the pipes exhibiting stray current described in section 10.3. If there is going to be much to see in an on-potential survey of the pipe, the results of section 10.3 should show it. Figures 10-10 and 10-11 show the on-potential distributions. Figure 10-11 has been split so it is apparent where the pipes are located with respect to the soil surface calculation. On-potential surveys near the anodes tend to only show the anodes. This is made

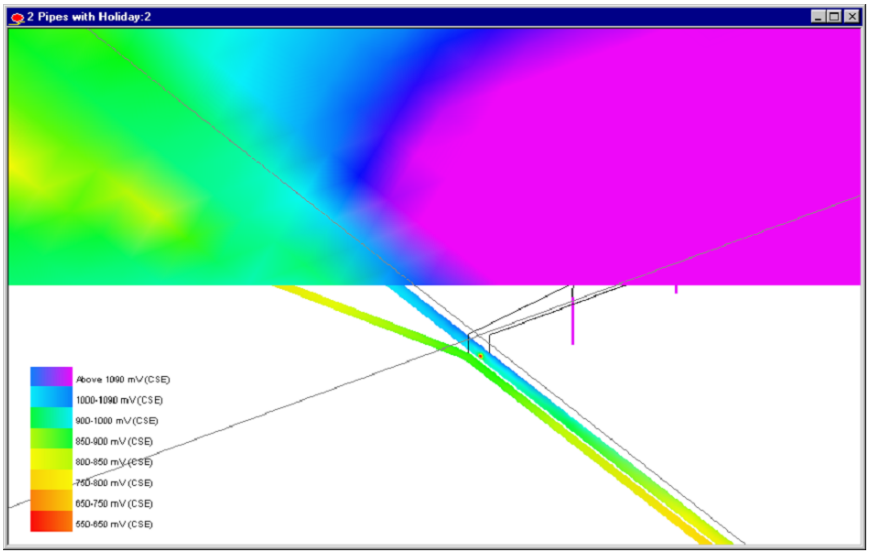

Figure 10-11: Distant view of soil surface on-potentials with a portion of the soil surface removed to see the pipe. The soil surface on-potential only indicates the presence of the anodes. The holiday is not seen.

apparent in the calculations. The interference of the anodes masks the behaviour of the pipes and even the stray current situation. The only indications of the pipe are in the upper left corner where a portion of the well-coated/well-protected section of pipe is seen.

10.5 Adjacent Holidays

An issue brought up in discussions with pipeline operators was whether an under-protected large coating holiday next to a small holiday would adversely effect the small holiday. To test the idea, a model was setup with two holidays very close to each other (see Figure 10-12). The large holiday exposed 17.7 cm^2 bare steel. The small holiday exposed 12.6 mm^2 of steel. The holidays were placed with 2.91 cm space between them. This was the closest that two holidays could be placed using the mesh generator. Both holidays were assumed to have the

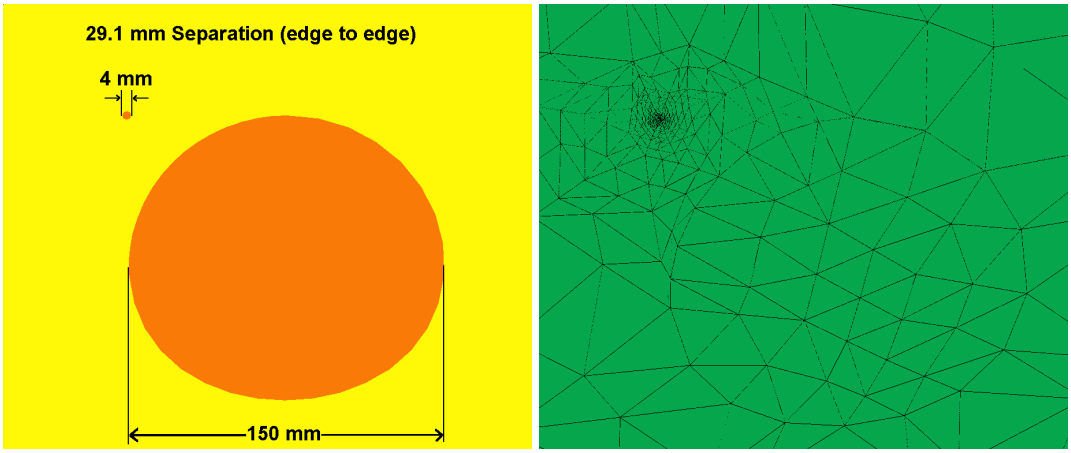

(a) Dimensions (b) Mesh

Figure 10-12: Setup for calculation of a pinhole holiday next to a large holiday: a) the dimensions of the holidays and b) the automatically generated mesh for the holidays.

same polarization curve (equation (1-23)) and parameters. The CP system was set such that the large holiday was under-protected. Figure 10-13 shows the off-potential distribution of the two holidays. From the color scale, it is apparent that all but the edges of the large holiday are under-protected. The small holiday remains well protected even though it is close to a holiday that is under-protected.

Therefore, the situations that should concern pipeline operators are large coating holidays. These are the most difficult to protect so monitoring systems need to indicate when a problem will occur on a large holiday versus a small one. Chapter 11 discusses one monitoring technique and how the size of holidays affect the technique.

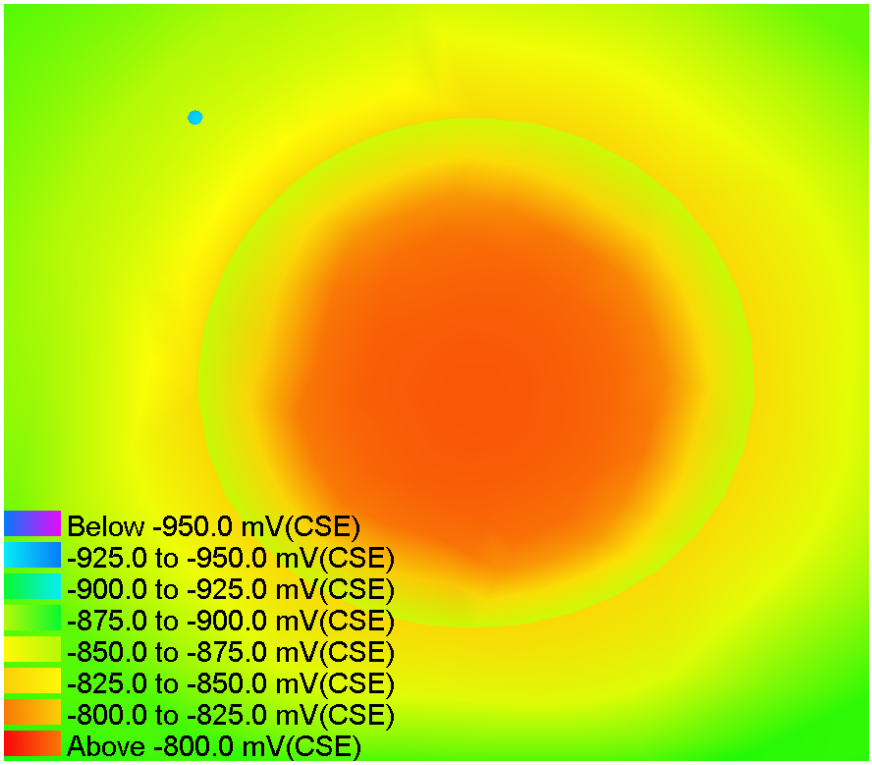

Figure 10-13: Off-potential distribution of a pinhole holiday next to a large holiday. The large holiday is under-protected by standard criteria while the pinhole is well protected.

CHAPTER 11
COUPONS

Coupons are a small piece of pipeline grade steel placed in the same soil environment as the pipeline. The coupon is connected to the CP system through a test station so the polarization level of the coupon can be monitored without affecting the CP provided to the pipe. It is thought that a coupon represents a holiday of similar size. Mathematical models were used to explore the conditions under which a coupon provides a conservative assessment of the level of cathodic protection provided to holidays on coating buried structures. The most conservative assessment of cathodic protection was obtained when the area of the coupon was larger than the area of the largest expected holiday. The performance of the coupon as a monitor of cathodic protection was found to be strongly influenced by the availability of oxygen in the soil.

11.1 Introduction

The true off-potential of holidays on cathodically protected buried pipelines can be difficult to ascertain. Normally, all that can be obtained is the off-potential of the pipeline itself which is said to represent some kind of a weighted average of the true off-potential of all the holidays. When one cannot remove all sources of current, it is not possible to get an off-potential measurement. Such complicating factors include direct bonded galvanic anodes, telluric currents, and stray currents.

The pipeline off-potential may not be representative of the off-potential at a large holiday if there are many smaller holidays also on the pipe which sum to a similar area as the larger holiday. One solution to this problem is to use a coupon. Coupons have been proposed to be an alternative or a complement to direct measurement of off-potentials for assessing cathodic protection of buried structures.[113, 114, 115] The coupon can be connected to the pipe or CP system through a test station in such a way that all sources of current to the coupon may be turned off without disrupting the current to the pipeline. It has been recommended that a coupon be as similar as possible to a section of the actual structure being protected.[3, 114] However, there has been little theoretical work done to show the relationship between a holiday of a given size on a pipeline and a coupon.

Stears *et al.*[114] and Lawson and Thompson[115] showed that the off-potentials measured for coupons varied with location relative to the pipeline. This result can be attributed to differences in soil environments. The mass-transfer-limited current density for reduction of oxygen has a critical influence on the corrosion potential, and variations due to differences in moisture content or soil composition will influence the coupon off-potential. Coupon configuration, location, and size can also influence coupon readings. Lawson and Thompson[115] observed that small coupons tended to be polarized more than large coupons. This observation is consistent with the calculations presented by Orazem *et al.*[33, 109, 110, 111] Lawson and Thompson[115] also reported that in some cases, the coupon off-potential was significantly more negative than the off-potential of the pipe, suggesting that the exposed surface area was greater on the pipe than on the coupon. The difference between coupon and pipe off-potentials was influenced by the amount of

cathodic protection current applied, although no general trend could be identified. The difference between coupon and pipe off-potential was generally small, but, in some cases, was on the order of 200 mV. The biggest differences were seen for cases where the coupon reading of -780 mV indicated that a 200 mV potential shift criterion was met but where the pipe off-potential of -580 mV suggested that the pipe was underprotected.

Safe utilization of coupons for assessing the level of protection afforded by a cathodic protection system requires a better understanding of the factors that influence the coupon readings relative to pipe condition. This work takes a first-principles approach to identify the relationship between the off-potential of a coupon and the off-potential of a holiday through the solution of the governing differential equations. Recently published experimental work [114, 115] provides a basis for comparison to the models. Their work indicates that there should be a relationship between the shift in the off-potential of a coupon due to a change in the setting of a rectifier and the change in the off-potential of a pipe with coating holidays and that they both change in the same direction.

It should be noted that, because the calculations provide detailed results for individual holidays, the modeling approach presented here should yield greater insight into the relationship among coupons and holidays than can be obtained from experiments conducted on pipelines where measured off-potentials reflect a weighted average of the behavior of all holidays.

Table 11.1: Polarization parameters used in the model.[41]

Parameter	Values
i_{lim,O_2}	0.1, 1.0, 3.16, 10.0 μA/cm^2
E_{Fe}	-526 mV(CSE)
β_{Fe}	59 mV/decade
E_{O_2}	-104 mV(CSE)
β_{O_2}	59 mV/decade
E_{H_2}	-955 mV(CSE)
β_{H_2}	118 mV/decade

11.2 Boundary Condition Parameters

The model is capable of assigning different individual polarization curves to each coupon and holiday. A coupon with a new bright finish, for example, would be characterized by a polarization curve with a large mass-transfer-limited current density for oxygen reduction; whereas, to account for the presence of scale deposits, a holiday on an old pipe would be characterized by a polarization curve with a smaller mass-transfer-limited-current density for oxygen reduction. The code can also handle many holidays on the same pipe, each sized differently and with different polarization curves.

The polarization curve used for bare metal surfaces (coupons and holidays) was equation (1-23). The parameter values for equation (1-23) are given in Table (11.1).

The coating was modeled using a set of equations given in Chapter 1. The values in Table 11.1 were used for the polarization behavior of the steel beneath the coating and the addition parameters listed in Table 11.2 determined from experimental data.[24, 111]

Table 11.2: Coating parameters used in model. Note: These parameters were determined after water uptake of the coating.[116]

Parameter	Values
A/A_{pore}	1000
ρ	5×10^9 Ohm-cm
δ	20 mil
α_{block}	0.99 (99% effective)

11.3 Approach

The pipeline used for the model was 6.44 km in length and had a diameter of 457 mm. The pipe was protected by a single impressed current ground bed at one end of the pipe section. The holiday-free sections of the pipe were assumed to have a uniform 0.5 mm (20 mil) FBE coating. Coating holidays were assumed to expose bare steel. The anode used for this model was an impressed-current ground bed, sized at 76 mm OD and 15.25 m length. Its current output could be adjusted until the desired reading of the off potential for the coupon was obtained.

Two coupon designs were used for the simple cases. The first was a band of bare steel of length 6.35 cm on a 5.08 cm diameter pipe which follows the design described by Stears *et al.*[114] The second was a 1.27 cm rod with an exposed tip of 2.5 cm which follows the design described by Lawson and Thompson.[115] Schematic representations of the coupons are given in Figures 11.1(a) and 11.1(b) respectively.

Two sets of calculations were performed. One set involved a single holiday with a single coupon. The coupon was placed 6 meters from the holiday with 1.2 m top cover over the exposed portion. For each of the coupon types, four ratios

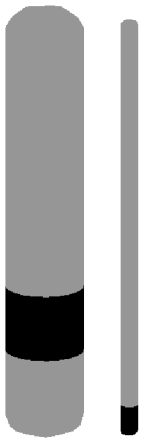

(a) (b)

Figure 11-1: Schematic representations of the two cylindrical coupons used in the simulations: a) large coupon[114] with a surface area of $\sim$ 50 cm^2; and b) smaller coupon[115] with a surface area of 9.5 cm^2.

of the holiday area to the coupon area were used. For each of these cases, four different polarization curves were used. Finally the current output of the anode was adjusted iteratively such that the average off-potential of the coupon was -750, -850, or -950 mV CSE. The calculation matrix therefore included 96 different cases.

The more complicated scenario involved the same pipe and anode, but the pipe was assumed to have five coating holidays of different sizes. Three of the of them were placed at the top of the pipe (0^o), and the remaining two were placed at the bottom (180^o). The bottom of the pipe was assumed to rest in water-saturated soil while the top was assumed to be in dry soil. To simulate the influence of water level, the holidays at the bottom of the pipe were assigned a polarization

curve with a i_{lim,O_2} that was an order of magnitude lower than that used for the holidays at the top of the pipe.

The design of the large coupon was changed for the more complicated scenario. From the results of the first simulations, it was apparent that there may be an effect associated with the geometry of the coupon. To provide a preliminary exploration of the role of coupon design, the large coupon was redesigned to match closely the design of the small coupon, Figure 11.1(b), but with the same surface area as the original coupon.

11.4 Results and Discussion

The difference between the measured potential of the coupon and the most positive potential on the holiday is presented in Figure 11-2 for the large coupon. The corresponding results for the small coupon are given in Figure 11-3.

The presentation of calculated results as the difference between the measured potential of the coupon and the most positive potential seen on the holiday emphasizes the behavior of the system where the corrosion rate is the highest. The sign on the y-axis indicates whether the holiday is at a more cathodic potential (negative sign in front) or at a more anodic potential than the coupon. Both sets of simulations used the same convention.

As seen in Figures 11-2 and 11-3, the coupon does not provide an exact mirroring of the behavior of the holidays. As reported by Lawson and Thompson,[115] a change in the rectifier output results in a similar shift in the off-potential of the coupon and the holiday. The reliability of the coupon off-potential as an indicator of the holiday off-potential depends strongly on the availability of oxygen

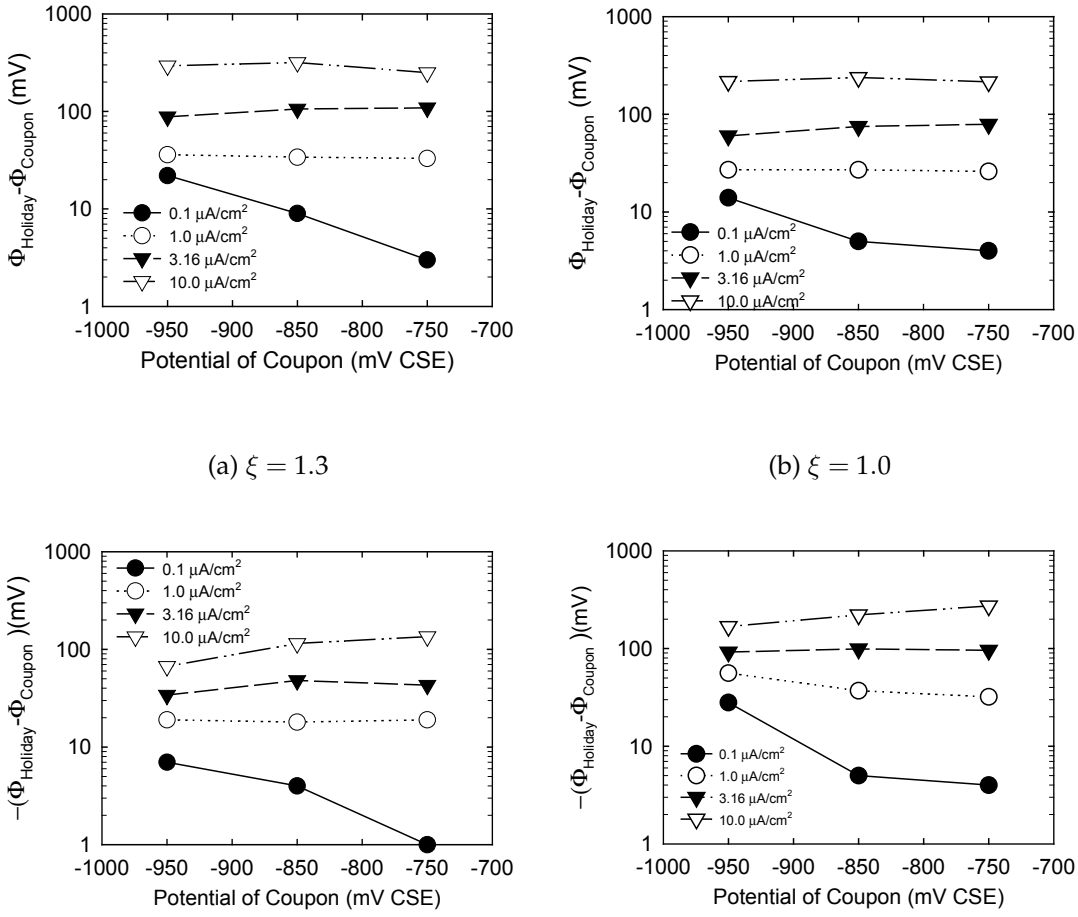

(a) $\xi = 1.3$

(b) $\xi = 1.0$

(c) $\xi = 0.1$

(d) $\xi = 0.01$

Figure 11-2: Large coupon - Difference between the most positive potential of the holiday and the coupon at three different rectifier outputs that result in the coupon potential being measured at -750, -850 and -950 mV (CSE). The negative sign on y-axis label indicates the holiday is at a potential cathodic to the coupon. The lack of a sign indicates the opposite. Panels a) through d) correspond to different values of $\xi = A_{\text{holiday}}/A_{\text{coupon}}$.

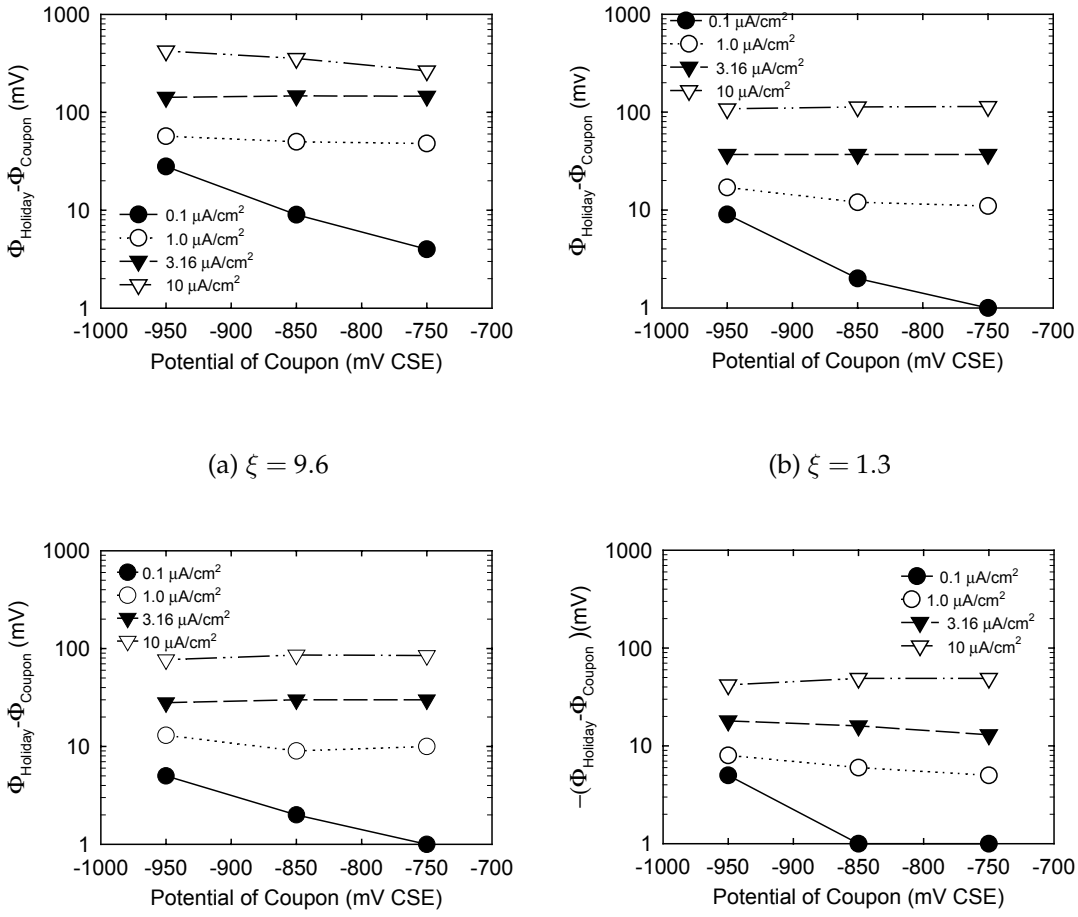

(a) $\xi = 9.6$

(b) $\xi = 1.3$

(c) $\xi = 1.0$

(d) $\xi = 0.089$

Figure 11-3: Small coupon - Difference between the most positive potential of the holiday and the coupon at three different rectifier outputs that result in the coupon potential being measured at -750, -850 and -950 mV (CSE). The negative sign on y-axis label indicates the holiday is at a potential cathodic to the coupon. The lack of a sign indicates the opposite. Panels a) through d) correspond to different values of $\xi = A_{\text{holiday}}/A_{\text{coupon}}$.

in the soil environment. An increase in i_{lim,O_2} increased the difference between the off-potential of the holiday and the off-potential of the coupon. The sign of the differences given in Figures 11-2 and 11-3 determines whether the coupon provides a conservative assessment of the state of the holiday. For coupons that are larger than the biggest holiday, the differences were negative, and the holiday was more protected than the coupon. For coupons that are smaller than the biggest holiday, the differences were positive, and the coupon was more protected than the holiday.

The ratio of holiday area to coupon area $\xi = A_{\text{holiday}}/A_{\text{coupon}}$ is an important parameter. While no specific critical value of ξ was found that gave consistently conservative results, all coupons with $\xi \geq 1$ over-predicted the level of cathodic protection applied to the holidays. To compare the effects the geometry has on the performance of the coupon, similar ratios of the holiday area to the coupon area can be used. By comparing Figure 11.2(a) and Figure 11.3(b), one can see the design of the smaller coupon, Figure 11.1(b), results in a slightly closer match to the off potential of the holiday at high values of i_{lim,O_2}. As seen in Figure 11.3(a), which represents a holiday with a surface area equal to the surface area of the large coupon, the small coupon seriously over-predicted the level of cathodic protection at the holiday. In this case, at high values of i_{lim,O_2}, the holiday potential was very close to the corrosion potential for conditions where the small coupon had an off-potential showing a 280 mV shift from the corrosion potential.

Ideally, a coupon should represent the off-potential of a holiday of similar size. If the coupons did behave this way, then all the plots in Figures (11-2) and (11-3) would have their lines at a 0 difference between the holiday and coupon at

Table 11.3: Results of two coupon model. The small coupon used a polarization curve with $i_{\lim,O_2} = 1.0\ \mu A/cm^2$ (curve 1). The large coupon used $i_{\lim,O_2}$ that was an order of magnitude smaller (curve 2).

Object	Size	Location	Pol. Curve	Pot. (CSE)	Avg. Curr. Den.
Holiday 1	7.81 cm^2	0^o	1	-839 mV	1.11 $\mu A/cm^2$
Holiday 2	12.9 cm^2	0^o	1	-834 mV	1.10 $\mu A/cm^2$
Holiday 3	130.6 cm^2	0^o	1	-787 mV	1.05 $\mu A/cm^2$
Holiday 4	64.5 cm^2	180^o	2	-847 mV	0.228 $\mu A/cm^2$
Holiday 5	6.45 cm^2	180^o	2	-855 mV	0.244 $\mu A/cm^2$
Small Coupon	9.36 cm^2	122 cm	1	-850 mV	1.13 $\mu A/cm^2$
Large Coupon	101 cm^2	167 cm	2	-854 mV	0.241 $\mu A/cm^2$

Table 11.4: Results of two coupon model. The large coupon used a polarization curve with $i_{\lim,O_2} = 1.0\ \mu A/cm^2$ (curve 1). The small coupon used a $i_{\lim,O_2}$ that was an order of magnitude lower(curve 2).

Object	Size	Location	Pol. Curve	Pot. (CSE)	Avg. Curr. Den.
Holiday 1	7.81 cm^2	0^o	1	-867 mV	1.19 $\mu A/cm^2$
Holiday 2	12.9 cm^2	0^o	1	-861 mV	1.18 $\mu A/cm^2$
Holiday 3	130.6 cm^2	0^o	1	-815 mV	1.08 $\mu A/cm^2$
Holiday 4	64.5 cm^2	180^o	2	-873 mV	0.312 $\mu A/cm^2$
Holiday 5	6.45 cm^2	180^o	2	-883 mV	0.350 $\mu A/cm^2$
Small Coupon	9.36 cm^2	167 cm	2	-884 mV	0.356 $\mu A/cm^2$
Large Coupon	101 cm^2	122 cm	1	-850 mV	1.13 $\mu A/cm^2$

all potentials. The results show that the coupon does not yield the off-potential of a holiday of similar size. However, a linear relationship was found between the difference between the off-potentials of the coupon and the holiday and the mass transfer limited current density for oxygen reduction ($i_{\lim,O_2}$). The ratio of the surface areas then indicates whether holiday will be cathodic or anodic to the coupon.

The results of the simulations for the multi-holiday, two-coupon system are summarized in Tables 11.3 and 11.4. The results shown in Tables 11.3 and 11.4

simulate the use of coupons for a pipeline with a distribution of holiday sizes and with the water table at the center-line of the pipe. Thus, the bottom of the pipe is in wet soil, and the top of the pipe is dry. The least conservative assessment of cathodic protection was obtained with the large coupon placed at the bottom of the pipe (Tables 11.3). In this case, both coupons met the protection criterion of −850 mV(CSE), yet only the smallest of the five holidays met the protection criterion. The most conservative assessment of cathodic protection was obtained with the large coupon placed at the top of the pipe (Tables 11.4). Again, both coupons met the protection criterion of −850 mV(CSE). Only the largest of the five holidays did not meet the protection criterion, and this holiday was only 35 mV short of -850 mV (CSE).

11.5 Coupon Performance Diagram

For cases where the polarization curves corresponding to electrochemical reactions on the coupon was the same as that on bare steel exposed by coating holidays, the most important parameters were $\xi = A_{\text{holiday}}/A_{\text{coupon}}$ and i_{O_2}, the current density for reduction of oxygen. All the calculated results could be placed on a coupon performance diagram, shown in Figure 11.5. Cases where coupons yield off-potentials more positive than exposed steel are indicated by black symbols, cases where coupons yield off-potentials more negative than exposed steel are indicated by open symbols, and cases where coupons yield off-potentials less than 15 mV more negative than exposed steel are indicated by gray symbols.

Calculations to the left of the line at $A_{\text{holiday}}/A_{\text{coupon}} = 0.8$ were considered to yield conservative results. This can be interpreted as meaning that a coupon

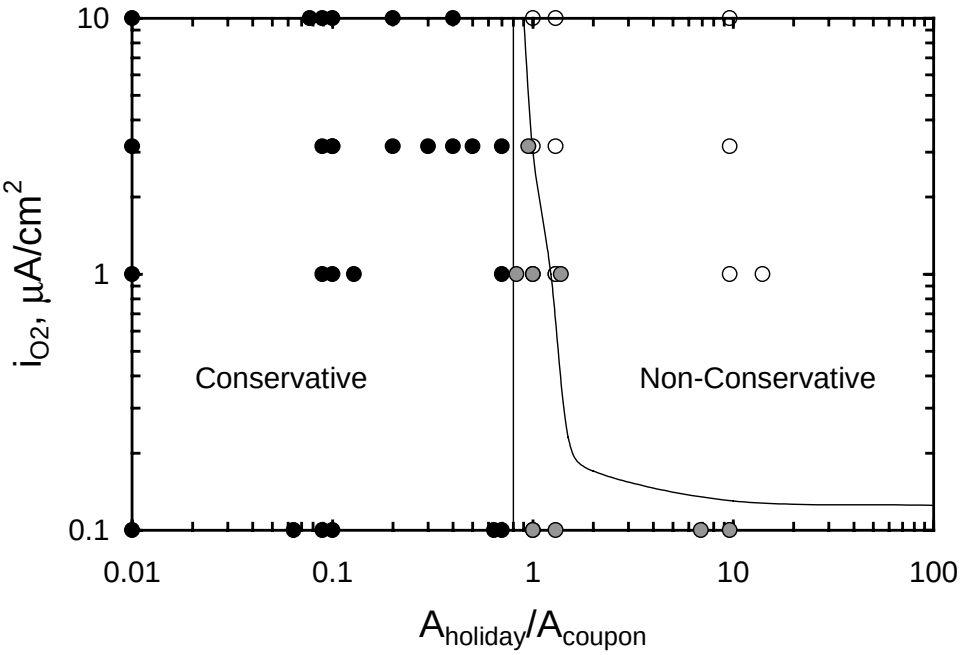

Figure 11-4: Coupon performance diagram for coupons placed in the same soil environment as the pipeline coating defects that expose bare steel. The soil resistivity was 10,000 Ω cm. Black symbols correspond to calculations where a protected coupon corresponded to a protected coating holiday. Open symbols correspond to calculations where the coupon could indicate adequate protection for pipes with coating holidays that are seriously underprotected. The gray symbols correspond to cases where the coupon reading is not conservative, but the error was less than 15 mV.

will yield a conservative assessment of the pipe condition so long as each coating holiday that exposes bare steel exposes no more than 80 percent of the coupon area. The dashed line indicates the approximate boundary for which the degree to which the coupon was not conservative was smaller than 15 mV.

The position of these boundaries was a weak function of soil resistivity. An increase in soil resistivity from 10,000 Ω cm to 100,000 Ωcm moved the position of the solid boundary line from $A_{\text{holiday}}/A_{\text{coupon}} = 0.8$ to 1.1.

Figure 11.5 did not provide a reliable indication of coupon performance for cases where the polarization curve for the coupon corresponded to a less aggressive environment than that experienced by the bare steel exposed by coating holidays. Coupons with an oxygen current an order of magnitude smaller than that of the steel gave consistently non-conservative results, even for coupons with areas 13 times the area of exposed steel. ($A_{\text{holiday}}/A_{\text{coupon}} < 0.077$).

It should be noted that the calculations presented here were for cases where the only coating defects on the pipe exposed bare steel. The present work does not address the use of coupons to assess the possible role of corrosion under intact disbonded coatings.

11.6 Conclusion

To be useful for monitoring the health of pipelines under cathodic protection, coupons should provide a conservative value such that the largest expected holiday is protected when the coupon is protected. The present work shows that the area of the coupon should be larger than the area of the largest expected holiday. The performance of the coupon as a monitor of cathodic protection is

strongly influenced by the availability of oxygen in the soil. If coupons of different sizes are to be used, the largest coupons should be placed in regions where the mass-transfer-limited current density is largest. The sensitivity of the coupon to the polarization curve indicates that coupons should be placed to sample all soil environments encountered by the pipeline. If only one coupon is to be used, it should be placed in the region of greatest oxygen availability. A coupon performance diagram could be constructed which reveals conditions under which a coupon yields a conservative assessment of cathodic protection to holidays exposing bare steel. The coupon performance diagram addressed both polarization behavior and the relative size of coupons and coating holidays.

CHAPTER 12
TANK BOTTOMS

Storage tanks are located at the terminus of most pipelines. They may be used to store crude oil unloaded from ships, furnace fuel waiting for the fall demand, or fuel depot reserves. Most cities have a fuel depot where gasoline, diesel, and other types of petroleum products are stored before distribution to filling stations. The storage facility allows pipelines to run continuously and efficiently, instead of having to be turned on and off while filling individual delivery trucks.

Storage facilities usually consist of many above-ground storage tanks called a tank farm. They are built of steel and rest on the soil. The tank bottom is then subject to the same materials problems as the buried pipelines. As the geometry of a tank is much different than pipelines, tanks have different problems with CP design than do pipes. Since tanks sit on the ground and are operated at atmospheric pressure, the steel is thinner (0.25") and, therefore, low corrosion rates can be catastrophic.[117]

Past tank failures and environmental problems have motivated installation of underlying cache basins to prevent any leakage from entering the aquifer. The liner of the cache basin is usually made of a very high dielectric membrane which does not allow passage of electrical current. The CP systems for these types of tanks are designed to place the anodes between the liner and the steel tank bottom.[118]

Concentration profiles for oxygen under a storage tank are cyclic in nature. The reason is that when the tank is empty, the center rises above the soil creating a void. The void fills will air and because the tank is no longer in contact with the soil, none of the oxygen in the soil at the center of the tank is consumed through the oxygen reduction reaction (second term of equation (1-23)). When the tank comes into contact with the soil again after filling, the mass-transfer-limited current density for oxygen reduction is the same at the center as at the periphery.

The model has been adapted to handle tank bottoms. It can also handle the insulating cache basin if it is assumed that no current can pass through the liner using the techniques derived in section 3.6.

12.1 Tank Bottom Mesh

The boundary element mesh for the tank bottom was created using isoparametric quadrilateral Lagrange elements and isoparametric quadratic triangles.[67] The triangles are used to increase the degrees of freedom as the mesh proceeds radially from the center. If the Lagrange elements where used exclusively, either the center of the tank would be over-meshed, or the outside edge would have a too-course mesh. The triangles are used to double the degrees of freedom by placing a triangle at every other element on the last ring of elements that would double the diameter from the previous spot where the number of degrees of freedom were doubled. Therefore, starting from the center, rings that use triangles are 1 (the center which is all triangles), 2, 4, 8, 16, etc (see Figure 12-1). The density of elements is then set by specifying the density at the center and the total

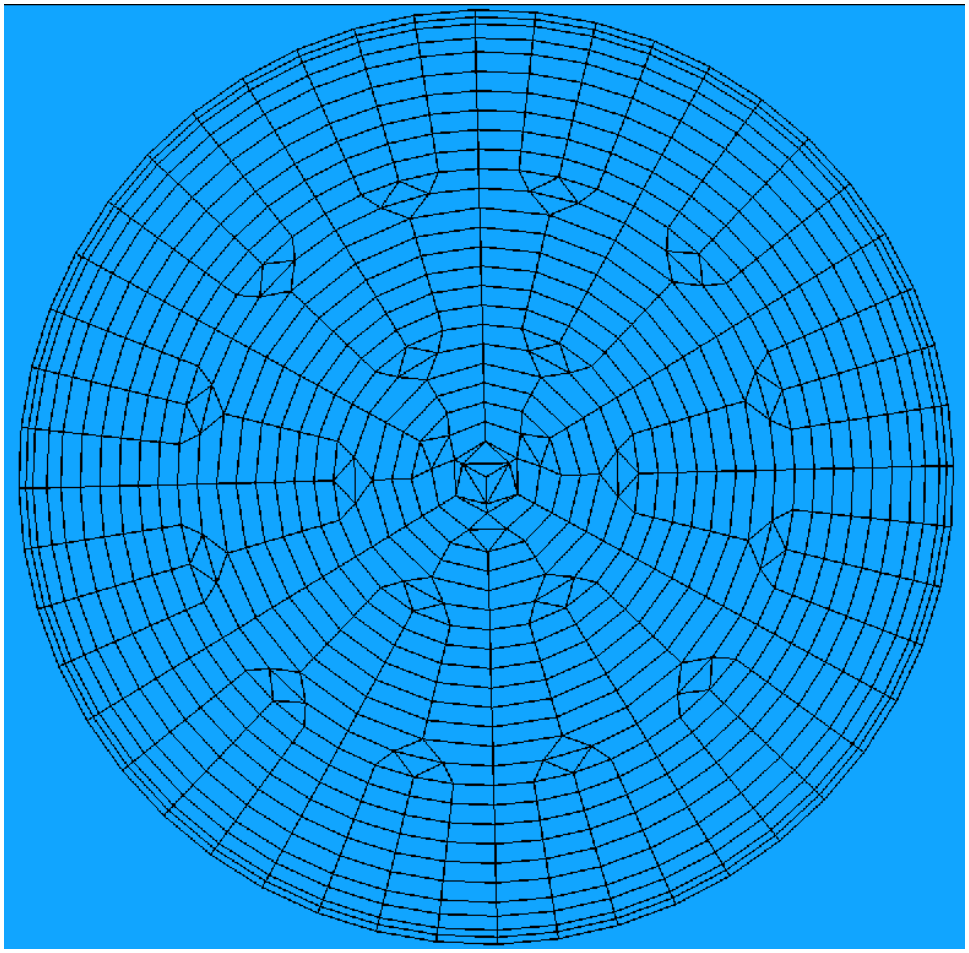

Figure 12-1: High resolution mesh used for the boundary element mesh.

number of rings. The mesh generator takes care of the rest. The last ring is divided into two rings to help handle the possible edge effects. The ring at the very edge is $\frac{1}{3}$ the size of the rest of the rings while the next to last is $\frac{2}{3}$ the size.

Individual rings of elements were assumed to have the same parameters for the polarization curve, equation (1-23). The axisymmetric setting of polarization curve parameters does not mean that an individual ring will have the same potential everywhere since different points in the rings can be at different points on the polarization curve defined by the boundary condition parameters. It does

mean that the concentration of oxygen in the soil near the ring was assumed to be constant for that ring. The implicit assumption is that oxygen is consumed and diffuses to the steel axisymmetrically. The assumption of the oxygen concentration having an axisymmetric profile is valid if all the oxygen that diffuses to any point on the steel is instantly consumed through the electrochemical reactions and that the diffusion constant for oxygen (D_{O_2}) does not change in any part of the soil domain.

12.2 Model for oxygen consumption

Oxygen can get to the steel of a tank bottom with or without an underlying cache basin through the soil around the edges of the tank. If it is assumed that the oxygen is consumed according to equation (1-23), and that the concentration does not vary with depth, then the consumption can be obtained through a balance equation

$$\frac{\partial c_{O_2}}{\partial t} = \nabla \cdot N_{O_2} - R_{O_2} \tag{12-1}$$

where the flux of oxygen, N, is given by

$$N_{O_2} = -D_{O_2} \nabla c_{O_2} \tag{12-2}$$

where D_{O_2} is the diffusion coefficient for oxygen transport through the soil. The rate of consumption of oxygen is proportional to the concentration of oxygen since virtually all of the oxygen that gets to the steel surface is reduced. This can be written as

$$R_{O_2} = kc \tag{12-3}$$

where k is the proportionality constant which accounts for the thin diffusion layer next to the steel surface (on the order of 50 microns[41]).

Substitution of equations (12-2) and (12-3) into (12-1) yields

$$\frac{\partial c_{O_2}}{\partial t} = -D_{O_2}\nabla^2 c_{O_2} - kc \tag{12-4}$$

Under assumptions of a steady state and that oxygen concentration does not vary with depth, equation (12-4) can be expressed in cylindrical coordinates as

$$D\frac{d^2c}{dr^2} + \frac{D}{r}\frac{dc}{dr} - kc = 0 \tag{12-5}$$

Upon moving the constants into the last term and multiplying through by r^2

$$r^2\frac{d^2c}{dr^2} + r\frac{dc}{dr} - \left(r\sqrt{\frac{k}{D}}\right)^2 c = 0 \tag{12-6}$$

which resembles a Bessel's equation. To get the equation into the standard form of Bessel's equation, a variable transformation is made

$$\xi = r\sqrt{\frac{k}{D}} \tag{12-7}$$

where the derivatives are

$$\frac{dc}{dr} = \sqrt{\frac{k}{D}}\frac{dc}{d\xi} \tag{12-8}$$

and

$$\frac{d^2c}{dr} = \left(\sqrt{\frac{k}{D}}\right)^2\frac{d^2c}{d\xi^2} \tag{12-9}$$

Upon substituting equations (12-7), (12-8), and (12-9) into equation (12-6), the modified Bessel"s equation of parameter 0 is obtained as

$$\xi^2\frac{d^2c}{d\xi^2} + \xi\frac{dc}{d\xi} - \xi^2 c = 0 \tag{12-10}$$

whose solution is a modified Bessel function. The boundary conditions for the original system in cylindrical coordinates are

$$\text{at } r = R, c = c_\infty \tag{12-11}$$

and

$$\text{at } r = 0, c \text{ is finite} \tag{12-12}$$

In the transformed coordinates, the boundary conditions become

$$\text{at } \xi = R\sqrt{\frac{k}{D}}, c = c_\infty \tag{12-13}$$

and

$$\text{at } \xi = 0, c \text{ is finite} \tag{12-14}$$

The solution to equation (12-10) is the modified Bessel function of the first kind. It takes the form

$$c(\xi) = AI_0(\xi) + B\left[ln(\xi)I_0(\xi) + \sum_{m=1}^{\infty}\left(\frac{(-1)^{m-1}}{2^{2m}(m!)^2}\sum_{n=1}^{m}\frac{1}{n}\right)\right] \tag{12-15}$$

where A and B are constants to be determined from the boundary conditions. Application of boundary condition (12-14) to equation (12-15) yields

$$c(\xi) = AI_0(\xi) \tag{12-16}$$

Upon applying boundary condition (12-13),

$$c(\xi) = \frac{c_\infty}{I_0(R\sqrt{\frac{k}{D}})}I_0(\xi) \tag{12-17}$$

The solution is presented as a function of radial position in Figure 12-2 for several values of the scaling parameter $R\sqrt{k/D}$.

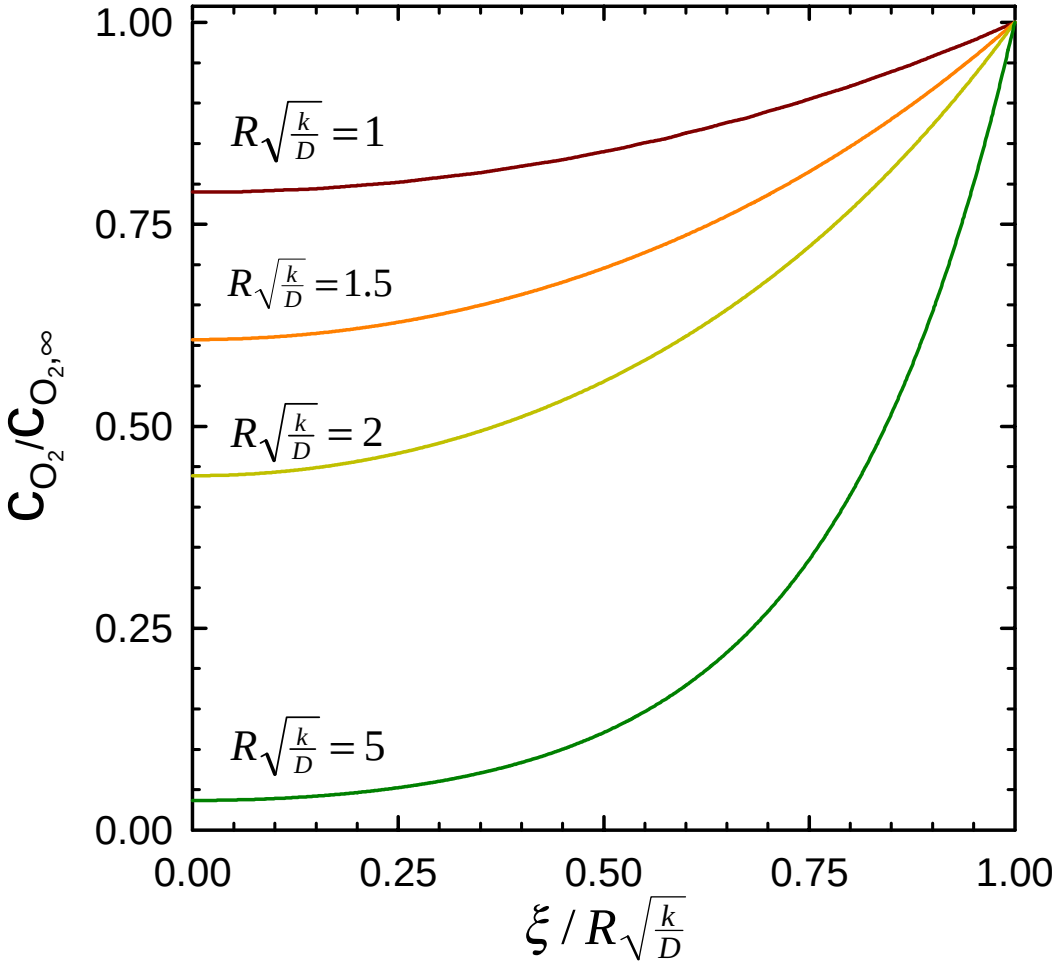

Figure 12-2: Oxygen concentration profile within the soil at several values of the scaling parameter $R\sqrt{k/D}$.

12.3 Implementation

The passage of current through the soil is governed by Laplace's equation which was solved using the boundary element method (BEM). The boundary condition for the bare steel was given by equation (1-23). The anodes were also allowed to be polarized according to equation (1-30).

The oxygen concentration distribution was applied through the boundary condition at the steel surface of the tank bottom. The parameter, i_{O_2} in equation (1-23) was adjusted according to equation (12-17). However, the value of i_{O_2} could only be adjusted in a step-wise manner. Each ring of elements in the boundary element mesh was assigned a single value of the parameter (see Figure 12-1 for the element layout) which remained constant in that ring.

In addition to forcing a constant value of i_{O_2} in each ring of elements, setting a different value at each ring introduced an error at the edge of the ring in the current density. The boundary element method compensates for the error at the center of the element. Therefore the point at which to sample the solution is critical for this type of simulation. The best points to sample are the Gauss points for a 2x2 point rule (square parent element).[119]

There were three anode arrangements used corresponding to the three standard anode arrangements used in industry.[120] The first was a remote ground-bed, the second a distributed arrangement of 8 anodes placed around the circumference of the tank and finally, ribbon anodes placed directly under the tank-bottom. The remote ground-bed cannot be used when there is an insulating cache basin under the tank.

12.4 Results

A single tank was modeled using the three anode arrangements described above. The tank was 100 feet diameter with bare steel exposed to the soil. In all cases the anode output was adjusted to 14.2 Amps. If the current density is uniform for the entire tank-bottom, a protection level of 1.9 $\mu A/cm^2$ would be achieved which would cause the steel to be somewhat over-protected.

The possibility of an insulating cache under the electrolyte where the CP system was installed was also modeled for the anode arrangements that can work with it. The model could account for the soil surface or tank bottom and an optional underlying insulator (see section 3.6).

The results are presented in a series of cases based upon the three possible anode arrangements, starting with the remote ground-bed.

12.4.1 Remote Ground-bed

Smyrl and Newman provide a criterion for determining the maximum size of tank that can be protected with a remote ground-bed without over-protection assuming a uniform current density.[121] The maximum radius is given by[12]

$$r_o = \frac{\Delta\Phi_o \kappa}{0.363 i_{\text{avg}}} \tag{12-18}$$

where $\Delta\Phi_o$ is the maximum over-polarization of the steel from the point of minimum protection (-850 mV CSE). If an undesirable rate of hydrogen evolution takes place at -1200 mV CSE, then $\Delta\Phi_o$ is equal to 350 mV. For an average current density of 1.9 $\mu A/cm^2$ and 10,000 Ωcm soil, the maximum radius is 51 cm. If the

soil resistivity is only 1000 Ωcm, then a tank of 5.1 m could be protected. A soil resistivity significantly less than 10,000 Ωcm is not usually seen.

The current distribution on the tank bottom is not necessarily uniform but is expected to be axisymmetric when a remote anode is used.[121] The outermost ring of the tank should have a much higher current density than the center if Tafel kinetics apply (hydrogen evolution).[122] If the center of the tank is poorly polarized, the net current density will be below the mass-transfer-limited current density for oxygen reduction and again, the current density distribution is nonuniform.[123] Therefore, it is not expected that equation (12-18) would be of much value for CP design. The polarization curve used in the model for bare steel can account for each of the above possibilities.

The cathodic protection system was modeled using a deep well remote groundbed at 250 feet below the tank. The groundbed output was 14.2 Amps. It was assumed that the soil resistivity was constant throughout the soil domain and equal to 10,000 Ωcm. Two cases were calculated, one for the uniform oxygen concentration when the tank is filled, and one with an oxygen concentration profile calculated from equation (12-17) to approximate the case when psudeo-steady-state has been reached.

Uniform Oxygen Distribution The first calculation assumed a uniform concentration of oxygen in the soil to simulate the conditions that exist when the tank has just been filled and the oxygen beneath the tank is not yet depleted. The anode output was adjusted to 14.2 Amps. Equation (12-18) would predict the difference in potential between the outer edge and the center of the tank to be -10.5 volts if there is a uniform current distribution. Figure 12-3 shows the off-potential

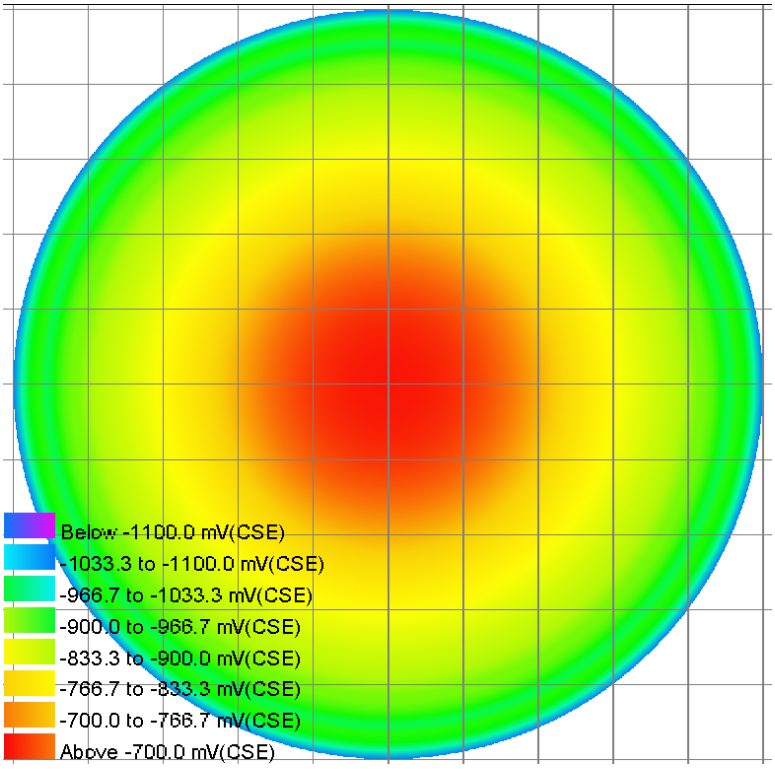

Figure 12-3: Potential distribution when the oxygen concentration is uniform at its largest value. This condition occurs when the tank has been recently filled after being empty. The grid spacing is 10 ft square.

distribution on the tank bottom. The center of the tank is at -605 mV $Cu/CuSO_4$ or -75 mV from the corrosion potential which is 25 mV underprotected by the -100 mV polarization shift criteria.[124] The outside edge of the tank is polarized to -1189 mV $Cu/CuSO_4$, which is significantly more positive than the -10.5 volts predicted by equation (12-18). The potential variation is smaller because the current density distribution was nonuniform, due to the role of corrosion and hydrogen-evolution reactions. The value of -1189 mV is very close to -1200 mV $Cu/CuSO_4$, which is a point where hydrogen evolution is a significant concern.

Figure 12-4 shows the complete off-potential and current-density distribution as a function of the radial position from the center of the tank. The current density

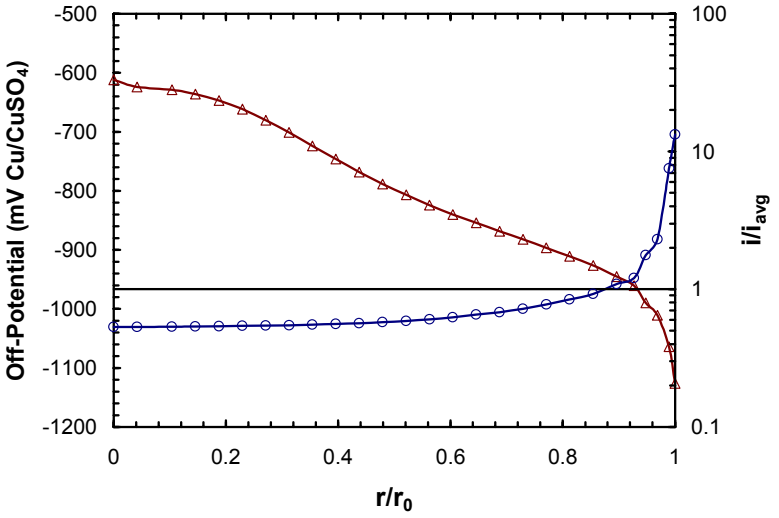

Figure 12-4: Radial potential and current density distribution when the oxygen concentration is uniform and at c_∞. Potential is given by the red line. The black line indicates where a uniform current density distribution would be.

distribution is nearly equivalent to the primary distribution for a disk electrode (see equation (7-1) on page 104). The value of J for the secondary distribution, described by Newman,[122] was equal to 536 (see equation (7-2) in section 7.1.2). Thus, any small change in the current density at the center of the tank used to increase the protection there, will result in significantly elevated current densities at the edge of the tank. The more nonuniform current density distribution results since increasing the average current density increases the value of J.

Nonuniform Oxygen Distribution As stated before, the solution to the oxygen distribution under the tank was implemented by changing the value of the mass-transfer-limited current density for oxygen reduction (i_{O_2}) to values predicted by the solution to the diffusion equation for oxygen given in equation (12-17). The profile for the oxygen distribution under the tank was taken using the scaling parameter, $R\sqrt{k/D}$, set to 2. The anode size and location was not changed for this

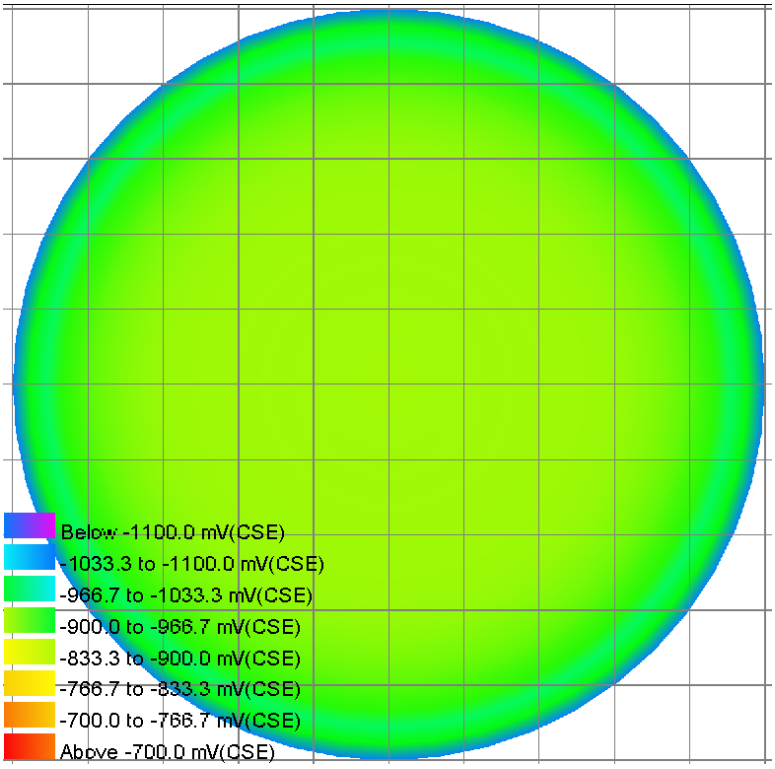

Figure 12-5: Potential distribution when the oxygen concentration follows the profile given in Figure 12-2 corresponding to $R\sqrt{k/D} = 2.0$. The grid spacing is 10 ft square.

simulation. The anode output was 14.2 Amps for the same potential setting as the first simulation. The off-potential distribution is shown in Figure 12-5. This time, the off-potential was much closer to being uniform. The polarization level at the center was also significantly improved to -906 mV $Cu/CuSO_4$. The corrosion potential at the center, where it is most negative, was -550 mV $Cu/CuSO_4$. Therefore the center was polarized by over 350 mV. As one proceeds radially from the center, the polarization level only increases. These results mean that the entire tank was over-protected and money has been wasted by running the anode at too high of a level.

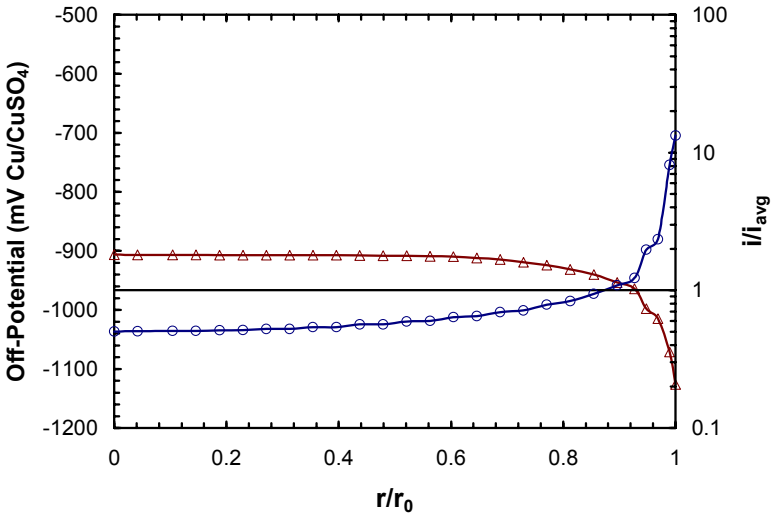

Figure 12-6: Radial potential and current density distribution when the oxygen concentration follows the profile given in Figure 12-2 corresponding to $R\sqrt{k/D} = 2.0$. Potential is given by the red line. The black line indicates where a uniform current density distribution would be.

Figure 12-6 shows both the potential and current distribution for the nonuniform oxygen concentration profile. Again, the current distribution approached the primary distribution and the total current was the same as before. The difference was in the potential distribution, especially at the center of the tank. A substantial reduction in current could be safely made while still maintaining protection. However, as soon as the tank goes through a emptying/refilling cycle, the current level would have to be increased again until the steady-state oxygen concentration profile achieved.

12.4.2 Distributed Anodes

Another anode arrangement that can be used is shallow distributed anodes where an arbitrary number of anodes are arranged in a circle around the outside edge of the tank. The anodes are close to the surface so it may be possible to use

this configuration with an underlying insulating containment membrane. For the following examples, 8 anodes were placed around the circumference of the the same 100 ft diameter tank used in the previous 2 examples. The total output of the anodes was set to match closely that of the previous two examples (14.2 Amps). The anodes were placed such that they were two feet from the edge of the tank. The soil resistivity was set to 10,000 Ωcm.

Uniform Oxygen Distribution Figure 12-7 shows the potential distribution for the tank when the oxygen concentration distribution is uniform. The center of the tank was polarized only -16 mV from the corrosion potential as opposed to the remote groundbed where the center was polarized by -75 mV at the same total current. The corrosion current density was 0.57 μA/cm^2 which is about half that expected for unprotected general corrosion.

A plot of the current density is shown in Figure 12-8. Since the distributions were no longer axisymmetric, the position that is selected for a plot of the distributions is important. The distribution is periodic however, with one period being the angular distance between two anodes. There are two possibilities for the plot, select a line from the center to a point closest to any one anode, or select a line from the center to a point between two anodes. For either case, where the primary distribution shows a value of i/i_{avg} equal to 0.5 at the center of the tank, the value for the distributed anodes is 0.25. Near the outside edge, there is a much sharper turn in the distribution as it goes toward infinity even though the value of J is the same as for the case with the remote groundbed ($J = 536$). The corrosion current at the center of the tank is more than an order of magnitude higher

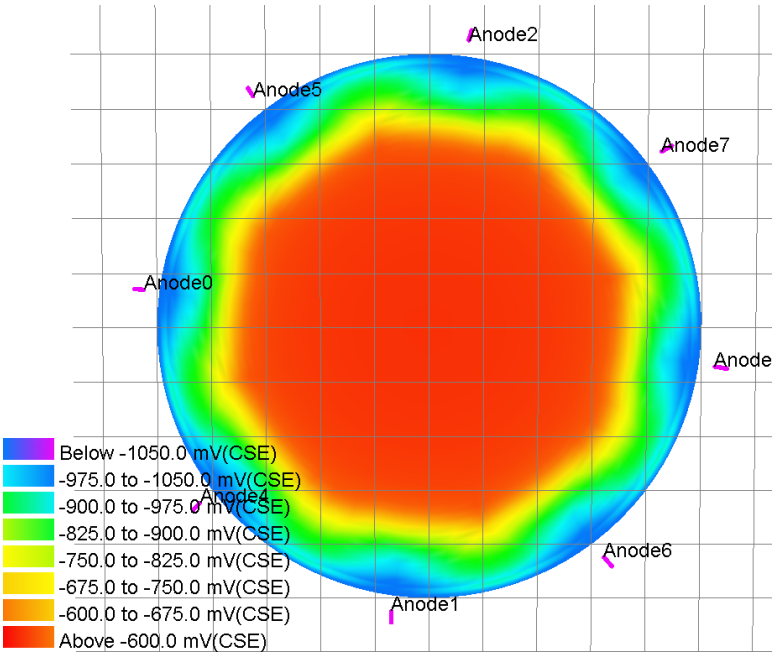

Figure 12-7: Potential distribution with distributed anodes and uniform oxygen concentration profile. The distribution is must worse than the primary distribution. The center is only polarized -16 mV

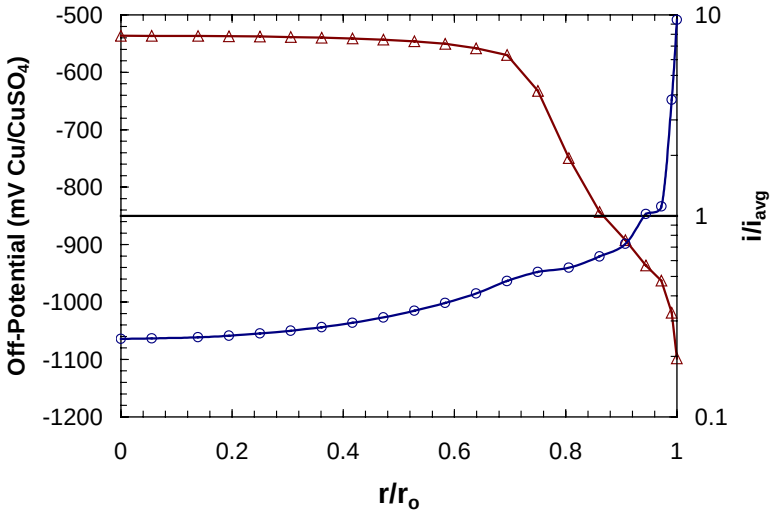

Figure 12-8: Current density distribution on tank bottom with distributed anodes and uniform oxygen concentration profile. The distribution was taken on a line that went from the center of the tank to a point on the edge exactly between two anodes.

than that of the remote groundbed. In this case $i_{corr,Fe}$ is equal to 0.57 $\mu A/cm^2$ compared to 0.0275 $\mu A/cm^2$ for the remote ground bed protected tank.

The reason for the poor performance of the distributed anodes is geometry. The edge of the tank is significantly closer to the anodes than the center. Therefore, is is much easier to drive current to the edge of the tank than to the center. When a remote anode is used, all points on the tank are equally distant from the anode.

Nonuniform Oxygen Distribution When distributed anodes were paired with the nonuniform oxygen concentration distribution, the potential and current distributions obtained showed better protection at the center of the tank with the was total current driven to the steel. The corrosion current is 3 orders of magnitude lower than when the oxygen concentration was uniformly high. The potential distribution on the tank is shown in Figure 12-9.

The potential and current density distribution are plotted in Figure 12-10. It is interesting to note that the current density at the center of the tank was the same as that for the uniformly high oxygen profile. The additional current needed to reduce the extra oxygen for the case with the high oxygen profile comes from the corrosion of the steel tank. Because the oxygen concentration was lower in the present case, the same current density was better able to protect the metal.

Underlying Insulating Cache Basin with Uniform Oxygen Distribution If there is an underlying electrically insulating layer such as a catch basin, remote groundbeds cannot be used. Distributed anodes can be used with an underlying membrane because they can be placed within the soil between the membrane and the

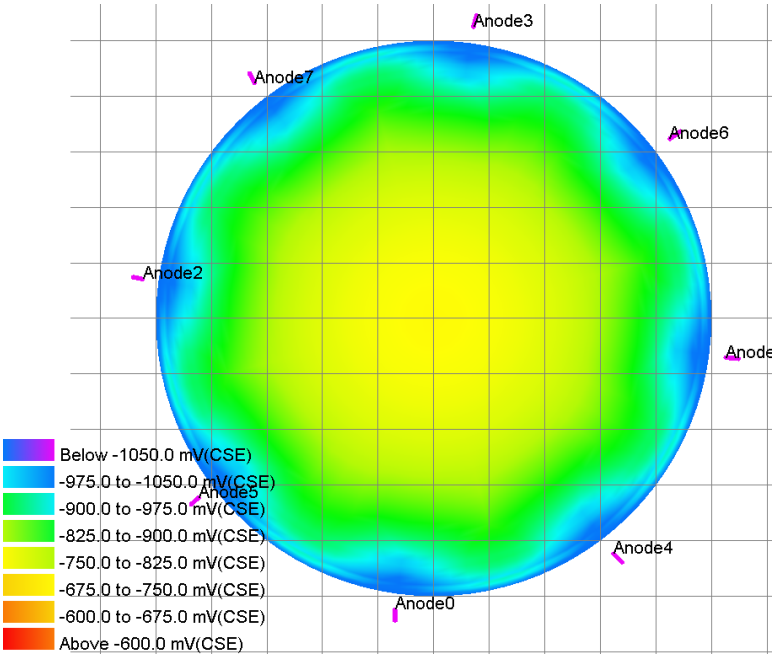

Figure 12-9: Potential distribution with distributed anodes and nonuniform oxygen concentration profile. The distribution is much worse than the primary distribution.

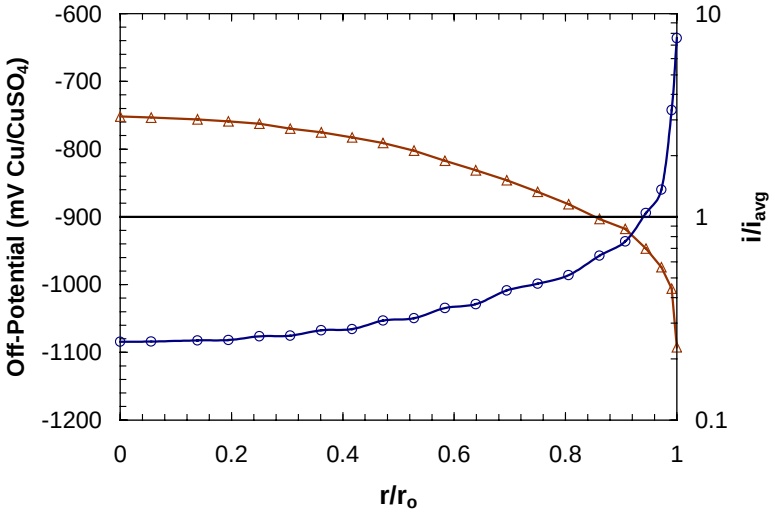

Figure 12-10: Potential and current density distribution on a tank bottom with distributed anodes and nonuniform oxygen concentration profile. The distribution was taken on a line went from the center of the tank to a point on the edge exactly between two anodes.

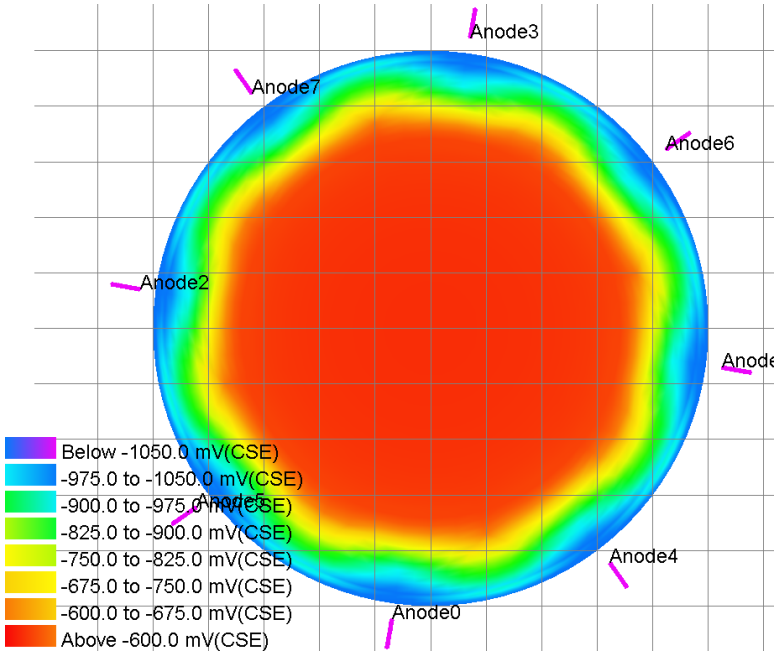

Figure 12-11: Potential distribution with distributed anodes, underlying insulating layer at 2 ft and uniform oxygen concentration profile. The distribution is the worst of all the examples even though all examples have the same total current being driven to the tank bottom. The center of the tank is polarized -13 mV from the corrosion potential.

tank. As might be expected the situation is worse than if the insulating layer did not exist. The reason to expect poorer performance is that there are significantly fewer current paths from the anode to the center of the tank due to the narrow layer of soil in which the current must flow. There should also then be an increase in the current density at the edge of the tank.

Figure 12-11 shows the potential distribution for a tank protected in such a manner. The center of the tank was polarized only -13 mV from the corrosion potential which is about 25% less than the case without the insulating cache basin. Therefore, intuition has served well. The current density at the center of the tank was 15% less than when there was no cache.

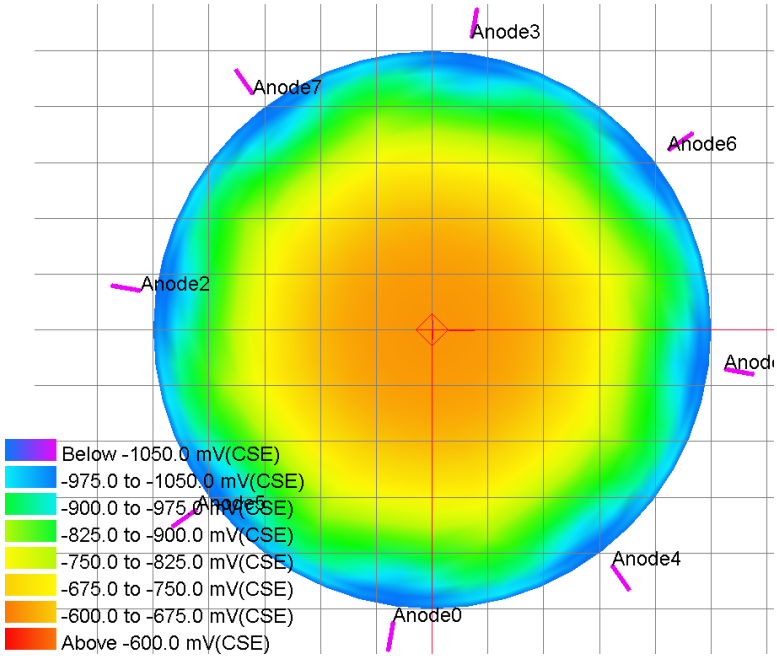

Figure 12-12: Potential distribution with distributed anodes, underlying insulating layer at 2 ft and nonuniform oxygen concentration profile. The center of the tank is polarized -80 mV from the corrosion potential.

Underlying Insulating Layer with Nonuniform Oxygen Distribution When the oxygen at the center of the tank has been consumed, the polarization improves significantly, but not to a required level. The center of the tank was only polarized by -80 mV. The remote groundbed with no cache basin was able to polarize the center of the tank by -350 mV. The potential distribution is shown in Figure 12-12. Again, the current density distribution was nearly identical for the two cases with an insulating cache liner.

12.4.3 Ribbon Anodes

A third method of applying cathodic protection is to use ribbon anodes placed very close to the tank-bottom. The ribbon configuration can yield a more uniform current distribution. Two anode arrangements were used for the evaluation of

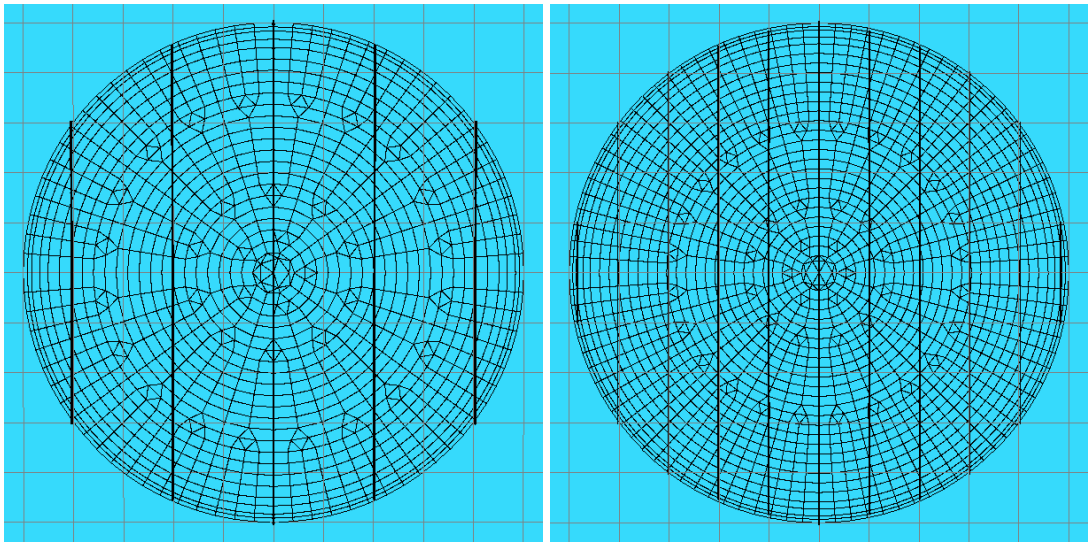

(a) Mesh for 5 Ribbons (b) Mesh for 11 Ribbons

Figure 12-13: Tank bottom with 5 and 11 parallel impressed current anodes. The gray grid lines are on 10 ft intervals. The tank with 5 anodes uses 4 inch diameter anodes and the one with eleven uses 1 inch diameter ribbons. The mesh for the tank with 11 ribbons is more refined.

ribbons. The first used 5 parallel impressed current ribbons of 4 inch diameter, the second used 11 1 inch anodes in a similar configuration. The setup for the two cases is shown in Figure 12-13.

The mesh for the tank that had 11 anodes was made to be finer than the one which had 5 anodes. A finer mesh was used to provide a reasonable level of detail with the more closely spaced anodes, since there would not even be an axi-periodic distribution seen with the distributed anodes. The anodes were assumed to be cylindrical and were discretized in both the axial and angular directions. The angular discretization could then account for the nonuniform current and potential distribution due to the proximity of the tank.

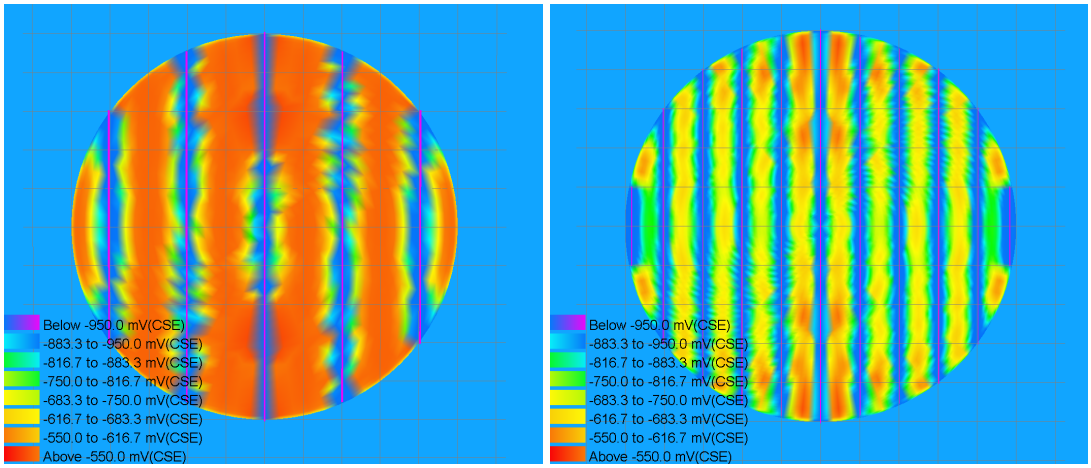

(a) 5 Ribbons (b) 11 Ribbons

Figure 12-14: Potential distribution for tank bottoms with 5 and 11 parallel impressed current anodes with secondary containment. The gray grid lines are on 10 ft intervals. Peak corrosion rate for tank with 5 anodes is an order of magnitude higher than that of the tank with 11 anodes. Total current driven to tank is 14.2 Amps for both cases.

Uniform Oxygen Distribution with Insulating Cache Basin For both anode design cases, the total current output to the tank bottom was adjusted to 14.2 Amps. The potential distributions for the two systems are shown in Figure 12-14. The peak corrosion current for the tank with 5 anodes was 1.6 μA/cm^2. This large value, higher than could be expected from oxygen reduction alone, was due to galvanic coupling between the highly polarized metal that is very close to an anode and the poorly polarized metal between the anodes. Poorly polarized regions are shown in red in Figure 12.14(a) and highly polarized regions are colored in blue. The same color scheme and scale are used in Figure 12.14(b). Here the potential distribution was much better, but not yet optimal, even though the anode surface area was half that of the example with 5 anodes. The anode-to-anode

distance was cut in half with the 11 anode system. The result is that 25% smaller driving force was needed to drive the same amount of current to the tank bottom, even with the reduced area of the anodes.

Uniform Oxygen Distribution without Insulating Cache Basin When the insulating cache basin was removed, some unexpected phenomena were observed while adjusting the impressed current setting in order to drive 14.2 Amps to the tank surface. It was estimated that roughly the same driving force would be required to achieve the same current levels as was used for the cases using the insulating cache. It was found, instead, that a substantial increase in driving force was needed to obtain the same total current. To understand why there is such a large disparity between the two systems, even though the anodes are identical, it helps to look at the current density distribution along the length of the anodes. The axial current density distribution for the long center anode for both the 5 and 11 anode cases is shown in Figure 12-15. In both cases, when there is no electrical insulator under the the anodes, most of the current comes from either end. The effect of more nonuniform current density distribution is to require a great deal more voltage to drive the same total current.

The current density and corrosion current distribution for the worst case of the 5 ribbons is shown in Figure 12-16 The largest corrosion current is next to the long center ribbon at either end. There is evidence of galvanic coupling about two-thirds of the distance from the center of the tank to the edge. The corrosion current density is about 2 μA/cm^2 which is double the rate due to general corrosion.

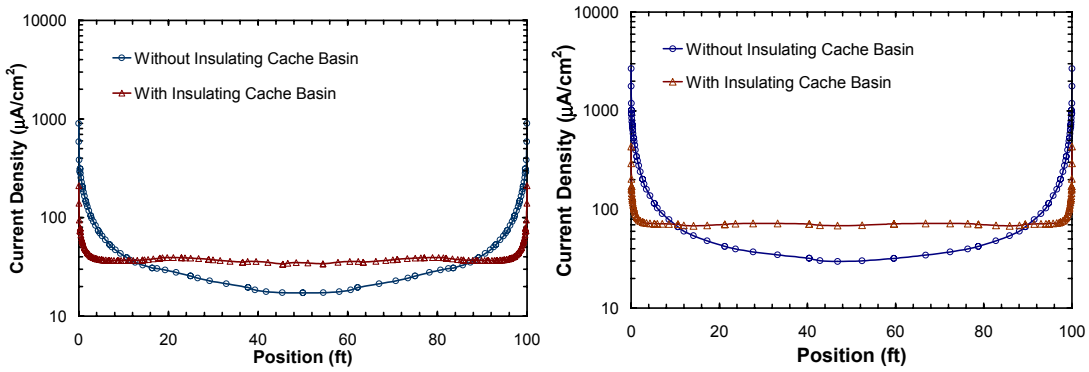

(a) 5 Ribbons

(b) 11 Ribbons

Figure 12-15: Axial current density distributions on anodes for both the 5 and 11 anode cases. For each case, the current density distribution is plotted for the situations of having an insulating cache basin and only having conductive soil under the tank.

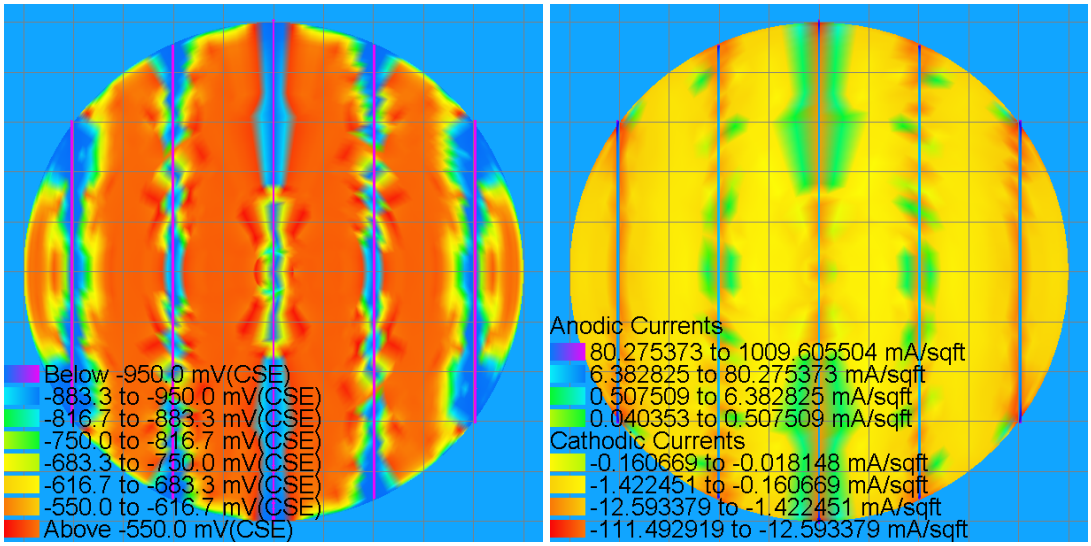

(a) 5 Ribbons

(b) 5 Ribbons (Corrosion current)

Figure 12-16: Potential and corrosion current distribution for tank bottoms with 5 parallel impressed current anodes with no secondary containment. The gray grid lines are on 10 ft intervals. Total current driven to tank is 14.2 Amps. There are significantly more anodic sections in this case with 5 anodes than for the case with an insulating cache basin.

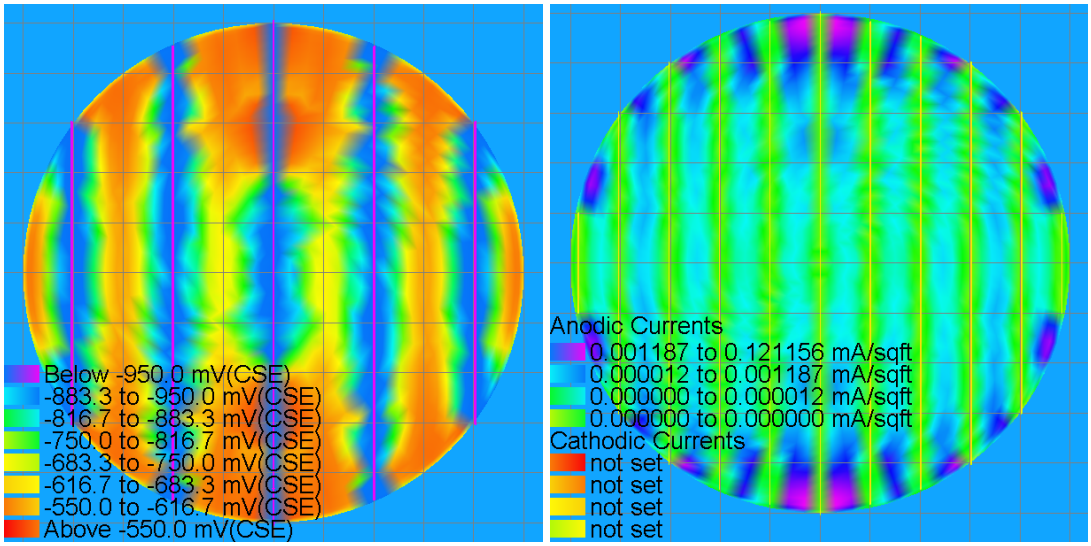

(a) 5 Ribbons (b) 11 Ribbons

Figure 12-17: Potential distribution for tank bottoms with 5 and 11 parallel impressed current anodes and secondary containment with nonuniform oxygen distribution. The gray grid lines are on 10 ft intervals. Total current driven to tank is 14.2 Amps for both cases. Center of tank is more polarized than in the case shown in Figure 12-14

Nonuniform Oxygen Distribution with Insulating Cache Basin The case of a nonuniform oxygen concentration profile was modeled for both the 5 and 11 anode CP systems. The anodes were again adjusted such that the total output was 14.2 Amps. The potential distributions are shown in Figure 12-17. As expected, the center of the tank was polarized to a more negative potential then that shown in Figure 12-14. The current distribution was nearly identical to that of the uniform oxygen case.

Nonuniform Oxygen Distribution without Insulating Cache Basin The last case involved removing the restriction of the underlying insulating cache. The

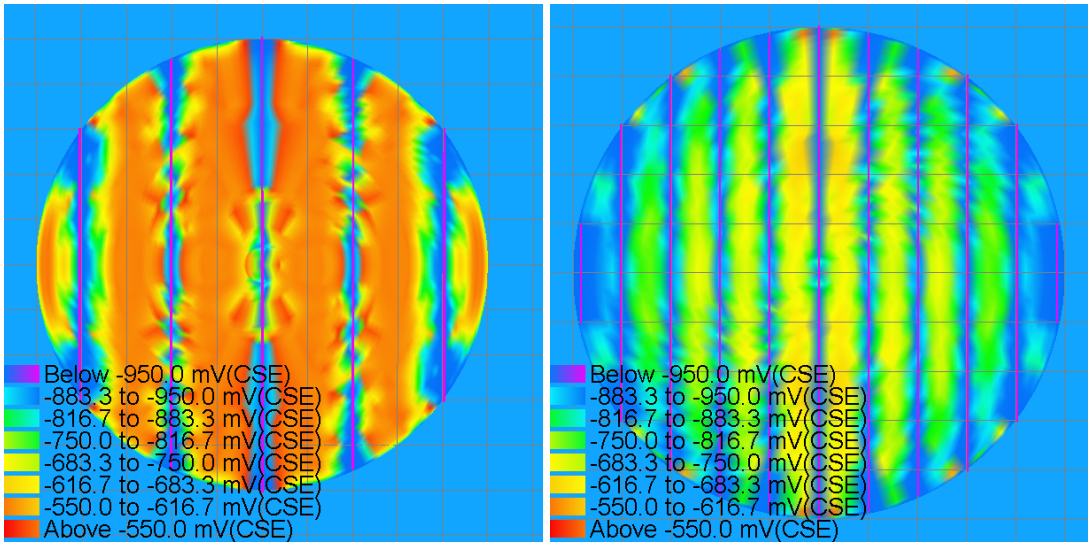

(a) 5 Ribbons (b) 11 Ribbons

Figure 12-18: Potential distribution for tank bottoms with 5 and 11 parallel impressed current anodes and no secondary containment with nonuniform oxygen distribution. The gray grid lines are on 10 ft intervals. Total current driven to tank is 14.2 Amps for both cases.

potential distribution is shown in Figure 12-18. In this case, the center of the tank was not as well polarized as in the case where the cache basin is present. Again, the absence of a catch basin caused a more nonuniform current distribution on the anodes. The current density was much lower at the centers of the anodes than it was with the cache membrane present. To compensate, the current density was higher at the ends of the anodes which, then, promoted a larger current density at the edge of the tank. The current was better distributed than when remote or distributed groundbeds were used.

Use of larger numbers of ribbons also served to improve the current distribution for all cases where ribbons were used. If the spacing was too large, there was a possibility of galvanic coupling between the sections of the tank that were more

polarized directly above the anodes and sections in between the anodes. For the 100-ft diameter tank bottom used in the examples, it appears that a 10-ft spacing between parallel ribbons represents an upper bound.

12.5 Conclusions

Even under the best of situations, it is very difficult to provide cathodic protection to the centers of tank bottoms. If remote anodes or anodes distributed around the circumference of the tank are used for protection, the best that can be hoped for is a current distribution that approaches the primary as given in equation (7-1). In the case of distributed anodes around the perimeter, the situation is much worse than for the remote ground-bed. Because of the proximity of the anodes to the outside edge of the tank, most of the current goes to polarizing the edge of the tank.

The only solution that can work is to place anodes directly under very close to the steel they are to protect. Design of such systems is required. If the spacing between anodes is too great, anodic regions can form on the steel between the anodes. The goal should also be to provide the largest amount of anode surface area possible to reduce to driving force needed to supply a sufficient total current to the tank. With a smaller driving force, there is significantly less likelihood of anodic regions forming on the tank bottom steel.

Cyclic oxygen concentration gradients along the tank bottom due to periodic emptying and filling of the tank can cause periodic over- and under-protection. Therefore, it may be important to include reference electrodes in the design of the CP system to monitor the polarization of the steel.

The location of the reference electrode is very dependent on the design of the CP system. If the design uses remote ground-beds, or a distributed ground-bed around the circumference of the tank, is is most important to monitor the center of the tank. Other design require modeling of the design to determine optimal locations. As shown in Figure 12-14 the optimal location is not at the center of the tank but near the longest ribbon about 3/4 of the distance from the center to the edge of the tank.

When a nonuniform oxygen distribution occurs, the parallel ribbon type anode system cannot be adjusted at the center of the tank. A high level of polarization occurs at the center because of the lack of controlability. A new design for the anode layout has been proposed by Koszewski.[118] The arrangement consists of individually controlled concentric ring anodes. Unfortunately, the model does not have the ability to create curved anodes.

In the end, it was quite by accident that the best means of properly protecting a tank bottom was found. By restricting the current paths, the lining plays an active role in cathodic protection design and forces a more uniform current distribution on the tank bottom. The requirement of the Environmental Protection Agency that all new tanks have secondary containment was designed to contain spills, but may have also resulted in an optimal CP design.[125]

CHAPTER 13
MULTIPLE SOIL DOMAINS

One of the assumptions made in deriving the governing differential equations in Chapter 2, was that the ionic strength of the electrolyte within the domain was constant. Many times, however, it may be desirable to relax that restriction. Changes in soil resistivity may need to be considered, for example, at a river crossing where a pipe passes through a section of water saturated soil.

Greens function solutions for these types of problems are very difficult to obtain. There have been some solutions reported[61] for the case when the conductivity is a linearly varying function in only one of the three dimensions. However, to use this solution, a region of constant conductivity must be placed on either side of the region with the linear variation. If one does not do this, then one end of the region will have a negative conductivity which has no physical meaning while the extreme other end will have near superconducting characteristics. If a Green's function cannot be used, the only alternative for the boundary element method is to divide the domain into regions. At the point of division between regions, a mesh must be created which adds to the computational load.

13.1 Continuity Equations

Often, such as at river crossings, the change in soil conductivity is abrupt and can be modeled as a plane. Figure 13-1 shows how the division must be modeled using the boundary element method. The point of the change in soil properties is

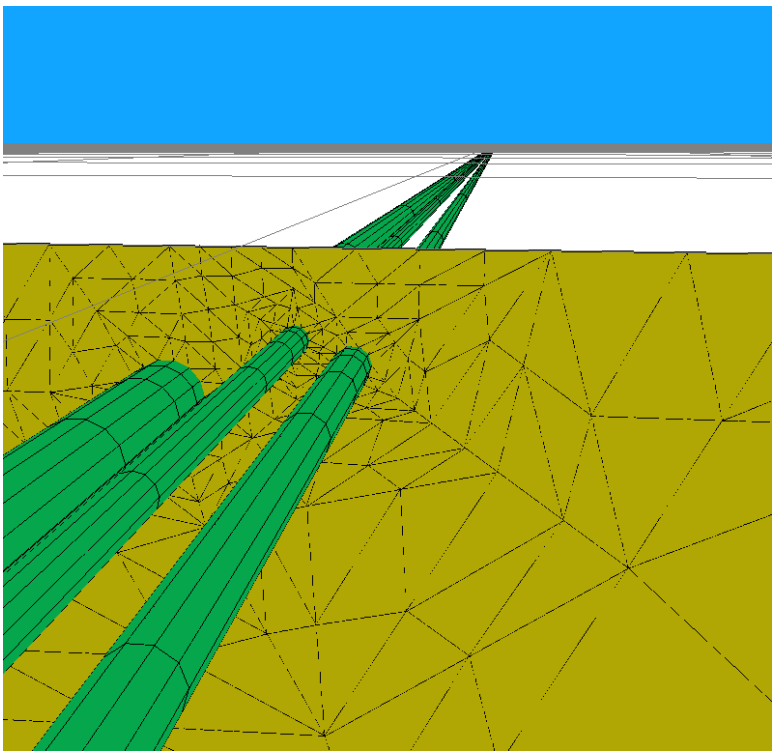

Figure 13-1: Plane meshed for a soil type change. Three pipes are shown passing through a point where the soil conductivity changes.

assumed to be a plane. The plane is then meshed since it is a boundary between two domains of constant conductivity. The two domains must then be coupled together through the common boundary of the mesh at the soil type division. If steady state is assumed, then there can be now accumulation of charge on any arbitrary plane within a domain governed by Laplace's equation.[68] Therefore, the continuity of current through the plane is given by

$$\kappa_I \left(\vec{n} \cdot \nabla \Phi_I\right) = -\kappa_{II} \left(\vec{n} \cdot \nabla \Phi_{II}\right) \tag{13-1}$$

where κ is the soil conductivity, $\vec{n}$ is the normal vector, and Φ is the potential on either side of the division. The reason for allowing separate values of potential on either side of the division is due to a phenomenon known as the liquid junction potential.[12] A liquid junction potential arises when there is a difference in ionic strength at either side of a junction and a difference in diffusion coefficients between the anions and cations. The change in potential can be calculated through the Henderson formula if the concentrations and diffusion coefficients for all the charged species are known. The continuity condition at the soil division becomes

$$\Phi_I = \Phi_{II} + \Phi_{\mathrm{LJ}} \tag{13-2}$$

where Φ_{LJ} is the liquid junction potential. Careful attention must be paid to the sign of the liquid junction potential.

13.2 Implementation

Soil divisions are implemented within the boundary element method only. Laplace's equation is written for each domain which is now bounded by the soil

surface (see section 3.5), and one or two soil type division half-planes. Then a set of algebraic equations from equation (4-1) can be written for for the first domain

$$\begin{bmatrix} \boldsymbol{H}_{j,j} & \boldsymbol{H}_{j,i} \\ \boldsymbol{H}_{i,j} & \boldsymbol{H}_{i,i} \end{bmatrix} \begin{bmatrix} \Phi_j \\ \Phi_i \end{bmatrix} = \begin{bmatrix} \boldsymbol{G}_{j,j} & \boldsymbol{G}_{j,i} \\ \boldsymbol{G}_{i,j} & \boldsymbol{G}_{i,i} \end{bmatrix} \begin{bmatrix} \vec{n} \cdot \nabla \Phi_j \\ \vec{n} \cdot \nabla \Phi_i \end{bmatrix} \tag{13-3}$$

where i represents nodes and elements on the soil division interface and j is for all other nodes and elements within the domain. The second domain would be written as

$$\begin{bmatrix} \boldsymbol{H}_{i,i} & \boldsymbol{H}_{i,k} \\ \boldsymbol{H}_{k,i} & \boldsymbol{H}_{k,k} \end{bmatrix} \begin{bmatrix} \Phi_i \\ \Phi_k \end{bmatrix} = \begin{bmatrix} \boldsymbol{G}_{i,i} & \boldsymbol{G}_{i,k} \\ \boldsymbol{G}_{k,i} & \boldsymbol{G}_{k,k} \end{bmatrix} \begin{bmatrix} \vec{n} \cdot \nabla \Phi_i \\ \vec{n} \cdot \nabla \Phi_k \end{bmatrix} \tag{13-4}$$

where i again represents nodes and elements on the same boundary as in equation (13-3) and k represents all nodes and elements not on the domain boundary and within domain two. Applying the continuity conditions from equations (13-1) and (13-2) results in

$$\begin{bmatrix} \boldsymbol{H}_{j,j} & \boldsymbol{H}_{j,i} & 0 \\ \boldsymbol{H}_{i,j} & \boldsymbol{H}_{i,i,1} + \boldsymbol{H}_{i,i,2} & \boldsymbol{H}_{i,k} \\ 0 & \boldsymbol{H}_{k,i} & \boldsymbol{H}_{k,k} \end{bmatrix} \begin{bmatrix} \Phi_j \\ \Phi_i \\ \Phi_k \end{bmatrix} =$$

$$\begin{bmatrix} \boldsymbol{G}_{j,j} & \boldsymbol{G}_{j,i} & 0 & 0 \\ \boldsymbol{G}_{j,j} & \boldsymbol{G}_{i,i,1} - \frac{\kappa_1}{\kappa_2}\boldsymbol{G}_{i,i,1} & \boldsymbol{G}_{i,k} & -\sum \boldsymbol{H}_{i,i,2} \\ 0 & -\frac{\kappa_1}{\kappa_2}\boldsymbol{G}_{k,i} & \boldsymbol{G}_{k,k} & 0 \end{bmatrix} \begin{bmatrix} \vec{n} \cdot \nabla \Phi_j \\ \vec{n} \cdot \nabla \Phi_i \\ \vec{n} \cdot \nabla \Phi_k \\ \Phi_{\mathrm{LJ},1-2} \end{bmatrix} \tag{13-5}$$

where the subscripts 1 and 2 refer the the domain the matrix elements come from and $\Phi_{\mathrm{LJ},1-2}$ comes from the liquid junction potential between domains 1 and 2 calculated using the Henderson formula. If there are n domains in the problem

then $n-1$ extra columns are added to the right-hand matrix to account for liquid junction potentials.

13.3 Steel Resistance in Multiple Soil Domains

The equations for the conduction of current through the pipe steel, bonds and anodes is solved exactly the same as described in section 3.7. The only caveat is that there are no entries in the finite element matrices for the soil domain divisions since they are not part of the steel domain where the FEM is applied. Again, the variable transformation described in section 4.9 is used to obtain

$$\begin{bmatrix} 0 & 0 & \boldsymbol{H}_{j,j} & \boldsymbol{H}_{j,i} & 0 & -4\pi \\ 0 & 0 & \boldsymbol{H}_{i,j} & \boldsymbol{H}_{i,i,1}+\boldsymbol{H}_{i,i,2} & \boldsymbol{H}_{i,k} & -4\pi \\ 0 & 0 & 0 & \boldsymbol{H}_{k,i} & \boldsymbol{H}_{k,k} & -4\pi \\ \boldsymbol{K}_j & 0 & \boldsymbol{K}_j & 0 & 0 & 0 \\ 0 & \boldsymbol{K}_k & 0 & 0 & \boldsymbol{K}_k & 0 \\ 0 & 0 & 0 & 0 & 0 & 0 \end{bmatrix} \begin{bmatrix} \Psi_j \\ \Psi_k \\ \Phi_j \\ \Phi_i \\ \Phi_k \\ \Phi_\infty \end{bmatrix} = \begin{bmatrix} \boldsymbol{G}_{j,j} & \boldsymbol{G}_{j,i} & 0 & 0 \\ \boldsymbol{G}_{j,j} & \boldsymbol{G}_{i,i,1}-\frac{\kappa_1}{\kappa_2}\boldsymbol{G}_{i,i,1} & \boldsymbol{G}_{i,k} & -\sum \boldsymbol{H}_{i,i,2} \\ 0 & -\frac{\kappa_1}{\kappa_2}\boldsymbol{G}_{k,i} & \boldsymbol{G}_{k,k} & 0 \\ \hat{\boldsymbol{F}}_j & 0 & 0 & 0 \\ 0 & 0 & \hat{\boldsymbol{F}}_k & 0 \\ A_j & 0 & A_k & 0 \end{bmatrix} \begin{bmatrix} \vec{n}\cdot\nabla\Phi_j \\ \vec{n}\cdot\nabla\Phi_i \\ \vec{n}\cdot\nabla\Phi_k \\ \Phi_{\mathrm{LJ},1-2} \end{bmatrix} \tag{13-6}$$

Many domains can be strung together using the above method. Figure 13-2 shows how the mesh for a system with two soil divisions and therefore three different soil types. This model setup may be appropriate for a situation where

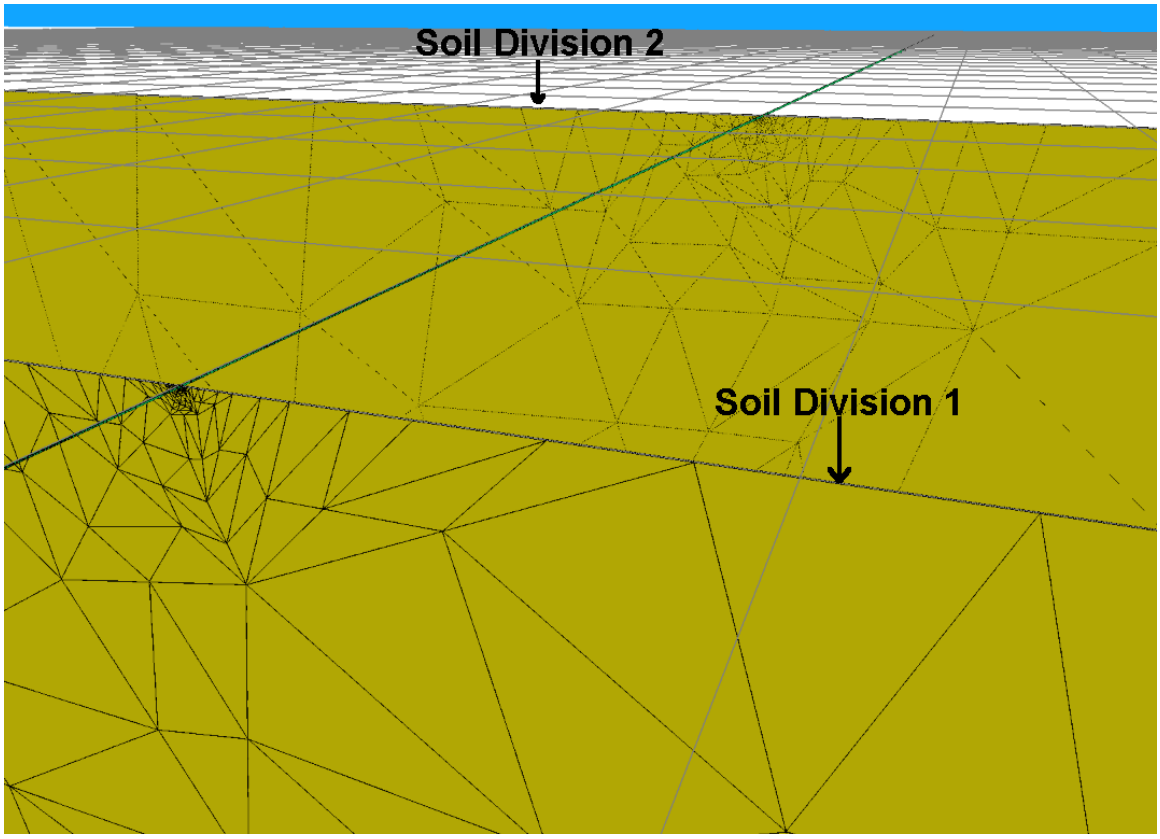

Figure 13-2: Three domain model setup utilizing two soil division meshes. The soil surface grid is drawn using 1 mile squares. There are two pipes of 24 in diameter in a 50 ft right-of-way.

two pipes are passing through a river bottom where the saturated section of soil is 5 miles wide. The system of equations would be assembled in a similar manner as in equation (13-6).

Equation (13-6) is solved using the same techniques as described in sections 4.5 and 4.9, following the procedure outlined in Figure 4-1. Sparse techniques can

be used to solve equation (13-6) if the variables are reordered to

$$\begin{bmatrix} \boldsymbol{H}_{j,j} & \boldsymbol{H}_{j,i} & 0 & 0 & 0 & -4\pi \\ \boldsymbol{H}_{i,j} & \boldsymbol{H}_{i,i,1}+\boldsymbol{H}_{i,i,2} & \boldsymbol{H}_{i,k} & 0 & 0 & -4\pi \\ 0 & \boldsymbol{H}_{k,i} & \boldsymbol{H}_{k,k} & 0 & 0 & -4\pi \\ \boldsymbol{K}_j & 0 & 0 & \boldsymbol{K}_j & 0 & 0 \\ 0 & 0 & \boldsymbol{K}_k & 0 & \boldsymbol{K}_k & 0 \\ 0 & 0 & 0 & 0 & 0 & 0 \end{bmatrix} \begin{bmatrix} \Phi_j \\ \Phi_i \\ \Phi_k \\ \Psi_j \\ \Psi_k \\ \Phi_\infty \end{bmatrix} =$$

$$\begin{bmatrix} \boldsymbol{G}_{j,j} & \boldsymbol{G}_{j,i} & 0 & 0 \\ \boldsymbol{G}_{j,j} & \boldsymbol{G}_{i,i,1}-\frac{\kappa_1}{\kappa_2}\boldsymbol{G}_{i,i,1} & \boldsymbol{G}_{i,k} & -\sum \boldsymbol{H}_{i,i,2} \\ 0 & -\frac{\kappa_1}{\kappa_2}\boldsymbol{G}_{k,i} & \boldsymbol{G}_{k,k} & 0 \\ \hat{\boldsymbol{F}}_j & 0 & 0 & 0 \\ 0 & 0 & \hat{\boldsymbol{F}}_k & 0 \\ A_j & 0 & A_k & 0 \end{bmatrix} \begin{bmatrix} \vec{n}\cdot\nabla\Phi_j \\ \vec{n}\cdot\nabla\Phi_i \\ \vec{n}\cdot\nabla\Phi_k \\ \Phi_{\mathrm{LJ},1-2} \end{bmatrix} \tag{13-7}$$

Sparse techniques cannot usually be used with mixed boundary condition problems under the formulation shown in equation (13-7). After all of the unknown boundary conditions are moved to the left-hand-side, many elements in the the 0 submatrices above the $\boldsymbol{K}$ submatrices are filled with $\boldsymbol{G}$ submatrices. When nonlinear boundary conditions are used, many of the remaining terms with zeros in the upper triangle above the $\boldsymbol{K}$ submatrices are filled with terms from the partial derivatives of the boundary conditions when the Newton-Raphson technique is implemented. The resulting matrices will not be sparse.

CHAPTER 14
CONCLUSIONS AND FUTURE WORK

14.1 Conclusions

Buried pipelines carry most of the United States' natural gas and petroleum products from wells to refineries and to final consumption points. All of the pipes are subject to corrosion and therefore have cathodic protection systems to protect them. To reduce the amount of current required to protect the pipes, high-resistivity coatings have been applied to the pipes. Coating defects expose portions of bare steel to the soil environment, and cathodic protection is consequently employed as a secondary measure. New mathematical models are required because the standard design equations cannot account for the behavior of the cathodic protection system when coating defects are present. The design of cathodic protection systems has been further complicated as demand has increased because new pipes have been placed next to old pipes in the same right-of-ways.

A numerical model has been developed to address the need to understand how cathodic protection systems behave in the complicated installations found today. New methods for treating the coating have been developed to predict more accurately the protection levels of coated pipes with holidays. Complete axial and angular current density and potential distributions can now be calculated for complicated pipeline networks.

Interactions between pipes with coating holidays have been shown in Chapter 10. Coating holidays produce a substantial "shadowing" effect on neighboring pipes.

It has been shown that the model can easily be extended to geometries other than pipes through the investigation of cathodic protection of tank bottoms. Through the investigation, it was shown how a fundamental understanding of potential and current distributions can influence the design of CP systems.

14.2 Future Work

The largest weakness of the model is the lack of good polarization data for both the bare and coated steel. Polarization parameters are strong functions of steel composition and pre-treatments, soil environment, time, and history. Ken Jeffers introduced a technique that could be used to provide high-quality, time-dependent parameters for the polarization curves.[41]

Incorporation of time-dependent polarization curves requires that the model be modified to integrate the time evolution of the system. Because the boundary conditions are time-dependent, additional derivations are needed. One attempt has been made by Santiago and Telles.[126, 127] They incorporated the time-dependent polarization curves for sea-water proposed by Nisancioglu.[20] Steve Carson has provided data for a similar formulation of the polarization curves for pipes in soil environments.[128]

The model can be easily extended to other applications. For example, ship hulls can be treated in a similar manner as pipes. The major modification needed is to provide a means to mesh the geometry of the hull and propellers, and to

provide polarization curves for the metals used in their construction. Wells could also be treated if a technique is available to account for the multiple soil layers the well passes though. One method may be to use the techniques described in Chapter 13. The domain divisions normal to the soil surface would be replaced by divisions parallel to the soil surface.

Cathodic protection of the interior of pipes, storage tanks, reactor vessels, heat exchangers can also be treated with some simple changes to the formulation. In all cases, high-quality polarization data would be needed for the specific environments.

APPENDIX A
PARTIAL DERIVATIVES OF THE BOUNDARY CONDITIONS

When solving the system of nonlinear equations that result from the boundary element method, the linearization process requires partial derivatives of the boundary conditions for each of the independent variables. Using the equation for bare metal

$$i = 10^{\frac{V-\Phi-E_{\mathrm{Fe}}}{\beta_{\mathrm{Fe}}}} - \left(\frac{1}{i_{\mathrm{lim},\mathrm{O}_2}} + 10^{\frac{V-\Phi-E_{\mathrm{O}_2}}{\beta_{\mathrm{O}_2}}}\right)^{-1} - 10^{\frac{-(V-\Phi-E_{\mathrm{H}_2})}{\beta_{\mathrm{H}_2}}} \tag{A-1}$$

where the variables are defined as in section 1.4, partial derivatives are needed with respect to V and Φ. They are

$$\begin{aligned}\frac{\partial i}{\partial V} &= \frac{\ln(10)}{\beta_{\mathrm{Fe}}}10^{\frac{V-\Phi-E_{\mathrm{Fe}}}{\beta_{\mathrm{Fe}}}} + \frac{\ln(10)}{\beta_{\mathrm{O}_2}}10^{\frac{V-\Phi-E_{\mathrm{O}_2}}{\beta_{\mathrm{O}_2}}}\left(\frac{1}{i_{\mathrm{lim},\mathrm{O}_2}} + 10^{\frac{V-\Phi-E_{\mathrm{O}_2}}{\beta_{\mathrm{O}_2}}}\right)^{-2} \\ &\quad + \frac{\ln(10)}{\beta_{\mathrm{H}_2}}10^{\frac{-(V-\Phi-E_{\mathrm{H}_2})}{\beta_{\mathrm{H}_2}}}\end{aligned} \tag{A-2}$$

and for Φ

$$\begin{aligned}\frac{\partial i}{\partial \Phi} &= -\frac{\ln(10)}{\beta_{\mathrm{Fe}}}10^{\frac{V-\Phi-E_{\mathrm{Fe}}}{\beta_{\mathrm{Fe}}}} - \frac{\ln(10)}{\beta_{\mathrm{O}_2}}10^{\frac{V-\Phi-E_{\mathrm{O}_2}}{\beta_{\mathrm{O}_2}}}\left(\frac{1}{i_{\mathrm{lim},\mathrm{O}_2}} + 10^{\frac{V-\Phi-E_{\mathrm{O}_2}}{\beta_{\mathrm{O}_2}}}\right)^{-2} \\ &\quad - \frac{\ln(10)}{\beta_{\mathrm{H}_2}}10^{\frac{-(V-\Phi-E_{\mathrm{H}_2})}{\beta_{\mathrm{H}_2}}}\end{aligned} \tag{A-3}$$

The equation for coatings as given in section 1.6 is more complicated. Equation (1-26) is really the sum of two equation eliminating i. The original two equations are

$$\begin{aligned}i &= \frac{A_{\mathrm{pore}}}{A}\left[10^{\frac{V-\Phi_{\mathrm{in}}-E_{\mathrm{Fe}}}{\beta_{\mathrm{Fe}}}}\right. \\ &\quad \left. - \left(\frac{1}{(1-\alpha_{\mathrm{block}})\,i_{\mathrm{lim},\mathrm{O}_2}} - 10^{\frac{V-\Phi_{\mathrm{in}}-E_{\mathrm{O}_2}}{\beta_{\mathrm{O}_2}}}\right)^{-1} - 10^{\frac{-\left(V-\Phi_{in}-E_{\mathrm{H}_2}\right)}{\beta_{\mathrm{H}_2}}}\right]\end{aligned} \tag{A-4}$$

and an IR drop

$$i = \frac{\Phi - \Phi_{\text{in}}}{\rho_{\text{film}} \delta_{\text{film}}} \tag{A-5}$$

Equations (A-4) and (A-5) are solved simultaneously to get the current density $\boldsymbol{i}$ using a Newton-Ralphson technique. The partial derivatives

$$\frac{\partial \boldsymbol{i}}{\partial \Phi} \tag{A-6}$$

and

$$\frac{\partial \boldsymbol{i}}{\partial V} \tag{A-7}$$

are obtained numerically.

Numerical differentiation is done with a central difference formula

$$\frac{\partial \boldsymbol{i}}{\partial \Phi} = \frac{\boldsymbol{i}(\Phi + h, V) - \boldsymbol{i}(\Phi + h, V)}{2h} \tag{A-8}$$

where h is a small number. The size of h must be carefully chosen such that $\boldsymbol{i}(\Phi + h, V) - \boldsymbol{i}(\Phi + h, V)$ is not equal to zero because h is smaller than the noise due to finite machine precision and $\boldsymbol{i}(\Phi + h, V) - \boldsymbol{i}(\Phi + h, V)$ does not straddle large variations in the function. The value of h is selected based on the magnitude of the variable it is modifying, *i.e.,* Φ. The value of the machine ϵ, the smallest number added to 1 such that the result is different than 1, is used to find h according to

$$h = \max(\Phi, 1.0)\sqrt{\epsilon} \tag{A-9}$$

In general, Φ is on the order of 1 Volt.

APPENDIX B
OpenGL CODE

OpenGL®* was used for the rendering of graphics for the model.[102] The drawing commands are platform independent, so code that utilizes OpenGL can easily be ported across different platforms. The only caveat is that the OpenGL device setup is not platform independent. The reason is that windows are created in different ways depending on the platform, *i.e.,* XWindows, Macintosh,† Windows NT,‡ Iris,§ Solaris,¶ AIX,‖ etc. Therefore, a small subset of code written by the operating system manufacturer must be used to initialize the OpenGL device.

B.1 The OpenGL Device

The OpenGL device on the Windows NT platform must be created and attached to a window before any drawing commands are issued. The device is created during the window creation subroutine. As soon as the operating system has created a generic window, a Pixelformat is specified for the OpenGL device based of the capabilities of the window. Once the the Pixelformat has been successfully chosen, the rendering device is created and attached to the window

*OpenGL is a registered trademark of Silicon Graphics, Inc.

†Macintosh is a registered trademark of Apple Computers, Inc.

‡Windows NT is a registered trademark of Microsoft Corp.

§Iris is a registered trademark of Silicon Graphics, Inc.

¶Solaris is a registered trademark of Sun Microsystems, Inc.

‖AIX is a registered trademark of IBM, Inc.

through the `wglCreateContext` command. Since only a single OpenGL context may be active at any given time, a command is given to the new context to make it the current one. The command must be issued every time a drawing cycle begins. Source listing B.1 contains the code used to set up the OpenGL device for the model.

Source Listing B.1: OpenGL window setup code.

```
int CObjView::OnCreate(LPCREATESTRUCT lpCreateStruct)
{
  // create the window
  if (CView::OnCreate(lpCreateStruct) == -1)
     return -1;

  // get the windows drawing device
  m_pDC=GetDC();

  // get pixel formats
  PIXELFORMATDESCRIPTOR PixFormat;

  // zero out the pixel format
  memset(&PixFormat, 0, sizeof(PIXELFORMATDESCRIPTOR));

  //set some desired variables
  PixFormat.nSize=sizeof(PIXELFORMATDESCRIPTOR);
  PixFormat.dwFlags=PFD_DRAW_TO_WINDOW |
    PFD_SUPPORT_OPENGL | PFD_DOUBLEBUFFER ;
  PixFormat.nVersion=1;
  PixFormat.iPixelType=PFD_TYPE_RGBA;
  PixFormat.cDepthBits=32; // the z-buffer
  PixFormat.iLayerType=PFD_MAIN_PLANE;
  // now choose the nearest format to the
  // above modification
  int rVal=ChoosePixelFormat(m_pDC->GetSafeHdc(),
    &PixFormat);
  if(rVal==0)
    return -1;

  // now set the pixformat for this view using
  // the just returned index
  if(!SetPixelFormat(GetDC()->GetSafeHdc(), rVal,
    &PixFormat))
```

```
    {
36    // failed to set the pixel format
      AfxMessageBox("Failed to set the pixel
38      format. Be sure that OpenGL is installed");
      return -1;
40    }

42    // check if a 256 color palate must be created
      DescribePixelFormat(m_pDC->GetSafeHdc(), rVal,
44      sizeof(PIXELFORMATDESCRIPTOR), &PixFormat);

46    if(PixFormat.dwFlags & PFD_NEED_PALETTE)
        GetOpenGLPalette();
48
      // now set the rendering context
50    m_hGLRC = wglCreateContext(GetDC()->GetSafeHdc());
      if(m_hGLRC==NULL)
52      return -1;

54    //make it the current context
      if(wglMakeCurrent(GetDC()->GetSafeHdc(),m_hGLRC)==FALSE)
56      return -1;

58    // one time Device setup parameters are also set here

60    // white background
      glClearColor(1.0f,1.0f,1.0f,1.0f);
62    // color properties of materials will be used
      glEnable(GL_COLOR_MATERIAL );
64
      // materials only on front of face, ambient color may change
66    glColorMaterial(GL_FRONT, GL_AMBIENT);

68    glEdgeFlag(TRUE);
      // polygons are numbered counterclockwise
70    glFrontFace(GL_CCW);
      // dont draw faces that face away from the viewer
72    glCullFace(GL_BACK);
      glClearDepth( 1.0 );
74    return 0;
  }
```

Line 4-47 are used to determine the number of colors OpenGL will use. The command to create the device is in line 50.

B.2 The Drawing Cycle

The drawing cycle begins with a message from the operating system or from the interactive code written by the programmer that says something within the window has changed and it needs to be redrawn. The first step is to make the windows OpenGL device the current one so that drawing commands are not sent to the wrong window. Next all the platform independent OpenGL drawing code is called. Finally `SwapBuffers` is called to place all the newly rendered objects into the window. The code below in source listing B.2 demonstrates the procedure.

Source Listing B.2: Draw command called by operating system whenever a window needs updating.

```
void CObjView::OnDraw(CDC* pDC)
{
  // get the size of the window
  CRect rect;
  GetClientRect(&rect);

  // get a handle to the current device so that it
  // can be restored when we are finished
  HDC hOldDC = wglGetCurrentDC();
  HGLRC hOldRC = wglGetCurrentContext();

  // make this windows devide the current device
  wglMakeCurrent( pDC->GetSafeHdc(), m_hGLRC );

  // create the 3-D fonts if they have not been
  CFont *pOldFont=pDC->SelectObject(m_pFont);
  if(m_bBuildFont)
  {
    wglUseFontBitmaps (pDC->GetSafeHdc(), 0, 255, 1000);
    m_bBuildFont=FALSE;
  }
  // Set the pointer to where the fonts are stored
  glListBase (1000);

  // do all the platform independent stuff
```

```
26  DrawRecFace(&rect);

28  // display all the rendered stuff created
    // in the last function
30  SwapBuffers(pDC->GetSafeHdc());
    // restore the old font
32  pDC->SelectObject(pOldFont);
    // restore the old rendering context
34  wglMakeCurrent( hOldDC,hOldRC );
}
```

B.3 Platform Independent Code

The platform independent code is all of the perspective transformation setup, lighting setup and texture setup. First, the perspective transform matrix is created and model view transform matrix are created. Then polygon rendering properties are set. Finally all the objects are asked to draw themselves into the OpenGL device.

Source Listing B.3: Platform independent code to setup to model view and projection transformation matrices.

```
void CObjView::DrawRecFace(CRect *prect)
2 {
  // and the view port to the window size
4 glViewport(0,0,prect->right,prect->bottom);
  // clear the color and the depth
6 glClear(GL_COLOR_BUFFER_BIT | GL_DEPTH_BUFFER_BIT);
  glEnable(GL_DEPTH_TEST);
8
  // set the projection view
10 glMatrixMode(GL_PROJECTION);
  glLoadIdentity();
12 // set clip to one tenth the eye distance and 5 times
  // the largest extent
14 gluPerspective(45.0,aspect,fabs(m_dzTrans)*0.1,5.0*
    pDoc->GetDataSize());
16
  // now translate the view point
18 // switch back to the model geometry stack
```

```
  glMatrixMode(GL_MODELVIEW);

  glLoadIdentity();
  // Position / translation / scale
  // move the eye back from the screen
  glTranslated(0.0,0.0,m_dzTrans);
  // rotate the drawing
  glRotated(m_dxRotation, 1.0, 0.0, 0.0);
  glRotated(m_dyRotation, 0.0, 1.0, 0.0);
  // now change to the z=depth coordinate system
  glMultMatrixd(m_dMatrixCorrd);
  // spot to lookat (world x, y, z corrd)
  glTranslated(m_dxTrans,m_dyTrans,m_dDepthTrans);
  glScaled(m_dScaling,m_dScaling,m_dScaling);

  // set the shade model
  switch(this->RenderStyle())
  {
  case DRAW_MIN_MAX:
  case DRAW_POINTS:
  case DRAW_WIREFRAME:
    glPolygonMode(GL_FRONT_AND_BACK,GL_LINE);
    glShadeModel(GL_FLAT);
    break;
  case DRAW_UNSHADED:
  case DRAW_FLAT_SHADED:
    glShadeModel(GL_FLAT);
    glPolygonMode(GL_FRONT,GL_FILL);
    glPolygonMode(GL_BACK,GL_LINE);
    break;
  case DRAW_SMOOTH_SHADED:
    glPolygonMode(GL_BACK,GL_LINE);
    glPolygonMode(GL_FRONT,GL_FILL);
    glShadeModel(GL_SMOOTH);
    break;
  }
  // Start rendering objects...
  pDoc->RenderScene(this, 0);
}
```

The `RenderScene` command cycles through all of the objects in the model, asking each to draw itself. It also draws reference objects such as the soil surface grid, sky and coordinate system origin marker.

An example piece of C++ code is given below in listing B.4 that draws a set of boundary elements to the OpenGL engine. It is set up to draw a wireframe rendering.

Source Listing B.4: Low level OpenGL code to draw a wireframe rendering of a single object.

```
void CBaseMesh::Render(PARAMS *pParas) {
  int ii, jj;
  // start drawing 4 node faces
  glBegin(GL_QUADS);
  // use black wires for a wire frame
  glColor3f(0.0f,0.0f,0.0f);
  for(ii=0; ii<m_nNumQuadFaces; ii++)
  {
    for(jj=0; jj<4; jj++)
    {
      glVertex3d(m_pNodes[m_pQuadFaces[ii].nPoints[jj]].x,
        m_pNodes[m_pQuadFaces[ii].nPoints[jj]].y,
        m_pNodes[m_pQuadFaces[ii].nPoints[jj]].z);
    }
  }
  glEnd();

  // start drawing 3 node faces
  glBegin(GL_TRIANGLES);
  for(ii=0; ii<m_nNumTriFaces; ii++)
  {
    for(jj=0; jj<3; jj++)
    {
      glVertex3d(m_pNodes[m_pTriFaces[ii].nPoints[jj]].x,
        m_pNodes[m_pTriFaces[ii].nPoints[jj]].y,
        m_pNodes[m_pTriFaces[ii].nPoints[jj]].z);
    }
  }
  glEnd();

  // draw the current vectors on the pipe
  if(pParams->bShowCV)
  {
    for(ii=0; ii<m_nNumCurrentVectors; ii++)
      m_ppvectorCurrents[ii]->Draw();
  }
}
```

As can be seen in listing B.4 lines 11 and 24, the actual boundary element or finite element mesh is used within the OpenGL commands.

B.4 Using the Mouse for Interaction

The mouse is used for much of the interaction with the model. All three buttons and the wheel are used. The middle mouse button is used strictly for OpenGL interactions. It used used to turn and rotate the model, zoom in and out, translate from one position to another, and change the depth the viewer is looking at. Much of the technique used to develop the interaction mechanisms was derived from the book "Interactive 3D Graphics in Windows."[103] Modifications to the techniques have been made to make make them consistent with the OpenGL API and to allow interactions specific to pipeline networks and buried structures.

B.4.1 Orienting an Object

Objects are moved around within the OpenGL window using the mouse. The a program responds to mouse movement and clicks by responding to messages sent from the operating system. There are several different messages depending on the type of mouse action. For each message, there is a corresponding function that is called in response: `OnLButtonDown, OnMButtonDown, OnRButtonDown, OnMouseMove, OnMouseWheel, OnContextMenu, OnLButtonUp, OnMButtonUp, OnRButtonUp, OnLButtonDblClk, OnMButtonDblClk,` and `OnRButtonDblClk`. The three functions used for changing the view of an OpenGL display are `OnMButtonDown, OnMButtonUp, OnMouseMove`. Three commands

are needed since the display should only move while the middle button is held down. The cycle for movement is

1. The user clicks and holds the middle mouse-button (sometimes a wheel) within an OpenGL window.

2. The user moves the mouse while holding the middle mouse button down. The display updates in real time as the mouse is moved. The number of updates of the display is dependent on the display adapter installed.

3. The user releases the middle mouse button.

A movie of the process is given in Figure B-1. The movie shows one of the possible modes of movement known as rotation and orbiting. It also shows how movement can improve the perception of depth.

The code used to accomplish the mouse control of movement utilizes several variables. The first is to set a flag to indicate whether or not the middle mouse button is depressed. It is set in the function `OnMButtonDown`

Source Listing B.5: Code to respond to the middle mouse button being depressed.

```
void CObjView::OnMButtonDown(UINT nFlags, CPoint point)
{
  // set flag that the mouse is depressed
  m_bMButtonDown=TRUE;
  // keep mouse with this program even
  // if the mouse moves outside its window
  SetCapture( );
  // save the point where the mouse is first clicked
  m_ptMDownPos = point;
}
```

The function `SetCapture()` allows the mouse to function within the current program even if the user drags the mouse outside the window for the program.

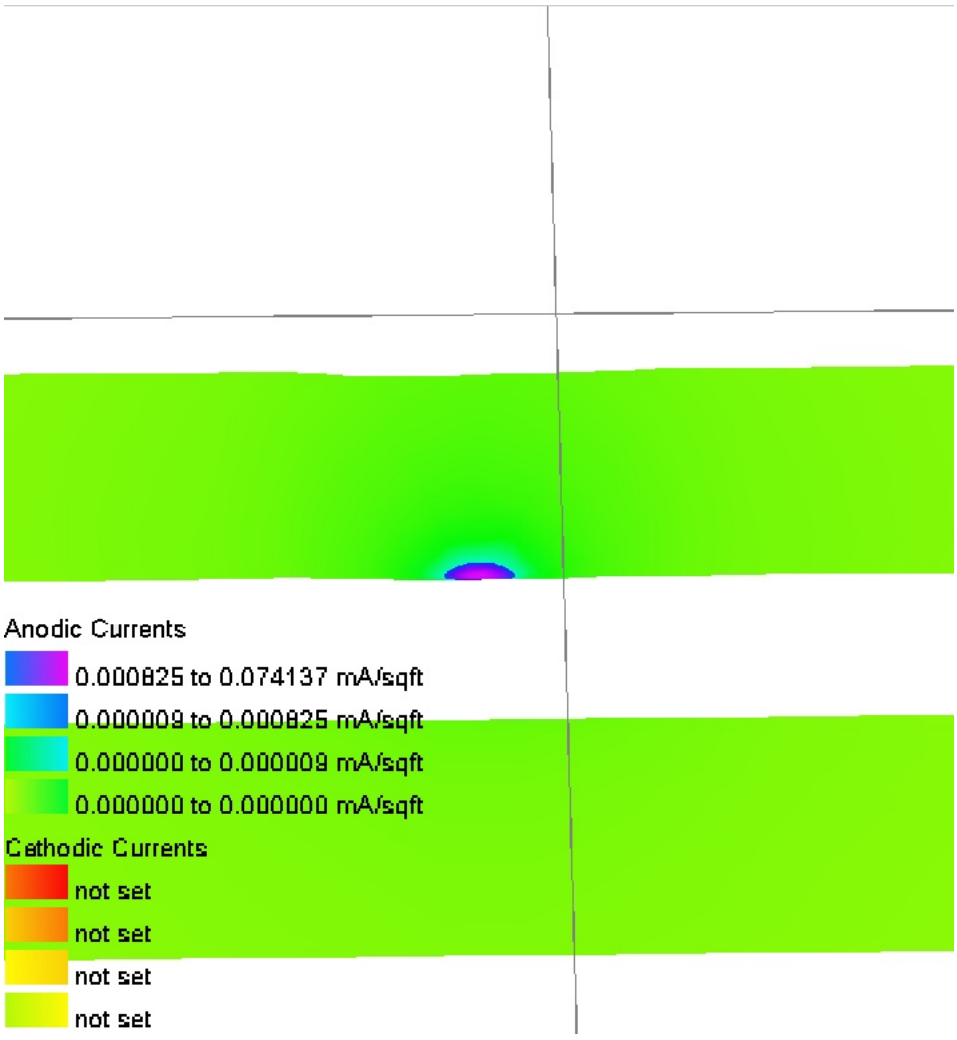

Figure B-1: A movie demonstrating how the user can use the middle mouse button the change the OpenGL view of two pipelines. This is one of the modes of movement. The movie is accessed by clicking on the above image.

The work of changing the appearance of the view window is done in the function `OnMouseMove`.

Source Listing B.6: Code to respond to mouse movement within the OpenGL window.

```
void CObjView::OnMouseMove(UINT nFlags, CPoint point)
{
  CRect rect;
  GetClientRect(&rect);
  // check if a button is depressed
  if(m_bMButtonDown)
  {
    CConView *pView=GetConView();
    // check which type of movement has been desired
    if(m_nMouseMode==0)
    {
      // Zoom mode
      m_dzTrans-=fabs(m_dzTrans)*(m_ptMDownPos.y-
        point.y)/(0.5*rect.bottom);
      if(m_dzTrans>0.0)
        m_dzTrans=-m_dzTrans;
    }
    else if(m_nMouseMode==1)
    {
      // Orbit and rotate mode
      m_dyRotation -= (m_ptMDownPos.x - point.x)/3.0;
      m_dxRotation -= (m_ptMDownPos.y - point.y)/3.0;
      //put limits on the rotation angles
      // or loop back to zero when 360 is exceeded
      if(m_dyRotation>360.0)
        m_dyRotation-=360.0;
      if(m_dyRotation<-360.0)
        m_dyRotation+=360.0;
      if(m_dxRotation>90.0)
        m_dxRotation=90.0;
      if(m_dxRotation<-90.0)
        m_dxRotation=-90.0;
    }
    else if(m_nMouseMode==2)
    {
      // translate across the soil surface
      // going to use both bottom and right member
      // first use x movement on screen to left -right
      // movement of the 3D soil surface
```

```
40      m_dxTrans+=((fabs(m_dzTrans)+1.)*sin((m_dyRotation)*
          PI/180.0)*(m_ptMDownPos.x - point.x)/rect.right);
42      m_dyTrans-=((fabs(m_dzTrans)+1.)*cos((m_dyRotation)*
          PI/180.0)*(m_ptMDownPos.x - point.x)/rect.bottom);
44
        // now up-down movement of the mouse should map to
46      // updown movement of the
        m_dyTrans+=(m_dxRotation<0.0?-1.0:1.0)*
48        ((fabs(m_dzTrans)+1.)*
          sin((m_dyRotation)*PI/180.0)*
50        (m_ptMDownPos.y - point.y)/rect.right);
        m_dxTrans+=(m_dxRotation<0.0?-1.0:1.0)*
52        ((fabs(m_dzTrans)+1.)*
          cos((m_dyRotation)*PI/180.0)*
54        (m_ptMDownPos.y - point.y)/rect.bottom);
      }
56    else
      {
58      // change the depth from the soil surface
        m_dDepthTrans-=(fabs(m_dzTrans)+1.)*(m_ptMDownPos.y-
60        point.y)/(rect.bottom);
      }
62    // save the current mouse position to account for the
      // delta position
64    m_ptMDownPos = point;
      pView->SetFeedBackData(-m_dxTrans, -m_dyTrans,
66      -m_dDepthTrans,m_dzTrans, m_dxRotation, -m_dyRotation);
      // cause the window to be updated with the new position
68    // info (cause an OpenGL draw cycle)
      InvalidateRect(NULL,FALSE);
70  }
    else ...
72 }
```

In the `OnMouseMove` function, the first thing done is a check for which mouse button has been depressed. For the case of the middle mouse button, there are 4 different modes of movement which are specified through the variable `m_nMouseMode`. The subroutine then modifies the values of the appropriate variable depending on the movement mode. Looking at the code for the OpenGL perspective and model view matrix transformations, it can be quickly seen how

modifying each of the variables with the mouse subroutines translates into some sort of movement of the objects being looked at.

Source Listing B.7: Code to change view of objects due to mouse control.

```
void CObjView::DrawRecFace(CRect *prect) {
  ...
  // set the projection view
  glMatrixMode(GL_PROJECTION);
  glLoadIdentity();
  // set clip to one tenth the eye distance and 5 times
  // the largest extent
  gluPerspective(45.0,aspect,fabs(m_dzTrans)*0.1,5.0*
    pDoc->GetDataSize());

  // now translate the view point
  // switch back to the model geometry stack
  glMatrixMode(GL_MODELVIEW);
  glLoadIdentity();
  // Position / translation / scale
  // move the eye back from the screen
  glTranslated(0.0,0.0,m_dzTrans);
  // rotate the drawing
  glRotated(m_dxRotation, 1.0, 0.0, 0.0);
  glRotated(m_dyRotation, 0.0, 1.0, 0.0);
  // now change to the z=depth coordinate system (right-handed)
  glMultMatrixd(m_dMatrixCorrd);
  // spot to look at (world x, y, z coord)
  glTranslated(m_dxTrans,m_dyTrans,m_dDepthTrans);
  ...
}
```

There are only two rotation modes used (lines 19 and 20 in listing B.7) because a third is redundant. Line 22 of the same listing is very important because OpenGL uses a left-handed coordinate system. All of the data is created using a right-handed coordinate system so the OpenGL coordinate system must be transformed to a right-handed system or a mirror image of the data is displayed. The variable `m_dMatrixCorrd` contains a 4 by 4 matrix that performs the coordinate system change.

B.4.2 Selecting Objects

Context menus are displayed within the OpenGL window when a using right-clicks on an object. The type of object determines the menu displayed. Since a 3D view can have several objects appear at the same place because one is directly in back of another, there has to be a mechanism to select the closest object. That method is called picking and is described in detail in the OpenGL 1.2 Programming Guide.[106] It involves rendering the seen through a special buffer to find the closest object to the viewer that is at the point the person clicked on. Once an object has been selected, the correct menu is displayed.

The picking code first creates a memory buffer to render into to find the object being selected (lines 4 and 19 of listing B.8) and tells the OpenGL engine to use the selection rendermode (line 22). It then sets up the OpenGL model and projection matrices to be identical to the ones used to display the objects (lines 28-37). After the objects have been rendered into the special buffer, the number of objects hit is returned (line 45). Then the code finds the hit with the smallest z depth (not depth in the soil but distance from the view straight into the computer screen). The selected hit is then identified in line 70.

Source Listing B.8: Code to find what object was clicked over.

```
int CObjView::ProcessMouseHit(int xPos, int yPos, BOOL bIsMenu) {
2   CObjDoc* pDoc = GetDocument();
    GLuint *buffer;
4   buffer=new GLuint[512];
    // save the sky variable (don't want
6   // hits to the sky faces)
    BOOL bUseSky=this->DisplaySky();
8   m_bDisplaySky=FALSE;
    GLint hits;
10  // clear the error buffer
    int nError=glGetError();
```

```
12
   // set the OpenGL device to what is currently
14 // used to draw to the computer screen
   GLfloat fAspect;
16 fAspect=m_viewport[3]==0?(float)m_viewport[2]:
      (float)m_viewport[2]/m_viewport[3];
18
   glSelectBuffer(512,buffer);
20 // tell the OpenGL device we are checking for
   // mouse clicks on a face
22 glRenderMode(GL_SELECT);
   // Set up the OpenGL Device
24 glInitNames();
   glPushName(0);
26 glEnable(GL_CULL_FACE);
   glEnable( GL_DEPTH_TEST );
28 glMatrixMode(GL_PROJECTION);

30 glLoadIdentity();
   gluPickMatrix((GLdouble)(xPos), (GLdouble)(m_viewport[3] -yPos),
32    1, 1, m_viewport);

34 glMultMatrixd(m_projMatrix);
   glMatrixMode(GL_MODELVIEW);
36 glPushMatrix();
   glLoadMatrixd(m_modelMatrix);
38
   // Start rendering...
40 pDoc->RenderScene(this, 1);
   glPopMatrix();
42 glFlush();

44 // return to regular mode
   hits = glRenderMode(GL_RENDER);
46 nError=glGetError();
   if(hits==-1)
48    AfxMessageBox("Overflow in hit buffer");
   glDisable(GL_CULL_FACE);
50 m_bDisplaySky=bUseSky;
   double zold=HUGE_VAL;
52 if (hits) {
      unsigned int names=0;
54    GLuint *ptr;
      ptr = (GLuint *) buffer;
56    // find the face closest to the viewer
```

```
        for(int nn=0; nn<hits; nn++)
58      {
           unsigned int name=(GLuint)*ptr;
60         ptr++;
           float z1=(float) *ptr/0x7fffffff;
62         ptr++;
           float z2=(float) *ptr/0x7fffffff;
64         ptr++;
           for(int ii=0; ii<(int )name; ii++)
66         {
              if(z1<zold)
68            {
                 // this face is closer
70               names=(unsigned int)*ptr;
                 zold=z1;
72            }
              ptr++;
74         }
        }
76      delete buffer;
        if(!(pDoc->HitObjType(names,UseFines())==OBJECT_TYPE_BOND))
78      {
           // fill in data for about the hit face
80         pDoc->UnProjectHit((FINENODE*)&m_pfFineNodeforHitTest,
              &m_faceUnProjected, names, UseFines(),
82            (double *)&m_modelMatrix, (double *)&m_projMatrix,
              (int *)&m_viewport, m_nRenderSoil==1?TRUE:FALSE);
84         // return the face number hit
           return names;
86      }
        else
88      {
           if(bIsMenu)
90            return names;
           else
92            return -1;
        }
94   }

96   delete buffer;
     // tell everyone that no faces were hit
98   return -1;
  }
```

Data returned in the call to `pDoc->UnProjectHit` is further treated to provide the user with data about the object under the point clicked. The mouse then works as a virtual-reference-electrode. A real reference electrode can only provide potential readings at the point it is placed. The virtual-reference-electrode can provide any type of data calculated on any surface. The soil does not restrict it. The model currently outputs potential, net current density, off-potential, and corrosion current density at the point where the virtual-reference-electrode is placed.

APPENDIX C
CODE STRUCTURE

The source code for the model was written as a Microsoft Windows NT application utilizing the OpenGL Application Programming Interface (API) for interactive display of the pipeline networks. The code uses a simple C++ structure to help manage code development. It may be best to explain the structure from the interface down through the data structures and then into the calculation engine. The code is divided into three major components: i) the interface ii) the calculation engine iii) remote integration module.

C.1 Interface

The interface is constructed in what is referred to as a Document/ View architecture. Each of the two parts is implemented as a C++ class. A C++ class is a piece of self contained code that can perform a specific task, manage a data set, provide a service, or one of a number of tasks. A comprehensive definition of a C++ class is far beyond the scope of this work. The reader is referred to some of the classic texts for C++ programming.[38, 129] Bruce Eckel has a very good explanation of C++ objects and classes in Chapter 1 of his book "Thinking in C++, Volume 1".[39]

The Document/View architecture dictates that is a Document class and a View class. The division of responsibilities is made under the premise that one class

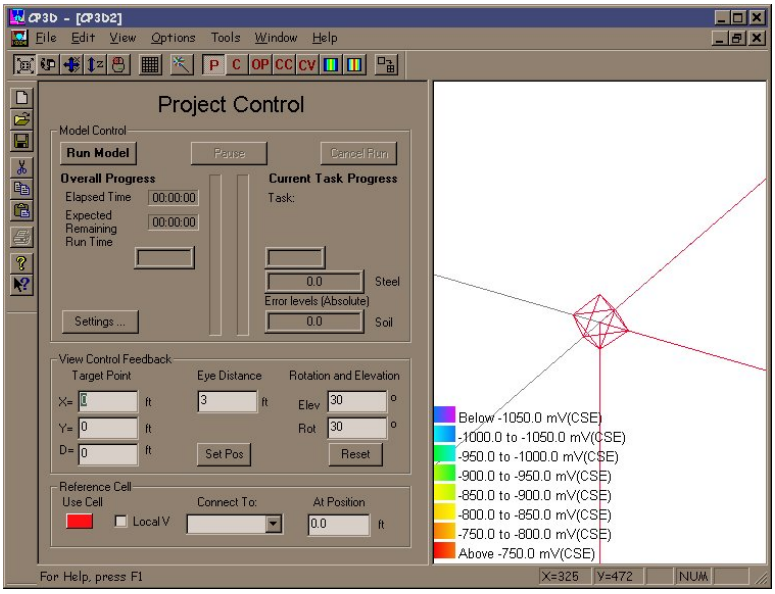

Figure C-1: A screen shot of the basic window with an empty model. The window has two parts: the first is for control and feedback, the other is for data display in 3 dimensions.

manages data (the Document) while the other class controls how the data appears to the use (the View).

The model adds a second View type class because of the nature of the data and its display. Figure C-1 shows the main window as it is divided into two section. The left half is a control window meaning it contains buttons, edit boxes and other controls. The right half contains the OpenGL 3D display of the pipes. Each half requires its own class to manage user input a feedback. Both classes are connected to the same data, so there is only one class for data management.

The names for the classes follow their purpose. The control console is called `CConView`, which is short for `Class Console View Window`. The OpenGL window class is call `CObjView` which is short for `Class Object ViewWindow`. The document class is called `CObjDoc`, which is short for `Class Object Document`.

There are also several support classes needed. The model is setup to allow any number of models to be open simultaneously. This is referred as a multi-document interface. Therefore there is a document manager class to keep track of all of the open models within the main program. The main program is built as a class. Its purpose is to establish how all of the classes are linked together to form a single coherent model. The last support class is the main frame window. This widow contains the standard menu, toll button bars and status bars. It takes messages when a user clicks a tool bar button or selects a menu item, passes the message to the document manager which then forwards the message to the top level model that is open within the main program. Details on this type of structure may be found in a number books[130, 131] and in the documentation for the Visual C++ programming environment.[132]

C.1.1 Data Management

The document class is used to manage all aspects of the the data. It owns all of the major data structures such as the boundary element and finite element meshes, boundary condition database and current and potential distribution solutions. It handles such tasks as saving and restoring the data to disk (persistence), creating new data such as pipes (allocation) and destruction of data (closing of a file, delete of a pipe from a model).

Data is saved or restored through a single function known as `Serialize()`. It takes a single argument of an `CArchive` object. The object contains all the methods needed to read or write data to a disk. Therefore, data owned by the class is written by calling functions from the `CArchive` object with the data as

parameters. However, there are very few variables within the Document class that are saved that way. Instead, the document `Serialize` function asks the data structures it owns to save themselves passing the `CArchive` object to the data structure's `Serialize` function. A typical document serialize function is listed in code listing C.1.

Source Listing C.1: Code to save and restore a model to persistant storage (disk).

```
void CObjDoc::Serialize(CArchive& ar)
{
   if (ar.IsStoring())
   {
      // sentinel (file version and format)
      ar<<m_dFileVersion;
   }
   else ... //read the file
   {
      // sentinel (file version and format)
      ar>>m_dFileVersion;
      // check version
      if(!CheckVersion())
      {
         throw(CFileException());
         return;
      }
   }
   // save all the pipes
   m_pPipeList->Serialize(ar);
   // color scales
   m_pclPotRange->Serialize(ar);
   // Boundary Condition database
   m_pBCDataBase->Serialize(ar);
   // render data
   ((CChildFrame *)GetParentFrame())->Serialize(ar);
   // calculation engine setup
   m_pBemSpec->Serialize(ar);
   // soilzone database
   m_pSoilZoneDB->Serialize(ar);
   // CP zone list
   m_pCPZoneNameList->Serialize(ar);
   // bond list
   m_pBondList->Serialize(ar);
```

```
    // soil-surface sections
36  m_pSoilSurfaceSectionList->Serialize(ar);
}
```

Of course, everything saved is binary data. The data structures are so large and complex, there is no point to using a human readable format. Also, a binary format saves many megabytes of disk space.

The document also passes commands from the View to appropriate data structures, or creates new structures as needed. For instance, the view will want all of the pipes to draw themselves into the client area of the window. It does this by asking the document. A function is called in the document by the view where the document then calls the appropriate data structures to draw themselves.

Source Listing C.2: Render scene code from the document. Code asks data structures to draw themselves.

```
void CObjDoc::RenderScene(CObjView *pView, int nMode) {
2
    int ii;
4   int nStart=0;
    if(pView->DisplaySky())
6   {
       // draw the sky
8      GLint polymode[2];
       glGetIntegerv(GL_POLYGON_MODE, polymode);
10     glPolygonMode(GL_FRONT , GL_FILL);
       m_pSky->Render();
12     glPolygonMode(GL_FRONT , polymode[0]);
    }
14  if(pView->RenderAxis()&& nMode==0)
       m_pAxis->Render();
16
    if(pView->RenderGrid() && nMode==0)
18     m_pGrid->Render();

20  // draw the pipe objects
    POSITION pos=m_pPipeList.GetHeadPosition();
22  while(pos!=NULL)
       m_pPipeList.GetAt(pos)->Render(pView);
24
```

```
    if(pView->ShowBonds())
26  {
       // draw the bonds
28     pos=m_pBondList.GetHeadPosition();
       while(pos!=NULL)
30        m_pBondList.GetNext(pos)->RenderBond(nMode);
    }
32  // draw the soil surface
    pos=m_pSoilSurfaceSection.GetHeadPosition();
34  while(pos!=NULL)
       m_pSoilSurfaceSection.GetAt(pos)->Render(pView);
36 }
```

The Document provides support for to the code that starts the calculation process by verifying the data before the process is allowed to start.

C.1.2 Data Interaction

The view class controls how the user interacts with the data. It is responsible for everything that happens or appears with the client area of the main window. The client area is the part of the window that is not the title bar, borders or resizing handles. It is also responsible for most of the menu items and toolbar buttons.

The view class must display dialog boxes as they are needed in response to user actions. It also handles how the objects appear to the user. The techniques used to display and interact with the objects in the model is described in Appendix B.

The second view class is used to support the console window (see Figure C-2). It provides code to respond to all of the controls in the console window and provide the feedback information. The upper half of the window is for the calculation engine, the lower half is for the OpenGL window and virtual reference electrode.

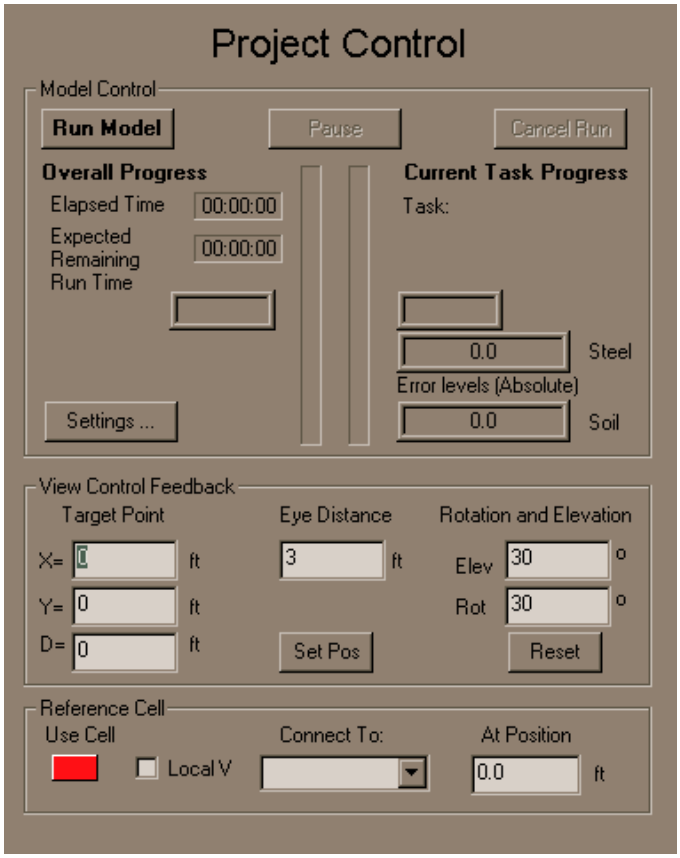

Figure C-2: Console window. This window provides model control, calculation control and feedback.

The most important of the functions is starting a calculation in response to the user clicking the "RunModel" button. The process begins by checking for necessary minimums in the model such as a pipe and at least one anode. It then checks to see if the model has ever been saved. If it has not yet been saved, the user must save it before the model can be run. The code then creates a data structure object to pass to the calculation engine. The object contains pointers to the pipe and anode data, the boundary condition database, and a pointer to functions needed to supply the user with where to model is in the progress of the calculation. After that, the file that contains the calculation engine is loaded into memory with a call to `LoadLibrary` (line 41 or 43 of listing C.3). If the library has been successfully loaded and is the correct version for the machine's CPU, a new thread is created to run the calculation. Multi-threaded applications are again far beyond the scope of this dissertation, so the reader is referred to some of the texts on building multi-threaded applications, especially ones that have an interface thread and a worker thread.

Source Listing C.3: Code to spin off a thread to run the calculation. Two functions are needed.

```
void CConView::OnConRunModel() {
  CObjView *pView=GetRenderView();
  CObjDoc* pDoc = pView->GetDocument();
  // make sure the CP systems have been organized
  pDoc->OrganizeCPSystems();
  // make sure there are some objects
  if(!pDoc->CheckCalcMins())
  {
    return;
  }
  // force a save if the document does not have a path yet
  if((pDoc->GetPathName( )).GetLength()==0 )
  {
    // force a save
    SendMessage(WM_COMMAND, ID_FILE_SAVE, 0);
```

```
16    }
      m_ctrlNRError.SetWindowText("not set");
18    m_ctrlFEMError.SetWindowText("not set");
      // start the elapsed timer
20    m_unStartTick=GetTickCount();
      // set auto update interval to 0.5 seconds
22    SetTimer(0x00000001, 500, NULL);
      m_ctrlRunModel.EnableWindow(FALSE);
24    m_ctrlPauseRun.EnableWindow(TRUE);
      m_ctrlCancelRun.EnableWindow(TRUE);
26    // fill in the nodes and elements in the bemspec
      pDoc->FillBemSpecForCalc();
28    BEMSTARTSTRUCT *pbstart;
      pbstart=new BEMSTARTSTRUCT[1];
30    pbstart->pSpecs=pDoc->GetBEMSpec();
      pbstart->pSpecs->SetParenthWnd(m_hWnd);
32    pbstart->pSpecs->SetBemStopFlag(FALSE);
      pbstart->pSpecs->SetBemPauseFlag(FALSE);
34    pbstart->pSpecs->SetBondList(&(pDoc->m_pBondList));
      pbstart->pSpecs->SetSoilSurfaceList(
36      pDoc->GetSoilSurfaceSecList());
      pbstart->pWnd=m_hWnd;
38
      // load the dll
40  #ifdef _DEBUG
      m_hInstEng=LoadLibrary("CalcEngd.dll");
42  #else
      m_hInstEng=LoadLibrary("CalcEng.dll");
44  #endif
      if(m_hInstEng==NULL)
46    {
        DWORD dwError=GetLastError();
48      if(dwError==1157)
          AfxMessageBox("Missing at least one library.");
50      else
          AfxMessageBox("Failed to
52          load the calculation engine.");

54      ResetControls();
        delete pbstart;
56      return;
      }
58    // check the cpu
      CPUCHECK checkcpu=(CPUCHECK)GetProcAddress(m_hInstEng,
60      "fnIsCPUCorrect");
```

```
    if(checkcpu==NULL)
62  {
      AfxMessageBox("Version of calculation engine wrong,
64      or cannot determine the cpu in this machine.
        Contact your software vendor.");
66    delete pbstart;
      ResetControls();
68    return;
    }
70  if(checkcpu()==FALSE)
    {
72    AfxMessageBox("The calculation engine installed will
        not work with the cpu on this machine.
74      Contact your software vendor.");
      delete pbstart;
76    ResetControls();
      return;
78  }
    pbstart->m_hInstEng=m_hInstEng;
80  if(m_hInstEng!=NULL)
    {
82    AfxBeginThread(MyControllingFunction, pbstart,
        THREAD_PRIORITY_BELOW_NORMAL);
84    pDoc->CanEdit(FALSE);
    }
86
  }
88
  UINT MyControllingFunction( LPVOID pParam ) {
90  PostMessage(((BEMSTARTSTRUCT *)pParam)->pWnd,
      WM_COMMAND, ID_MSG_SET_TASK_DESCRIPTION, 1);
92  // function address variable
    MYPROC runbem;
94  int test;
    // get the address of the calculation engine
96  runbem = (MYPROC) GetProcAddress(
      ((BEMSTARTSTRUCT *)pParam)->m_hInstEng, "fnCalcEng");
98  if(runbem!=NULL)
    {
100   // run the calculation
      test=runbem(((BEMSTARTSTRUCT *)pParam)->pSpecs);
102 }
    else
104   AfxMessageBox("Failed to Load the calculation engine.
        Please check your installation.");
```

```
106
     // cleanup
108  ((BEMSTARTSTRUCT *)pParam)->pSpecs->DeleteElementPointers();

110  // tell the interface code it done
     PostMessage(((BEMSTARTSTRUCT *)pParam)->pWnd,
112    WM_COMMAND, ID_MSG_CLEAN_UP_BEM, 0);
     //delete the the data passed to this function
114  delete (BEMSTARTSTRUCT *)pParam;
     return 0;
116 }
```

C.2 Calculation Engine

The calculation engine is divided into several sections. The first is the calculation of the coefficient matrices corresponding the boundary element method and the finite element method. The matrices are kept in separate files because of the sparse nature of the coupled system (see section 4.8). The actual integration is performed by a separate section of code described in section C.3. After the matrices have been assembled, the boundary conditions are applied and a solution obtained. With the solution in hand, post-solution calculations are done. Currently, only on-potential distributions on the soil surface within user specified rectangles are calculated.

C.2.1 Assembly of Boundary Element Matrices

The coefficients of the boundary element matrices (equation (4-2) are the integrals given in equation (4-1). The two types of integrals are placed into their respective matrices as each set of integrals is completed. A set consists of the integrals resulting from a collocation point - element pair. If the element has nine nodes, then there are 18 integrals in the set, half of which belong to the $\boldsymbol{H}$ matrix

of equation (4-2), and the other half go into the $\boldsymbol{G}$ matrix. For the six node triangles, 12 integrals are calculated with the same division between matrices. The data is aligned within the $\boldsymbol{G}$ matrix such that all of the results for a given element are next to each other if the storage format is row major. Therefore, the transpose of the matrix must be taken after all of the integrals are completed. The results of the integration belonging to the $\boldsymbol{G}$ matrix are fed directly to the harddrive as each integral set is completed. The results for the $\boldsymbol{H}$ matrix are retained in memory. The final format of the files on disk must be column major. This has significant performance advantages for all later portions of the calculation (application of the boundary conditions and solution of the set of nonlinear equations) as discussed in section 9.7. Column major means that columns are written sequentially to disk instead of rows. Row major is the default method for C/C++ for both matrices in memory and on disk. Fortran always uses column major and owes much of its performance advantage to this.

The integration makes use of remote processing which means that many computers can contribute to the completion of the integrals in parallel. Section C.3 discusses how the remote integration is accomplished. In fact, the integrals to be calculated on the local machine use the same integration technique as used for the remote machines.

C.2.2 Assembly of Finite Element Matrices

The finite element matrices are assembled directly by the calculation engine without the use of any remote processing. The code has been written for parallel computation on the local machine so all processors are utilized. The reason for

local computation only is that the finite element calculation is essentially a two dimensional problem and can be completed in seconds on a Pentium III/500 for all but the largest models.

The code is written as a C++ class that either reads the data from disk, or performs the calculation. The outer loop of the assembly code is over the elements and calls a function to create the element stiffness matrix. The outermost loop of the element stiffness matrix code is over the Gauss points to greatly reduce the overhead of calculating the Jacobian matrix. The inner loop is over each of the entries in the element stiffness matrix. Since the element stiffness matrix is symmetric, only the upper triangle needs to be calculated. However, the complete matrix must be used when integrated with the BEM because the BEM is not symmetric. Even if it was, the solution technique for the nonlinear set of equations would destroy the symmetry (see sections 4.5 through 4.9).

C.2.3 Solution of Nonlinear System

Once the boundary element and finite element matrices are complete, the boundary conditions can be applied and the system of nonlinear equations can be solved. It starts by reordering the variables in equation (4-39) such that all of the unknowns are on the left-hand-side. The result is equation (4-41). The solution continues with an initial guess of the unknown boundary conditions and then a calculation of the known boundary conditions from the guessed conditions. The first residual vector is then calculated and a sum of squares error is made to estimate how far off the initial guess is. If the guess is not close enough to the solution, the line search (damped) Newton-Raphson technique is used to

minimize the norm of the residual. The code for the line search is given in code listing C.5.

Source Listing C.4: Code to solve nonlinear system.

```
void CLinearSystem::SolveSystem(CBEM *pBEM) {
  // and swap columns in the H and G matrices
  // reorder system
  ReorderSystem(pBEM);
  // if the user canceled the calculation, quit
  if(m_pBemSpecs->GetBemStopFlag())
    return;

  // vector to hold the Potentials in the soil
  Vector<double> Phi(m_nNumNodes);
  // build vector of Known boundary conditions
  BuildRHVector(m_pdRhV, m_pdKnV, m_pnKode, pBEM, Phi);

  // get the residual error
  double f;
  f=UpdateResidual(pBEM, m_vR, m_vX);

  // post the current error
  if(pBEM->UseAttenuation())
  {
    int ONE=1;
    // Use BLAS vector norm calc
    m_dNRError=cblas_dnrm2(m_nNumNodes, &m_vR(1), ONE);
    m_dFEMError=cblas_dnrm2(m_nNumNodes+
      m_pBemSpecs->GetNumCPSystems(),
      &m_vR(m_nNumNodes+1), ONE);
    PostMessage(m_pBemSpecs->GetParentWnd(), WM_COMMAND,
      32802, (LPARAM)(&m_dNRError));
    PostMessage(m_pBemSpecs->GetParentWnd(), WM_COMMAND,
      32841, (LPARAM)(&m_dFEMError));
  }
  else
  {
    int ONE=1;
    m_dNRError=cblas_dnrm2(NPZ, &m_vR(1), ONE);
    m_dFEMError=0.0;
    PostMessage(m_pBemSpecs->GetParentWnd(), WM_COMMAND,
      32802, (LPARAM)(&m_dNRError));
  }
  double xTOL=m_pBemSpecs->GetMatrixConv();
```

```
    if(m_dNRError+m_dFEMError > xTOL)
    {
      int niter=m_pBemSpecs->GetMaxIterations();
      LineSearchSolve(pBEM, nLim, xTOL, niter, f);
    }
    // make sure the known boundary conditions are updated
    ResetKnowns(pBEM, Phi); // m_pdKnV filled in here
    // calculate the current vector in the steel
    BuildCurrentVectors(pBEM, V);
    // reorder the solution so one vector contains potentials
    // and the other contains the normal electric field
    ReorderSolution(pBEM, Phi);
    // calculate the corrosion current densities
    GetCorCur();
}
```

Source Listing C.5: Code to perform line search.

```
void CLinearSystem::LineSearchSolve(CBEM *pBEM, int nLim,
  double xTol, int niter, double f) {

  // nLim is order of system (size of A)
  // get the step max for the line search
  double stpmax=0.0, sum;
  sum= cblas_ddot(nLim, &m_vX(1), inc, &m_vX(1), inc);
  stpmax=STPMAX*_MAX(sqrt(sum), (double)nLim);

  // declare some variables
  Vector<double> g(nLim);
  Vector<double> xold(nLim);
  Vector<double> p(nLim);
  int NRcount=0;
  while(NRcount<niter)
  {
    //Build the Jacobian of the boundary conditions
    BuildJVThrd(pBEM, m_vJV, m_vX);
    // Get the Jacobian of the nonlinear system
    // The matrix A in Ax=b
    GetA(&m_mA(1,1), pBEM, m_vJV, nLim);

    // save the residual (b vector) for later
    // it is used in case the whole thing fails
    Vector<double> oldb(m_vR);
    // get gradient of b for the line search
    cblas_dgemv(CblasColMajor, CblasTrans,
          nLim, nLim, alpha, &m_mA(1,1), LDA,
```

```
            &m_vR(1), inc, beta, &g(1), inc);

      // save the old unknown variables
      xold=m_vX;
      // and the old f
      fold=f;
      // and the residual
      // this one is updated at each iteration
      // and used to check for slow convergence
      p=m_vR;
      // condition the matrix system
      ConditionSystem(m_mA, p);
      N=nLim;
      NRHS=1;

      Info=0;
      char trans='N';
      int strlength=1;
      /*****************************************************/
      // solve Ax=b
#ifdef _DEBUG
      int rVal;
      Vector<Subscript> ipiv(nLim);
      rVal=LU_factor(m_mA,ipiv, (UPDATEF)UPDATE);
      if(rVal==-1)
      {
        AfxMessageBox("Singular Matrix, Cannot solve.");
        m_pBemSpecs->SetBemStopFlag();
        m_mA.newsize(0,0);
        return;
      }
      LU_solve(m_mA,ipiv,p);
#else
      Vector<Fortran_integer> index(nLim);
      DGESV(&N, &NRHS, &m_mA(1,1), &LDA, &index(1),
        &p(1), &LDB, &Info, (void *)UPDATE);
      if(Info>0)
      {
        AfxMessageBox("Singular Matrix, exiting engine.");
        m_pBemSpecs->SetBemStopFlag();
        m_mA.newsize(0,0);
        return;
      }
      pBEM->UpdateStatus(89, 4);
#endif
```

```
74
      /*****************************************************/
76    // update the user interface
      PostMessage(m_pBemSpecs->GetParentWnd(), WM_COMMAND,
78      32822, 10);
      // do the line search
80    // lnsrch tries to find lambda <=1.0 such
      // that the norm of the residual is reduced
82    // lambda is the fraction of the full Newton step
      lnsrch(pBEM, nLim, m_vR, xold, fold, g, p, m_vX,
84      &f, stpmax, &Info);

86    m_nNR++; // one iteration complete
      double test=0.0;
88    // get error
      for(ii=0; ii<nLim; ii++)
90    {
        if(fabs(m_vR[ii])>test)
92        test=fabs(m_vR[ii]);
      }
94    if(m_pBemSpecs->GetBemStopFlag())
        return;
96
      // get NRerror
98    if(pBEM->UseAttenuation())
      {
100     int ONE=1;
        m_dNRError=cblas_dnrm2(m_nNumNodes, &m_vR(1), ONE);
102     m_dFEMError=cblas_dnrm2(NPZ, &m_vR(m_nNumNodes+1), ONE);
        PostMessage(m_pBemSpecs->GetParentWnd(), WM_COMMAND,
104       32802, (LPARAM)(&m_dNRError));
        PostMessage(m_pBemSpecs->GetParentWnd(), WM_COMMAND,
106       32841, (LPARAM)(&m_dFEMError));
      }
108   else
      {
110     int ONE=1;
        m_dNRError=cblas_dnrm2(nLim, &m_vR(1), ONE);
112     PostMessage(m_pBemSpecs->GetParentWnd(), WM_COMMAND,
          32802, (LPARAM)(&m_dNRError));
114   }
      if(test<xTol)
116     break; // break the while loop

118   test=0.0;
```

```
      // check for slow convergence
120   for(ii=0; ii<nLim; ii++)
      {
122     temp=(fabs(m_vX[ii]-xold[ii]))/_MAX(fabs(m_vX[ii]), 1.0);
        if(temp>test)
124       test=temp;
      }
126   if(test<xTol/10.)
        break;
128 }
}
```

C.2.4 Soil Surface On-Potentials

Soil surface on and off-potentials are calculated using equation (3-8). Again, remote integration is used to actually calculate the integrals necessary to find Φ at the soil surface. This time, the source points are not on a boundary, so there are no singular integrals. The results of the integration are again placed in a pair of matrices that are written to the harddrive.

C.3 Remote Integration

The remote integration module consists of two parts: a client and a server. The server is a piece of code the actually performs the integration. The client requests a particular integral or set of integrals to be calculated. Communication between the client and server is handled through Remote Procedure Calls (RPC). RPC is a subset of the OpenGroup's Distributed Computing Environment (DCE). RPC functions by taking and ordinary function call and passing it over a network to another computer or to another program on the same computer where the function is actually executed. The results of the function are then passed back to the calling program.

C.3.1 Interface Definition

To create a callable function that resides on a remote machine, a special piece of code is created called an interface definition. It contains the definitions of the data structures that are to be passed to the function in terms of basic data types such as *double*, *int*, or *char*. It also contains a globally unique identifier to insure that no-one anywhere else in the world has made a definition the same as this one. Finally the code contains the definitions of the functions that are to be called. Each parameter passed to the function contains a label as to whether the parameter is an input, output or both. This is done to reduce the amount of data that must be transported across the network when the function is called and when it returns. The interface definition for pipeline model integration subroutines is

Source Listing C.6: Interface definition for remote integration module.

```
[ uuid
(e4e1a780-df39-11d3-80c0-00c04f6b9a47),
 version(4.0),
 pointer_default(unique)
] interface CPInt{

typedef struct _NODE{
  double x;
  double y;
  double z;
  }NODE;

typedef struct _ELEMENT{
  NODE theNodes[9];
  long nEletype;
  }ELEMENT;


typedef struct _INTPARAMETERS{
  double dRelErr;
  double dLedgePos;
  long  nUseLedgePos;
  long  nIntScheme; //pos means singular
```

```
24    long  nUseHighSpeed;
    }INTPARAMETERS;
26
  typedef struct _INTDATA{
28    ELEMENT theElement;
    NODE theColnode;
30    INTPARAMETERS thePrams;
    }INTDATA;
32
  typedef struct _RESULTS{
34    double theResults[18];
    }RESULTS;
36
  typedef struct _DOMAINRESULTS{
38    double theResults[3][18];
    }DOMAINRESULTS;
40
  DOMAINRESULTS IntegrateDomainPoints(
42    [in] handle_t hBind,
    [in] INTDATA data);
44
  RESULTS IntegrateElement(
46    [in] handle_t Binding,
    [in] INTDATA theData);
48
  long GetNumProcessors(
50    [in] handle_t Binding);
  };
```

There is an extra function added to tell the client program how many processors are available to do calculations. Then the client program can create as many parallel called threads as there are processors.

The above code is written in what is called Interface Definition Language (IDL). It is also used by another remote procedure technique called CORBA. A CORBA interface has also been written for the model code.

C.3.2 Data Marshaling

DCE RPC has been built with cross-platform capability in mind. Cross-platform means the client and server do not have to be on the same operating system or hardware type. Therefore, a standard must be created for the transport of data between the client and server so that when the data is reassembled, it is identical to the original that was sent. If the client has Little Endian hardware (least significant byte first) and the server is a Big Endian machine (most significant byte first), there must be mechanisms to correctly assemble the data. This is where data marshaling in needed. Data marshaling takes the data being sent from one machine to another and translates it into a standard byte stream format. Then the bytes can be reasembled into the original data using the appropriate standard for the hardware of the machine.

The code to marshal the data is created by an IDL compiler. The compiler reads the IDL file and creates a client stub that exposes the functions to the client program, marshals the data and sends the function call and data to the remote machine. The compiler also creates the server stub that calls the function on the remote machine. The server stub also takes the data sent to it and formats it into the proper variables for the server function call.

Transport across the network is handled by a standard packet technique such TCP or UDP which are protocols in the TCP/IP family of network protocols. In the case of this code, only TCP is used.

C.3.3 Server Side

The server portion of the code is a stand-alone program that runs on every computer that will be used in the parallel computation. Since it would be very inconvenient to start each program manually, the code is written as a system service and network listener. That way, the code is always ready to do a calculation but does not use any computer time when not in use.

The code is loaded into memory whenever the computer boots and does not shut down again until the computer is shutdown. It also listens on a TCP port for requests to calculate an integral. Since the computer can possibly receive requests from several computers simultaneously, or the server computer may have more than one CPU, the code is multi-threaded. This means there can be more than one calculation running at the same time.

When the code is loaded into memory, a startup routine is called which then blocks on a listen command until the computer is shutdown. The sequence of task at startup is

1. Select a protocol for network transport. This is the language used to communicate data between the client program and the server program.

2. Register the existence of the listener with the RPC endpoint mapper.

3. Listen for calls to calculate integrals.

The first task is accomplished by the code shown is listing C.7.

Source Listing C.7: Selection of communication protocol for remote procedure call.

```
  // use tcp/ip protocol ncacn
2 status=RpcServerUseProtseqEp(
```

```
    (unsigned char *)"ncacn_ip_tcp", // protocol
    cMaxCalls, // max simultaneous threads
    (unsigned char *)"3643", // port to listen on
    pszSecurity); // security requirements
if(status)
    goto cleanup;
// use non network protocol ncalrpc
// this listener only works when the client is
// located on the same machine
status=RpcServerUseProtseqEp(
    (unsigned char *)"ncalrpc", //local only
    cMaxCalls, // max simultaneous threads
    (unsigned char *)"cp3dint400", //endpoint name
    pszSecurity); // security requirements
if(status)
    goto cleanup;
// let the operating system known we are still alive
ReportStatusToSCMgr(
    SERVICE_START_PENDING, // service state
    NO_ERROR,        // exit code
    3000);           // wait hint
```

Then the listener is registered with the RPC endpoint mapper with calls to the RPC service as shown in listing C.8.

Source Listing C.8: Registration of RPC server.

```
// interface to register
status = RpcServerRegisterIf(CPInt_v4_0_s_ifspec,
                    NULL, // MgrTypeUuid
                    NULL);

// get the binding vector handle
status = RpcServerInqBindings(&pBindingVector);

if (status)
    goto cleanup;
// register the endpoints
status = RpcEpRegister(CPInt_v4_0_s_ifspec,
                pBindingVector,
                NULL,
                NULL);
```

Finally, the code tells the operating system that all is well and the program is listening for requests as shown in listing C.9. There is one more step in the code, setting the priority class for the service in line 6 of listing C.9. It is set to *idle* so that the code does not interfere with other processes the user of the machine may be using. In essence, the code will only use what would otherwise be unused CPU cycles.

Source Listing C.9: Code to start listening for integration calculation requests.

```
ReportStatusToSCMgr(
  SERVICE_RUNNING, // service state
  NO_ERROR,    // exit code
  0);
// set the priority
SetPriorityClass(GetCurrentProcess(),
  IDLE_PRIORITY_CLASS);
//start listening for calls
status = RpcServerListen(cMinCalls,
                 cMaxCalls,
                 fDontWait );
```

The code blocks on the call `RpcServerListen()` until shutdown. In order for the code to respond to requests, extra threads are created that actually run the functions.

C.3.4 Client Side

The client side of the remote integration procedure is implemented within the calculation engine of the main program. It consists of two classes that work together to complete all of the integration with the least amount of local CPU effort. The first of the two classes (`CDomainData`) will have only one instance during the life of the integration process, while there will be one instance of the

second class (`CRpcIntegrate`) for every CPU on every machine involved with the integration.

The integration process starts by creating a list of "jobs" to be done. Each job consists of either 12 or 18 integrals to be completed depending on if the element over which the integrals are to be computed are triangles or rectangles. Each job is stored in a last-in-first-out (LIFO) stack saved to disk. This task is carried out by the first class described above (`CDomainData`). Once the data has been sorted and placed as discrete jobs in a stack, the main program spawns off a new thread for each CPU. Each thread creates an instance of `CRpcIntegrate` with the parameters of the machine name that the thread should send integration requests to and a handle to the `CDomainData` object.

Source Listing C.10: Code to spin off integration threads for each CPU on each machine.

```
void CLinearSystem::AssembleMatrices(CBEM *pBEM) {
  ...
  // start a thread for each machine
  POSITION pos=pDB->GetHeadPos();
  while(pos!=NULL)
  {
    CComputerRecord *pRec=pDB->GetNext(pos);
    CString str=pRec->GetName();

    // find number of CPUs on this system
    int nCPUs=GetNumCPUs( str);
    // start a new thread with this name
    for(int jj=0; jj<nCPUs; jj++)
    {
      pData=new INTSTARTDATA;
      pData->pData=m_pBemThreadData;
      pData->bIsGroundCalc=FALSE;
      pData->bUseLocalRpc=FALSE;
      pData->strName=str;
      if(m_pBemSpecs->GetConvTolSetting()==0)
        pData->bUseHighSpeed=TRUE;
      else
```

```
      pData->bUseHighSpeed=FALSE;
24    pData->bWantSing=FALSE;
      DWORD dwThreadID;
26    pThread=CreateThread(NULL, 0,
        (LPTHREAD_START_ROUTINE)IntegrationControl,
28      pData, CREATE_SUSPENDED, &dwThreadID);
      // set thread priority high
30    SetThreadPriority(pThread, THREAD_PRIORITY_ABOVE_NORMAL);
      ResumeThread(pThread);
32    pThreadList.AddTail(pThread);
    }
34  }
  BOOL done=FALSE;
36  // now monitor
  unsigned int count=0;
38  while(!done)
  {
40   count++;
    Sleep(250); // sleep a quarter second
42  BOOL bStillAlive=FALSE;
    DWORD bStatus;
44  POSITION pos=pThreadList.GetHeadPosition();
    while(pos!=NULL)
46  {
      HANDLE pT=pThreadList.GetNext(pos);
48    GetExitCodeThread(pT , &bStatus);
      if(bStatus==STILL_ACTIVE )
50      bStillAlive=TRUE;
    }
52  if(!bStillAlive)
      done=TRUE;
54  }
}
```

Listing C.10 shows the code that creates the threads that send integration jobs to remote machines. Line 26 contains the code that starts a new thread in a suspended state. This allows the main thread to set the thread priority before its execution is resumed. The high priority level given to the service threads may seem as though they should cause poor execution of other tasks in the program.

That is not true, however, because most the the time the thread is blocked waiting for a remote procedure call to complete (see line 96 of listing C.11).

The `CRpcIntegrate` object starts by making a connection to the machine it is to talk to. It then goes into a loop consisting of three tasks: 1) get a job from `CDomainData`, 2) make a remote procedure call, 3) If the call succeeds, write the results to the matrices; otherwise write the job to the error stack for some other thread to complete.

Source Listing C.11: Client code to make a remote procedure call.

```
int CRpcIntegrate::Integrate() {
2
  unsigned long ulCode;
4 unsigned char * pszStrBinding = NULL;
  unsigned char * pszOptions = NULL;
6 unsigned char * pszUuid = NULL;
  RPC_BINDING_HANDLE hCP3D;
8 RPC_STATUS status;
  int fContinue=1;
10 RpcTryExcept {
   EnterCriticalSection(&CRPCIntThread::m_csDataLock);
12  {
    if(!m_bUseLocalRPC)
14  {
     status=RpcStringBindingCompose( pszUuid,
16     (unsigned char *) "ncacn_ip_tcp",
       (unsigned char *)m_strMachineName,
18     (unsigned char *) "3643",
       pszOptions,
20     &pszStrBinding);
    }
22  else
    {
24   status=RpcStringBindingCompose( pszUuid,
       (unsigned char *) "ncalrpc",
26     NULL,
       (unsigned char *) "cp3dint400",
28     pszOptions,
       &pszStrBinding);
30  }
   }
```

```
  LeaveCriticalSection(&CRPCIntThread::m_csDataLock);
}
RpcExcept(1) {
  ulCode = RpcExceptionCode();
  fContinue = 0;
}
RpcEndExcept
if(status!=RPC_S_OK)
  return -1;

// get the binding
RpcTryExcept {
  EnterCriticalSection(&CRPCIntThread::m_csDataLock);
  {
    status = RpcBindingFromStringBinding(pszStrBinding,
            &hCP3D);
  }
  LeaveCriticalSection(&CRPCIntThread::m_csDataLock);
}
RpcExcept(1) {
  ulCode = RpcExceptionCode();
  fContinue = 0;
}
RpcEndExcept
if(status!=RPC_S_OK)
{
  RpcBindingFree(&hCP3D);
  return -1;
}
//else we are good to go with a live connection

BOOL bDone=FALSE;
BOOL bGotSing;
INTDATA intData; // data to be sent
JOBSTACK job; // job to do
CBemSpecs *pSpecs;
CSoilZoneDataBase *pSZDB;
EnterCriticalSection(&CRPCIntThread::m_csFileLock);
{
  pSpecs=m_pThreadData->GetBemSpecs();
  pSZDB=pSpecs->GetSoilZoneDB();
}
LeaveCriticalSection(&CRPCIntThread::m_csFileLock);
CSoilZoneRecord *pRec;
int ii;
```

```
while(!bDone)
{
  EnterCriticalSection(&CRPCIntThread::m_csDataLock);
  {
    if(!m_pThreadData->GetJob(job, &bGotSing,
      m_bWantSing))
    {
      LeaveCriticalSection(
        &CRPCIntThread::m_csDataLock);
      bDone=TRUE;
      break;
    }
  }
  LeaveCriticalSection(&CRPCIntThread::m_csDataLock);
  BOOL bResultsGood=TRUE;
  RESULTS theResults; // the returned data
  // make the RPC call
  RpcTryExcept
  {
    theResults = IntegrateElement(hCP3D, intData);
  }
  RpcExcept(1) {
    ulCode = RpcExceptionCode();
    fContinue = 0;
    bResultsGood=FALSE;
    HandleRPCError(pSpecs, job, intData, hCP3D);
    EnterCriticalSection(&CRPCIntThread::m_csDataLock);
    {
      // check for quit message
      if(m_pThreadData->ShouldStopCalc())
      {
        LeaveCriticalSection(
          &CRPCIntThread::m_csDataLock);
          return 0;
      }
    }
    LeaveCriticalSection(&CRPCIntThread::m_csDataLock);
  }
  RpcEndExcept
  if(bResultsGood)
  {
    EnterCriticalSection(&CRPCIntThread::m_csDataLock);
    {
      m_pThreadData->WriteFinishedWork(job,
        &theResults);
```

```
122       }
          LeaveCriticalSection(&CRPCIntThread::m_csDataLock);
124     }
      }
126   RpcBindingFree(&hCP3D);

128   return 0;
    }
```

A byproduct of this technique is that it implicitly balances the computational load over a heterogeneous network of workstations. The balancing is done because the technique supplies a relatively small packet of information that can be completed in about 1 second on a Pentium III 500 mhz CPU.

REFERENCES

1. *Gas Facts - Distribution and Transmission Miles of Pipeline*, Technical report, American Gas Association (1999). Http://www.aga.org/StatsStudies/GasFacts/2131.html.

2. NTSB, *Pipline Accident Summary Report: Pipeline Rupture, Liquid Butane Release, and Fire, Lively, Texas August 24 1996*, Technical report, National Transportation Safety Board, Washington, D.C. (1998).

3. J. Morgan, *Cathodic Protection*, 2nd edition (Houston, TX: NACE, International, 1993).

4. M. L. Wald, "Conglomerate, Accused of Allowing Spills to Cut Costs, Is Fined $30 Million," *New York Times*, (January, 14 2000).

5. Gorton, "Pipeline Safety Improvement Act of 2000," in *Congressional Record*, 102nd Congress, 2nd Session (Government Printing Office, 2000) S8225.

6. McCain, "AMENDMENT NO. 4130 to Pipeline Safety Improvement Act of 2000," in *Congressional Record*, 102nd Congress, 2nd Session (Govenment Printing Office, 2000) S8231.

7. J. Wagner, *Cathodic Protection Design I*, NACE, International, Houston, TX (1994).

8. C. Kasper, "The Theory of the Potential and the Technical Practice of Electrodeposition: IV. The Flow between and to Circular Cylinders." *Transactions of the Electrochemical Society*, **78** (1940) 147–161.

9. J. O. M. Bockris and A. K. N. Reddy, *Modern Electrochemistry: Ionics*, volume 1, 2nd edition (New York: Plenum Press, 1998).

10. J. O. M. Bockris and A. K. N. Reddy, *Modern Electrochemistry: Electrodics*, volume 2, 2nd edition (New York: Plenum Pub, 2000).

11. A. J. Bard and L. R. Faulkner, *Electrochemical Methods: Fundamentals and Applications* (New York: Wiley, 1980).

12. J. S. Newman, *Electrochemical Engineering*, 2nd edition (Englewood Cliffs, New Jersey: Prentice-Hall, 1991).

13. J. O. Bockris, D. Drazic, and A. R. Despic, "The Electrode Kinetics of the Deposition and Dissolution of Iron," *Electrochimica Acta*, **4** (1961) 325–361.

14. M. E. Orazem and J. M. Esteban, *Phase II Final Report: A Three Dimensional Model for the Cathodic Protection of an Underground PIpeline*, Technical report, University of Florida (1994).

15. G. Jerkiewicz, "Hydrogen Sorption At/In Electrode," *Progress in Surface Science*, **57** (1998) 137–186.

16. M. de Chialvo and A. Chialvo, "The Tafel-Heyrovsky route in the kinetic mechanism of the hydrogen evolution reaction," *Electrochemistry Communications*, **1** (1999) 379–382.

17. M. de Chialvo and A. Chialvo, "Existence of two sets of kinetic parameters in the correlation of the hydrogen electrode reaction," *Journal of the Electrochemical Society*, **147** (2000) 1619–1622.

18. A. Lasia and D. Gregoire, "General Model of Electrochemical Hydrogen Absorption Into Metals," *Journal of the Electrochemical Society*, **142** (1995) 3393–3399.

19. L. J. Bai, "Behavior of a Hydride Phase Formed in the Hydrogen Evolution Reaction at a Rotating Pt Electrode - Analysis of Potential Relaxation Transients from a Kinetic Approach," *Journal of Electroanalytical Chemistry*, **355** (1993) 37–55.

20. K. Nisancioglu, "Predicting the Time Dependence of Polarization on Cathodically Protected Steel in Seawater," *Corrosion*, **43** (1987) 100–111.

21. K. Nisancioglu, P. O. Gartland, T. Dahl, and E. Sander, "Role of Surface Structure and Flow Rate on the Polarization of Cathodically Protected Steel in Seawater," *Corrosion*, **43** (1987) 710–718.

22. P. Nisancioglu, K. Gartland, "Current Distribution with Dynamic Boundary Conditions," in *I. Chem. Symposium Series No. 112: Conference on Electrochemical Engineering* (Loughborough: Loughborough University of Technology, 1989) .

23. J. F. Yan, S. N. R. Pakalapati, T. V. Nguyen, R. E. White, and R. B. Griffin, "Mathematical Modeling of Cathodic Protection Using the Boundary Element Method with a Nonlinear Polarization Curve," *Journal of the Electrochemical Society*, **139** (1992) 1932–1936.

24. K. Kennelley, L. Bone, and M. Orazem, "Current and Potential Distribution on a Coated Pipeline with Holidays Part I - Model and Experimental Verification." *Corrosion*, **49** (1993) 199–210.

25. D. A. Jones, *Principles and Prevention of Corrosion* (Upper Saddle River, NJ: Prentice Hall, 1996).

26. A. Korzhenko, M. Tabellout, and J. Emery, "Dielectric Relaxation Properties of the Polymer Coating During its Exposition to Water," *Materials Chemistry and Physics*, **65** (2000) 253–260.

27. C. Corfias, N. Pebere, and C. Lacabanne, "Characterization of a Thin Protective Coating on Galvanized Steel by Electrochemical Impedance Spectroscopy and a Thermostimulated Current Method," *Corrosion Science*, **41** (1999) 1539–1555.

28. I. Margarit and O. Mattos, "About Coatings and Cathodic Protection: Possibilities of Impedance as Monitoring Technique," in *Electrochemical Methods in Corrosion Research VI, Parts 1 and 2* (Zurich-Eutikon: Transtec Publications, 1998) 279–292.

29. I. Thompson and D. Campbell, "Interpreting Nyquist Responses From Defective Coatings on Steel Substrates," *Corrosion Science*, **36** (1994) 187–198.

30. F. Bellucci and L. Nicodemo, "Water Transport in Organic Coatings," *Corrosion*, **49** (1993) 235–247.

31. D. Riemer and M. Orazem, "Development of Mathematical Models for Cathodic Protection of Multiple Pipelines in a Right of Way," in *Proceedings of the 1998 International Gas Research Conference*, Gas Research Institute (Chicago: GRI, 1998) 117. Paper TSO-19.

32. D. Riemer and M. Orazem, "Cathodic Protection of Multiple Pipelines with Coating Holidays," in *Procedings of the NACE99 Topical Research Symposium: Cathodic Protection: Modeling and Experiment*, M. E. Orazem, editor, NACE (Houston, TX: NACE International, 1999) 65–81.

33. M. Orazem, J. Esteban, K. Kenelley, and R. Degerstedt, "Mathematical Models for Cathodic Protection of an Underground Pipeline with Coating Holidays: Part 1 - Theoretical Development," *Corrosion*, **53** (1997) 264–272.

34. D. Diakow, G. Van Boven, and M. Wilmott, "Polarization Under Disbonded Coatings: Conventional and Pulsed Cathodic Protection Compared," *Materials Performance*, **37** (1998) 17–23.

35. T. R. Jack, "External Corrosion of Line Pipe - a Summary of Research Activities," *Materials Performance*, **35** (1996) 18–24.

36. J. A. Beavers and N. G. Thompson, "Corrosion Beneath Disbonded Pipeline," *Materials Performance*, **36** (1997) 13–19.

37. R. Aris, *Vectors, Tensors and the Basic Equations of Fluid Mechanics* (New York: Dover Publications, Inc., 1962).

38. H. M. Deitel and P. J. Deitel, *C++: How to Program*, 3rd edition (Upper Sadle River, NJ: Prentice Hall, 2000).

39. B. Eckel, *Thinking in C++, Volume 1*, 2nd edition (Upper Saddle River, NJ: Prentice Hall, 2000).

40. A. W. Peabody, *Control of Pipeline Corrosion* (Houston, TX: NACE, 1978).

41. K. E. Jeffers, *Electrochemical Impedance Spectroscopy for the Characterization of Corrosion and Cathodic Protection of Buried Pipelines*, Master's thesis, University of Florida, Gainesville, Florida (1999).

42. D. R. Baker, M. W. Verbrugge, and J. Newman, "A Transformation for the Treatment of Diffusion and Migration. Application to Stationary Disk and Hemispherical Electrodes," *Journal of Electroanalytic Chemistry*, **314** (1991) 23–44.

43. D. R. Baker, "Reducing Nonlinear Systems of Transport Equations to Laplace's Equation," *SIAM Journal of Applied Math*, **53** (1993) 419–439.

44. B. Pillay and J. Newman, "Modeling Diffusion and Migration in Dilute Electrochemical Systems Using the Quasipotential Transformation," *Journal of the Electrochemical Society*, **140** (1993) 414–420.

45. M. W. Verbrugge, D. R. Baker, and J. Newman, "Dependent-Variable Transformation for the Treatment of Diffusion, Migration, and Homogeneous Reactions," *Journal of the Electrochemical Society*, **140** (1993) 2530.

46. K. Allahar and M. Orazem, "Modeling Disbonded Coatings using the Quasipotential Transformation," in *Passivity and Localized Corrosion*, R. G. Kelly, B. MacDougall, M. Seo, and H. Takahashi, editors, volume PV-99-27 (Pennington, N.J.: Electrochemical Society, Inc., 1999) 609.

47. H. S. Carslaw and J. C. Jaeger, *Conduction of Heat in Solids* (New York: Oxford University Press, 1959).

48. H. F. Moulton, "Current Flow in Rectangular Conductors," *Proceedings of the London Mathematical Society*, **ser. 2** (1905) 104–110.

49. F. Bowman, *Introduction to Elliptic Functions with Applications* (New York: John Wiley and Sons, 1953).

50. M. E. Orazem and J. Newman, "Primary Current Distribution and Resistance of a Slotted-Electrode Cell," *Journal of the Electrochemical Society*, **131** (1984) 2857–2861.

51. M. E. Orazem, "Calculation of the Electrical Resistance of a Compact Tension Specimen for Crack-Propagation Measurements," *Journal of the Electrochemical Society*, **132** (1985) 2071–2076.

52. M. E. Orazem and W. Ruch, "An Improved Analysis of the Potential Drop Method for Measuring Crack Lengths in Compact Tension Specimens," *International Journal of Fracture*, **31** (1986) 245–258.

53. C. B. Diem, B. Newman, and M. E. Orazem, "The Influence of Small Machining Errors on the Primary Current Distribution at a Recessed Electrode," *Journal of the Electrochemical Society*, **135** (1988) 2524–2530.

54. C. A. Brebbia and J. Dominguez, "Boundary Element Methods for Potential Problems," *Applied Mathematical Modelling*, **1** (1977) 371–378.

55. S. Aoki, K. Kishimoto, and M. Sakata, "Boundary Element Analysis of Galvanic Corrosion," in *Boundary Elements VII*, C. A. Brebbia and G. Maier, editors, volume 1 (Berlin: Springer-Verlag, 1985) 73–83.

56. J. Telles, L. Wrobel, W. Mansur, and J. Azevedo, "Boundary Elements for Cathodic Protection Problems," in *Boundary Elements VII*, B. C. M. G, editor, volume 1 (Springer-Verlag, 1985) 63–71.

57. N. Zamani and J. Chuang, "Optimal-Control of Current in a Cathodic Protection System - A Numerical Investigation," *Optimal Control Applications & Methods*, **8** (1987) 339–350.

58. F. Brichau and J. Deconinck, "Numerical model for cathodic protection of buried pipes," *Corrosion*, **50** (1994) 39–49.

59. F. Brichau, J. Deconinck, and T. Driesens, "Modeling of Underground Cathodic Protection Stray Currents," *Corrosion*, **52** (1996) 480–488.

60. S. Aoki and K. Amaya, "Optimization of Cathodic Protection SYstem by BEM," *Engineering Analysis with Boundary ELements*, **19** (1997) 147–156.

61. S. Aoki, K. Amaya, and M. Miyasaka, "Boundary Element Analysis of Cathodic Protection for Complicated Structures," in *Procedings of the NACE99 Topical Research Symposium: Cathodic Protection: Modeling and Experiment*, M. E. Orazem, editor, NACE (Houston, TX: NACE International, 1999) 45–65.

62. C. Brebbia and J. Dominguez, *Boundary Elements: An Introductory Course* (Avon, Great Britain: McGraw-Hill, The Bath Press, 1989).

63. C. A. Brebbia, J. C. F. Telles, and L. C. Wrobel, *Boundary Element Techniques* (Springer-Verlag, 1984).

64. F. Hartmann, C. Katz, and B. Protopsaltis, "Boundary Elements and Symmetry," *INGENIEUR ARCHIV*, **55** (1985) 440–449.

65. L. Gray and G. Paulino, "Symetric Galerkin Boundary Integral Formulation for Interface and Multi-zone Problems," *International Journal for Numerical Methods in Engineering*, **40** (1997) 3085–3101.

66. I. Stakgold, *Greens Functions and Boundary Value Problems* (New York: John Wiley & Sons, 1979).

67. D. S. Burnett, *Finite Element Analysis* (Reading Mass: Addison-Wesley, 1987).

68. J. W. Gibbs, *The Scientific Papers Vol. II* (New York: Dover Pub. Inc., 1961).

69. J. C. F. Telles and F. A. D. Paula, "Boundary Elements with Equilibrium Satisfaction - a Consistent Formulation for Potential and Elastostatic Analysis," *International Journal of Numerical Methods in Engineering*, **32** (1991) 609–621.

70. J. Trevelyan and H. Hack, "Analysis of stray current corrosion problems using the boundary element method," in *Boundary Element Technology IX* (Boston: Computational Mechanics Publications, 1994) 347–356.

71. S. Aoki and K. Kishimoto, "Application of BEM to Galvanic Corrosion and Cathodic Protection," in *Topics in Boundary Element Research: Electrical Engineering Applications*, C. Brebbia, editor, volume 7 (Heidelberg, Germany: Springer-Verlag, 1990) 103–120.

72. W. Press, S. A. Teukolsky, W. T. Vetterling, and B. P. Flannery, *Numerical Recipes in C: the Art of Scientific Computing*, 2nd edition (New York: Cambridge University Press, 1992).

73. S. Burton, K. E. Garbow, J. J. Hillstrom, and Others, "Modified Powell Method with Analytic Jacobian," Software source code hybrdj.f (1980). Argonne National Laboratory. minpack project. www.netlib.org/minpack.

74. T. J. Hughes, *The Finite Element Method: Linear Static and Dynamic Finite Element Analysis* (Englewood Cliffs, New Jersey: Prentice-Hall, 1987).

75. J. R. Shewchuk, "Triangle: Engineering a 2D Quality Mesh Generator and Delaunay Triangulator," in *First Workshop on Applied Computational Geometry* (Philidelphia: ACM, 1996) 124–133.

76. J. Ruppert, "A Delaunay Refinement Algorithm for Quality 2-Dimensional Mesh Generation," *Journal of Algorithms*, **18** (1995) 548–585.

77. J. R. Shewchuck, "Triangle: Engineering a 2D Quality Mesh Generator and Delaunay Triangulator," in *Applied Computational Geometry: Towards Geometric Engineering*, M. C. Lin and D. Manocha, editors, volume 1148 of *Lecture Notes in Computer Science* (Philadelphia, PA: Springer-Verlag, 1996) 203–222, 203–222. From the First ACM Workshop on Applied Computational Geometry.

78. J. R. Shewchuck, "Triangle.c: A Two-Dimensional Quality Mesh Generator and Delaunay Triangulator," Source Code (1996). www.netlib.org/voroni/triangle.shar and www.cs.cmu.edu/∼quake/triangle.html.

79. G. Beer and J. Meek, "Inifinte Domain Elements," *International Journal of Numerical Methods in Engineering*, **17** (1981) 43–52.

80. M. Aliabadi and W. Hall, "Taylor Expansions for Singular Kernals in the Boundary Element Method," *International Journal of Numerical Methods in Engineering*, **21** (185) 2221–2236.

81. M. Cristescu and G. Loubignac, "Gaussian Quardrature Formulas for Functions with Singularities in $1/r$ over Triangles and Quadrangles," in *Boundary elements VII : proceedings of the 7th international conference, Villa Olmo, Lake Como, Italy, September 1985*, C. Brebbia and G. Maier, editors (New York: Springer-Verlag, 1985) 375–390.

82. H. Pina, J. Fernandes, and C. Brebbia, "Some Numerical Integration Formulae over Triangles and Squares with a $1/r$ Singularity," *Applied Mathematical Modelling*, **5** (1981) 209–211.

83. M. Guiggiani and C. Paolo, "Direct Computation of Cauchy Principal Value Integrals in Advanced Boundary Elements," *Intenational Journal for Numerical Methods in Engineering*, **24** (1987) 1711–1720.

84. M. Guiggiani and A. Gigante, "A General Algorithm for Multidimensional Cauchy Principal Value Integrals in the Boundary Element Method," *Journal of Applied Mechanics*, **57** (1990) 906–915.

85. D. Rosen and D. Cormack, "Singular and Near Singular Integrals in the BEM: A Global Approach," *Society for Industrial and Applied Mathematics: Journal of Applied Mathematics*, **53** (1993) 340–357.

86. O. Almeida Pereira and P. Parreira, "Direct Evaluation of Cauchy Principal Value Integrals in Boundary Elements for Infinte and Semi-infinite Three-Dimensional Domains," *Engineering Analysis with Boundary Elements*, **13** (1994) 313–320.

87. W. Sun and N. Zamani, "An Adaptive h-r Boundary Element Algorithm for the Laplace Equation," *Intenational Journal for Numerical Methods in Engineering*, **33** (1992) 537–552.

88. N. Kamiya and M. Koide, "Adaptive Boundary Element for Multiple Subreqions," *Computational Mechanics*, **12** (1993) 69–80.

89. A. Karafiat, "Adaptive Integration Techniques for Almost Singular Functions in the Boundary Element Method," *Computers Mathematics with Applications*, **32** (1996) 11–30.

90. M. Guiggiana, G. Krishnasamy, T. J. Rudolphi, and F. J. Rizzo, "A General Algorithm for the Numerical Solution of Hypersingular Boundary Integral Equations," *Journal of Applied Mechanics*, **59** (1992) 604–614.

91. R. Cools, D. Laurie, and L. Pluym, *A User Manual for Cubpack++ version 1.1*, K.U. Leuven, Belgium (1997).

92. I. Visual Numerics, "IMSL Subroutines," Software Library (2000).

93. E. De Donker and I. Robinson, "Algorithm for Automatic Integration over a Triangle using Non-linear Extrapolation," *ACM-Tran.s Math. Soft.*, **10** (1984) 1–16.

94. E. De Donker and I. Robinson, "Triex: Integration over a Triangle using Non-linear Extrapolation," *ACM-Tran.s Math. Soft*, **10** (1984) 17–22. *Source code available from http://www.netlib.org/toms/612, May 10, 1999.*

95. R. Cools, D. Laurie, and L. Pluym, "Algorithm 764: Cubpack++: A C++ Package for Automatic Two-Dimensional Cubature," *ACM Transactions on Mathematical Software*, **23** (1997) 1–15.

96. "LAPACK – Linear Algebra PACKage," Source Code (2000). www.netlib.org/lapack accessed November 2, 2000 - version 3.0 available.

97. "BLAS - BLAS (Basic Linear Algebra Subprograms)," Source Code (2000). www.netlib.org/blas accessed November 2, 2000.

98. "Intel® Math Kernal Library," Libaries (archive) (2000). developer.intel.com/vtune/perflibst/mkl Accessed November 2, 2000.

99. J. Newman, "Resistance for Flow of Current to a Rotating Disk," *Journal of the Electrochemical Society*, **113** (1966) 501–502.

100. N. W. Cluts, *Programming the Windows 95 User Interface* (Microsoft Press, 1996).

101. M. Corporation, editor, *The Windows Interface: Guidelines for Software Design* (Microsoft Press, 1995).

102. "OpenGL 3-D Rendering Software v. 1.2," Software Library, Silicon Graphics (1999). www.opengl.org.

103. R. Hall and D. Forsyth, *Interactive 3D Graphics in Windows* (New York: Springer-Verlag, 1995).

104. C. in Perspective, "Joey Toolkit, vers. 5.6," Software (1998). *Windows 95/98/NT, 10MB compressed file*.

105. R. S. Wright and M. Sweet, *OpenGL SuperBible*, 2nd edition (Waite Group, 1999).

106. M. Woo, J. Neider, T. David, D. Shriner, and T. Davis, *OpenGL(r) 1.2 Programming Guide, Third Edition: The Official Guide to Learning OpenGL, Version 1.2*, 3rd edition (Addison-Wesley, 1999).

107. A. J. Davies, "Parallel Implementations of the Boundary Element Method," *Computers Math. Applic*, **31** (1996) 33–40.

108. E. De Santiago and H. Kincho, "A Distributed Finite Element Method for Solving the Incompressible Navier-Stokes Equations," *International Journal for Numerical Methods in Engineering*, **39** (1996) 4243–4258.

109. K. J. Kennelley, L. Bone, and M. E. Orazem, "Current and Potential Distribution on a Coated Pipeline with Holidays: 1. Model and Experimental Verification," *Corrosion*, **49** (1993) 199–210.

110. M. E. Orazem, K. J. Kennelley, and L. Bone, "Current and Potential Distribution on a Coated Pipeline with Holidays: 2. A Comparison of the Effects of Discrete and Distributed Holidays," *Corrosion*, **49** (1993) 211–219.

111. M. E. Orazem, J. M. Esteban, K. J. Kennelley, and R. M. Degerstedt, "Mathematical Models for Cathodic Protection of an Underground Pipeline with Coating Holidays: 2. Case Studies of Parallel Anode CP Systems," *Corrosion*, **53** (1997) 427–436.

112. R. M. Degerstedt, K. J. Kennelley, M. E. Orazem, and J. M. Esteban, "Traditional Cathodic Protection Design Methods for Coated Pipelines and the Necessity of Computer Modeling," *Materials Performance*, **35** (1996) 16–20.

113. S. P. Turnipseed and G. Nekoksa, "Potential Measurement on Cathodically Protected Structures Using an Integrated Salt Bridge and Steel Ring Coupon," *Materials Performance*, **35** (1996) 21–25.

114. C. D. Stears, O. C. Moghissi, and L. Bone, "Use of Coupons to Monitor Cathodic Protection of an Underground Pipeline," *Materials Performance*, **37** (1998) 23–31.

115. K. M. Lawson and N. G. Thompson, "The Use of Coupons for Monitoring the Cathodic Protection of Buried Structures," in *Corrosion 98* (Houston, TX: Nace International, 1998) Paper No. 672.

116. K. J. Kennelley, M. E. Orazem, J. M. Esteban, and R. M. Degerstedt, "Full-Scale Laboratory Evaluation of Parallel Anode CP Systems for Coated Pipelines with Comparison to 2 and 3-D Models," in *Proceedings of Corrosion/95* (Houston, Texas: National Association of Corrosion Engineers, 1995) Paper 528.

117. P. A. Collins, K. C. Garrity, C. J. Pieper, R. P. Siegel, P. J. Smith, and G. E. Tesch, editors, *Aboveground Storage Tanks: Current Issues - Design, Operations, Maintenance, Inspection and the Environment* (Houston, TX: NACE, 1992).

118. L. Koszewski, "Retrofitting Asphalt Storage Tanks with an Improved Cathodic Protection System," *Materials Performance*, **38** (1999) 20–24.

119. M. Abramowitz and I. A. Stegun, *Handbook of Mathematical Functions* (New York, New York: Dover Publications, 1972).

120. D. H. Kroon, "Cathodic Protection of Aboveground Storage Tank Bottoms," *Materials Performance*, **33** (1994) 26–30.

121. W. H. Smyrl and J. Newman, "Detection of Nonuniform Current Distribution on a Disk Electrode," *Journal of the Electrochemical Society*, **119** (1972) 208–212.

122. J. Newman, "Current Distribution on a Rotating Disk below the Limiting Current," *Journal of the Electrochemical Society*, **113** (1966) 1235–1241.

123. W. H. Smyrl and J. Newman, "Ring-Disk and Sectioned Disk Electrode," *Journal of the Electrochemical Society*, **119** (1972) 212–219.

124. NACE, NACE Standard Recomended Practice RP0169, *Control of External Corrosion on Underground or Submerged Metallic Piping Systems*, NACE, Houston, TX (revised 1983).

125. "U.S. Environmental Protection Agency, Title40 Code of Federal Regulations, Parts 280 and 281," (1988).

126. J. A. F. Santiago and J. C. F. Telles, "On Boundary Elements for Simulation of Cathodic Protection Systems with Dynamic Polarization Curves," *International Journal of Numerical Methods in Engineering*, **40** (1997) 2611–2627.

127. S. J.A.F. and T. J.C.F., "A Solution Technique for Cathodic Protection with Dynamic Boundary Conditions by the Boundary Element Method," *Advances in Engineering Software*, **30** (1999) 663–671.

128. S. L. Carson, *Cathodic Protection as a Function of Soil Type*, Master's thesis, University of Florida, Gainesville, FL (1995).

129. B. Stroustrup, *The C++ Programming Language*, 3rd edition (Addison-Wesley Publishing Co., 1997).

130. G. Shepherd, S. Wingo, D. D. McCrory, and S. Wingo, *MFC Internals : Inside the Microsoft Foundation Class Architecture* (Addison-Wesley Publishing Co., 1996).

131. J. Prosise, *Programming Windows With MFC*, 2nd edition (Microsoft Press, 1999).

132. "Visual C++ Enterprise Edition version 6.0," Software and Documentation (1998).

BIOGRAPHICAL SKETCH

The author attended the University of Florida in Gainesville, Florida where he received a Bachelor of Science in Chemical Engineering in 1994 with honors. Following that, he worked for Pipeline Research Council, International, developing "user-friendly" computer models for cathodic protection. In January 1997, the author started attendance at the University of Florida, under the direction of Professor Mark E. Orazem to work toward a Ph.D. in chemical engineering. In October 2000, he received the "Excellence in Scientific Research" award for his presentation at the Graduate Association of Chemical Engineers symposium. Following graduation the author will take up residence in New Jersey where he will work for OLI Systems, Inc., at the position of Scientist.